Author:
James, Alyn D N

Title:
The effect of local correlations on the wave functions and experiment-theory comparisons within strongly and weakly correlated materials

The effect of local correlations on the wave functions and experiment-theory comparisons within strongly and weakly correlated materials

ALYN DAVID NEIL JAMES

Department of Physics
UNIVERSITY OF BRISTOL

A dissertation submitted to the University of Bristol in accordance with the requirements of the degree of DOCTOR OF PHILOSOPHY in the Faculty of Physics.

MARCH 2021

H. H. Wills Physics Laboratory,
University of Bristol,
Tyndall Avenue,
Bristol, BS8 1TL

ABSTRACT

Many-body theories such as dynamical mean-field theory (DMFT) provide a description of the local electron correlation effects that are missing in current density functional theory (DFT) calculations. This thesis presents DFT with DMFT (DFT+DMFT) studies for various materials in which the predicted description of the local electron correlations yields improved agreement with the experiment for certain quantities.

Here, the methodology of the newly developed ELK-TRIQS interface is presented, including how to calculate DFT+DMFT wave functions which can be used to calculate DFT+DMFT wave-function-dependent quantities. This is first illustrated by calculating the electron localisation function (ELF) in monolayer $SrVO_3$ and $CaFe_2As_2$, which provides a means of visualising their chemical bonds. Monolayer $SrVO_3$ ELFs are sensitive to the charge redistribution between the DFT, one-shot DFT+DMFT and fully charge self-consistent DFT+DMFT calculations. In both tetragonal and collapsed tetragonal $CaFe_2As_2$ phases, the ELF changes weakly with correlation induced charge redistribution of the hybridised As p and Fe d states.

The magnetic Compton profiles (MCPs) of Ni and the Compton profiles of V, using both DFT and DFT+DMFT, are presented. For Ni, the theoretical MCPs were calculated using the full potential linear augmented plane wave method with the numerically exact continuous-time quantum Monte Carlo DMFT solver, along with the Korringa-Kohn-Rostoker (KKR) method with the perturbative spin-polarised T-matrix fluctuation exchange approximation DMFT solver. The spin magnetic moments decrease with the intra-atomic Coulomb repulsion U, which is also reflected in the corresponding MCPs. The total magnetic moment obtained from the superconducting quantum interference device measurements can be reproduced by intermediate values of U. However, the MCP shape still disagrees with the experiment. The spectral function reveals that the minority X_2 Fermi surface pocket shrinks and gets shallower with respect to the DFT calculations. For V, The addition of DMFT improves the Compton profile directional differences significantly, but these differences are fairly independent of the U values used. There are improvements in the spectral function with respect to the corresponding experimental quantities, except for the N-hole ellipsoid Fermi surface pocket sizes which worsen. For both Ni and V, there is a vital need to include the missing electron correlations beyond the DFT+DMFT picture.

With the increasing interest in superlattice systems described by DMFT, here the metal-insulator transition (MIT) of strongly correlated $3d$ electrons in $SrVO_3$ superlattices is shown to be due to quantum confinement. By producing excellent agreement between experiment and theoretical spectroscopic quantities, the underlying physics in these systems is captured by DMFT. New light is shed on the microscopic mechanism of the MIT and previously reported anomalous subband mass enhancement, both of which arise as a direct consequence of the quantization of V $xz(yz)$ states in the $SrVO_3$ layers. Therefore, quantum confinement can tune the strength of electron correlations.

ACKNOWLEDGEMENTS

Firstly, I would like to thank my supervisor Stephen Dugdale for the PhD project he offered and the experiences it led onto. With his guidance, I've learnt a lot about academia and many other life skills. During my time working with him, I've learnt that when he's impressed, he pats the person on the shoulder or maybe that's unique to me because of the height difference.

Secondly, I'm very grateful for the work I did with Jude Laverock, who not only mentored me during the first six months of my PhD (where I took many lectures and courses which were a part of the Centre of Doctoral Training in Condensed Matter Physics [CDT-CMP] PhD program), but we have also collaborated with each other throughout the duration of my post-graduate research. I thoroughly enjoyed the many hours we spent in his office discussing and interpretating results.

I would like to acknowledge Eddie Harris-Lee, who is another PhD student of Stephen's and started several months after me. We've spent many hours discussing the physical phenomena in different materials predicted from the theories we used. However, I've enjoyed more the time we spent together socially, at SPring-8 (in Japan), and the holiday we had with Ciara Mackellar exploring the Kansai region of Japan. I've also enjoyed the time I spent with Stephen's other current PhD students - Ciara, Wenhan Chen, and Max Favaro-Bedford. I wish them all the best with their PhD and I hope they'll enjoy it as much as I did.

Next, I would like to thank Markus Aichhorn who graciously invited me to visit him and his group in Graz, Austria, where I learnt a lot about DMFT from him and his (old and recent) PhD students. I am very fortunate to be in continuous contact with them since. I would also like to thank Markus and the other TRIQS developers for inviting me to their developers meeting in Paris, France, where I was lucky to be given such a unique opportunity to discuss my work with many leading experts in the field, as well as making new contacts and learning a lot from everyone there. This is where I met Alex Hampel and we went on to collaborate with my interface project.

I cannot continue without mentioning Jon Duffy, Jon Taylor, Sean Giblin and Dave Billington who are the "usual suspects" when it came to joining us for the Compton scattering experiments. Their fruitful knowledge and discussions (which often tended to not be about physics!) helped pass the time at SPring-8. During the recent unprecedented times, escaping to the infamous cave is more appealing with each day that passes. I would like to give thanks to Nakamura-san (who was Dave's boss when they worked at SPring-8) for the XMCD collaboration as well as the insightful suggestions he made for the Japan holiday.

I was fortunate to go to the ELK workshop in Halle, Germany, where I met (John) Kay Dewhurst and Sangeeta Sharma who are the main ELK code developers. Eddie and I stayed afterwards, where we discussed our work with them and they gave me some very valuable tips for code development. They were very kind and welcoming with an invite to dinner with them, it was there where I unexpectedly learnt of Kay's hobby of constructing bicycles!

Near the end of my PhD, I had the wonderful opportunity to collaborate with Liviu Chioncel

and (Mikheil) Misha Sekania who are based in Augsburg, Germany. They are leading experts in the DFT+DMFT EMD calculations. Unfortunately, I did not manage to meet them in person (because of the small matter of the global pandemic), but hopefully this will be rectified in the foreseeable future. However, we did have many Skype meetings where their light hearted character was able to shine through. I'm grateful for the knowledge I have learnt from them.

There are a few other people who I would like to acknowledge who have finished their time in academia. Tom Millichamp (one of the people who inspired me to work with Stephen), Hannah Robarts, Daniel Lagos, Dan O'Neill, Dave Hughes, Abi Coveney, and Dave Ernsting all of whom I have got to know either during my PhD, masters or summer internship with Stephen. I appreciate the discussions we had about physics (but we mainly chatted about unrelated topics). Also, I like to acknowledge Ashraf Alam who was Stephen's PhD supervisor, and, like many retired academics, he was found to be still in the office (before the pandemic!), where we had many interesting conversations which were barely related to physics.

Of course, I gratefully acknowledge the (now discontinued) CDT-CMP and all of the amazing admin and lecturers who worked behind the scenes for us PhD students. I would like to thank everyone in all of the cohorts for the socials we had (trying to break the stereotype of being unsociable physicists!). Also, I would like to thank Callum Wright and the other admin at the Advanced Computing Research Centre for helping me with the issues I came across when using the University's supercomputers. I graciously acknowledge the funding I received from the engineering and physical sciences research council (EPSRC) via the CDT-CMP.

I cannot emphasise more the gratitude that I have for all of my close friends in and outside of academia who have supported me through the last several years. I'm lucky to know such wonderful people. Unfortunately, it would take entire length of the thesis to express my appreciation for each individual!

Lastly, I want to give my love and appreciation to my family, especially my mum, dad, and sister. I would not have done any of this if it wasn't for your encouragement, thoughtfulness, and helpfulness (in all possible ways). I am indeed a very lucky person to have such unrelenting support from some incredibly people. Finally, I want to acknowledge my dog Indianna (named by me for obvious reasons), as she knows when I've spent too long doing work and not paying her enough attention!

For my Uncle Rob
Although now, new experiences are no longer an option,
here, in these words, your memory will not be forgotten.

AUTHOR'S DECLARATION

I declare that the work in this dissertation was carried out in accordance with the requirements of the University's Regulations and Code of Practice for Research Degree Programmes and that it has not been submitted for any other academic award. Except where indicated by specific reference in the text, the work is the candidate's own work. Work done in collaboration with, or with the assistance of, others, is indicated as such. Any views expressed in the dissertation are those of the author.

SIGNED: ALYN JAMES DATE: 1/3/2021

Table of Contents

ACRONYMS

Notation	Description
1BZ	First Brilluoin Zone
1D, 2D, 3D	One, Two, Three Dimensional
2D-ACAR	Two-Dimensional Angular Correlation of Annihilation Radiation
AFM	Anti-FerroMagnetic
AIM	Anderson Impurity Model
AMF	Around the Mean-Field
APW	Augmented Plane-Wave
APW+lo	Augmented Plane-Waves with local orbitals
ARPES	Angle Resolved Photoemission Spectroscopy
BCC	Body-Centred Cubic
BZ	Brillouin Zone
CCD	Charge Coupled Device
CF	Crystal Field
CTAUX	Continuous-Time AUXilary-field (solver)
CTHYB	Continuous-Time HYBridisation expansion (solver)
CTINT	Continuous-Time INTeraction expansion (solver)
cLDA	constrained-Local Density Approximation
cRPA	constrained-Random Phase Approximation
CTQMC	Continuous-Time Quantum Monte Carlo
DFT	Density Functional Theory
DFT+DMFT	Density Functional Theory with Dynamical Mean-Field Theory
dHvA	de Haas van Alphen
DMFT	Dynamical Mean-Field Theory
DΓA	Dynamical vertex (Γ) Approximation
DOS	Density Of States
ELF	Electron Localisation Function
EMD	Electron Momentum Density
FCC	Face-Centred Cubic
FCSC	Fully Charge Self-Consistent
FLEX	FLuctuating EXchange approximation
FLL	Fully-Localised Limit
FP	Full Potential
FWHM	Full-Width-at-Half-Maximum
GGA	Generalised Gradient Approximation

GW	Hedin's GW approximation
G0W0	one-shot GW
HEG	Homogeneous Electron Gas
HF	Hartree-Fock
IBZ	Irreducible Brillouin Zone
imp	impurity
KKR	Korringa-Kohn-Rostoker
KKR+DMFT	Korringa-Kohn-Rostoker with Dynamical Mean-Field Theory
LAPW	Linearised Augmented Plane-Wave
LDA	Local Density Approximation
LDA+U	Local Density Approximation with U parameter
LSAT	$(LaAlO_3)_{0.3}(Sr_2TaAlO_6)_{0.7}$
LSDA	Local Spin Density Approximation
MCP	Magnetic Compton Profile
MEM	Maximum Entropy Method
MIT	Metal-Insulator Transition
MT	Muffin-Tin
NM	Non-magnetic
OS	One-Shot
PBE	Perdew-Burke-Ernzerhof
PSD	Position Sensitive Detector
PP	Pseudo Potential
QP	QuasiParticle
QSGW	Quasiparticle Self-consistent GW
QSGW+DMFT	Quasiparticle Self-consistent GW with Dynamical mean-field theory
QTB	Quantized Tight-Binding
QW	Quantum Well
RIXS	Resonant Inelastic X-ray Spectroscopy
SCAN	Strongly Constrained and Appropriately Normed
SL	SuperLattice
SOC	Spin-Orbit Coupled
SQUID	Superconducting QUantum Interference Device
TB	Tight-binding
TRIQS	Toolbox for Research on Interacting Quantum Systems
UHB	Upper Hubbard Band
XAS	X-ray Absorption Spectroscopy

LIST OF TABLES

LIST OF FIGURES

FIGURE **Page**

CHAPTER 1

INTRODUCTION

The field of condensed matter physics has been the pivotal component in the continual advances and innovation in modern day technologies. A poignant example of the impact of condensed matter physics research is the semiconductor revolution [1]. The continual improvement of semiconductor components has allowed for the electronic devices to reduce in size as well as increasing in computational power. Such a profound development of electrical components led to Gordon Moore in 1965 to propose that the number of components that could be crammed into an integrated circuit would double every two years for the foreseeable future; this is now commonly referred to as Moore's law [2].

Over the last several decades, the experimental probes and theoretical techniques have become more sophisticated which has helped to unravel the origin of certain material properties, where this is the focus of certain topics within modern day research. These topics range from topological [3] and unconventional superconductors [4], Hund and Mott materials [5–7], and the quantum critical point [8]. It was only very recently that the highly desired room temperature superconductivity has been achieved [9], but it has some way to go before it will have practical applications. However, all of these phenomena come down to the complex electron correlations within the materials of interest. Within the so-called "strongly correlated" materials, where the (screened) interaction energy between electrons is comparable with their kinetic energy, their electron-electron interactions lead to many-body behaviour beyond the Fermi-liquid regime and are responsible for the emergence of qualitatively new phenomena [10]. Examples of such materials are transition metal oxides which have properties as diverse as colossal magnetoresistance, high-temperature superconductivity, and Mott insulating phases, each of which have huge potential for future device and technology applications [11–13]. It is the study of the electronic structure in crystalline materials which has unravelled the previously unexplained secret driving force behind the observed phases of matter, which could be used for future technologies. Therefore,

there is a drive to synthesise new materials with properties from these prominent electron correlations, but in order to do so effectively, an understanding of the electron correlations present in real materials, as well as powerful predictive tools, is needed. This way, the technological push will be able to continue.

The motivation of this thesis is to understand and address the discrepancies between the experimental data and start-of-the-art theoretical techniques for several materials in which the electron correlations play a significant role, either in the case where the material is "strongly correlated" or "weakly correlated" (in which the interaction energy between electrons is relatively small compared with their kinetic energy, such that the system can be described within the Fermi-liquid regime). The focus will be on improving the theoretical description of real materials with the (many-body) dynamical mean-field theory (DMFT) merged with density functional theory (DFT) – the DFT+DMFT method – and how this better agrees with the experimental data. Not only will the spectroscopic properties be presented here, as has been done for a plethora of many-body studies for real materials, but so will the relatively rarely investigated wave-function-dependent quantities of materials, such as the electron momentum density (EMD). Here, a wave-function-dependent quantity is an observable which is an explicit function of the wave functions and occupation functions. Importantly, these wave-function-dependent quantities do not require analytic continuation, which avoids the issues which may arise from that method. These quantities give another valuable perspective of the electron correlations in the electronic structure. Comprehending the importance of these electron correlations is vital for resolving and understanding the discrepancies within the presented materials, and this will lead onto clearer interpretations of the vast amount of exotic behaviour the electron correlations are responsible for in other materials.

The first important milestone in understanding the electronic structure came from the discovery of the electron itself, which is a charged particle with an intrinsic magnetic moment known as spin, and obeys both the Pauli exclusion principle and Fermi-Dirac statistics. Without these properties, matter would behave very differently. The next step was the description of how electrons manifest themselves in atoms and then crystalline solids, as explained within the quantum mechanical framework. These concepts of crystal structures led to the fundamental theories of electronic structure properties. More complex models build on these fundamental concepts. If it was not for the ever evolving theoretical models, the observed physical phenomena (such as those previously mentioned) would still remain a mystery. Although many physical phenomena have been understood for many decades, they have mainly been predicted in simpler "toy" theoretical models which do not have the complexity of real materials. Chapter 2 of this thesis will discuss the core concepts and theories which are needed for this thesis.

The biggest challenge in solving the many-body Hamiltonian for the electrons in real materials is that it would require solving the system for all $\sim 10^{24}$ electrons present. However, there is a way to reformulate this problem to make it computationally solvable by using DFT. This is

a powerful tool used to predict the electronic structure of real materials, but it has practical limitations. The main limitation is that the approximations used in DFT are unable to describe the complex electron correlations in many materials. Therefore, it has been the ambition to improve upon these limitations to get better agreement with experimental quantities. Within the last 30 years or so, significant developments have been made to predict the missing information in DFT calculations. These ever evolving improvements have been implemented for real material calculations, with the focus being on the DFT+DMFT method in this thesis. However, DMFT has its own approximations and limitations. These concepts will be the focus of Chapter 3.

This thesis presents the interface between the ELK code [14] and the toolbox for research on interacting quantum systems (TRIQS) library [15] (both of which are open source), so that DFT+DMFT calculations can be performed with these codes. The results of testing this interface are shown in Chapter 4. The benchmarking of this interface with the previous established WIEN2K interface [16] is also discussed in that chapter, along with introducing the calculation of the DFT+DMFT electron localisation function (ELF) wave-function-dependent quantity. This was computed with the DFT+DMFT wave functions (and occupations) for monolayer $SrVO_3$ and $CaFe_2As_2$. However, the ELF does not have an experimental counterpart to compare with.

With the further development of the theoretical techniques, it is important to ensure that there are sufficient high quality experimental data to compare the theory to. Not only will improving the theoretical models aid in (hopefully) better experiment-theory comparisons, but the comparisons will help to understand the effect the improvement in the theory has on describing real materials. One of the important concepts of the electronic structure is the Fermi surface – the isosurface which separates occupied and unoccupied electron states. Many properties are associated to the Fermi surface, such as the conduction, magnetism, structural phase and so on [17]. Compton scattering is a technique which can measure the Fermi surface and is the subject of Chapter 5. There are many other techniques which can measure the Fermi surface such as quantum oscillations (such as de Haas van Alphen), angle-resolved photoemission spectroscopy (ARPES), and 2D angular correlation of annihilation radiation (2D-ACAR). Each of these techniques have their own advantages and disadvantages which will be discussed. The DFT+DMFT results of Ni and V in Chapter 5 will focus on the comparison of experimental data from Compton scattering measurements with the related quantities derived from the wave-function-dependent EMD. Compton scattering is the only experiment which can truly probe the many-body ground-state electron wave function [18–21]. This chapter will also present and discuss other experiment-theory comparisons using the materials' calculated spectral function and the corresponding experimental quantities.

Chapter 6 discusses the DFT+DMFT study on $SrVO_3/SrTiO_3$ superlattices (SLs) previously measured with resonant inelastic X-ray scattering (RIXS) and X-ray absorption spectroscopy (XAS) [22]. These correlated SLs have been experimentally proven to show a metal insulator transition (MIT) with respect to the number of $SrVO_3$ layers. This chapter reproduces the

experimental results as well as explaining the origin of the MIT – here, a quantum confinement induced transition – made possible by the strong correlations present. This may have significant implications in the research of electronics with correlated materials.

Finally, Chapter 7 summarises the work presented in this thesis as well as providing an outlook into other theoretical methods which account for the remaining deficiencies within DFT+DMFT. Including these theories will improve upon the theoretical description and hopefully reduce the experiment-theory discrepancies for (at least) the materials discussed in this thesis.

Parts of this thesis are based on results which have been presented in Refs. [23–25]. For clarity, each relevant chapter will explicitly state which reference the chapter is based on and who else contributed to the presented work.

The calculations presented in this thesis were performed using the computational facilities of the Advanced Computing Research Centre, University of Bristol [26]. The VESTA package [27] has been used in the preparation of some figures in this thesis.

CHAPTER 2

ELECTRONS IN CRYSTALS

2.1 Core condensed matter concepts

From the discovery of the electron by J. J. Thomson [28, 29] to the Drude model [30, 31], it has been the ambition to understand the dynamics of electrons in materials and how this relates to the material's macroscopic properties. To that point, decent predictions can be made by using relatively simple models. However, more sophisticated models, some of which have been used in this thesis, have been developed with their own successes and failures. Before those types of models are discussed in depth, this chapter will establish the fundamental concepts needed for the work presented in this thesis.

For further reading, the fundamental concepts, and the free and nearly-free electron models are taught in many condensed matter undergraduate courses and a lot of the material can be found in the following Refs. [32–37]. The second half of this chapter delves into second quantization and other concepts required for many-body theory; useful references for this content include Refs. [37–40]. This chapter ends with a discussion of Fermi-liquid theory which is described in references such as Refs. [32, 37, 39, 41, 42]. This chapter draws on ideas developed in some of the aforementioned references.

In this thesis, the presented equations will be in terms of natural (atomic) units. In these units, the electric charge (e), reduced Planck constant ($\hbar$), electron mass (m_e), and Bohr radius (a_0) values[1] are equal to one (and therefore they do not appear in the equations).

Crystals, or crystalline solids, in terms of condensed matter physics refer to materials which can be described by a Bravais lattice – a lattice structure with each lattice point representing a basis of atoms. The Bravais lattice has translation symmetry which means that a unit cell

[1] This also means that the Coulomb constant ($[4\pi\epsilon_0]^{-1}$) is equal to one.

can be used to describe any region of the lattice (assuming that the shape of the unit cell is constructed such that it encloses the space without overlapping or leaving voids when it is translated throughout the system). One choice for the smallest unit cell in real-space is called the Wigner-Seitz cell and the cell boundaries are derived from points which are equidistant from the nearest-neighbour lattice points. The three-dimensional (3D) real-space translation or position ($\mathbf{R}$) can be mathematically represented by

$$\mathbf{R} = n_1\mathbf{a}_1 + n_2\mathbf{a}_2 + n_3\mathbf{a}_3, \tag{2.1}$$

where $\mathbf{a}_i$ is the ith dimension lattice basis vector and n_i is an integer for the ith dimension. However, in many X-ray diffraction experiments such as Laue diffraction, the reciprocal lattice is measured instead of real-space lattice. The reciprocal lattice ($\mathbf{G}$) is the equivalent of the real-space lattice in Fourier space with the condition

$$\mathbf{G}\cdot\mathbf{R} = 2n\pi, \tag{2.2}$$

where n is an integer and $\mathbf{G}$ is expressed as

$$\mathbf{G} = h\mathbf{b}_1 + k\mathbf{b}_2 + l\mathbf{b}_3 \tag{2.3}$$

with coefficients h, k, l, and the reciprocal lattice vectors $\mathbf{b}_i$ being related to the real-space lattice vectors by

$$\mathbf{b}_1 = 2\pi\frac{\mathbf{a}_2\times\mathbf{a}_3}{\mathbf{a}_1\cdot(\mathbf{a}_2\times\mathbf{a}_3)};\quad \mathbf{b}_2 = 2\pi\frac{\mathbf{a}_3\times\mathbf{a}_1}{\mathbf{a}_1\cdot(\mathbf{a}_2\times\mathbf{a}_3)};\quad \mathbf{b}_3 = 2\pi\frac{\mathbf{a}_1\times\mathbf{a}_2}{\mathbf{a}_1\cdot(\mathbf{a}_2\times\mathbf{a}_3)}. \tag{2.4}$$

It is more natural to work within reciprocal space as many quantities which are compared with experiment (such as energy eigenvalues) are more easily obtained in this formalism. The reciprocal lattice has the same translational symmetry condition as real-space and as such, has a smallest reciprocal lattice unit cell derived in the same manner as the Wigner-Seitz cell. This cell in reciprocal space is called the first Brillouin zone (1BZ). By the use of rotation and other symmetry operations, the 1BZ can be reduced into a smaller fraction of the cell called the irreducible Brillouin zone (IBZ). The use of the IBZ instead of the 1BZ in computational modelling drastically reduces the computation time.

Now that the framework of modelling materials with a lattice structure has been established, the behaviour of electrons in such systems can be investigated.

2.1.1 Free and nearly-free electron systems

To understand the outputs of real material models, the solutions of simpler systems such as the free electron model and the nearly-free electron model are needed to be understood. In these models, the electrons are treated as being within a perfect lattice system and they are independent of each other[2]. The free electron model is formulated using the time-independent Schrödinger equation

$$H\Psi_j(\mathbf{r}) = \epsilon_j \Psi_j(\mathbf{r}), \tag{2.5}$$

where $\Psi_j(\mathbf{r})$ is the jth independent electron wave function at position $\mathbf{r}$, ϵ_j is the energy eigenvalue of that electron, and H is the Hamiltonian operator which has the form

$$H = \frac{1}{2}\nabla^2, \tag{2.6}$$

where ∇ is the differential operator. There is no potential term in this Hamiltonian. The solution to a Schrödinger equation describing the perfect lattice system requires the Born-von Karman boundary condition which avoids any surface effects in the system. Therefore, for an independent electron (i.e. dropping the j index), the wave functions (which are plane-waves in this model) and energy eigenvalues are

$$\Psi_{\mathbf{k}}(\mathbf{r}) = \frac{1}{\sqrt{V}} e^{i\mathbf{k}\cdot\mathbf{r}} \quad \text{and} \quad \varepsilon_{\mathbf{k}} = \frac{1}{2}|\mathbf{k}|^2, \tag{2.7}$$

where V is the volume of the crystal and $\mathbf{k}$ is the k-point within the crystal, along with the Born-von Karman boundary condition (in 3D) ($\frac{2\pi m_x}{L_x}$, $\frac{2\pi m_y}{L_y}$, $\frac{2\pi m_z}{L_z}$), where L_i is the length of the system for dimension i and m_i is an integer of the dimension i. For large values of L_i[3], these solutions give a quasi-continuous $\varepsilon_{\mathbf{k}}$ verses $\mathbf{k}$ spectrum.

To start to model a more realistic crystal system (which we will assume has a perfect lattice with the Born-von Karman boundary condition), an additional potential term needs to be added to the Hamiltonian. The time-independent Schrödinger equation with a potential term in the Hamiltonian is

$$H = \frac{1}{2}\nabla^2 + v(\mathbf{r}), \tag{2.8}$$

[2]Note that the free electron model has zero periodicity in the system as there is no periodic potential term in the Hamiltonian (the periodic term in the electron's "Bloch wave function" is constant). Here instead, we assume that the free electron model is of the electrons within a lattice with no periodic potential (the potential is assumed to be zero), which is referred to as the empty lattice approximation.

[3]Otherwise, this leads to (distinct) discrete energies and momenta, with this discrete nature being referred to as quantization. This leads to other physical phenomena which is the subject of Chapter 6.

where $v(\mathbf{r})$ is the potential term and has discrete translational invariance $v(\mathbf{r}) = v(\mathbf{r}+\mathbf{R})$. The solutions of this Hamiltonian produce wave functions of the form

$$\Psi_{\mathbf{k}}(\mathbf{r}) = e^{i\mathbf{k}\cdot\mathbf{r}} u_{\mathbf{k}}(\mathbf{r}), \tag{2.9}$$

where $u_{\mathbf{k}}(\mathbf{r})$ is a function which has translational symmetry $u_{\mathbf{k}}(\mathbf{r}) = u_{\mathbf{k}}(\mathbf{r}+\mathbf{R})$. These wave functions are the general form of the solution to this Hamiltonian which are derived from Bloch's theorem. This important theorem allows the wave function to be written in a form similar to the plane-waves in the free electron model, but with an additional function which incorporates the periodicity of the crystal potential. The nearly-free electron model is a similar system to the free electron model with a system of independent electrons[4], but the potential term is simple and weak.

The inclusion of this weak potential term causes noteworthy changes to the solutions of this system with respect to the free electron model. In Fig. 2.1 (a), the quasi-continuous $\varepsilon_{\mathbf{k}}$ verses $\mathbf{k}$ spectrum is plotted (along a path of desired $\mathbf{k}$ values) for both models. A consequence of solving the nearly-free model is the introduction of distinct bands with band gaps between them. The $\varepsilon_{\mathbf{k}}$ verses $\mathbf{k}$ spectrum in Fig. 2.1 (a) is commonly referred to as a band structure which, by translational invariance, the entire energy spectrum can be translated into the 1BZ (the energy spectrum has been plotted within the reduced zone scheme). For 3D systems, band structures are normally plotted along high-symmetry directions in the BZ(s).

The other important condition required in these models is the conservation of the number of electrons. Due to the electrons being fermions (and obeying Fermi-Dirac statistics), the number of electrons (N) can be calculated by

$$N = \int_{-\infty}^{\infty} D(\varepsilon) f(\varepsilon, T) d\varepsilon, \tag{2.10}$$

with $D(\varepsilon)$ being the density of states (DOS) and $f(\varepsilon, T)$ is the Fermi-Dirac function at temperature T. The 3D free electron $D(\varepsilon)$ and Fermi-Dirac function have the form

$$D(\varepsilon) = \frac{\mathrm{d}N}{\mathrm{d}\varepsilon} = \frac{V}{\pi^2}(2\varepsilon)^{1/2} \quad \text{and} \quad f(\varepsilon, T) = [1 + \exp(\beta\varepsilon)]^{-1}, \tag{2.11}$$

where β equals to $(k_{\mathrm{B}}T)^{-1}$ with k_{B} referring to the Boltzmann constant. For a metal at 0 K, the $D(\varepsilon)f(\varepsilon, T)$ function steps down sharply to zero at a certain energy (with this step being smoothed out for non-zero temperatures). This energy is referred to as the Fermi level, ε_{F} (or Fermi energy at 0 K). The (3D) isosurface at ε_{F} in the 1BZ is called the Fermi surface, see Fig. 2.1 (b). Formally, the Fermi surface is defined as the boundary between occupied and unoccupied (crystal) momentum states. This boundary can be seen in the electron occupation function $n_{\mathbf{k}}$ where there

[4] Technically electron quasiparticles.

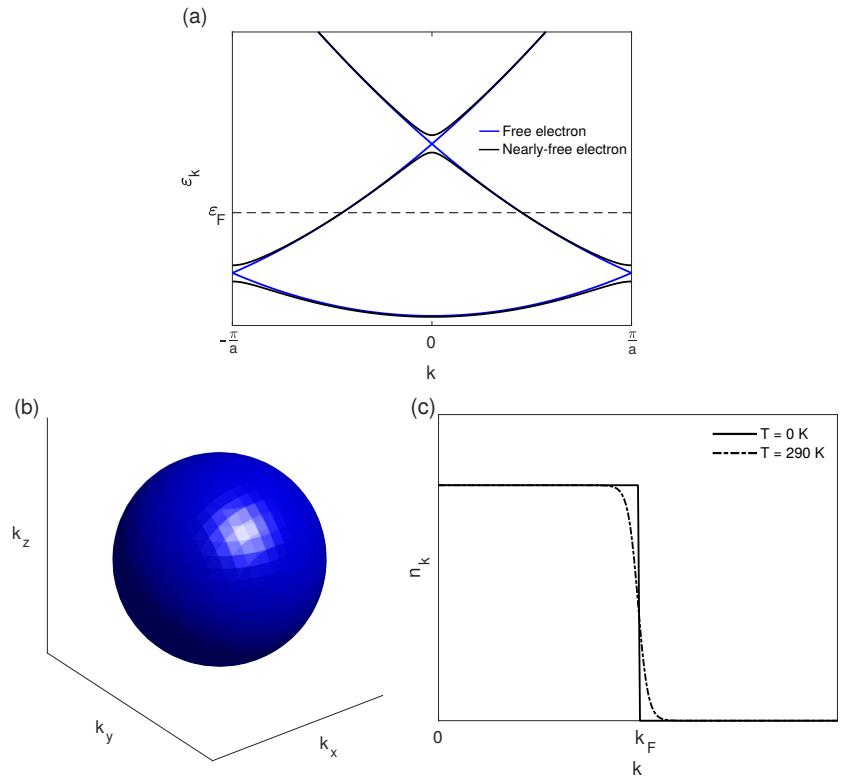

Figure 2.1: (a) The 'free' and 'nearly-free' electron band structures along a path starting and ending at the BZ boundaries of $\pm\pi/a$ and passing though the 1BZ centre ($k = 0$). The Fermi energy is denoted as ε_F. The 'free' electron (b) 3D isotropic Fermi surface and (c) (Fermi-Dirac) occupation function along one of the reciprocal axes and evaluated at different temperatures T. (This occupation function will be same along any k-path starting at $k = 0$ and ending at the 1BZ boundary due to the isotropic nature of the 'free' electron Fermi surface.)

is a sharp discontinuity at 0 K at the Fermi wave vector $\mathbf{k}_F$ in Fig. 2.1 (c). This discontinuity is smeared at non-zero temperatures, as shown in Fig. 2.1 (c).

In the nearly free electron model, it is possible to have a completely filled band (which corresponds to two electrons per unit cell in this model, due to Pauli's exclusion principle) at the Fermi level – this results in the system being an insulator. For an insulator, $D(\varepsilon)$ is zero at the Fermi level (as all of the states are occupied) and as such, insulators do not have a Fermi surface and the Fermi level is often defined to be the mid-point of the energy band gap.

2.2 Introduction to many-body theory concepts

Up to this point, we have looked at the non-interacting case of electrons, but treating the interactions becomes a difficult task. There are tricks in which this can be simplified for certain systems, such as using canonical transformations [43, 44], or performing perturbation theory which is only valid for small perturbations. When those methods cannot solve the problem, an

alternative strategy (which is the subject of this chapter) is to use the methods from quantum field theory, namely Feynman diagrams [38, 45]. This section will introduce simple concepts relating to how to go about solving the many-body theory, along with the tools required to do so.

The previous sections have discussed electrons in terms of their wave functions. However, the system can be represented in the Heisenberg formalism where the operators evolve with time instead of the wave function – this formalism is used within many-body theories.

First, the single-electron propagator, $G(\mathbf{r}_2, \mathbf{r}_1, t_2 - t_1)$, needs to be defined. This is the probability amplitude of adding an electron at ($\mathbf{r}_1$,t_1) to the ground state interacting system and then observe that system in its ground state with the added electron at ($\mathbf{r}_2$,t_2). During this time interval, the propagator will describe all the interactions this electron has with the interacting medium[5]. The square of the modulus of the probability amplitude $|G|^2$ is equal to the probability of the propagation occurring. The propagator is in fact called a Green's function[6]. Therefore, from this point onwards, the propagator will be referred to as the Green's function.

The general form of the Green's function is given by (in k-space)

$$G(\mathbf{k}_2, \mathbf{k}_1, t_2 - t_1) = -i \left\langle \Psi_0 \left| \mathcal{T} \left\{ c_{\mathbf{k}_2}(t_2) c^{\dagger}_{\mathbf{k}_1}(t_1) \right\} \right| \Psi_0 \right\rangle, \tag{2.12}$$

where $|\Psi_0\rangle$ is the ground state interacting system, $c^{(\dagger)}_{\mathbf{k}_1}(t_1)$ is the annihilation (creation) operator at state $\mathbf{k}_1$ and t_1. Here these operators are in the Heisenberg picture, with the time evolution defined as

$$c^{(\dagger)}_{\mathbf{k}_1}(t_1) = e^{iHt_1} c^{(\dagger)}_{\mathbf{k}_1} e^{-iHt_1}. \tag{2.13}$$

Finally, the $\mathcal{T}$ is the time-ordering operator which ensures causality (or "proper time order"):

$$\begin{aligned} \mathcal{T} \left\{ c_{\mathbf{k}_2}(t_2) c^{\dagger}_{\mathbf{k}_1}(t_1) \right\} &= c_{\mathbf{k}_2}(t_2) c^{\dagger}_{\mathbf{k}_1}(t_1) \qquad \text{for } t_2 > t_1 \\ &= -c^{\dagger}_{\mathbf{k}_1}(t_1) c_{\mathbf{k}_2}(t_2) \qquad \text{for } t_2 \leq t_1. \end{aligned} \tag{2.14}$$

Lastly, from the time ordering, the Green's function can be split into two Green's functions called the retarded (G^+) and advanced (G^-) Green's functions

$$G(\mathbf{k}_2, \mathbf{k}_1, t_2 - t_1) = G^+(\mathbf{k}_2, \mathbf{k}_1, t_2 - t_1) + G^-(\mathbf{k}_2, \mathbf{k}_1, t_2 - t_1) \tag{2.15}$$

with both types of Green's function having the following expressions

[5] Note that this definition can be extended to the two particle propagator, and so on, with additional particles added at different intervals.

[6] A "true" Green's function is an operator used to solve differential equations, which in this case would be used to solve the Hamiltonian.

$$
\begin{aligned}
G^{+}(\mathbf{k}_2,\mathbf{k}_1,t_2-t_1) &= -i\theta_{t_2-t_1}\left\langle \Psi_0 \left| \left[c_{\mathbf{k}_2}(t_2), c^{\dagger}_{\mathbf{k}_1}(t_1) \right]_{+} \right| \Psi_0 \right\rangle \\
G^{-}(\mathbf{k}_2,\mathbf{k}_1,t_2-t_1) &= +i\theta_{t_1-t_2}\left\langle \Psi_0 \left| \left[c_{\mathbf{k}_2}(t_2), c^{\dagger}_{\mathbf{k}_1}(t_1) \right]_{+} \right| \Psi_0 \right\rangle,
\end{aligned}
\tag{2.16}
$$

where $[\ ]_+$ means the anticommutator, and $\theta_{t_2-t_1}$ is a (Heaviside) step function[7] with the property

$$
\theta_x \begin{cases} = 1, & \text{for } x > 0 \\ = \frac{1}{2}, & \text{for } x = 0 \\ = 0, & \text{for } x < 0. \end{cases}
\tag{2.17}
$$

Now that the Green's function has been defined, we can look at the free electron Green's function as an example of a non-interacting system. At t_2, the free electron wave function $\psi(\mathbf{k}_1)$ of the added free electron which started at t_1 is equal to $\psi(\mathbf{k}_1)e^{-i\varepsilon_{\mathbf{k}_1}(t_2-t_1)}$. The Green's function is calculated by the overlap of this time-evolved state with $\psi(\mathbf{k}_2)$. Therefore, by using $t = t_2 - t_1$ and the fact that the free electron wave functions are orthonormal, so only the $\mathbf{k}_1 = \mathbf{k}_2 = \mathbf{k}$ electron wave function remains in the overlap, the (free electron) non-interacting Green's function is

$$
G^0(\mathbf{k},t) \begin{cases} = -i\left[\theta_t \theta_{\varepsilon_{\mathbf{k}}-\varepsilon_{\mathrm{F}}} e^{-i\varepsilon_{\mathbf{k}}t} - \theta_{-t}\theta_{\varepsilon_{\mathrm{F}}-\varepsilon_{\mathbf{k}}} e^{-i\varepsilon_{\mathbf{k}}t}\right], & t \neq 0 \\ = +i\theta_{\varepsilon_{\mathrm{F}}-\varepsilon_{\mathbf{k}}}, & t = 0. \end{cases}
\tag{2.18}
$$

Fourier transforming $G^0(\mathbf{k},t)$ into frequency (ω) space, results in the following (more familiar) form

$$
G^0(\mathbf{k},\omega) = \frac{1}{\omega - \varepsilon_{\mathbf{k}} + i\delta_{\mathbf{k}}},
\tag{2.19}
$$

where the term $i\delta_{\mathbf{k}}$ is an infinitesimal small imaginary part which is needed to ensure that the (free electron) non-interacting Green's function converges to a solution when performing the Fourier transform. Here, $\delta_{\mathbf{k}}$ has the form

$$
\delta_{\mathbf{k}} \begin{cases} = +\delta, & \varepsilon_{\mathbf{k}} > \varepsilon_{\mathrm{F}} \\ = -\delta, & \varepsilon_{\mathbf{k}} < \varepsilon_{\mathrm{F}}. \end{cases}
\tag{2.20}
$$

Here, $\delta_{\mathbf{k}}$ has this change of sign above and below the Fermi level to ensure that only the occupied states are included in the (complex contour) integrals. Another way to think of this is that the sign of $\delta_{\mathbf{k}}$ relates to the zero temperature (non-interacting) occupation function.

Now that the (free electron) non-interacting Green's function has been derived, the next step would be to calculate the full interacting Green's function $G(\mathbf{k},\omega)$. All of the interactions the

[7] Here we have used the definition of $\theta_0 = 1/2$.

particle has with the interacting medium (in this case, of the single electron Green's function) are described in terms of Feynman diagrams, which gives a visual aid to the probability amplitudes of the different types of interactions present. The total Green's function (probability amplitude) will be the sum of all of the possible Feynman diagrams existing in this system. However, it still remains a challenge to sum all the diagrams and as such, a lot of the many-body physics Green's functions are described by partial sums of certain types of diagrams. How these partial sums are done or further details about Feynman diagrams will not be discussed in detail here. Only a passing knowledge about them is required for this thesis and further elaboration will require a lot more explanation (Ref. [38] is a nice introduction to Feynman diagrams within many-body theory).

In fact, the interacting Green's function is related to the non-interacting Green's function by the Dyson equation. This can be derived by considering an interacting Hamiltonian H to be a linear sum of the non-interacting Hamiltonian H^0 and the interactions V (assuming this is perturbative for now), such that $H = H^0 + V$ [39]. Now, both Green's functions have the relation

$$\left(\omega\mathbf{I} - H^{(0)}\right) G^{(0)}(\omega) = \mathbf{I}, \tag{2.21}$$

with $\mathbf{I}$ being the identity matrix (with dimensions equal to the number of particles (electrons) in the system). Hence the Green's function can be expressed as $G^{(0)}(\omega) = [\omega\mathbf{I} - H^{(0)}]^{-1}$, which is referred to as the resolvant operator. Expanding the terms in Eq. 2.21 for the interacting system in terms of H^0 and V, and then multiplying the left side by the non-interacting Green's function and subsequently using the non-interacting resolvant operator gives

$$\begin{aligned} \left(\omega\mathbf{I} - H^0 - V\right) G(\omega) &= \mathbf{I} \\ \left(\omega\mathbf{I} - H^0\right) G(\omega) - VG(\omega) &= \mathbf{I} \\ G^0(\omega)\left(\omega\mathbf{I} - H^0\right) G(\omega) - G^0(\omega)VG(\omega) &= G^0(\omega) \\ G(\omega) - G^0(\omega)VG(\omega) &= G^0(\omega), \end{aligned} \tag{2.22}$$

where these matrix expressions arise from discretising the real-space or (crystal) momentum of the system. Rearranging gives the Dyson equation of this system,

$$G(\omega) = G^0(\omega) + G^0(\omega)VG(\omega). \tag{2.23}$$

For the general many-body interacting system (which can be similarly derived by considering the Feynman diagrams of the interactions [38]), the Dyson equation is expressed as

$$G(\mathbf{k},\omega) = G^0(\mathbf{k},\omega) + G^0(\mathbf{k},\omega)\Sigma(\mathbf{k},\omega)G(\mathbf{k},\omega), \tag{2.24}$$

where the continuum limit is taken such that these quantities are a function of both continuous $\mathbf{k}$ and ω. This expression can be reduced to[8]

$$G(\mathbf{k},\omega)^{-1} = G^0(\mathbf{k},\omega)^{-1} - \Sigma(\mathbf{k},\omega). \tag{2.25}$$

The $\Sigma(\mathbf{k},\omega)$ term is called the self-energy. The self-energy contains all of the many-body interactions the electron has with the interacting medium. The real part of the self-energy can shift the energy eigenvalues and the imaginary part introduces smearing in the DOS[9], depending on which interactions are included – see "Fermi liquid theory" in Section 2.3 as an example of this.

To determine the electron properties from the Green's function such as the DOS, occupation number, band structures and so on, we must calculate the spectral function, $A(\mathbf{k},\omega)$, which is formally defined by

$$\begin{aligned} G(\mathbf{k},t) &= -i\int_{-\infty}^{\infty} A^+(\mathbf{k},\omega)e^{-i(\omega+\mu)t}d\omega, \quad t>0 \\ &= +i\int_{-\infty}^{\infty} A^-(\mathbf{k},\omega)e^{i(\omega-\mu)t}d\omega, \quad t\le 0, \end{aligned} \tag{2.26}$$

where μ is the chemical potential[10]. For $G(\mathbf{k},\omega)$,

$$\begin{aligned} A^+(\mathbf{k},\omega-\mu) &= -\tfrac{1}{\pi}\,\mathrm{Im}G(\mathbf{k},\omega), \quad \omega>\mu \\ A^-(\mathbf{k},\mu-\omega) &= +\tfrac{1}{\pi}\,\mathrm{Im}G(\mathbf{k},\omega), \quad \omega<\mu. \end{aligned} \tag{2.27}$$

The spectral function itself obeys some important relations:

$$\begin{aligned} &A^{\pm}(\mathbf{k},\omega)\ge 0, \\ &\textstyle\int_{-\infty}^{\infty}\left[A^+(\mathbf{k},\omega)+A^-(\mathbf{k},\omega)\right]d\omega = 1 \quad \text{(sum rule)}\,. \end{aligned} \tag{2.28}$$

Another important quantity that can be derived from the Green's function is the occupation function $n_{\mathbf{k}}$, which is given by

$$n_{\mathbf{k}} = -i\lim_{t\to 0^-} G(\mathbf{k},t), \tag{2.29}$$

where 0^- means an infinitesimal time interval below $t=0$[11]. Also, $n_{\mathbf{k}}$ can be evaluated via the spectral function using

[8] For the case of a system with no external potential [38].

[9] The imaginary part of the self-energy is related to the lifetime of the electron quasiparticle - see Section 2.3.

[10] The additional energy of the ground state with the added electron: $\mu = E_0(N+1)-E_0(N)$, where $E_0(N)$ is the ground state energy of N electrons

[11] This limit is used to ensure that $n_{\mathbf{k}}$ converges; the same reason as why δ is used for the non-interacting Green's function. This is the case for any quantity including 0^- (or 0^+).

$$n_{\mathbf{k}} = \int_{-\infty}^{\mu} A(\mathbf{k},\omega)d\omega, \tag{2.30}$$

where we have integrated up to μ to included all of the occupied states.

The Green's function so far has been assumed to be propagating at zero temperature. To introduce temperature to the Green's functions, we must use grand canonical statistical methods from thermodynamics. Therefore, the Green's function at temperature T is defined as

$$\begin{aligned} G^T(\mathbf{k}, t_2 - t_1) &= -i\left\langle \mathscr{T}\left\{c_{\mathbf{k}}(t_2)c^{\dagger}_{\mathbf{k}}(t_1)\right\}\right\rangle \\ &= -i\frac{\mathrm{Tr}\left[\mathscr{T}\left\{c_{\mathbf{k}}(t_2)c^{\dagger}_{\mathbf{k}}(t_1)\right\}\varrho\right]}{\mathrm{Tr}[\varrho]}, \end{aligned} \tag{2.31}$$

where $\varrho = e^{-\beta(H-\mu N)}$ and is defined as the distribution operator. In real space, this temperature dependent Green's function is difficult to work with as it will involve an expansion in terms of temperature which will complicate the problem even further. However, by treating time as a complex variable with t on the real axis and β on the imaginary axis, the imaginary time (τ) relates to the temperature. Therefore, the presented formalism used to calculate the interacting Green's function at zero temperature can be kept when dealing with finite temperatures, but imaginary time dependent Green's functions are used instead. The real time (or frequency) dependent Green's function can be obtained by using analytic continuation methods (see Section 3.5). The imaginary time dependent Green's function has the form[12]

$$G(\mathbf{k}, \tau_2 - \tau_1) = -\left\langle \mathscr{T}\left\{c_{\mathbf{k}}(\tau_2)c^{\dagger}_{\mathbf{k}}(\tau_1)\right\}\right\rangle, \tag{2.32}$$

for $0 < \tau_1, \tau_2 < \beta$. This imaginary Green's function is similar to the finite temperature Green's function (Eq. 2.31) definition but with the following replacements

$$\begin{aligned} H &\to H - \mu N \\ it &\to \tau. \end{aligned} \tag{2.33}$$

The imaginary time Green's function obeys the quasi-periodic boundary condition on the interval (-β,β) such that

$$G(\mathbf{k}, \tau) = -G(\mathbf{k}, \tau + \beta) \quad \text{for} \quad -\beta < \tau < 0. \tag{2.34}$$

[12]Note that the imaginary time dependent Green's function is an entirely different function from its real time counterpart. It is written in the same manner here as this is commonly done.

The imaginary Green's function is periodic beyond the (-β,β) interval. This Green's function can be Fourier transformed to a frequency space on the imaginary axis, which is called the "Matsubara frequency" space, $G(\mathbf{k}, i\omega_n)$. Here, the frequencies are discretised with

$$\omega_n = \frac{(2n+1)\pi}{\beta}, \tag{2.35}$$

for fermions. The temperature dependent (free electron) non-interacting Green's function has the form

$$G^0(\mathbf{k}, \tau_2 - \tau_1) = -\left[\theta_{\tau_2-\tau_1} f^+(\varepsilon_\mathbf{k} - \mu, T) - \theta_{\tau_1-\tau_2} f(\varepsilon_\mathbf{k} - \mu, T)\right] e^{-(\varepsilon_\mathbf{k}-\mu)(\tau_2-\tau_1)}, \tag{2.36}$$

which includes the Fermi-Dirac distribution built into it [here, $f^+(\varepsilon_\mathbf{k} - \mu, T) = 1 - f(\varepsilon_\mathbf{k} - \mu, T)$]. In Matsubara frequency space, the (free electron) non-interacting Green's function is

$$G^0(\mathbf{k}, i\omega_n) = \frac{1}{i\omega_n - \varepsilon_\mathbf{k} + \mu}. \tag{2.37}$$

The Dyson equation (Eqs. 2.24 and 2.25) has the same form but ω is replaced by $i\omega_n$. The useful energy dependent information about the Green's function will require analytically continuing back into the real time/frequency domain. However, $n_\mathbf{k}$ can still be determined on the imaginary time domain by using Eq. 2.29, but it has a alternate form of

$$n_\mathbf{k} = -\lim_{\tau \to 0^-} G(\mathbf{k}, \tau). \tag{2.38}$$

However, this can be evaluated in Matsubara frequency space by

$$n_\mathbf{k} = \frac{1}{\beta} \sum_n G(\mathbf{k}, i\omega_n) e^{i\omega_n 0^+}. \tag{2.39}$$

This avoids any of the issues which arises from the analytic continuation process.

Now this section has briefly introduced all the tools required to calculate interacting systems in this thesis. Before ending this chapter, Fermi-liquid theory (which is an example of an interacting electron system) will be reviewed to see what happens when the electron-electron interactions are included.

2.3 Fermi liquid theory

As the free and nearly-free electron models have been discussed, and the mathematical formalism used for interacting electron systems has been described, the next step is to see what happens to

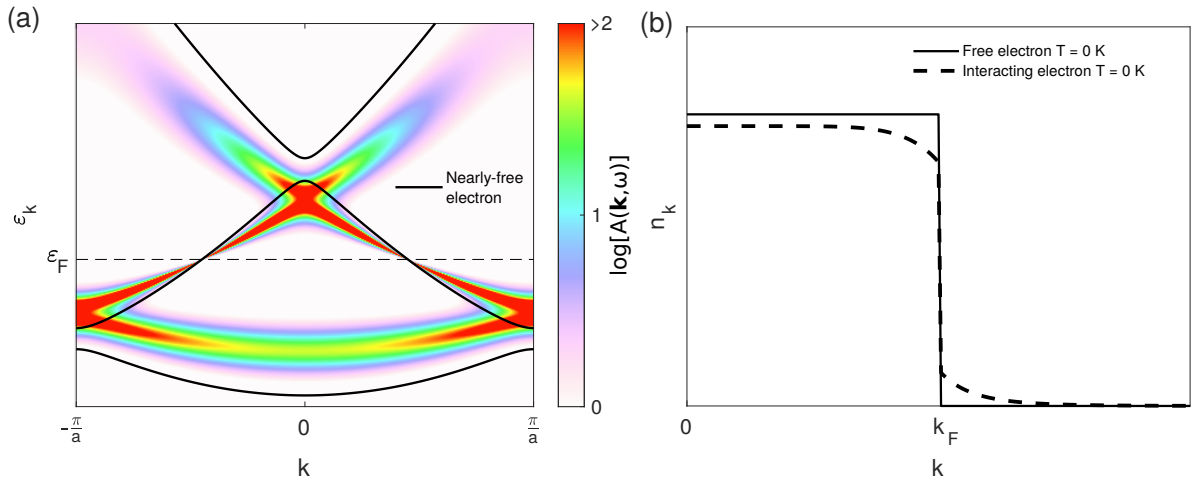

Figure 2.2: (a) The interacting ('nearly-free') Fermi-liquid spectral function with its corresponding non-interacting 'nearly-free' electron band structure overlaid on top; both are plotted along the same k-path as in Fig 2.1 (a). The spectral function was constructed at $T = 0$ K by using Eqs. 2.40 and 2.43 in Eq. 2.45. The natural log of the spectral function was used for clarity, and the Fermi energy is denoted as ε_F. (b) The comparison of the occupation functions used in the non-interacting electron model (the Fermi-Dirac function) and in the interacting Fermi-liquid model; both occupation functions are plotted along one of the reciprocal axes starting from the centre of the 1BZ ($k = 0$) to the 1BZ boundary. The interacting occupation function used here is the empirical formula, using $z = 0.713$ (which is the height of the discontinuity at k_F [Z_{k_F}]), proposed by Schülke *et al.* [46].

an electron model when the electrons are no longer independent of each other. The best place to start is to look at Fermi liquid theory, as understanding the main results of this will be sufficient for the rest of the thesis.

Let's start with the free electron gas in which it is assumed that the interactions can be adiabatically turned on, and $\mathbf{k}$ and σ (spin) are still good quantum numbers. Before turning on the interactions, some concepts about electron scattering should be established. When an electron is excited from an occupied state to an empty state above the Fermi level (by thermal fluctuations for example), this electron will most likely come from an occupied state around the Fermi level (as less energy is required to excite them). The excited electron will then leave an empty state behind. It is easier to treat these empty states like particles, which are called holes[13]. There will be an energy region around the Fermi level in which the creation of electron-hole pairs occur. The electrons away from the Fermi level will require higher energies to scatter above the Fermi level and as such are less likely to be excited.

Turning the interactions on adiabatically, the electrons can interact with one another to create an electron-hole pair. Consequently, this interacting system is an excited state of the ground state non-interacting system. As an interacting electron moves in the system, it will

[13]These hole excitations have the same properties as electrons, but they have opposite charge and exists below the Fermi level.

interact with nearby electrons which in turn will interact with it. Therefore, these interactions cause a "cloud" of constantly scattering electrons and holes around the moving electron. This defines the electron quasiparticle (QP) – a bare electron with an interaction cloud[14]. Within this QP, the holes surround and screen the negative charge from the bare electron. As long as the QPs are sufficiently far apart from each other (such that their interaction clouds do not overlap), the interactions between QPs are weak due to the screening. Therefore, these QPs can be treated as being (nearly) independent of one another. However, they have different properties compared with the electron. The QPs will have energy $E_{\mathbf{k}}$ and for the interacting gas

$$E_{\mathbf{k}} = \frac{|\mathbf{k}|^2}{2m^*}, \tag{2.40}$$

where m^* is the correlated effective mass (in natural units). The effective mass can be expressed as

$$m^* = \left(\frac{\partial^2 E_{\mathbf{k}}}{\partial |\mathbf{k}|^2}\right)^{-1}, \tag{2.41}$$

where the QP effective mass is influenced by band structure effects and electron-electron interactions. This also leads to an expression for the Fermi velocity of these QPs:

$$\mathbf{v}_{\mathrm{F}}^* = \nabla_{\mathbf{k}} E_{\mathbf{k}}\big|_{\mathbf{k}=\mathbf{k}_{\mathrm{F}}} \quad \left(= \frac{\mathbf{k}_{\mathrm{F}}}{m^*}\right). \tag{2.42}$$

Due to the interactions between the electrons (and the medium), the QPs will scatter to a new state after an average time $\tau_{\mathbf{k}}$, called the QP lifetime. On the other hand, the electrons in the non-interacting system have an infinite lifetime. The QPs in the interacting electron gas have a finite lifetime (derived from the momentum and energy conservation arguments) of

$$\tau_{\mathbf{k}}^{-1} = a\,(\epsilon_{\mathbf{k}} - \epsilon_{\mathrm{F}})^2 + b(k_{\mathrm{B}}T)^2, \tag{2.43}$$

where a and b are constants. This is specific to the QP picture. Generally $\tau_{\mathbf{k}}^{-1}$ is related to the imaginary part of the self energy by

$$\tau_{\mathbf{k}}^{-1} = -\operatorname{Im}\Sigma(\mathbf{k}, E_{\mathbf{k}}). \tag{2.44}$$

[14] QPs are not limited to the electron-electron interaction picture. Even in the nearly-free electron model, the system is made up of QPs as these electrons are surrounded by the "cloud" of the periodic Coulomb charge from the (perfect) lattice ions. This leads to an effective mass in this model, but the lifetime is still infinite as the charge from the lattice ions is periodic. (Any imperfections in the lattice, on the other hand, will disrupt this charge periodicity which in turn causes the electrons to scatter; hence the QPs will then have a finite lifetime).

The consequence of this can be seen in the spectral function, $A(\mathbf{k},\omega)$. To illustrate this, let's look at the QP band structure. From Fig 2.2 (a), in the non-interacting case, the bands are infinitesimally narrow (in energy) as the lifetime is infinite (so the non-interacting $A(\mathbf{k},\omega)$ is a Dirac-delta function). In the interacting case, the finite lifetime means that $A(\mathbf{k},\omega)$ now has the form

$$A(\mathbf{k},\omega) = -\frac{1}{\pi}\frac{\mathrm{Im}\,\Sigma(\mathbf{k},\omega)}{(\omega-\varepsilon_{\mathbf{k}}+\mu-\mathrm{Re}\,\Sigma(\mathbf{k},\omega))^2+(\mathrm{Im}\,\Sigma(\mathbf{k},\omega))^2}, \tag{2.45}$$

for the general case.

Note that the QP picture holds if these excitations are considered to be well-defined and independent of one another. This means that these excitations require a reasonably long lifetime. Consequently, this imposes the condition of

$$\tau_{\mathbf{k}}^{-1} \ll E_{\mathbf{k}} - E_{\mathrm{F}} = E'_{\mathbf{k}}, \tag{2.46}$$

where E_{F} $(= \varepsilon_{\mathrm{F}} - \mu)$ is the interacting Fermi level. The QP picture breaks down for energies further away from the Fermi level. However, the electrons further below the Fermi level are less likely to be involved in the interactions (for reasons stated before) unless strong external perturbations are involved in the model.

Now, the interacting Green's function for the interacting electron gas can be written as

$$G(\mathbf{k},\omega) = \frac{Z_{\mathbf{k}}}{\omega - E'_{\mathbf{k}} + i\tau_{\mathbf{k}}^{-1}}, \tag{2.47}$$

where $Z_{\mathbf{k}}$ is called the QP residue, which is expressed by

$$Z_{\mathbf{k}} = \left[1 - \frac{\partial\,\mathrm{Re}[\Sigma(\mathbf{k},\omega)]}{\partial\omega}\bigg|_{\omega=E'_{\mathbf{k}}}\right]^{-1}. \tag{2.48}$$

This $Z_{\mathbf{k}}$ (at 0 K) is within the range $0 \leq Z_{\mathbf{k}} \leq 1$ for interacting systems, whereas it is equal to either 0 or 1 for unoccupied or occupied states, respectively, in the non-interacting system. One way $Z_{\mathbf{k}}$ manifests itself physically is in $n_{\mathbf{k}}$, where Fig 2.2 (b) shows this $n_{\mathbf{k}}$ distribution at 0 K. There still exists a discontinuity at $\mathbf{k}_{\mathrm{F}}$ which means that the Fermi surface (in Fig. 2.1 (b)) still exists when the interactions are included, but $\mathbf{k}_{\mathrm{F}}$ may shift depending on the included electron-electron correlations. This discontinuity has a magnitude of $Z_{\mathbf{k}_{\mathrm{F}}}$.

The QP residue is linked to many other modifications to the observables such as the band width reduction [as seen in Fig. 2.2 (a)] and the (correlated) mass enhancement m^*/m, where m refers to the effective mass of the independent electron system[15]. This enhancement due to correlations can be determined from

[15]The effective mass here refers to the electron mass which has been altered by band structure effects.

$$\frac{m}{m^*} = Z_{|\mathbf{k}_\mathrm{F}|}\left(1 + \frac{m}{|\mathbf{k}_\mathrm{F}|}\frac{\partial}{\partial|\mathbf{k}|}\mathrm{Re}[\Sigma(\mathbf{k},E_\mathrm{F})]\Big|_{|\mathbf{k}|=|\mathbf{k}_\mathrm{F}|}\right), \tag{2.49}$$

where $\frac{\partial}{\partial|\mathbf{k}_\mathrm{F}|}\mathrm{Re}[\Sigma(\mathbf{k},E_\mathrm{F})]|_{|\mathbf{k}|=|\mathbf{k}_\mathrm{F}|}$ can be either negative or positive resulting in the correlated effective mass being larger or smaller than the effective mass (m) of the independent electron system. However, when the self-energy is k-independent, Eq. 2.49 reduces to

$$\frac{m}{m^*} = Z_{|\mathbf{k}_\mathrm{F}|}, \tag{2.50}$$

which is always larger than the effective mass (m) of the independent electron system.

There are many alterations to other electron properties in this interaction model which have not been discussed here. The interactions described in this section are relevant for this thesis and it is only a segment of the vast types of interactions an electron can have with the interacting medium. This is why diagram techniques help to quantify the types of interactions and how to calculate the interacting Green's function from (a portion of) them. Please refer to the aforementioned references at the beginning of this chapter for further information.

CHAPTER 3

ELECTRONIC STRUCTURE THEORETICAL METHODS

The many-body Hamiltonian of a crystal is known, but the issue lies in solving this problem for modelling a real material. The Hamiltonian describing a perfect crystal system of electrons and ions (in the non-relativistic limit) with no external potentials is given by [47, 48]

$$H = -\frac{1}{2}\sum_i \nabla_i^2 - \sum_I \frac{1}{2m_I}\nabla_I^2 + \frac{1}{2}\sum_{i\neq j}\frac{1}{|\mathbf{r}_i - \mathbf{r}_j|} + \frac{1}{2}\sum_{I\neq J}\frac{Z_I Z_J}{|\mathbf{R}_I - \mathbf{R}_J|} - \sum_{i,I}\frac{Z_I}{|\mathbf{r}_i - \mathbf{R}_I|}, \tag{3.1}$$

where the first and second terms are describing the kinetic energy of the electrons and ions, each with mass m_e(=1 in natural units) and m_I, respectively. The third and fourth terms are the electron-electron and ion-ion Coulomb repulsion. The fifth term is the attractive electron-ion Coulomb term. The complexity of this Hamiltonian can be further reduced by assuming that the motion of the electrons are instantaneous in response to the ionic motions, meaning that the motion of the electrons and ions can be decoupled – this is the Born-Oppenheimer approximation [49, 50]. From this, the motion of the ions is neglected and therefore the ions are treated as being static. Consequently, the interaction energy between the ions is constant and as such, this term only offsets the Hamiltonian (i.e. it only shifts the energies but it does not change the wave functions) and so it can also be ignored. Therefore, the many-body crystal Hamiltonian is reduced to looking at the electron terms:

$$H = -\frac{1}{2}\sum_i \nabla_i^2 + \frac{1}{2}\sum_{i\neq j}\frac{1}{|\mathbf{r}_i - \mathbf{r}_j|} - \sum_{i,I}\frac{Z_I}{|\mathbf{r}_i - \mathbf{R}_I|}. \tag{3.2}$$

The electronic structure of the crystal is responsible for many of the material's properties. The Hamiltonians in both Eqs. 3.1 and 3.2 cannot be solved by a set of independent particles due to the significant interaction terms between the particles. Consequently, Eqs. 3.1 and 3.2 are only

solvable by using a coupled system of equations with approximately 10^{24} variables describing the electrons, which is numerically infeasible. Therefore, alternative methods are required to simplify the many-body Hamiltonian to be solvable within a certain degree of accuracy.

The first notable attempts to solve the electronic structure many-body problem were the Hartree [51] and Hartree-Fock (HF) [52–55] methods. These methods assumed that the electron many-body wave function can be approximated as a product of a set of independent single-electron orbitals which can be used to self-consistently solve a set of single-body Schrödinger equations containing mean-field (Coulomb) interaction terms. The HF method improves upon the Hartree method by representing the single-electron orbitals in terms of the Slater determinant [54, 56]. This Slater determinant takes into account the exact electron-electron exchange interactions by incorporating the anti-symmetric fermionic property of electrons. Even with this improvement, many electron correlations in the system are still unaccounted for because the single Slater determinant approximation is not able to take into account the electron correlations from the electrons' Coulomb charge.

The continual work into solving the many-body problem led to the formulation of density functional theory (DFT). This is such a powerful tool that it continues to be used to this day and has been used throughout this thesis. The next few sections will discuss the formulation of DFT and the basis used for the calculations presented. However, DFT calculations use approximations to account for the correlations, but these approximations will be missing electron correlations which are vital to explain certain observed physical phenomena. Even though there are functionals which try to describe these missing electron correlations, there has been work into combining many-bodies theories with DFT to capture some of these missing electron correlations.

This thesis uses the dynamical mean-field theory (DMFT) many-body technique in conjunction with DFT (the DFT+DMFT method) to improve the description of the local electron correlations compared with DFT. This chapter will review the origins, core concepts, and implementations of DMFT and then it will finish with the discussion of the DFT+DMFT method used within this thesis. The analytic continuation method, which was required to extract the spectroscopic quantities from the DFT+DMFT calculations presented in this thesis, will be reviewed. Additionally, this chapter will define what wave-function-dependent quantities are in the context of this thesis.

3.1 Density functional theory

DFT tackles the many-body problem by reformulating it in terms of the electron density instead of using the electron wave function (therefore DFT is not a wave function method). This consequently reduces the problem down to be a solvable system with three degrees of freedom instead of a problem with $\sim 10^{24}$ degrees of freedom. To get the electronic structure from DFT, an auxiliary effective single-body (non-interacting) static Hamiltonian, with a static and time independent effective potential encapsulating the interactions of the many-body system, is solved. This section

will discuss the key concepts of DFT. Further details (such as extension to spin systems, including relativistic effects and so on) are discussed in Refs. [47, 48, 54, 55].

3.1.1 Hohenberg-Kohn theorems

This section will discuss the Hohenberg-Kohn theorems [57], the proof of which are given in the aforementioned reference. The general Hamiltonian for electrons is [48]

$$H = -\frac{1}{2}\sum_i \nabla_i^2 + \frac{1}{2}\sum_{i\neq j}\frac{1}{|\mathbf{r}_i - \mathbf{r}_j|} + \sum_i v_{\text{ext}}(\mathbf{r}_i), \tag{3.3}$$

which is a generalised version of Eq. 3.2 for a system of interacting electrons in an external potential $v_{\text{ext}}(\mathbf{r})$; this external potential term will include the electron-ion Coulomb term (and it can be extended to include other potential terms such as magnetism, spin orbit coupling, and so on). The first Hohenberg-Kohn theorem states that for any interacting particle system with an external potential $v_{\text{ext}}(\mathbf{r})$, this potential is uniquely determined (except for an addition of a constant) by the ground-state particle density $\rho_0(\mathbf{r})$, i.e.

$$\rho_0(\mathbf{r}) \Leftrightarrow v_{\text{ext}}(\mathbf{r}). \tag{3.4}$$

This leads to the second theorem which states that a universal energy functional $E[\rho]$ can be defined in terms of $\rho(\mathbf{r})$, which in turn is valid for any $v_{\text{ext}}(\mathbf{r})$. The ground-state energy of the system is a global minimum of $E[\rho]$ where the density which minimises it is $\rho_0(\mathbf{r})$;

$$E[\rho_0] \leq E[\rho]. \tag{3.5}$$

This means that $E[\rho]$ alone is sufficient to determine the ground-state energy and density. These theorems are also valid for spin dependent systems as well. The energy functional can be written as

$$E[\rho] = T[\rho] + U[\rho] + V[\rho], \tag{3.6}$$

which is similar to Eq. 3.3, but with $T[\rho]$ describing the kinetic energy of the system, $U[\rho]$ describing the electron-electron interaction energy, and $V[\rho]$ being the interaction energy from external fields, which relates to $v_{\text{ext}}(\mathbf{r})$. The $T[\rho]$ and $U[\rho]$ are universal operators as they are independent of $v_{\text{ext}}(\mathbf{r})$.

These theorems allow the many-body problem to be reformulated in terms of the electron density from which the many-body potential and wave function can be determined. However, even though this formalism is still exact for the many-body system, it does not give any insight into solving the problem. This is done by using the Kohn-Sham approach [58] and here is where the approximations emerge and ultimately cause discrepancies with experiment.

3.1.2 Kohn-Sham equations

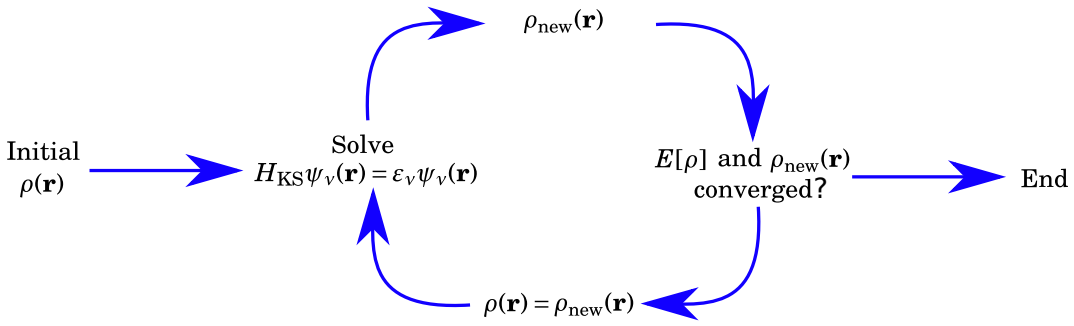

Figure 3.1: A flow chart illustrating the Kohn-Sham self-consistent cycle. The initial guess of the electron density $\rho(\mathbf{r})$ is used to construct the Kohn-Sham Hamiltonian. The resulting Kohn-Sham (auxiliary) wave functions and energy eigenvalues from solving the Hamiltonian are then used to generate the new electron density and total energy, which are compared with those generated in the previous cycle (if present). If these quantities are not the same within the convergence criteria then the new electron density is used to construct a new Kohn-Sham Hamiltonian and this cycle continues. The cycle stops when the convergence criteria have been satisfied.

The Kohn-Sham approach [58] uses an auxiliary system of non-interacting particles to solve the many-body problem, with each orbital having the wave function $\psi_v(\mathbf{r})$ (where v labels the orbital). This is often referred to as the Kohn-Sham system and it is based on two assumptions. The first assumption is that ground-state density of the Kohn-Sham system represents the true $\rho_0(\mathbf{r})$ and the second one is that the Kohn-Sham Hamiltonian uses an effective local potential $V_{\text{eff}}(\mathbf{r})$.

To understand where the Kohn-Sham equations come from, the energy functional in Eq. 3.6 can be rearranged to be

$$\begin{aligned} E[\rho] &= T_s + U_H[\rho] + [(T[\rho] - T_s) + (U[\rho] - U_H[\rho])] + V[\rho] \\ &= T_s + U_H[\rho] + E_{xc}[\rho] + V[\rho], \end{aligned} \tag{3.7}$$

such that all of the unknown electron-electron interaction terms are grouped into the exchange-correlation term, $E_{xc}[\rho]$. This $E_{xc}[\rho]$ contains the electron kinetic energy and electron-electron Coulomb interactions beyond the known forms of the single particle kinetic energy T_s (which doesn't depend of ρ) and Coulomb electron density interaction (Hartree interaction) $U_H[\rho]$. It should be noted that $E_{xc}[\rho]$ can be split into the $E_x[\rho]$ and $E_c[\rho]$ terms, which describe the exchange and correlation independently. Here, $\hat{E}_x[\rho]$ describes the lowering of the energy due to the antisymmetric nature of electrons (i.e. like-spin electrons avoiding each other). On the other hand, $\hat{E}_c[\rho]$ lowers the energy of the system due to the electrons (of either spin) avoiding each other (due to Coulomb interactions). This tendency of the electrons to avoid each other gives rise to a region around each electron with reduced probability of finding another electron, which is referred to as exchange-correlation hole.

The Kohn-Sham equations are derived by finding the global minimum of $E[\rho]$ of Eq. 3.7, giving

$$\begin{aligned} 0 = \quad \frac{\partial E[\rho]}{\partial \psi_\nu^*(\mathbf{r})} &= \frac{\partial T_s}{\partial \psi_\nu^*(\mathbf{r})} + [\frac{\partial U_H[\rho]}{\partial \rho(\mathbf{r})} + \frac{\partial E_{xc}[\rho]}{\partial \rho(\mathbf{r})} + \frac{\partial V[\rho]}{\partial \rho(\mathbf{r})}] \frac{\partial \rho}{\partial \psi_\nu^*(\mathbf{r})} \\ &= \frac{\partial T_s}{\partial \psi_\nu^*(\mathbf{r})} + v_{\mathrm{KS}}(\mathbf{r}), \end{aligned} \tag{3.8}$$

where the Kohn-Sham potential v_{KS} has the form

$$v_{\mathrm{KS}}(\mathbf{r}) = \frac{\partial U_H[\rho]}{\partial \rho(\mathbf{r})} + \frac{\partial E_{xc}[\rho]}{\partial \rho(\mathbf{r})} + \frac{\partial V[\rho]}{\partial \rho(\mathbf{r})} = v_H(\mathbf{r}) + v_{xc}(\mathbf{r}) + v_{\mathrm{ext}}(\mathbf{r}). \tag{3.9}$$

Using this, Lagrange multipliers (from the constraint that the Kohn-Sham orbitals are independent and orthonormal), and the following relations:

$$\frac{\delta T_s}{\delta \psi_\nu^*(\mathbf{r})} = -\frac{1}{2}\nabla^2 \psi_\nu(\mathbf{r}); \quad \frac{\delta \rho(\mathbf{r})}{\delta \psi_\nu^*(\mathbf{r})} = \psi_\nu(\mathbf{r}), \tag{3.10}$$

the Kohn-Sham Hamiltonian is derived with the form of

$$H_{\mathrm{KS}} \psi_\nu(\mathbf{r}) = \left[\frac{1}{2}\nabla^2 + v_{\mathrm{KS}}(\mathbf{r})\right] \psi_\nu(\mathbf{r}) = \varepsilon_\nu \psi_\nu(\mathbf{r}), \tag{3.11}$$

where ε_ν is the νth electron energy eigenvalue (which is technically the Lagrange multiplier [54, 55]). These auxiliary electron wave functions are then used to calculate the ground-state electron density from the following relation

$$\rho(\mathbf{r}) = \sum_\nu^N n_\nu |\psi_\nu(\mathbf{r})|^2, \tag{3.12}$$

with n_ν representing the (Fermi-Dirac) occupation number of the νth orbital. Equations 3.9, 3.11 and 3.12 are referred to as the Kohn-Sham equations. The ground-state of this electronic system is determined by solving the Kohn-Sham equations via a self-consistent method by updating $\rho(\mathbf{r})$ after each cycle until it has converged within a certain tolerance. The electronic structure also determines the ground-state total energy of the system through

$$E[\rho] = \sum_\nu^N \varepsilon_\nu - U_H[\rho] - \int v_{\mathrm{ext}}(\mathbf{r})\rho(\mathbf{r}) d\mathbf{r} + E_{xc}[\rho], \tag{3.13}$$

which also has to be converged within a specified tolerance in the DFT calculation. The self-consistent cycle of solving the Kohn-Sham equations is illustrated in Fig. 3.1.

All but the $E_{xc}[\rho]$ energy functional is exactly known in the Kohn-Sham system. Therefore, approximations are made to estimate $E_{xc}[\rho]$ which can lead to either good or bad agreement with experimental quantities (such as band gaps, magnetic moments, and so on), depending on the electron correlations present in the system.

3.1.3 Exchange-correlation approximation functionals

Although $E_{xc}[\rho]$ is approximated to solve the Kohn-Sham equations, there are some general features it must have. The $E_{xc}[\rho]$ can be written as

$$E_{xc}[\rho] = \int \rho(\mathbf{r})\epsilon_{xc}(\rho)|_{\mathbf{r}} d^3\mathbf{r} = \frac{1}{2}\int\int \rho(\mathbf{r})\frac{\eta_{xc}(\mathbf{r},\mathbf{r'})}{|\mathbf{r}-\mathbf{r'}|} d^3\mathbf{r} d^3\mathbf{r'}, \tag{3.14}$$

where $\epsilon_{xc}(\rho)|_{\mathbf{r}}$ [= $\epsilon_x(\rho)|_{\mathbf{r}}$+$\epsilon_c(\rho)|_{\mathbf{r}}$] is the exchange-correlation energy density and $\eta_{xc}(\mathbf{r},\mathbf{r'})$ is the exchange-correlation hole distribution which is linked to $\epsilon_{xc}(\rho)|_{\mathbf{r}}$ by

$$\epsilon_{xc}(\rho)|_{\mathbf{r}} = \frac{1}{2}\int \frac{\eta_{xc}(\mathbf{r},\mathbf{r'})}{|\mathbf{r}-\mathbf{r'}|} d^3\mathbf{r'}. \tag{3.15}$$

Here, $\eta_{xc}(\mathbf{r},\mathbf{r'})$ [= $\eta_x(\mathbf{r},\mathbf{r'})$ + $\eta_c(\mathbf{r},\mathbf{r'})$] is the hole density describing the reduction in the probability of encountering an electron at $\mathbf{r'}$ given an electron at $\mathbf{r}$ due to the exchange-correlation effects [48, 54, 55]. The physical meaning of Eq. 3.14 is that $E_{xc}[\rho]$ is given by the Coulomb interaction of the electron with its exchange-correlation hole which is reduced in magnitude by a kinetic energy contribution corresponding to the energy required to remove the hole. The $\eta_{xc}(\mathbf{r},\mathbf{r'})$ function obeys the following sum rules:

$$\int \eta_{xc}(\mathbf{r},\mathbf{r'}) d^3\mathbf{r'} = \int [\eta_x(\mathbf{r},\mathbf{r'}) + \eta_c(\mathbf{r},\mathbf{r'})] d^3\mathbf{r'} = -1 + 0 = -1. \tag{3.16}$$

It is understanding this $\eta_{xc}(\mathbf{r},\mathbf{r'})$ function which enables improvements to the approximations used to estimate $E_{xc}[\rho]$. These possible improvements are constrained by the sum rules. The exact form of $\epsilon_x(\rho)|_{\mathbf{r}}$ is known through HF theory, but it is $\epsilon_c(\rho)|_{\mathbf{r}}$ which remains elusive and hence explains why approximations are needed for both quantities in order to satisfy the sum rules.

The first universally successful exchange-correlation functional was the local density approximation (LDA), which is based around a homogeneous electron gas (HEG) with constant electron density. The energy densities are approximated by $\epsilon_x^{HEG}(\rho)|_{\mathbf{r}}$ and $\epsilon_c^{HEG}(\rho)|_{\mathbf{r}}$. Here $\epsilon_x^{HEG}(\rho)|_{\mathbf{r}}$ is explicitly known and has the form of

$$\epsilon_x^{HEG}(\rho)|_{\mathbf{r}} = -\frac{3}{4}\left(\frac{3}{\pi}\right)^{\frac{1}{3}} \rho(\mathbf{r})^{\frac{4}{3}}, \tag{3.17}$$

but $\epsilon_c^{HEG}(\rho)|_{\mathbf{r}}$ has no analytic form. However, $\epsilon_c^{HEG}(\rho)|_{\mathbf{r}}$ has been determined by fitting an expression to the highly precise quantum Monte Carlo (QMC) calculations of this electron system, done by Ceperley and Alder [59], which is the most commonly used parameterised form. This led to the commonly used LDA functional described in Ref. [60] and the corresponding form of the LDA potential is

$$v_{\mathrm{xc}}^{\mathrm{LDA}}(\mathbf{r}) = \frac{\delta E_{\mathrm{xc}}^{\mathrm{LDA}}[\rho]}{\delta \rho} = \epsilon_{\mathrm{xc}}^{\mathrm{HEG}}(\rho)\Big|_{\mathrm{r}} + \rho(\mathbf{r})\frac{\partial \epsilon_{\mathrm{xc}}^{\mathrm{HEG}}(\rho)\big|_{\mathrm{r}}}{\partial \rho}, \tag{3.18}$$

which can be determined and used in the Kohn-Sham equations. The LDA functional can be extended to include spin, which is referred to the local spin density approximation (LSDA) [60].

The L(S)DA functional is widely successful and still used to this day, but it does fail to describe many aspects of many systems. L(S)DA is no good for determining accurate values for molecular bond energies, band gaps in insulators and systems in which the electron density varies significantly, such as in Fe [61, 62]. Therefore, the gradient of the electron density needs to be considered.

The next improvement of the exchange-correlation approximation encapsulated the electron density gradient. Therefore, functions of form $\epsilon_{xc}(\rho, \nabla\rho)|_{\mathbf{r}}$ (which depend on both the density and its gradient, as well as satisfying the sum rules) are used[1]. These function types give the generalised gradient approximation (GGA) of the exchange-correlation energy functional with the general form of

$$E_{xc}^{GGA}[\rho] = \int \rho(\mathbf{r})\epsilon_{xc}(\rho, |\nabla\rho|)|_{\mathbf{r}} d^3\mathbf{r}. \tag{3.19}$$

The corresponding form of the GGA potential is

$$v_{\mathrm{xc}}^{\mathrm{GGA}}(\mathbf{r}) = \frac{\delta E_{\mathrm{xc}}^{\mathrm{GGA}}[\rho]}{\delta \rho} = \epsilon_{\mathrm{xc}}(\rho)\Big|_{\mathrm{r}} + \rho(\mathbf{r})\frac{\partial \epsilon_{\mathrm{xc}}(\rho)\big|_{\mathrm{r}}}{\partial \rho} - \nabla.\left(\rho(\mathbf{r})\frac{\partial \epsilon_{\mathrm{xc}}(\rho)\big|_{\mathrm{r}}}{\partial \nabla\rho}\right), \tag{3.20}$$

which is then used in the Kohn-Sham equations. The different GGA functionals which exist in the literature differ by the manner in which $\epsilon_{xc}(\rho, \nabla\rho)|_{\mathbf{r}}$ was constructed [65]. One commonly used GGA functional is that of Perdew-Burke-Ernzerhof (PBE) [64], and this is the one which was used for the GGA calculations in this thesis.

The GGA functionals are a major improvement to the L(S)DA (which was their main intention), resulting in GGA calculations predicting the correct structure of magnetic Fe. However, GGA tends to overestimate band gaps whereas L(S)DA tends to underestimate them. L(S)DA and GGA are the main approximations for the exchange-correlation energy functionals which give agreeable results depending on the system they are used for.

There are other exchange-correlation energy functionals which can be used, such as the meta-GGA functionals which include the kinetic energy density term $\tau(\mathbf{r})$ in the exchange-correlation energy density function. The inclusion of the kinetic energy density enables meta-GGAs to treat different chemical bonds. In Chapter 4, the recent strongly constrained and appropriately

[1]Note that initial work of including the gradient term in the exchange-correlation approximation involved using an expansion series and was called the 'Gradient Expansion Approximation', but due to it not being able to satisfy the sum rules L(S)DA does, it produced worse results compared with L(S)DA [63, 64].

normed (SCAN) meta-GGA functional [66] was used. The SCAN functional satisfies all 17 exact constraints that a meta-GGA can, and is appropriately normed on systems for which semi-local functionals can be exact or nearly-exact. The SCAN meta-GGA produces accurate energies of rare-gas atoms and nonbonded interactions (such as Hydrogen and van der Waals bonds). The SCAN functional did not use fits to any real (bonded) system in its construction, and thus is considered non-empirical. However, SCAN tends to over estimate the magnetic moment in itinerant ferromagentic materials [67, 68]. In Ref. [68], they concluded that there is currently no single GGA or meta-GGA functional which produces satisfying results for itinerant metals and strongly correlated anti-ferromagnetic (AFM) oxides.

Finally, a better treatment of non-local exchange can be included by using hybrid functionals which combine the DFT correlation description with the HF exchange. The list is endless with more obscure functionals which are found to work well in certain systems, but which are not generally useful. However, the exchange-correlation functionals which go beyond L(S)DA and GGA (and potentially meta-GGA) do not tend to be universally better.

3.1.4 Wave function basis

There are many different electron wave function bases that can be used, all depending on what approach is best to determine the electronic structure of the system. These approaches range from using pseudo-potentials to approximate the potential for the regions around the atoms [69] to using Green's functions instead of wave functions in the Korringa-Kohn-Rostoker (KKR) method [70]. In this thesis, the DFT calculations used the full potential (FP) method with the augmented plane-waves with local orbitals (APW+lo) basis, which will be described in this section. This is also nicely described in Ref. [69].

The potential is strongly varying and spherical symmetric around the atomic sites, but it varies smoothly in between these sites. Therefore, the FP method splits the potential into two separate regions. The first is referred to as the muffin-tin (MT) region (S_α) which is spherically centred around each atomic site (α), but which does not overlap with the other MTs in the crystal. The second region describes the space between the MTs and is referred to as the interstitial region (I). The potential in the MT is expanded in terms of spherical harmonics with lattice symmetry constraints, whereas the potential is expanded in terms of a Fourier series in the interstitial region. This results in the potential of the form [69, 71]

$$V(\mathbf{r}) = \begin{cases} \sum_{lm,\alpha} V_{lm,\alpha}(r_\alpha) Y_{lm}(\hat{\mathbf{r}}_\alpha) & \text{for } \mathbf{r} \in S_\alpha \\ \sum_{\mathbf{G}} V_{\mathbf{G}} \exp(i\mathbf{G}\cdot\mathbf{r}) & \text{for } \mathbf{r} \in I. \end{cases} \tag{3.21}$$

Here, $V_{lm,\alpha}(r_\alpha)$ are the radial coefficients of the potential which have the lattice symmetry, $V_{\mathbf{G}}$ are the Fourier coefficients describing the potential, $Y_{lm}(\hat{\mathbf{r}}_\alpha)$ are the spherical harmonics, and lm are the angular momentum indices.

The consequences of having two separate regions to describe the lattice is that there will also be two sets of basis functions to describe the Kohn-Sham orbitals $\psi_\nu(\mathbf{r})$. The Kohn-Sham orbitals are described by a set of basis functions $\phi^{\mathbf{G}}_{\nu,\mathbf{k}}(\mathbf{r})$ via

$$\psi_{\nu,\mathbf{k}}(\mathbf{r}) = \sum_{\mathbf{G}} c^{\mathbf{G}}_{\nu,\mathbf{k}} \phi^{\mathbf{G}}_{\nu,\mathbf{k}}(\mathbf{r}), \tag{3.22}$$

where $c^{\mathbf{G}}_{\nu,\mathbf{k}}$ are the coefficients of the expansion in terms of the basis functions $\phi^{\mathbf{G}}_{\nu,\mathbf{k}}(\mathbf{r})$. Consequently, the Kohn-Sham equations only need to determine these coefficients for the occupied orbitals such that the total energy is minimised. This is done by solving the secular equation (for each $\mathbf{k}$ point within the IBZ)

$$(\mathbf{H} - \varepsilon_{\nu,\mathbf{k}}\mathbf{S})\mathbf{c}_{\nu,\mathbf{k}} = 0, \tag{3.23}$$

where $\mathbf{c}_{\nu,\mathbf{k}}$ is the eigenvector with elements $c^{\mathbf{G}}_{\nu,\mathbf{k}}$ for each of the basis functions and both $\mathbf{H}$ and $\mathbf{S}$ are square Hermitian matrices (with a size equal to the number of basis functions) of the Kohn-Sham Hamiltonian and wave function overlaps, respectively, with elements of the form

$$H_{\mathbf{G},\mathbf{G}'} = < \phi^{\mathbf{G}}_{\nu,\mathbf{k}} | H | \phi^{\mathbf{G}'}_{\nu,\mathbf{k}} > \qquad \text{and} \quad S_{\mathbf{G},\mathbf{G}'} = < \phi^{\mathbf{G}}_{\nu,\mathbf{k}} | \phi^{\mathbf{G}'}_{\nu,\mathbf{k}} > . \tag{3.24}$$

The $\phi^{\mathbf{G}}_{\nu,\mathbf{k}}(\mathbf{r})$ wave functions are split into atomic-like orbitals in the MT and plane-wave functions in the interstitial region. This is the core concept of the augmented plane-wave (APW) method. These wave functions have the form

$$\phi^{\mathbf{G}}_{\mathbf{k}}(\mathbf{r}) = \begin{cases} \sum_{lm,\alpha} A_{lm,\alpha} u_{l,\alpha}(r, E_{l,\alpha}) Y_{lm}(\hat{\mathbf{r}}_\alpha) & \text{for} \quad \mathbf{r} \in S_\alpha \\ \Omega^{-1/2} \sum_{\mathbf{G}} c_{\mathbf{G}} e^{i(\mathbf{k}+\mathbf{G}).\mathbf{r}} & \text{for} \quad \mathbf{r} \in I. \end{cases} \tag{3.25}$$

The interstitial plane-waves are normalised to the 1BZ volume Ω and have expansion coefficients of $c_{\mathbf{G}}$. The MT wave functions are described by the spherical harmonics together with an energy dependent radial function $u_{l,\alpha}(r, E_{l,\alpha})$, which is the solution of the radial dependent Schrödinger equation

$$\left[-\frac{\mathrm{d}^2}{\mathrm{d}r^2} + \frac{l(l+1)}{r^2} + V(r) - E_{l,\alpha} \right] r u_{l,\alpha}\left(r, E_{l,\alpha}\right) = 0 \quad r \in S_\alpha, \tag{3.26}$$

where $V(r)$ here is the spherical part of the potential within the MT. Finally, $A_{lm,\alpha}$ are the MT expansion coefficients with the criteria of matching the plane-wave coefficients at the MT boundary. This ensures that the wave function is continuous over the MT boundary (a core condition of the APW method). This results in

$$A_{lm,\alpha} = \frac{4\pi i^l}{\Omega^{1/2} u_{l,\alpha}\left(R_\alpha, E_{l,\alpha}\right)} \sum_{\mathbf{G}} c_{\mathbf{G}} j_l\left(|\mathbf{k}+\mathbf{G}|R_\alpha\right) Y^*_{lm}(\mathbf{k}+\mathbf{G}), \tag{3.27}$$

where R_α is the MT radius of atom α and $j_l\left(|\mathbf{k}+\mathbf{G}|R_\alpha\right)$ is the Bessel function of order l.

The biggest problem with using just APWs is that the radial functions are energy dependent meaning that this is a non-linear energy eigenvalue problem. Consequently, solutions to the Kohn-Sham equations can only be determined if $E_{l,\alpha}$ equals the Kohn-Sham energy eigenvalues. This makes solving the Kohn-Sham system too computationally demanding.

This led to the linearised augmented plane-wave (LAPW) method [72] which overcomes this energy dependence issue by expanding the radial function as a Taylor series in terms of the energy. This series can be truncated to (and include) the energy derivative radial function $\dot{u}_{l,\alpha}(r, E_{l,\alpha})$, where this function is evaluated at some fixed energy $E_{l,\alpha}$. This means that the wave functions have variational freedom in energy ε as the energy dependent radial function is in terms of a linear combination of the radial functions evaluated at $E_{l,\alpha}$, i.e.

$$u_{l,\alpha}(r_\alpha, \varepsilon) = u_{l,\alpha}\left(r_\alpha, E_{l,\alpha}\right) + \left(\varepsilon - E_{l,\alpha}\right) \dot{u}_{l,\alpha}(r_\alpha, \varepsilon)\big|_{\varepsilon = E_{l,\alpha}} + O\left(\left(\varepsilon - E_{l,\alpha}\right)^2\right), \tag{3.28}$$

where $O\left(\left(\varepsilon - E_l^0\right)^2\right)$ denotes the quadratic errors in this combination. Therefore, the wave functions remain valid within a large energy window. The wave functions within the LAPW method have the form

$$\phi^{\mathbf{G}}_{\mathbf{k}}(\mathbf{r}) = \begin{cases} \sum_{lm,\alpha} [A_{lm,\alpha} u_{l,\alpha}(r, E_{l,\alpha}) + B_{lm,\alpha} \dot{u}_{l,\alpha}(r, E_{l,\alpha})] Y_{lm}(\hat{\mathbf{r}}_\alpha) & \text{for} \quad \mathbf{r} \in S_\alpha \\ \Omega^{-1/2} \sum_{\mathbf{G}} c_{\mathbf{G}} e^{i(\mathbf{k}+\mathbf{G}).\mathbf{r}} & \text{for} \quad \mathbf{r} \in I, \end{cases} \tag{3.29}$$

where $B_{lm,\alpha}$ are the matching coefficients for $\dot{u}_{l,\alpha}(r, E_{l,\alpha})$, where these coefficients are determined from Eq. 3.27 but with $\dot{u}_{l,\alpha}(r, E_{l,\alpha})$ instead, and $\dot{u}_{l,\alpha}(r, E_{l,\alpha})$ is a solution to the radial equation

$$\left[-\frac{\mathrm{d}^2}{\mathrm{d}r^2} + \frac{l(l+1)}{r^2} + V(r) - E_{l,\alpha}\right] r\dot{u}_{l,\alpha}\left(r, E_{l,\alpha}\right) = r u_{l,\alpha}\left(r, E_{l,\alpha}\right) \quad r \in S_\alpha. \tag{3.30}$$

Even though the Kohn-Sham eigenvalues can be determined from one diagonalisation of the secular equation with the LAPWs, this method requires a greater number of plane-waves (which increases the plane-wave cutoff) to describe the basis and hence increases the basis size. Another noteworthy point is the possible appearance of ghost bands. The valence states within the MT are *approximately* orthogonal to the semi-core states which do not vanish at the MT boundary, and therefore choosing a fixed $E_{l,\alpha}$ to describe both states is difficult and can lead to producing these undesirable ghost bands.

These issues can be avoided by using a set of local orbitals with the APW basis, and this is known as the APW+lo method. This method benefits from the smaller APW basis along with the

variational freedom in energy (as with the LAPW method) and a better description of the valence and semi-core states. In this method, the APW radial functions are evaluated at fixed energy $E^1_{l,\alpha}$ (i.e. replace $E_{l,\alpha}$ with $E^1_{l,\alpha}$ in Eq. 3.29) and the local orbitals have the general form

$$\phi^{lo}_{lm,\alpha}(r) = \sum_{lm}[A^{lo}_{lm}u_{l,\alpha}(r,E^1_{l,\alpha}) + B^{lo}_{lm}\dot{u}_{l,\alpha}(r,E^1_{l,\alpha}) + C^{lo}_{lm}u_{l,\alpha}(r,E^2_{l,\alpha})]Y_{lm}(\hat{\mathbf{r}}) \quad \mathbf{r}\in S_\alpha. \tag{3.31}$$

The A^{lo}_{lm}, B^{lo}_{lm} and C^{lo}_{lm} coefficients are defined such that the value and the gradient of the local orbital go to zero at the MT boundary. Also, $u_{l,\alpha}(r,E^2_{l,\alpha})$ is the radial function evaluated at the fixed energy $E^2_{l,\alpha}$. The local orbitals are not subject to the (L)APW matching conditions, which leaves the size of the plane-wave cutoff unaffected. More local orbitals can be used to better describe the valence and semi-core states if required. All of this results in reduced computational cost and increased speed compared with the LAPW method.

The APW+lo basis is used by the ELK [14] and WIEN2K [71] DFT codes, both of which were used in this thesis. The codes, in their default configurations, are slightly different when solving the Kohn-Sham equations. The MT wave functions within ELK are APW+lo by default, but they can include more radial terms and local orbitals (with more radial terms). Therefore, the general MT wave function within ELK is described by [14]

$$\phi^{\mathrm{MT}}_{\alpha lm\nu\mathbf{k}}(r) = \sum_{\mathbf{G}} c^{\nu\mathbf{k}}_{\mathbf{G}} \sum_{j=1}^{M^\alpha_l} A^\alpha_{jlm}(\mathbf{G}+\mathbf{k})u^\alpha_{jl}(r) + \sum_{j=1}^{N^\alpha} c^{\nu\mathbf{k}}_{(\alpha,j,m)}\phi^{lo}_{\alpha j}(r)\delta_{l,l_j}, \tag{3.32}$$

where M^α_l is the number of APW radial functions $[u^\alpha_{jl}(r)]$ and coefficients for a given l of atom α, and N^α is the number of local orbitals for atom α. Also, ELK solves non-collinear potential terms using spinor wave functions and formulating the Kohn-Sham equations in terms of a 2×2 spinor block (see Ref. [73]). It solves the additional spin-dependent potentials using a second variational approach. ELK solves the spin independent Hamiltonian first (the first-variational step) and then adds the spin-dependent potentials to the Hamiltonian and solves this by using the first-variational Kohn-Sham wave functions as a basis set. On the other hand, the default version of WIEN2K uses collinear spin potentials in its Hamiltonian and solves the two spin Hamilitonians separately. However, spin-orbit coupled (SOC) systems are calculated by using a second-variational step in WIEN2K, but is restricted to being collinear. Consequently, there will be differences between certain quantities used in calculating the electronic structure, namely the local orbitals and the SOC symmetry set used in WIEN2K compared with ELK. The (minor) differences in the results of calculated electronic structures from different DFT codes have been explored in Ref. [74].

3.1.5 The success and failures within DFT implementations

It should be emphasised that DFT calculations will only reproduce the true electron density and total energy of the system. The electronic structure calculated via this simplified auxiliary

single-body system is only a sophisticated mean-field approximation to it. However, calculated band structures and Fermi surfaces use the Kohn-Sham eigenvalues as they produce qualitatively good agreement with the experiments of certain materials. However, other quantities which depend on the Kohn-Sham energy eigenvalues, such as the band widths and band gaps, are often inconsistent with observations for the universal (LDA and GGA) exchange-correlation approximation functionals.

The biggest problem with DFT implementations is the $E_{xc}[\rho]$. For delocalised electrons in real space (electrons with wide energy bandwidths), their kinetic energy dominates and as such current $E_{xc}[\rho]$ approximations work fairly well (i.e. it works fairly well where the electron correlations are weak). However, there are still important electron correlations which are missing within the universal $E_{xc}[\rho]$ approximations. For example, for localised electrons in real space (electrons with narrow energy band widths), the Coulomb interaction is significant with respect to the kinetic energy which in turn causes strong correlations between the electrons. Therefore, the DFT approximation fails to adequately predict the behaviour of localised electrons (such as d and f orbitals). Although it is theoretically possible to describe this with the correct $E_{xc}[\rho]$, there is (currently) no existing exact exchange-correlations functional which can predict these properties for all materials, therefore, alternative theories are required.

3.2 The Hubbard model

Another approach to the many-body problem is to reformulate it in terms of a real space picture (using the second quantization formalism) where the basis set of independent electron wave functions are (atomic-like) localised orbitals, see Refs. [75–77] for further details. As the effective single-body electron-electron Coulomb potential $v_{eff}(\mathbf{r}_i)$ (from Kohn-Sham[2]) along with the form of the Coulomb interaction between the electrons in the system is known, the residual Coulomb potential, $\tilde{v}_{ee}\left(\mathbf{r},\mathbf{r}'\right)$, of a system of N electrons is

$$\tilde{v}_{ee}\left(\mathbf{r}_i,\mathbf{r}_j\right) = \frac{1}{\left|\mathbf{r}_i-\mathbf{r}_j\right|} - \frac{1}{N}\left[v_{eff}\left(\mathbf{r}_i\right)+v_{eff}\left(\mathbf{r}_j\right)\right]. \tag{3.33}$$

Here, $\tilde{v}_{ee}\left(\mathbf{r}_i,\mathbf{r}_j\right)$ represents the screened Coulomb interaction, where in reality screening is a dynamical process which involves collective charge fluctuations on the scale of the plasma frequency[3].

An interacting Hamiltonian H_{int}, which is dependent on $\tilde{v}_{ee}\left(\mathbf{r}_i,\mathbf{r}_j\right)$, can be reintroduced into the single-body Hamiltonian with the form

[2]For the Kohn-Sham system, $v_{eff}(\mathbf{r}_i) = v_H(\mathbf{r}_i) + v_{xc}(\mathbf{r}_i)$.

[3]The dynamical screened Coulomb interaction $W(\omega)$ is used in Hedin's equations (and in Hedin's GW approximation) [78]. The static limit $W(\omega \longrightarrow 0)$ of this screened interaction is normally used in the Hubbard model [79, 80]. Also, there may be some plateaus in $W(\omega)$ at certain frequency ranges (see for example [81]), so it may be reasonable to use a static U corresponding to these values.

$$\begin{aligned} H &= H_0 + H_{\text{int}} \\ H &= H_0 + \tilde{V}_{ee}, \end{aligned} \tag{3.34}$$

where H_0 is the single-body Hamiltonian (such as H_{KS}). This new Hamiltonian is a complicated quantity (which of course cannot be solved by a set of independent electron orbitals). However, this complexity can be reduced by only considering the dominant contributions to the Hamiltonian. This leads to the Hubbard model Hamiltonian [82–84] which usually restricts the interactions to the (assumed dominant) contributions from the nearest-neighbour and next-nearest neighbour atomic sites. Also, the residual Coulomb potential has been reduced to the local intra-atomic Coulomb interaction $U_{m,m',m'',m'''}$ (i.e. the residual screened Coulomb potential on the atomic site)[4], with the m, m', m'', m''' variables representing the single particle state indices (most likely in the lm basis). This results in the following multi-band Hubbard Hamiltonian in second quantization:

$$\begin{aligned} H =& H_0 + H_{\text{int}} \\ H =& -\sum_{ij}\sum_{mm'\sigma} t_{mm'ij} c^{\dagger}_{m\sigma i} c_{m'\sigma j} + \sum_{i}\sum_{\substack{m,m',m'',m''' \\ \sigma,\sigma'}} U_{m,m',m'',m'''} c^{\dagger}_{im\sigma} c^{\dagger}_{im'\sigma'} c_{im'''\sigma'} c_{im''\sigma}, \end{aligned} \tag{3.35}$$

where $t_{mm'ij}$ is the electron hopping integral between nearest-neighbour and next-nearest neighbour atomic sites i and j. The $c^{\dagger}_{m\sigma i}$ ($c_{m\sigma i}$) terms are the electron creation (annihilation) operator with electron spin index σ. For a single band system, the Hubbard Hamiltonian reduces to

$$H = -\sum_{ij}\sum_{\sigma} t_{ij} c^{\dagger}_{\sigma i} c_{\sigma j} + U \sum_{i} n_{i\uparrow} n_{i\downarrow}, \tag{3.36}$$

where U is the on-site (intra-orbital) Coulomb interaction strength, $n_{m\sigma} = c^{\dagger}_{m\sigma} c_{m\sigma}$ and the electron spin indices are explicitly expressed for the on-site Coulomb interaction term (as it does not complicate the equation to do so). Breaking down the Hubbard Hamiltonian in Eqs. 3.35 and 3.36, the first term describes the kinetic energy ($t_{mm'ij}$) of the electrons 'hopping' around the atomic sites. The hopping integral can be related to the Fourier transform of the non-interacting energy dispersion relation $\varepsilon_{mm'\mathbf{k}}$ by

$$t_{mm'ij} = \int \phi^{i}_{m}(\mathbf{r})^{*} H_0 \phi^{j}_{m'}(\mathbf{r}) d^3\mathbf{r} = \frac{1}{N}\sum_{\mathbf{k}} e^{-i(\mathbf{r}_i - \mathbf{r}_j).\mathbf{k}} \varepsilon_{mm'\mathbf{k}}, \tag{3.37}$$

where $\phi^{i}_{m}(\mathbf{r})$ are atomic-like electron orbitals [these are 'tightly bound' around the atoms and normally described by atomic orbitals (such as MTs) or Wannier wave functions (which are

[4] Here, $U_{m,m',m'',m'''}$ is rotationally invariant, see Section 3.3.1.

described in Section 3.7.1)]. If H_0 is H_{KS}, the energy eigenvalues $\varepsilon_{mm'\mathbf{k}}$ will be of the Kohn-Sham system (in the lm basis) and this is the foundation of the tight-binding method [76]. As we are using second quantization, the lattice Green's function (ignoring any spin dependence for now[5]) of the Hubbard model (in the lm basis) is

$$G^{\mathrm{lat}}_{mm'}(\mathbf{k},z) = \left(z - \varepsilon_{mm'\mathbf{k}} - \Sigma^{\mathrm{lat}}_{mm'}(\mathbf{k},z)\right)^{-1}, \tag{3.38}$$

with the lattice self-energy $\Sigma^{\mathrm{lat}}_{mm'}(\mathbf{k},z)$, and z defines either the real or Matsubara frequencies (i.e. this relates to the retarded or Matsubara Green's functions, respectively). For the Hubbard model with $H_{\mathrm{int}} = 0$ (no Coulomb interaction term), the Hubbard Hamiltonian will revert to the tight-binding description of the Kohn-Sham system.

The second term in the Hubbard Hamiltonian(s) expresses both the energy cost of double occupation of the atomic orbital and the inter-orbital Coulomb interaction, as well as Hund's physics which describes the preferred arrangement of maximal spin and orbital angular momentum (all of this is captured in $U_{m,m',m'',m'''}$). The form of $U_{m,m',m'',m'''}$ will be discussed in Section 3.3.1. In the case where $t_{mm'ij} = 0$, the electrons are unable to hop between the atomic sites and so the electron wave functions become localised.

Even though the solution Hubbard Hamiltonian can be determined in the limit where one of the terms dominate, the interplay of these terms away from these limits are difficult to solve and is subject to modern day research. These terms compete with each other as the kinetic part favours the electrons being as mobile as possible, while the interaction energy is minimal when electrons stay apart from each other which results in them being localised on the atomic sites. Strongly correlated electron systems are neither fully itinerant nor fully localised.

There are certain Hubbard models which can be solved exactly, such as the one-dimensional (1D) chain [77, 88] and the half-filled (where there is one electron per atomic site) Bethe lattice[6] model [85–87]. These solutions bring the correlation physics lost in the DFT calculations, such as the Mott insulator [90]. This insulating phase is a collection of localised electrons bound to atoms because of the Coulomb cost being too great for the double occupied states to exist. The density of states of these localised electrons form peaks at the ionisation energy[7] and the electron affinity[8] of the atom (these are the local "atomic" excitations and are broadened by the hopping of electrons away from the atom) [87]. These atomic-like states are referred to as the "Hubbard bands". The metal-insulator transition (MIT) can be modelled by increasing the magnitude of

[5]For magnetic systems, $\Sigma^{\mathrm{lat}}_{mm'}(\mathbf{k},z)$ will be spin dependent. For DFT+DMFT, however, $\varepsilon_{mm'\mathbf{k}}$ could also be spin dependent if the DFT+DMFT calculation used spin-polarised DFT inputs - this means that there are two methods to calculate magnetic DFT+DMFT outputs, see Section 5.3 for example.

[6]The Bethe lattice is a (Cayley tree) lattice which has infinitive connectivity (dimensions) to each site and no translational symmetry. This lattice simplifies the DMFT equations and enables the problem to be solved with the Bethe ansatz [86]. The Bethe ansatz is an exact method to calculate the eigenvalues and eigenvectors of certain types of quantum many-body model systems [89].

[7]The energy required to remove an electron from an atom.

[8]The energy required to add an electron to an atom.

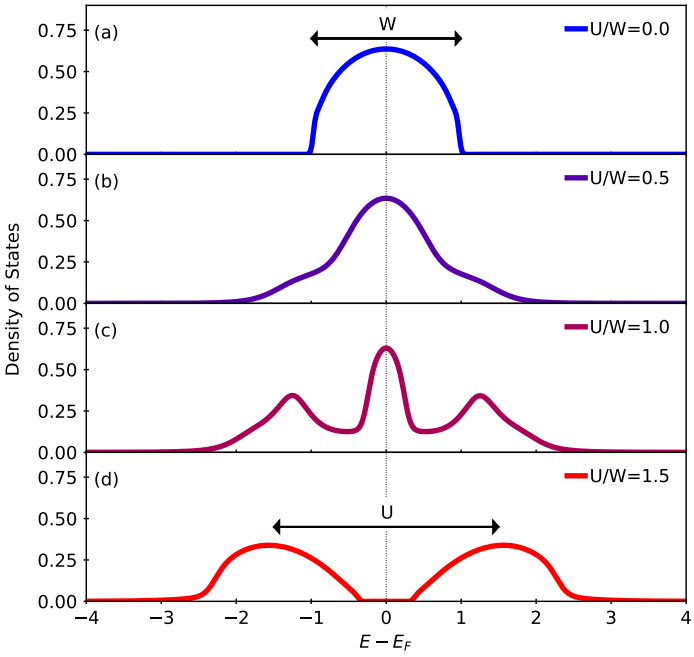

Figure 3.2: The effect of local correlations on the density of states leading to the Mott insulator. This was modelled by solving the single band Hubbard model using the DMFT equations (see Section 3.4.1) on the half-filled Bethe lattice using the iterative perturbative theory solver, such as in Ref. [85, 86]. Here, a range of U values were used with the hopping integral magnitude $t = 0.5$ and non-interacting band width $W = 4t$. The energy axes of the plots are with respect to the Fermi level which equals 0 here. (a) The non-interacting density of states with bandwidth W and interaction $U = 0$. (b) The weak correlation regime where the electrons can be described as QPs. The Fermi liquid model accounts for the narrowing of the peak. (c) Strong correlation metal regime where the spectrum has the characteristic three-peak structure comprised of the QP peak and Hubbard bands. (d) The Mott insulator which occurs when the electron interactions are sufficiently strong enough to cause the QP peak to vanish as a result of transferring its spectral weight to the Hubbard bands. Here, the Hubbard band peaks are at $\pm U/2$ and the energy difference between the peaks is equal to U. Note that this figure is similar to that in Ref. [87].

the (single band Hubbard model) Coulomb interaction U until a critical value, U_{MIT}, where it is energetically unfavourable for the system to be metallic, and hence transitions to the (Mott) insulating state[9]. Figure 3.2 (for a half-filled system within the single band DMFT framework) illustrates this MIT, which is the result of the transfer of spectral weight from the QP peak to the Hubbard bands of the (strongly) correlated metallic state. This spectral weight transfer forms a three peak structure for intermediate U values [i.e. Fig. 3.2 (c)]. This three peak structure is

[9]Note that this Mott MIT is present in the multi-orbital Hubbard Hamiltonian. It is clearer to discuss this by knowing that the full Coulomb interaction term can be being parameterised by U and the Hund's coupling term (J) - see Section 3.3.1. Therefore, the MIT still happens by changing this U through U_{MIT}.

composed of the QP peak at the Fermi level which is surrounded by the upper and lower Hubbard bands (in energy)[10]. As in Fermi liquid theory, the QP peak relates to the excited electron-hole states discussed in Section 2.3.

3.3 Incorporating the interaction Hamiltonian

As the Hubbard model includes the interactions lost in the exchange-correlation approximations, the DFT+U method (which refers to any DFT functional plus the Hubbard U term) [47, 91–94] was the first method to incorporate the interaction Hamiltonian with DFT, and it improves upon the DFT calculations by introducing the local intra-atomic Coulomb interaction from the Hubbard model to describe the correlated local (d and f) orbitals which are *static* in this method. This is done by adding the Coulomb interaction term as a functional of the orbital density matrix $\hat{n}$ (corresponding to the local states). Therefore, the DFT+U energy functional of this system is

$$E^{\mathrm{DFT+U}}[\rho,\hat{n}] = E^{\mathrm{DFT}}[\rho] + E^{\mathrm{e-e}}[\hat{n}] - E^{\mathrm{DC}}[\hat{n}], \tag{3.39}$$

where $E^{DFT}[\rho]$ is the total energy functional from the DFT method, $E^{\mathrm{e-e}}[\hat{n}]$ is the Coulomb interaction term energy functional. As parts of both $E^{\mathrm{DFT}}[\rho]$ and $E^{\mathrm{e-e}}[\hat{n}]$ describe the same electron-electron interactions, this leads to the double counting of these contributions which $E^{DC}[\hat{n}]$ (the double counting term) approximates and is used to remove them.

To implement the DFT+U method, the Coulomb interaction term is applied to the desired atoms with the localised (d or f) orbitals. In the FP APW+lo basis, the orbital density matrix, Coulomb interaction, and double counting are constructed in the MT basis of the desired orbitals. For further details about the full implementation of the DFT+U calculation in the FP APW+lo basis (used within ELK), see Ref. [93]. Although this thesis does not include any DFT+U calculations, a lot of the parameterisation used in DFT+U is used in (DFT+)DMFT (where the local orbitals are *not* static). The rest of this section will discuss the different forms in which the local intra-atomic Coulomb interaction can be parameterised, how the interaction Hamiltonian is simplified for certain systems to reduce the cost of the calculation, and the different types of double counting. These parameters are needed for the DFT+DMFT calculations presented in this thesis.

3.3.1 Parameterisation of the residual Coulomb potential

When performing calculations dependent on $U_{m,m',m'',m'''}$, this parameter needs to be calculated, but the true value of this in the material is not known. However, it can be estimated through use of the constrained-LDA (cLDA) or constrained random phase approximation (cRPA) [79,

[10]The lower Hubbard band is the lower energy peak and is affiliated to the ionisation energy, and the upper Hubbard band (higher energy peak) relates to the electron affinity.

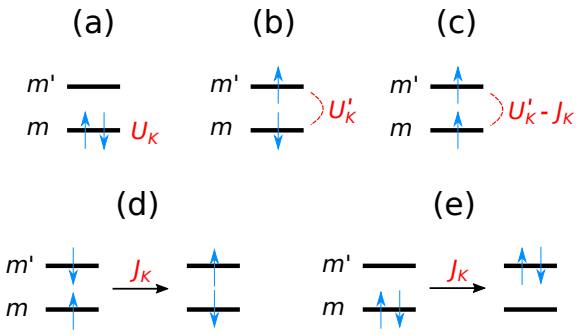

Figure 3.3: An illustration of the multi-orbital interaction terms within the Hubbard-Kanamori Hamiltonian. (a) is the intra-orbital Coulomb interaction given by the first term of Eq. 3.42. (b) and (c) are the inter-orbital interactions with anti-parallel and parallel spins, respectively; these are described by the second term of Eq. 3.42. (d) demonstrates the spin-flip interaction given in the first term within the square brackets of Eq. 3.42, and (e) illustrates the pair-hopping interaction as described in the second term within the square brackets of that equation.

80, 91, 94, 95]. On the other hand, this parameter may be estimated empirically to match with experimental results, but this must be done with care as the calculation may not include all exchange and correlations required to describe the true physical phenomena.

The $U_{m,m',m'',m'''}$ parameter can be expressed as

$$\begin{aligned} U_{m,m',m'',m'''} &= \textstyle\sum_{k=0}^{2l} a_k(m,m',m'',m''')F_k, \\ a_k\left(m,m',m'',m'''\right) &= \tfrac{4\pi}{2k+1} \textstyle\sum_{q=-k}^{k} \left\langle m \left| Y_q^k \right| m'' \right\rangle \left\langle m' \left| Y_q^{k*} \right| m''' \right\rangle, \end{aligned} \tag{3.40}$$

where F_k are the Slater integrals [56, 96] and Y_q^k are the spherical harmonics [79, 95]. These integrals relate to both the intra-orbital Coulomb interaction strength (U) and the Hund's coupling term (J) by [79]

$$\begin{aligned} U &= \tfrac{1}{(2l+1)^2} \textstyle\sum_{m,m'} \sum_{k=0}^{2l} a_k(m,m',m,m')F_k = F_0, \\ J &= \tfrac{1}{2l(2l+1)} \textstyle\sum_{m\neq m'} \sum_k a_k(m,m',m',m)F_k, \end{aligned} \tag{3.41}$$

where J=(F_2+F_4)/14 and F_4/F_2 = 0.625 for d orbitals[11]. These U and J parameters are conventionally quoted for the DFT+U or DFT+DMFT calculations in the literature. The interaction Hamiltonian is constructed to be rotationally invariant, which means that $U_{m,m',m'',m'''}$ is independent of the spin and orbital basis being used.

The interaction Hamiltonian can be simplified (which reduces computational costs) in systems with cubic symmetry, such as transition metal oxides. For these types of systems, the interaction Hamiltonian can be reduced to the Hubbard-Kanamori interaction Hamiltonian ($H_{\text{int}}^{\text{Kan}}$). In this thesis, the d orbitals in correlated cubic symmetric systems are investigated, where the fivefold

[11] TRIQS uses 0.63 instead.

degeneracy of the d orbitals is partially lifted, resulting in a threefold degenerate orbital set ($t_{2g} = [xy, xz, yz]$) and a twofold degenerate orbital set ($e_g = [z^2, x^2 - y^2]$) in the cubic environment.

The Hubbard-Kanamori Hamiltonian describes the density-density, spin-flip, and pair-hopping interactions (illustrated in Fig. 3.3) and has the form [96, 97]

$$\begin{aligned} H_{\text{int}}^{\text{Kan}} =& U_K \sum_m n_{m\uparrow} n_{m\downarrow} + \sum_{m>m'} \sum_{\sigma\sigma'} \left(U'_K - J_K \delta_{\sigma\sigma'}\right) n_{m\sigma} n_{m'\sigma'} \\ & - J_K \sum_{m\neq m'} \left[\left(c^\dagger_{m\downarrow} c^\dagger_{m'\uparrow} c_{m'\downarrow} c_{m\uparrow} + \text{H.c} \right) + \left(c^\dagger_{m'\uparrow} c^\dagger_{m'\downarrow} c_{m\uparrow} c_{m\downarrow} + \text{H.c} \right) \right], \end{aligned} \tag{3.42}$$

where H.c stands for Hermitian conjugate. These new Kanamori parameters connect to the Slater integrals for the t_{2g} orbitals via [79, 96]

$$\begin{aligned} U_K &= U_{mmmm} = F_0 + \tfrac{4}{49}(F_2 + F_4) = U + \tfrac{8}{7}J \\ U'_K &= U_{mm'mm'} \left(m \neq m'\right) = F_0 - \tfrac{2}{49}F_2 - \tfrac{4}{441}F_4 \\ J_K &= U_{mm'm'm} \left(m \neq m'\right) = U_{mmm'm'} \left(m \neq m'\right) = \tfrac{3}{49}F_2 + \tfrac{20}{441}F_4, \end{aligned} \tag{3.43}$$

along with $U_K = U'_K + 2J_K$. These equalities between the Slater integrals and the Kanamori parameters hold assuming that the spherical symmetry of the system holds[12]. When not restricting the orbitals used with this Hamiltonian to the t_{2g} subspace, the equality of the Kanamori parameters and the $U_{m,m',m'',m'''}$ matrix elements no longer holds, meaning that there are more than three parameters needed to describe the interaction Hamiltonian.

3.3.2 Double counting

As DFT already treats electronic interactions on the mean-field level, care is needed to avoid treating the Hartree interaction twice. In this regard, a correction is subtracted from the DMFT self energy (or DFT+U energy functional) – the so-called double counting correction. The exact double counting is still unknown for DFT+U and DFT+DMFT calculations, but a good approximation can be used depending on factors such as which interaction Hamiltonian was used and the occupancy of the correlated orbitals. This section will give the list of double counting terms (just the potential expressions) used in this thesis.

The (spin dependent) fully-localised limit (FLL) double counting originates from DFT+U [98] and has the form of

$$\text{FLL:} \quad \left[\Sigma^{dc}\right]^\sigma_{mm'} = (U - J)(\eta^\sigma_{mm'} - \frac{1}{2}\delta_{mm'}), \tag{3.44}$$

where $\eta^\sigma_{mm'}$ is the spin-resolved occupancy matrix of the correlated orbital and $\delta_{mm'}$ is the Kronecker delta. This approximation is used when the trace of $\eta^\sigma_{mm'}$ is an integer, or close to

[12] Note that often for cubic systems they are not spherically symmetric [96].

an integer. For systems where this trace is not an integer, the (spin-dependent) around the mean-field (AMF) approximation is used [98], which has the form

$$\text{AMF:} \quad \left[\Sigma^{dc}\right]^{\sigma}_{mm'} = (U-J)(\eta^{\sigma}_{mm'} - n^{\sigma}\delta_{mm'}), \tag{3.45}$$

where $n^{\sigma} = N^{\sigma}/(2l+1)$, with $N^{\sigma} = \mathrm{Tr}[\eta^{\sigma}_{mm'}]$.

However, note that care may need to be taken for the Hubbard-Kanamori Hamiltonian, as the U interactions are different for inter- and intra-orbital interactions (as discussed in Section 3.3.1). Therefore, one may need to average U over the diagonal and off-diagonal elements, see Refs. [99, 100] for further details. Alternatively, there are other double counting approximations used for this Hamiltonian, for example, see Ref. [101].

3.4 Dynamical mean-field theory

The DFT+U method includes the local intra-atomic Coulomb interaction as a static term to the Hamiltonian, which leads to improved descriptions of materials which are (Mott) insulators. However, there are still many materials in which DFT+U poorly describes the strong local correlations present. In certain materials, the (temporal) dynamics of the electrons hopping to and from the atomic sites are important. The treatment of these dynamical fluctuations leads to DMFT, which models the dynamics of the electrons present within the correlated orbital without being biased to either the strong or weak local interaction limits. The 'mean-field' part of DMFT comes from the model being spatially static. The key premise of DMFT is to map the many-body Hubbard model onto an Anderson impurity model (AIM) [102], which approximates the many-body system by considering the dynamical interactions between an impurity and an effective bath [86]. There are a few models which can derive the DMFT equations, such as the Cavity method [86] and the Wolff method [86, 103], but this thesis will focus on the AIM description. This section introduces DMFT along with its approximations and the self-consistent cycle. A good description of the DMFT method can be found in Refs. [87, 101, 104].

3.4.1 Anderson impurity model

The AIM describes the interaction between an impurity and a bath (of electrons in the system) and was originally used to solve the Kondo problem[13] [108, 109]. In the context of DMFT, we

[13]The Kondo effect describes the scattering mechanism of conduction electrons in a metal due to magnetic impurities (which have a local magnetic moment due to the spin of unpaired electrons in its atomic-like d or f shell) [105], which accounts for the $\log(1/T)$ contribution to the electrical resistivity in agreement with previous experimental measurements [106]. For low temperatures (below the Kondo temperature T_K), the $\log(1/T)$ description breaks down which led to the Kondo problem (which was the result of the derivation of the Kondo effect being from perturbation theory). Therefore, methods beyond perturbation theory (such as the AIM) were introduced to tackle this problem, see Ref. [107] for more details about the solution to the Kondo problem.

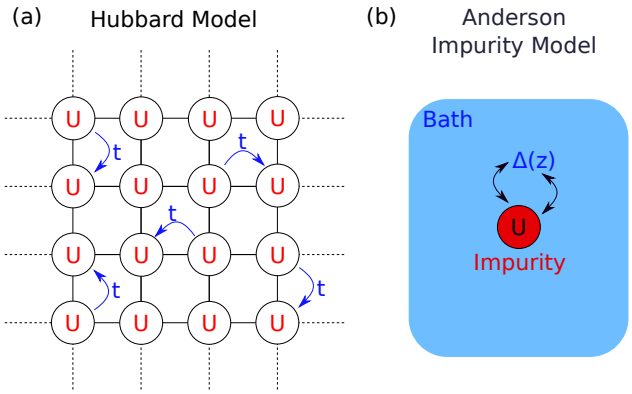

Figure 3.4: Illustrations of the Hubbard model (a) and the Anderson impurity model (b). (a) shows the single band Hubbard model with the electrons hopping (with kinetic energy t) across the lattice, but there is a Coulomb repulsion energy penalty (U) for double occupation on the same site. (b) represents the Anderson impurity model where an impurity is embedded within a bath. The bath is a source of electrons, which flow to and from the impurity, where the bath and the hybridisation of the bath with the impurity are described by the hybridisation function $\Delta(z)$ (where z here represents either the real or Matsubara frequencies). In effect, this hybridisation function replaces the lattice (excluding the impurity site) with an effective (dynamical) mean-field.

approximate the lattice problem described by the Hubbard Hamiltonian as an AIM (both models are illustrated in Fig. 3.4) with a Hamiltonian given by [86, 102]

$$H_{\mathrm{AIM}} = \sum_{n,\sigma} \varepsilon_n^{\mathrm{bath}} b_{n\sigma}^\dagger b_{n\sigma} + \sum_{mm',\sigma} \varepsilon_{mm'}^{\mathrm{loc}} c_{m\sigma}^\dagger c_{m'\sigma} + H_{\mathrm{int}} + \sum_{mn,\sigma} \zeta_{mn} \left(c_{m\sigma}^\dagger b_{n\sigma} + b_{n\sigma}^\dagger c_{m\sigma} \right). \tag{3.46}$$

The first term in Eq. 3.46 describes the energies of the bath, where $\varepsilon_n^{\mathrm{bath}}$ is the energy of the bath with $b_{n\sigma}^\dagger$ ($b_{n\sigma}$) representing the bath's electron creation (annihilation) operator. Whereas $\varepsilon_{mm'}^{\mathrm{loc}}$ and $c_{m\sigma}^\dagger$ ($c_{m'\sigma}$) are the impurity non-interacting energy and creation (annihilation) operator. The H_{int} term describes the many-body interaction on the impurity. Finally, the hybridisation between the impurity and the bath is described by the last term in the AIM Hamiltonian, with matrix elements ζ_{mn}.

To solve this Hamiltonian for the impurity, the bath contribution needs to be integrated out. This leads to the introduction of the hybridisation function

$$\Delta_{mm'}(z) = \sum_n \frac{\zeta_{mn}^* \zeta_{nm'}}{z - \varepsilon_n^{\mathrm{bath}}}, \tag{3.47}$$

where z defines either the real or Matsubara frequencies. This function describes the dynamic hopping of electrons to and from the impurity originating from the bath (i.e. it describes the coupling of the impurity and the bath). Therefore, the effective impurity bare Green's function (the non-interacting Green's function of the impurity), $\mathcal{G}_{mm'}^0(z)$, can be expressed by

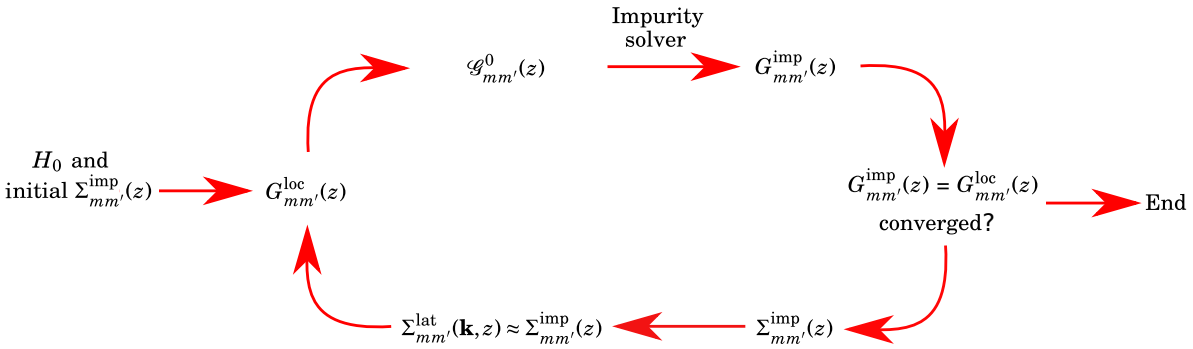

Figure 3.5: A flow chart of how the DMFT equations can be solved self-consistently. First, a non-interacting Hamiltonian H_0 and an initial guess of the impurity self-energy $\Sigma^{\text{imp}}_{mm'}(z)$ (where z defines either the real or Matsubara frequencies) are used to generate the local Green's function $G^{\text{loc}}_{mm'}(z)$ via Eqs. 3.38 and 3.51. This is then used to generate the impurity bare Green's function $\mathcal{G}^0_{mm'}(z)$ (Eq. 3.52) which in turn is used to generate the interacting impurity Green's function $G^{\text{imp}}_{mm'}(z)$ via an impurity solver. The cycle continues if $G^{\text{imp}}_{mm'}(z) \neq G^{\text{loc}}_{mm'}(z)$ outside of a tolerance. In that case, a new $\Sigma^{\text{imp}}_{mm'}(z)$ is determined from the Dyson equation shown in Eq. 3.49, which is then approximated to being the lattice self-energy $\Sigma^{\text{lat}}_{mm'}(\mathbf{k},z)$ (Eq. 3.50). This new self-energy is used to generate a new $G^{\text{loc}}_{mm'}(z)$ and the cycle continues until convergence has been achieved.

$$\mathcal{G}^0_{mm'}(z) = (z - \varepsilon^{\text{loc}}_{mm'} - \Delta_{mm'}(z))^{-1}. \tag{3.48}$$

The interacting impurity Green's function ($G^{\text{imp}}_{mm'}(z)$) is calculated by using an impurity solver, see Section 3.4.2. The impurity self-energy $\Sigma^{\text{imp}}_{mm'}(z)$ is then determined by the Dyson equation

$$\Sigma^{\text{imp}}_{mm'}(z) = \left(\mathcal{G}^0_{mm'}(z)\right)^{-1} - \left(G^{\text{imp}}_{mm'}(z)\right)^{-1}. \tag{3.49}$$

For DMFT, the AIM equations are linked back to the lattice of the Hubbard model by approximating that the lattice self-energy is local ($\mathbf{k}$-independent) meaning that

$$\Sigma^{\text{lat}}_{mm'}(\mathbf{k},z) \approx \Sigma^{\text{imp}}_{mm'}(z). \tag{3.50}$$

The local Green's function is therefore equal to the weighted sum of the lattice Green's function

$$G^{\text{loc}}_{mm'}(z) = \sum_{\mathbf{k}} G^{\text{lat}}_{mm'}(\mathbf{k},z). \tag{3.51}$$

Consequently, $\mathcal{G}^0_{mm'}(z)$ can be determined by

$$\left(\mathcal{G}^0_{mm'}(z)\right)^{-1} = \left(G^{\text{loc}}_{mm'}(z)\right)^{-1} + \Sigma^{\text{imp}}_{mm'}(z). \tag{3.52}$$

This means that a new $G^{\text{imp}}_{mm'}(z)$ can be calculated from the impurity solver, which then produces a new impurity self-energy to be used to generate the next $\mathcal{G}^0_{mm'}(z)$. This DMFT self-consistent cycle, which is illustrated in Fig. 3.5, continues until $G^{\text{imp}}_{mm'}(z) = G^{\text{loc}}_{mm'}(z)$ within a tolerance. Often, an initial guess of $\Sigma^{\text{imp}}_{mm'}(z)$ is used at the start of the DMFT self-consistent cycle. It should be noted that there can potentially be two converged solutions depending on the choice of the initial $\Sigma^{\text{imp}}_{mm'}(z)$. This has been seen in the hysteresis of the U_{MIT} value [6, 104]. The DMFT solutions are exact in the limits of no interaction ($U = 0$), $H_{\text{AIM}} = H_{\text{int}}$, and for the Bethe lattice (i.e. infinite coordination).

3.4.2 Continuous-time quantum Monte Carlo impurity solver

As discussed in the last section, an impurity solver is needed to calculate $G^{\text{imp}}_{mm'}(z)$ from the $\mathcal{G}^0_{mm'}(z)$ and H_{int} inputs. This is where the great computational expense lies. There have been many impurity solvers implemented for this problem, each having their own strengths and flaws. Without going into detail about the solvers, there are some general remarks that can be made. Solvers (such as continuous-time quantum Monte Carlo [CTQMC] [110], exact diagonalisation [111], fork tensor-product states [112], and so on) which capture the entire physics of the model do so at the cost of time and computational resources. There are other solvers which remedy this resource issue (such as iteration perturbation theory [86], fluctuating exchange approximation (FLEX) [113], and so on), but at the cost of losing certain descriptions of the physical processes (as these solvers often come from perturbation theory). Also, certain solvers only operate on the τ (or $i\omega_n$) axis (such as CTQMC), which requires analytic continuation to get the t (or ω) dependent quantities to be compared with the experiment. Analytic continuation has its own challenges and will be discussed in Section 3.5. The current popular choice of solver is the CTQMC. The CTQMC solvers have different formulations, namely the interaction expansion (CTINT) [114], the auxiliary-field (CTAUX) [115], and the hybridisation expansion (CTHYB) [116]. This thesis used the CTHYB solver. The rest of this chapter will introduce the general concepts of how the CTHYB solver works. The full derivation is beyond the scope of this thesis, but further information can be found in Ref. [110].

The CTQMC solvers actually sample the partition function $\mathcal{Z}$. This time-ordered (denoted by $\mathcal{T}_\tau$) function is dependent on the Hamiltonian (H) which itself can be split into two terms H_a and H_b ($H = H_a + H_b$). These two terms are the generic form for any CTQMC solver, but for CTHYB, H_a represents the bath and the impurity, whereas H_b represents the hybridisation between the bath and impurity. Therefore, $\mathcal{Z}$ has the form

$$\begin{aligned} \mathcal{Z} &= \operatorname{Tr} e^{-\beta H} = \operatorname{Tr}\left(\mathcal{T}_\tau e^{-\beta H_a} \exp\left[-\int_0^\beta H_b(\tau) d\tau\right]\right) \\ &= \sum_{k=0}^{\infty} (-1)^k \int_0^\beta \cdots \int_{\tau_{k-1}}^\beta \operatorname{Tr}\left(e^{-\beta H_a} H_b(\tau_k) \cdots H_b(\tau_1)\right) d\tau_k \cdots d\tau_1, \end{aligned} \tag{3.53}$$

where the second line has expanded $\mathcal{Z}$ as a power series of $H_b(\tau_k)$, with k representing the

perturbation order. As H_a can be separated again by the bath and impurity contributions, this and introducing the hybridisation function into $\mathcal{Z}$ leads to the CTHYB $\mathcal{Z}$ of

$$\begin{aligned}\mathcal{Z} = \quad & \mathcal{Z}_{\text{bath}} \sum_{k=0}^{\infty} \int \cdots \int \sum_{j_1 \cdots j_k} \sum_{j'_1 \cdots j'_k} \\ & \left(\text{Tr} \left[\mathcal{T}_\tau e^{-\beta H_{\text{loc}}} c_{j_k}(\tau_k) c^\dagger_{j'_k}(\tau'_k) \cdots c_{j_1}(\tau_1) c^\dagger_{j'_1}(\tau'_1) \right] \det \Delta \right) d\tau_1 \cdots d\tau'_k,\end{aligned} \tag{3.54}$$

where j represents "flavour" (i.e. spin, site, orbital and so on) indices, H_{loc} is the impurity Hamiltonian containing the impurity's non-interacting and interacting terms from H_{AIM} (in Eq. 3.46), and $\mathcal{Z}_{\text{bath}}$ is the bath partition function which has an analytic expression. It should be noted that the hybridisation function here is a $k \times k$ matrix with elements $\Delta_{xy} = \Delta_{j_x j_y}(\tau_x - \tau_y)$. This partition function is a complicated expression, but it can be thought of in another way. It is made up of different configurations which represent whether a creation or annihilation operator acts at τ_k over the entire range of τ (i.e. a (τ) timeline describing the dynamics of the electrons hopping on and/or off the impurity). Therefore, $\mathcal{Z}$ is calculated by sampling many different configurations. New configurations are purposed by using the Markov chain process in which the likelihood and acceptance of the proposed change to the configuration which, if accepted, updates previous configuration (an example could be inserting/removing an operator). This process is often calculated by using the Metropolis-Hastings algorithm [117, 118]. If the new configuration is accepted, this is added to the previous list of configurations which is then used to sample $\mathcal{Z}$. A reliable $\mathcal{Z}$ is calculated from a sufficiently large number of sampled configurations. The impurity Green's function is then determined by re-weighting the $\mathcal{Z}$ (or more specifically, it is determined from the Δ^{-1}).

The expansion coefficients of $\mathcal{Z}$ have been assumed to be positive or zero, as the contribution (the weight as it's most commonly described) of each configuration has been determined by probability densities. However, in actuality these weights could be negative, due to factors such as the anti-commutation relations between fermionic operators, meaning that they cannot be strictly treated with probability densities. The way around this is to sample the average of the observable(s) $\langle A \rangle$ [which represents quantities such as the impurity Green's function] with the absolute weight ($|p|$) and re-weight the measurements by

$$\langle A \rangle = \frac{\langle A \, \text{sgn(p)} \rangle_{|p|}}{\langle \text{sgn(p)} \rangle_{|p|}}, \tag{3.55}$$

which can be evaluated by sampling the numerator and denominator separately with respect to the absolute weight $|p|$. This equation introduces the sign function (sgn(p)=$p/|p|$) where the average of this sign function has the form

$$\langle \text{sgn(p)} \rangle_{|p|} = \frac{\int \text{sgn}(p(\mathbf{x})) |p(\mathbf{x})| d\mathbf{x}}{\int |p(\mathbf{x})| d\mathbf{x}} = \frac{\mathcal{Z}}{\mathcal{Z}_{|p|}} = e^{-\beta \Delta F}, \tag{3.56}$$

where $\langle \mathrm{sgn(p)} \rangle_{|p|}$ has been determined by integrating over all configurations (**x**). This means that better statistics are required to calculate $\langle A \rangle$ if the average sign is smaller than unity. The last part of the equality relates the sign to the free energy difference ΔF between the system with partition function $\mathcal{Z}$ and the "bosonic" system with partition function $\mathcal{Z}_{|p|}$ composed of positive weights $|p|$. Consequently, this means that the average sign decreases exponentially as the temperature is lowered or if the volume of the system increases. This is referred to as the sign problem and it is (believed to be) inherent to CTQMC solvers. This is also basis dependent, so to help reduce the effect of the sign problem, a diagonal basis in $\Delta(z)$ should be chosen as the frequency dependence of the off-diagonal elements are less clearly defined.

The error (noise) from the CTHYB output impurity Green's function (and self-energy) increases with $|\omega_n|$ which could lead to instabilities and/or nonphysical behaviour in the DMFT cycle. This is addressed in this thesis by fitting a tail to the Green's function and self-energy. The Green's function and self-energy tend to zero for high frequencies, so their tails are fitted by a high-frequency Laurent expansion of the Green's function or self-energy, up to a finite order.

3.5 Analytic continuation

As mentioned in previous sections, the real frequency quantities are derived by analytically continuing them from the imaginary time (or Matsubara axis). This is an ill-posed problem meaning that directly continuing the imaginary time (or Matsubara frequency) quantities will be very sensitive to the numerical noise (such as from the CTQMC solver or any other contribution). This has resulted in many different analytical continuation algorithms to tackle this problem with methods such as Padé [119], maximum entropy method (MEM) [120], and stochastic optimisation [121] being the current popular choices. This thesis used the MEM for analytically continuing the imaginary time dependent quantities. These quantities in τ-space were used instead of the corresponding Matsubara frequency dependent quantities as only the real part of the spectral function $A(\omega)$ is connected to the real part of $G(\tau)$ and the same for the imaginary parts of these quantities [whereas the real and imaginary parts of $G(i\omega_n)$ and $A(\omega)$ are coupled]. This section introduces the MEM analytic continuation formalism which follows the key concepts of the methodology presented in [120, 122], and the implementation within the TRIQS library is discussed in [123–125].

The spectral function is related to $G(\tau)$ by

$$G(\tau) = \int \frac{e^{-\omega\tau}}{1+e^{-\omega\beta}} A(\omega) d\omega. \tag{3.57}$$

This is handled numerically by discretizing the Green's function ($G_n = G(\tau_n)$) and spectral function ($A_m = A(\omega_m)$) into vectors such that $\mathbf{G} = \mathbf{KA}$, where $\mathbf{K}$ is the kernel of the transform with the matrix elements

$$K_{mn} = \frac{e^{-\omega_m \tau_n}}{1 + e^{-\omega_m \beta}} \Delta\omega_m. \tag{3.58}$$

Getting $G(\tau)$ from $A(\omega)$ is straightforward, but calculating $A(\omega)$ using $\mathbf{A} = \mathbf{K}^{-1}\mathbf{G}$ is the aforementioned ill-posed problem. The origin of this problem comes from the $\mathbf{K}$ kernel matrix which is almost singular due to the exponentials in the matrix elements (i.e. it has a large condition number). This means that calculating the inverse is prone to large numerical errors.

The premise of analytic continuation techniques is to calculate a spectral function which reproduces the features of $G(\tau)$ [$\mathbf{G}_{\text{rec}} = \mathbf{KA}$], but with reduced effects from the noise. Unfortunately, minimising the misfits χ^2 of G and G_{rec} leads to uncontrollable errors [119]. This leads to the MEM adding an entropic term $S(A)$ to be minimised as well. The entropy term prevents overfitting to the noisy data of $G(\tau)$ to make $\mathbf{A}$, and its features, as smooth as possible. The $S(A)$ has the form of

$$S(A) = \int \left[A(\omega) - D(\omega) - A(\omega) \log \frac{A(\omega)}{D(\omega)} \right] d\omega, \tag{3.59}$$

where $D(\omega)$ is the default model. For this thesis, a flat $D(\omega)$ model was used [this corresponds to having no prior knowledge about $A(\omega)$]. So, the new minimised term Q_α thus has the form of

$$Q_\alpha = \frac{1}{2}\chi^2 - \alpha S(A), \tag{3.60}$$

where α is a weight (sometimes called the "hyperparameter") given to the entropy term which needs to be optimised to get the desired $A(\omega)$. The consequences of minimising this Q_α function instead is to have a resulting $A(\omega)$ which does not over-fit the noisy spectrum of $G(\tau)$ when using an appropriate value of α. If large values of α are used, $A(\omega)$ tends to $D(\omega)$.

Previous implementations of MEM either under-fits or over-fits the data when using their α parameters [123, 124]. In this thesis, the value of α was calculated by the $LinearFitAnalyser$ method [123–125]. This consists of fitting two lines to the $\log[\chi^2(\log[\alpha])]$ vs. $\log[\alpha]$ spectra. The first line fits the noise region (low α values), which has a slope of zero and the other line fits the information region (in which $\log[\chi^2(\log[\alpha])]$ behaves linearly). The intersection of these lines gives the optimal α.

Within this thesis, the local Green's function is analytically continued using the aforementioned process, but analytically continuing the local self-energy, on the other hand, requires a slightly different method. Strictly speaking, there is currently no direct analytic continuation formula which relates the self-energy on the real axis to the self-energy on the imaginary axis. Instead, an auxiliary Green's function ($G_{\text{aux}}(\tau)$) is constructed from the self-energy, which is then continued. The steps to get the analytically continued self-energy from $G_{\text{aux}}(\tau)$ are: construct $G_{\text{aux}}(i\omega_n)$ from $\Sigma(i\omega_n)$; inverse Fourier transform $G_{\text{aux}}(i\omega_n)$ to get $G_{\text{aux}}(\tau)$; analytically continue

$G_{\text{aux}}(\tau)$ to get $A_{\text{aux}}(\omega)$; construct $G_{\text{aux}}(\omega + i0^+)$ from $A_{\text{aux}}(\omega)$ using the Kramers-Kronig relations; then finally obtain $\Sigma(\omega + i0^+)$ from $G_{\text{aux}}(\omega + i0^+)$. This thesis uses the inversion method in which $G_{\text{aux}}(z)$ (where z is either ω or $i\omega_n$) has the form

$$G_{\text{aux}}(z) = [z + C - \Sigma(z)]^{-1}, \tag{3.61}$$

where C is a constant usually set to $C = \Sigma(\infty) + \mu$ where $\Sigma(\infty)$ is the high-frequency expansion of $\Sigma(z)$. The other possible $G_{\text{aux}}(z)$ expression (which was not used in this thesis) is

$$G_{\text{aux}}(z) = \Sigma(z) - \Sigma(\infty). \tag{3.62}$$

It should be noted that $G_{\text{aux}}(z)$ in Eq. 3.62 is not a true Green's function as its off-diagonal elements do not have the correct analytic high-frequency behaviour (it has $1/\omega_n$ instead of the true Green's function high frequency behaviour of $1/(\omega_n)^2$). Lastly, the analytically continued spectral function directly from the Green's function using MEM is susceptible to artificial noise around $\omega = 0$, as discussed in Ref. [126]. However, this may be suppressed when using the analytically continued self-energy to calculate the spectral function.

3.6 Wave-function-dependent quantities

There are certain quantities which can be extracted from the Matsubara frequency and/or imaginary time axes without the need of analytical continuation, circumventing any of the aforementioned issues from this technique. There are several which have been used previously, such as the DFT+DMFT electron density, discussed in Section 3.7.3, as well as other quantities extracted directly from the Matsubara (and imaginary time) Green's functions and self-energies – see, for example, Section 6.4. The work in this thesis introduces two DFT+DMFT quantities which also do not require analytic continuation: the electron localisation function (ELF) and electron momentum density (EMD), which are discussed in Sections 4.2 and 5.2, respectively.

In this thesis, the ELF, EMD, and electron density are referred to as wave-function-dependent quantities. What this means is that these quantities are explicitly determined from the wave functions (and occupations), or in other words, they are functions of the wave functions (for example, the electron density is calculated from the square modulus of the occupied wave functions in Eq. 3.12). It should be noted that all of the calculated quantities are implicitly dependent on the wave functions of the system as the wave functions are needed to solve the Hamiltonian. However, certain quantities are not computed from the wave functions, such as the spectral function. This function is determined from the imaginary part of the Green's function, which in turn is determined from the energy eigenvalues (and so on) of the system. The wave functions from DFT, DFT+DMFT or otherwise are not needed to compute the spectral function,

ergo, the spectral function is not a wave-function-dependent quantity with respect to the definition above.

3.7 DFT+DMFT

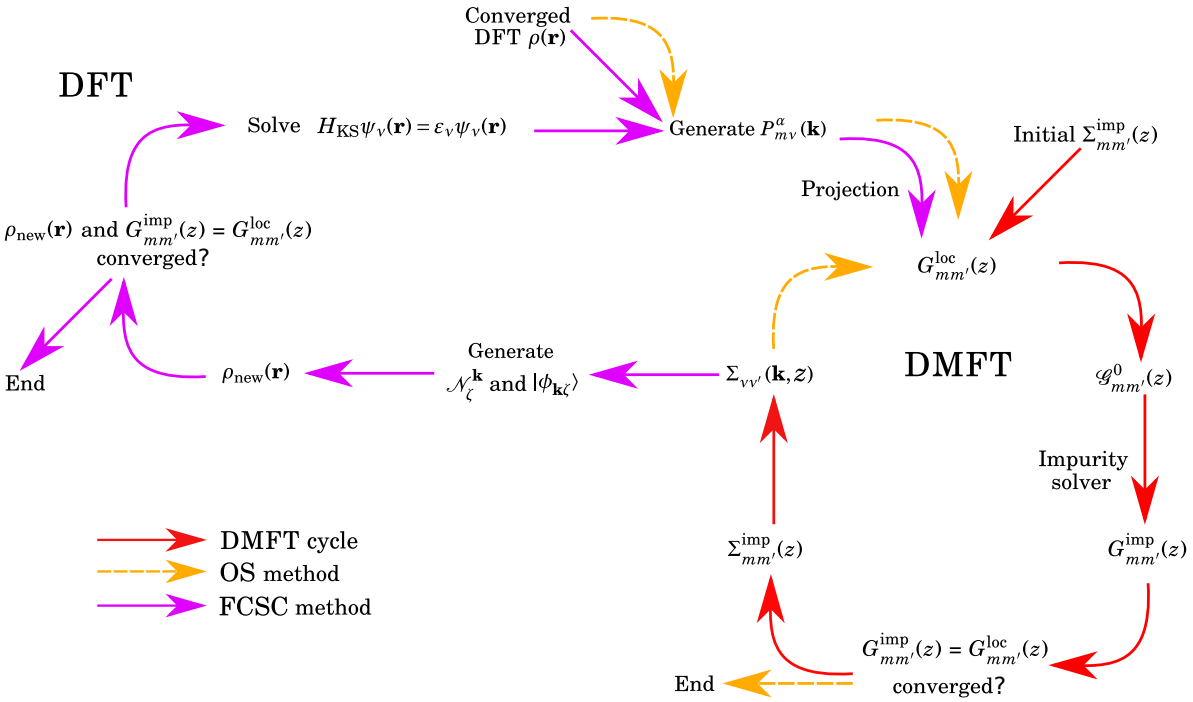

Figure 3.6: The flow chart illustrating the one-shot (OS) and fully charge self-consistent (FCSC) DFT+DMFT methods used in this thesis (ignoring spin indices for simplicity), where the different steps used by the OS and FCSC DFT+DMFT methods are represented by the dashed yellow and solid purple arrows, respectively. The details of these methods are discussed in Sections 3.7.1, 3.7.2, and 3.7.3. First, the Wannier projectors $P^{\alpha,\sigma}_{m\nu}(\mathbf{k})$ are generated from the converged DFT calculation and are used (along with the Kohn-Sham energy eigenvalues) to calculate the local Green's function $G^{\mathrm{loc}}_{mm'}(z)$ (where z defines either the real or Matsubara frequencies), which leads onto solving the DMFT equations shown in Fig. 3.5. The subtle difference here is that projection methods are used in the DMFT cycle, for example, the lattice self-energy is determined by upfolding the impurity self-energy (see Section 3.7.2). For the OS method, The calculation ends when $G^{\mathrm{imp}}_{mm'}(z) = G^{\mathrm{loc}}_{mm'}(z)$ within a tolerance. The FCSC method, on the other hand, builds on the OS method (and often uses the converged results from the OS calculation) to generate the DFT+DMFT wave functions and occupations as described in Section 3.7.3. These are then used to generate a new (DFT+DMFT) electron density $\rho(\mathbf{r})$ and if this is equal to the electron density from the previous cycle, as well as $G^{\mathrm{imp}}_{mm'}(z) = G^{\mathrm{loc}}_{mm'}(z)$, within a tolerance, then the FCSC DFT+DMFT calculation stops. Otherwise, the new (DFT+DMFT) electron density generates a new Kohn-Sham Hamiltonian which is then used to determine a new set of Kohn-Sham wave functions and energy eigenvalues. Subsequently, these are used to generate a new set of Wannier projectors and the FCSC DFT+DMFT calculation continues until convergence has been reached.

Unfortunately, performing DMFT calculations on all of the orbitals within real materials is too computationally demanding; therefore DMFT is typically used to model the strongly correlated local states in combination with DFT – the DFT+DMFT method. Now that both the DFT and DMFT self-consistent cycles have been established, this section will discuss the method used to combine these two theories together. In this thesis, the DFT outputs are projected into real space by using Wannier projectors. The DMFT lattice and local Green's functions are constructed from the DFT electronic structure and these projectors. The two DFT+DMFT methods used in this thesis, the one-shot (OS) and fully charge self-consistent (FCSC) methods, will be discussed, with the self-consistent cycles of these DFT+DMFT methods being illustrated in Fig. 3.6. The formulas in the next few sections will be given in terms of the collinear spins for clarity. Non-collinear projectors and so on are discussed in Appendix 3.8. These sections will be discussed from the perspective of the implementation of DFT+DMFT within ELK-TRIQS, see Ref. [23].

3.7.1 Wannier functions and projectors

The electron orbitals required for the impurity sites used in DMFT are in real space, localised, and atomic-like whereas the Bloch wavefuntions used in DFT are periodic and delocalised in real space. However, the Bloch wave functions can be Fourier transformed into a localised real basis set of orbitals. This basis set is referred to as Wannier wave functions $|w_{\mathbf{R},m}\rangle$ which have the multiband form of

$$|w_{\mathbf{R},m}\rangle = \frac{\Omega}{(2\pi)^3}\int_{\mathrm{BZ}} e^{-i\mathbf{k}\cdot\mathbf{R}}\sum_{\nu}^{N}\mathscr{M}^{\mathbf{k}}_{m\nu}\,|\psi_{\mathbf{k}\nu}\rangle\, d\mathbf{k}, \tag{3.63}$$

with Ω being the unit cell volume, $\mathbf{R}$ is a real-space lattice vector, N is the number of bands, $|\psi_{\nu\mathbf{k}}\rangle$ is the Bloch wave function and $\mathscr{M}^{\mathbf{k}}_{m\nu}$ is a N dimension unitary matrix which describes the mixing of the (ν) band states before the Fourier transform. Note that a subset of bands can be used to construct the Wannier wave function. Due to the gauge freedom in $\mathscr{M}^{\mathbf{k}}_{m\nu}$, the Wannier wave functions are not unique and therefore constructing them requires a few extra steps. One commonly used technique is to construct maximally localised Wannier functions (MLWFs), which constructs $\mathscr{M}^{\mathbf{k}}_{m\nu}$ to satisfy a localisation criterion. Further details can be found in Ref. [127].

Another method of constructing the Wannier wave functions is from the Wannier projection method [127–130]. However, only the Wannier projectors from this method are needed for calculating the DMFT quantities, and consequently, the Wannier wave functions were not generated here, which results in a reduction of the computational effort required. Another benefit of using this projection method is that the lattice symmetries can be used on these projectors, which helps reduce the computational effort for BZ integrations. Generating the Wannier projectors, $P^{\alpha,\sigma}_{m\nu}(\mathbf{k})$, within the correlated subspace first requires calculating the inner product between a trial local function and the Bloch wave function. This inner product is referred to as a temporary projector, $\hat{P}^{\alpha,\sigma}_{m\nu}(\mathbf{k})$. By default in the ELK part of the ELK-TRIQS interface, the trial local function is chosen to

be the APW radial function $[|\tilde{\chi}_m^{\alpha,\sigma}\rangle = |u_l^{\alpha,\sigma}(E_{l,\alpha}^1)Y_{lm}\rangle]$ within the MT sphere at the corresponding linearisation energy $E_{l,\alpha}^1$. Note that ELK treats magnetism as a second variational step, hence $|u_l^{\alpha,\sigma}(E_{l,\alpha}^1)Y_{lm}\rangle$ is not spin/spinor dependent meaning that $|\tilde{\chi}_m^{\alpha,\sigma}\rangle$ is also spin/spinor independent. The states within the interstitial region are too delocalised to be included, but the information about this region is included in the APW matching coefficients. Here, $|\tilde{\chi}_m^{\alpha,\sigma}\rangle$ does not need to resemble the Wannier wave functions closely, but it needs to be located on the desired site (atom) with the appropriate angular character. The temporary projectors are directly computed from the second variational wave functions by

$$\widetilde{P}_{m\nu}^{\alpha,\sigma}(\mathbf{k}) = \langle \tilde{\chi}_m^{\alpha,\sigma} | \psi_{\mathbf{k}\nu}^{\sigma} \rangle, \quad \nu \in \mathscr{W}, \tag{3.64}$$

where $\mathscr{W}$ is the correlated energy window. To calculate local quantities[14], we have to integrate over the entire 1BZ by using a (weighted) summation over the IBZ with symmetry operations as given by the following generic formula

$$\sum_{\mathbf{k}}^{1\mathrm{BZ}} \mathbf{A}(\mathbf{k}) = \sum_{s=1}^{N_s} \sum_{\mathbf{k}}^{\mathrm{IBZ}} \mathscr{S}_s \mathbf{A}(\mathbf{k}) \mathscr{S}_s^{\dagger}, \tag{3.65}$$

using N_s symmetry operations with each $\mathscr{S}_s$ symmetry matrix. Therefore, this integration requires a symmetrisation in a global coordinate system (basis). For equivalent atoms, the temporary projectors thus far are equivalent, as they are in a local coordinate basis. Subsequently, the temporary projectors need to be transformed into a global basis[15]. This is done by using the matrix transformation of

$$\widetilde{P}_{m\nu}^{\mathrm{global},\alpha',\sigma}(\mathbf{k}) = \mathscr{S}^{\alpha,\alpha'} \widetilde{P}_{m\nu}^{\mathrm{loc},\alpha,\sigma}(\mathbf{k}), \tag{3.66}$$

with $\mathscr{S}^{\alpha,\alpha'}$ specifying the symmetry matrix which transforms the projector to the equivalent atom site. At this point, an lm basis transformation can also be applied here (after the symmetry transformation). Therefore a subset of lm values (such as the t_{2g} orbitals) could be chosen and/or a diagonal lm basis could be used to help reduce issues with the sign problem.

These temporary projectors are then orthonormalised via

$$P_{m\nu}^{\alpha,\sigma}(\mathbf{k}) = \sum_{\alpha' m'} \left\{ [O(\mathbf{k},\sigma)]^{-1/2} \right\}_{m,m'}^{\alpha,\alpha'} \widetilde{P}_{m'\nu}^{\alpha',\sigma}(\mathbf{k}), \tag{3.67}$$

to form the complete Wannier projector set. Here, $O_{m,m'}^{\alpha,\alpha'}(\mathbf{k},\sigma)$ are the overlap matrix elements which, in terms of the temporary projectors, have the form

[14] The DMFT cycle is within a local coordinate basis, but the lattice Green's function is in a global coordinate basis.

[15] ELK does not use a local rotation matrix as in WIEN2K, so the global-local basis transformations just use lattice symmetries.

$$O^{\alpha,\alpha'}_{m,m'}(\mathbf{k},\sigma) = \sum_{\nu\in\mathscr{W}} \widetilde{P}^{\alpha,\sigma}_{m\nu}(\mathbf{k})\widetilde{P}^{\alpha',\sigma*}_{\nu m'}(\mathbf{k}). \tag{3.68}$$

The projection method works as long as $\{[O(\mathbf{k},\sigma)]^{-1/2}\}^{\alpha,\alpha'}_{m,m'}$ does not become singular (or is close to being so). This depends on a sensible choice of $\mathscr{W}$[16]. Also, without the normalisation of projectors, the DMFT procedure would induce charge leakage – some charge would not be captured by the projection.

For the ELK-TRIQS interface [23], the temporary projectors are constructed from the Kohn-Sham second variational wavefunctions which are then orthonormalised to generate the Wannier projectors. These steps which generate the Wannier projectors are done within ELK. These projectors, along with energy eigenvalues, symmetries and so on, are then read by the TRIQS library.

3.7.2 One-shot DFT+DMFT

The OS DFT+DMFT calculation employs the following method. Using the Matsubara frequency axis, (the initial guess of) the self-energy with the double counting term is projected (upfolded[17]) from the local basis into the Kohn-Sham basis by

$$\Sigma^{\sigma}_{\nu\nu'}(\mathbf{k},i\omega_n) = \sum_{\alpha mm'} P^{\alpha,\sigma*}_{\nu m}(\mathbf{k})[\Delta\Sigma^{\alpha,\sigma,\mathrm{imp}}_{mm'}(i\omega_n)]^{\mathrm{global}}P^{\alpha,\sigma}_{m'\nu'}(\mathbf{k}), \tag{3.69}$$

with the basis transformation to the global basis

$$[\Delta\Sigma^{\alpha,\sigma,\mathrm{imp}}_{mm'}(i\omega_n)]^{\mathrm{global}} = \mathscr{S}^{\alpha,\alpha'}[\Delta\Sigma^{\alpha',\sigma,\mathrm{imp}}_{mm'}(i\omega_n)]^{\mathrm{local}}\mathscr{S}^{\alpha,\alpha'\dagger}, \tag{3.70}$$

where

$$[\Delta\Sigma^{\alpha',\sigma,\mathrm{imp}}_{mm'}(i\omega_n)]^{\mathrm{local}} = [\Sigma^{\alpha',\sigma,\mathrm{imp}}_{mm'}(i\omega_n)]^{\mathrm{local}} - \left[\Sigma^{dc}\right]^{\sigma}_{mm'}. \tag{3.71}$$

Then the lattice Green's function is calculated from the DFT eigenvalues using

[16] The choice of $\mathscr{W}$ will also have other effects such as on the Wannier charge which depends on the included occupied and unoccupied states used in the projector calculation. Also, U may depend on the choice of $\mathscr{W}$, for example, see the $SrVO_3$ calculations in Ref. [130]. One issue, not covered by DMFT, is that in reality U is frequency dependent [$W(\omega)$], see, for example, Ref. [81]. This is hard to treat, and hence we approximate $W(\omega)$ with a constant U [which is often $W(\omega \longrightarrow 0)$]. The energy window tends to increase the dynamical trend of U when the window is small; hence a smaller window might also induce some extra source of error.

[17] The upfolding of the self-energy (Eq. 3.69) and the downfolding of the lattice Green's function (Eq. 3.73) is separable meaning that causality is preserved, see Ref. [131].

$$G^{\sigma}_{\nu\nu'}(\mathbf{k}, i\omega_n)^{-1} = \left(i\omega_n + \mu - \epsilon^{\sigma}_{\mathbf{k}\nu}\right)\delta_{\nu\nu'} - \Sigma^{\sigma}_{\nu\nu'}(\mathbf{k}, i\omega_n). \tag{3.72}$$

Subsequently, the local Green's function is calculated by

$$G^{\alpha,\sigma,\mathrm{loc}}_{mm'}(i\omega_n) = \sum_{\mathbf{k},\nu\nu'} P^{\alpha,\sigma}_{m\nu}(\mathbf{k}) G^{\sigma}_{\nu\nu'}(\mathbf{k}, i\omega_n) P^{\alpha,\sigma *}_{\nu' m'}(\mathbf{k}), \tag{3.73}$$

which is used to calculate the effective bare impurity Green's function to be solved in the (CTHYB) impurity solver, as described in Sections 3.4.1 and 3.4.2. The new self-energy is calculated by solving the Dyson equation in Eq. 3.49. This self-energy is then upfolded to begin the DMFT cycle again. This cycle continues until convergence (as described in Section 3.4.1).

3.7.3 Fully charge self-consistent DFT+DMFT

The FCSC DFT+DMFT calculation involves updating the Kohn-Sham electron density from the DMFT lattice Green's function. The FCSC method is performed after getting convergence in the one-shot method. This helps reduce the number of FCSC DFT+DMFT cycles and any potential instabilities caused by solving the Kohn-Sham system from the updated electron density in the FCSC DFT+DMFT calculation.

After converging the OS DFT+DMFT calculation, the interacting charge density matrix $N^{\mathbf{k},\sigma}_{\nu\nu'}$ is calculated from the summation of $G^{\sigma}_{\nu\nu'}(\mathbf{k}, i\omega_n)$ over the Matsubara frequencies[18],

$$N^{\mathbf{k},\sigma}_{\nu\nu'} = \frac{1}{\beta}\sum_{n} G^{\sigma}_{\nu\nu'}(\mathbf{k}, i\omega_n) e^{i\omega_n 0^+}, \quad \nu \in \mathscr{W}. \tag{3.74}$$

Then $N^{\mathbf{k},\sigma}_{\nu\nu'}$ is read into ELK.

In general, $\Sigma^{\sigma}_{\nu\nu'}(\mathbf{k})$ has non-diagonal elements which consequently means that $N^{\mathbf{k},\sigma}_{\nu\nu'}$ would also have non-diagonal elements. To construct a diagonal set of wave functions (as is conventionally used in DFT), first the total density matrix ($N'^{\mathbf{k},\sigma}_{\nu\nu'}$) within the Kohn-Sham basis is constructed by combining the DMFT density matrix within the correlated energy window $\mathscr{W}$ ($N^{\mathbf{k},\sigma}_{\nu\nu'}$, $\nu \in \mathscr{W}$) with the DFT density matrix outside that window ($n^{\mathbf{k},\sigma}_{\nu\nu'}$, $\nu \notin \mathscr{W}$). This total density matrix includes all the DFT+DMFT state indices ν, both within and outside $\mathscr{W}$. A new set of diagonal DFT+DMFT occupation numbers $\mathscr{N}^{\mathbf{k},\sigma}_{\zeta}$, and DFT+DMFT wave functions $|\phi^{\sigma}_{\mathbf{k}\zeta}\rangle$ are determined by a unitary transformation $\mathscr{U}$ given by diagonalising the total density matrix (as in Ref. [132]):

$$\mathscr{N}^{\mathbf{k},\sigma}_{\zeta}\delta_{\zeta\zeta'} = \sum_{\nu\nu'} \mathscr{U}^{\sigma}_{\zeta\nu} N'^{\mathbf{k},\sigma}_{\nu\nu'} \mathscr{U}^{\sigma *}_{\nu'\zeta'}; \quad |\phi^{\sigma}_{\mathbf{k}\zeta}\rangle = \sum_{\nu} \mathscr{U}^{\sigma}_{\zeta\nu} |\psi^{\sigma}_{\mathbf{k}\nu}\rangle, \tag{3.75}$$

[18] The summation in Eq. 3.74 involves, in principle, tracing over a slowly decaying function in the high frequency limit. Therefore, care is needed when including the high frequency tail of the Green's function in the summation (for example, the tail can be approximated by a Laurent expansion and the integral of the high frequency tail can be analytically evaluated by using this expansion).

where $\delta_{\zeta\zeta'}$ is the Kronecker delta. These DFT+DMFT wave functions can be used to generate quantities that are solely dependent on the wave functions and occupations. The FCSC DFT+DMFT cycle uses these wave functions and occupations to calculate the new DFT+DMFT electron density, $\rho(\mathbf{r})$, which is now

$$\rho(\mathbf{r}) = \sum_{\zeta,\mathbf{k},\sigma} \mathcal{N}_{\zeta}^{\mathbf{k},\sigma} \langle \mathbf{r}|\phi_{\mathbf{k}\zeta}^{\sigma}\rangle\langle\phi_{\mathbf{k}\zeta}^{\sigma}|\mathbf{r}\rangle. \tag{3.76}$$

The density matrix includes information about both occupied incoherent and coherent QP states as these are included in the Matsubara lattice Green's function, and the density matrix is derived from the summation of this Green's function in Eq. 3.74. This is equivalent to integrating the occupied spectral function on the real frequency axis but note that it does not require any analytic continuation which complicates that approach. The influence of these coherent and incoherent states changes the occupation function (derived from the density matrix) from a Fermi-Dirac function in DFT to something more similar to the Fermi-liquid occupation function.

Finally, the total energy in the FCSC DFT+DMFT formalism is the same as in previous implementations [16, 132]

$$E = E_{\mathrm{DFT}}[\rho] + \sum_{\mathbf{k},\sigma}\sum_{\nu\in\mathscr{W}} (N_{\nu\nu}^{\mathbf{k},\sigma} - f_{\nu,\mathbf{k}}^{\sigma})\varepsilon_{\nu\mathbf{k}}^{\sigma} + E_{\mathrm{corr}}\left[\hat{G}\right] - E_{\mathrm{DC}}\left[\hat{G}\right], \tag{3.77}$$

where $E_{\mathrm{DFT}}[\rho]$ is the DFT total energy functional evaluated with the DFT+DMFT electron density, $f_{\nu,\mathbf{k}}^{\sigma}$ is the DFT occupation function, $\varepsilon_{\nu\mathbf{k}}^{\sigma}$ is the DFT energy eigenvalues and both $E_{\mathrm{corr}}\left[\hat{G}\right]$ and $E_{\mathrm{DC}}\left[\hat{G}\right]$ are the correlation and double counting correction energies calculated from the DMFT Green's function. The Galitskii-Migdal formula [133, 134]

$$E_{\mathrm{corr}}\left[\hat{G}\right] \approx \frac{1}{2\beta}\sum_{m}\sum_{n}\Sigma_{mm}^{\mathrm{imp}}(i\omega_n)G_{mm}^{\mathrm{imp}}(i\omega_n), \tag{3.78}$$

was used to calculate $E_{\mathrm{corr}}\left[\hat{G}\right]$ in this thesis. From these updates, a new set of second-variational wave functions can be generated from $\rho(\mathbf{r})$, by solving the Kohn-Sham cycle once, to produce new Wannier projectors and then follow the one-shot method again[19]. The electron density is updated again and hence completing an FCSC DFT+DMFT cycle. This FCSC DFT+DMFT method continues until both DFT and DMFT convergence criteria are met within a sensible tolerance (however, there is no total energy tolerance criteria in FCSC DFT+DMFT calculation).

3.8 Appendix: Spinor Wannier projectors

In this section, the treatment of the Wannier projectors of the spinor wave functions is discussed. These spinor Wannier projectors are generated for SOC systems and non-collinear magnetism,

[19] typically only doing one DMFT cycle here, but more cycles can be used to reduce instabilities

which means that the corresponding Green's functions, self-energies, and so on have to be treated as 2×2 spin-block matrices[20]. This section, in part, will follow the theory used to calculate the spinor projectors and Green's functions presented in Refs. [124, 135], but will discuss this theory in terms of its implementation in the ELK-TRIQS package.

As in the collinear case, the temporary spinor Wannier projectors are directly computed from the second variational wave functions by

$$\left[\tilde{P}^{\alpha,\sigma}_{m\nu}(\mathbf{k})\right]^{\lambda} = \left\langle \tilde{\chi}^{\alpha,\sigma}_{m} | \psi^{\lambda}_{\mathbf{k}\nu} \right\rangle, \quad \nu \in \mathscr{W}, \tag{3.79}$$

where λ is the spinor index. Note that the trial local function is spin independent in ELK unlike in WIEN2K. This is because ELK treats the APW radial functions in the first variational step, so technically $|\tilde{\chi}^{\alpha,\sigma}_{m}\rangle$ is the same for all σ spin indices.

The symmetry matrix here becomes a 2×2 spin-block matrix. The coefficients of each spin-block within the symmetry matrix are calculated from a SU(2) matrix defined by the spin-axis (from the Pauli matrices). A full description of this non-collinear treatment of symmetries can be found in Ref. [136]. These spin-block symmetries are also used to calculate the non-collinear Brillouin zone integrals (in Eq. 3.65). This, along with the global-local basis transformation, leads to the global temporary projectors being calculated by

$$\left[\tilde{P}^{\text{global},\alpha',\sigma}_{m\nu}(\mathbf{k})\right]^{\lambda} = \mathscr{S}^{\alpha,\alpha'}_{\sigma,\lambda} \left[\tilde{P}^{\text{loc},\alpha,\sigma}_{m\nu}(\mathbf{k})\right]^{\lambda}. \tag{3.80}$$

For ELK, the symmetries helps to introduce the non-collinear spin direction to the Wannier projectors. The 'global' label from this point onwards has been omitted for clarity. Again, an lm basis transformation can also be applied here (after the symmetry transformation). Therefore, a diagonal lm basis could be used to help reduce issues with the sign problem.

These temporary projectors are then be orthonormalised via

$$\left[P^{\alpha,\sigma}_{m\nu}(\mathbf{k})\right]^{\lambda} = \sum_{\alpha' m',\sigma'} \left\{[O(\mathbf{k},\sigma,\sigma')]^{-1/2}\right\}^{\alpha,\alpha'}_{m,m'} \left[\tilde{P}^{\alpha',\sigma'}_{m'\nu}(\mathbf{k})\right]^{\lambda}, \tag{3.81}$$

to form the complete Wannier projector set. Here, $O^{\alpha,\alpha'}_{m,m'}(\mathbf{k},\sigma,\sigma')$ which, in terms of the temporary projectors, has the form

$$O^{\alpha,\alpha'}_{m,m'}(\mathbf{k},\sigma,\sigma') = \sum_{\nu\in\mathscr{W}} \sum_{\lambda,\lambda'} \left[\tilde{P}^{\alpha,\sigma}_{m\nu}(\mathbf{k})\right]^{\lambda} \left[\tilde{P}^{\alpha',\sigma'}_{\nu m'}(\mathbf{k})\right]^{\lambda'*}. \tag{3.82}$$

The spinor lattice Green's function has the following form of

[20] The spin is described by Pauli matrices.

$$G^{\lambda,\lambda'}_{\nu\nu'}(\mathbf{k},i\omega_n)^{-1} = \left(i\omega_n + \mu - \varepsilon_{\mathbf{k}\nu}\right)\delta_{\nu\nu'}\delta_{\lambda,\lambda'} - \Sigma^{\lambda,\lambda'}_{\nu\nu'}(\mathbf{k},i\omega_n), \tag{3.83}$$

with the DFT non-collinear energy values $\varepsilon_{\mathbf{k}\nu}$. The local Green's function is now

$$G^{\alpha,\sigma,\sigma',\mathrm{loc}}_{mm'}(i\omega_n) = \sum_{\mathbf{k},\nu\nu',\lambda,\lambda'} \left[P^{\alpha,\sigma}_{m\nu}(\mathbf{k})\right]^{\lambda} G^{\lambda,\lambda'}_{\nu\nu'}(\mathbf{k},i\omega_n) \left[P^{\alpha,\sigma'}_{\nu'm'}(\mathbf{k})\right]^{\lambda'*}, \tag{3.84}$$

and the upfolding of the impurity self-energy is performed by

$$\Sigma^{\lambda,\lambda'}_{\nu\nu'}(\mathbf{k},i\omega_n) = \sum_{\alpha mm'\sigma\sigma'} \left[P^{\alpha,\sigma}_{\nu m}(\mathbf{k})\right]^{\lambda*} \Delta\Sigma^{\alpha,\sigma,\sigma',\mathrm{imp}}_{mm'}(i\omega_n) \left[P^{\alpha,\sigma'}_{m'\nu'}(\mathbf{k})\right]^{\lambda'}. \tag{3.85}$$

Here, $\Delta\Sigma^{\alpha,\sigma,\sigma',\mathrm{imp}}_{mm'}(i\omega_n)$ is in the global basis which is calculated from the basis transformation described in Eq. 3.70, but using the $\mathscr{S}^{\alpha,\alpha'}_{\sigma,\lambda}$ symmetry matrices instead.

The DMFT Green's functions and self-energies are 2×2 spin-block matrices which can cause difficulties when using the CTQMC solver due to the previously discussed sign problem. These difficulties can be reduced by performing a basis transformation such that the local Green's function is diagonal in the σ and m basis (by diagonalising the 2×2 spin-block local density matrix, as calculated from the local Green's function). Non-collinear DFT+DMFT calculations are not discussed in depth in this thesis as only the spinor Wannier projectors are presented. Nonetheless, the non-collinear DFT+DMFT calculations are possible with the ELK-TRIQS package.

CHAPTER 4

ELK-TRIQS INTERFACE

As discussed in Chapter 3, the DFT+DMFT method used in this thesis requires Wannier projectors to convert the DFT quantities from Bloch space into real space for use in DMFT. The author coded the calculation of the Wannier projectors in ELK as the code did not have pre-existing capabilities to construct these projectors which could then be used by the TRIQS library. The first part of this chapter will compare the Wannier DOS calculated from the ELK-TRIQS with the established WIEN2K-TRIQS interface [16]. The latter part of the chapter will discuss the electron localisation function (ELF) and applying it on two materials: monolayer $SrVO_3$ and $CaFe_2As_2$. This follows the work in Ref. [23]. The author did all the calculations apart from the meta-GGA which was done by E. I. Harris-Lee. The author was the principal author of this article.

4.1 Wannier projector tests

The methodology of the ELK-TRIQS interface has been laid out in Section 3.7. This section will look at the ELK-TRIQS DFT Wannier DOS in comparison with that generated by the WIEN2K-TRIQS setup for three different types of DFT calculations, namely non-magnetic, magnetic and non-collinear spin-orbit coupled systems. However, the interface is not limited to these systems, but the aforementioned three systems can be directly compared with the WIEN2K-TRIQS setup. The presented Wannier DOS for the ELK-TRIQS and WIEN2K-TRIQS calculations were generated within the TRIQS library.

4.1.1 Non-magnetic projectors: $SrVO_3$

Bulk $SrVO_3$ is a prototypical correlated material which has been the subject of many DFT+DMFT studies [13, 86, 137–141]. Often only the V $3d$ t_{2g} states around the Fermi level are used in the

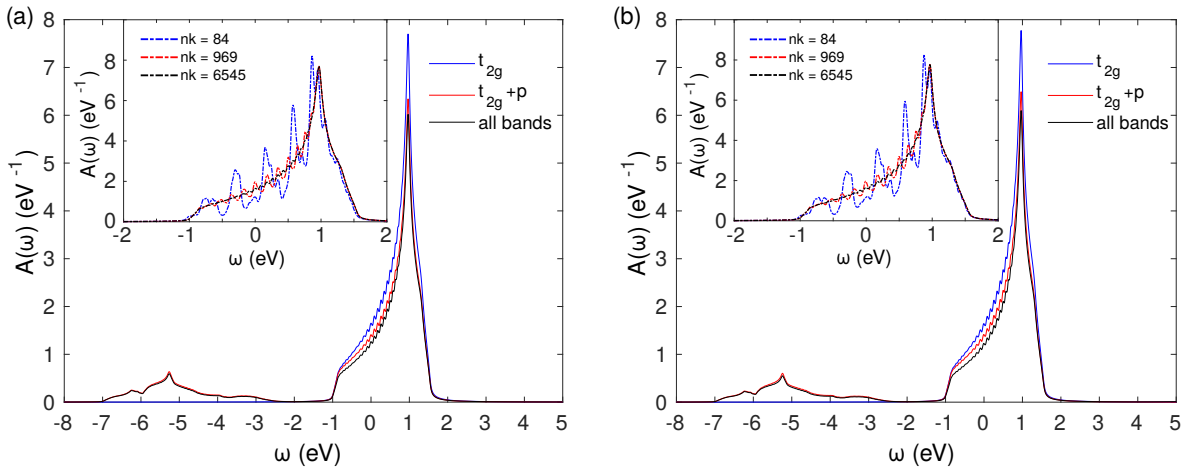

Figure 4.1: The DFT Wannier DOS [$A(\omega)$] calculated using Wannier projectors constructed from different correlated energy windows of [-2, 2] eV (t_{2g} model), [-8, 2] eV (t_{2g}+p model), and all of the bands. Panels (a) and (b) show the ELK-TRIQS and WIEN2K-TRIQS results respectively. The energy axes (ω) of the plots are with respect to the Fermi level which equals 0 here. The insets show only the t_{2g} model DFT Wannier DOS around the Fermi level with a different number of irreducible k-points (nk) used for the DOS BZ integration.

DMFT calculations; the e_g states were not considered as correlated as they do not hybridise with the t_{2g} states and are also unoccupied. In general, $3d$ QP bands at low excitation energies lead to a well-defined Fermi surface [142, 143], while localised states form incoherent Hubbard sidebands at an energy scale comparable with the Coulomb repulsion parameter, U [138, 144, 145]. Together, these yield the familiar three-peaked spectral function [13, 86] (for example, see Fig. 3.2 (c)) . While DFT often adequately describes QP states (once renormalisation is accounted for), it is not capable of capturing the many-body behaviour, e.g. the Hubbard sidebands are completely absent. However, DMFT is able to describe all of the on-site local correlations [13, 86], and has been well-tested on $SrVO_3$ with very good results, including the energetics and spectral weight of Hubbard sidebands and QP renormalisation [13, 138–141]. On the other hand, recent GW+DMFT work in Ref. [146] reinterprets $SrVO_3$ as a weakly correlated material with low static local interactions, since their results show pronounced plasmonic satellites due to screening.

Here, the DFT Wannier DOS is calculated in the both the ELK-TRIQS and WIEN2K-TRIQS setups for comparison and validity of the ELK specific projector routine. Both packages used the same bulk simple cubic lattice parameter of 3.84 Å along with the same k-meshes, correlated energy windows, LDA, and their respective default inputs (such as the plane wave cut-offs, radial meshes, local orbitals, and so on). Figures 4.1 (a) and (b) show a comparison of the results from the two packages. Each data set corresponds to the correlated window used to generate the projectors and DFT Wannier DOS: [-2, 2] eV (t_{2g} model), [-8, 2] eV (t_{2g}+p model), and all of the ELK valence bands. The insets of both panels show the t_{2g} model DFT Wannier DOS k-point dependence (the legend gives the number of irreducible Monkhorst-Pack k-points used) results from both

packages. The oscillations in the panels are due to the sampling of the IBZ, so a higher density of k-points would be needed for the DOS BZ integration to get a smoother Wannier DOS. Often in DFT codes, this integration is done by interpolation (such as using the tetrahedron method), but interpolation cannot be used to calculate the Wannier DOS due to the projectors containing the non-unique Bloch wave function phase (i.e. the gauge freedom discussed in Section 3.7.1). There are slight differences in Figs. 4.1 (a) and (b) which can be ascribed to the different methodologies and default parameter settings used in the two DFT codes (see Ref. [74] for how the results from these DFT codes may differ from each other). However, the effect of this is significantly small.

4.1.2 Spin-polarised projectors: Ni

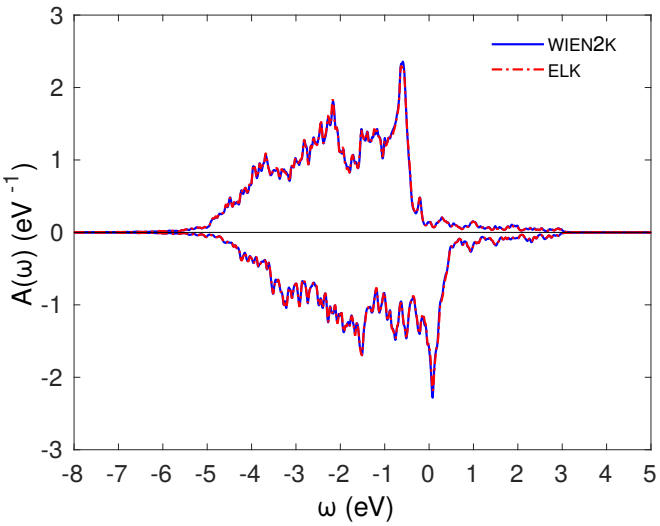

Figure 4.2: The magnetic Ni DFT Wannier DOS [$A(\omega)$] from ELK-TRIQS and WIEN2K-TRIQS calculated using projectors constructed within the correlated energy window of [-10, 3] eV. The energy axes (ω) of the plots are with respect to the Fermi level which equals 0 here.

To test the ELK spin-polarised projectors, the spin polarised Ni DFT Wannier DOS was calculated from both packages and the results are compared with each other. Ni is an itinerant ferromagnetic face-centred cubic (FCC) material with lattice parameter of 3.52 Å, and is discussed in more detail in Section 5.3. The Wannier projectors were generated for the 3d states using the correlated energy window of [-10, 3] eV on a Monkhorst-Pack k-mesh of 20×20×20. Figure 4.2 shows the spin-polarised Wannier DOS generated by both ELK-TRIQS and WIEN2K-TRIQS which are in excellent agreement with each other. The noise and slight differences between the two figures are due to a crude BZ integration from the density of the k-mesh (as only 252 irreducible k-points were used and BZ interpolation is not possible for the BZ integration of the Wannier spectral function) and the other reasons discussed in Section 4.1.1.

4.1.3 Spin-orbit coupled projectors: Ba_2YIrO_6

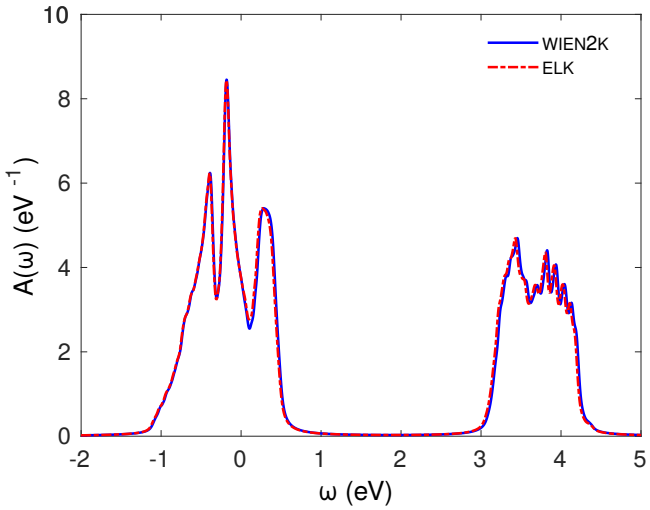

Figure 4.3: The SOC Ba_2YIrO_6 DFT Wannier DOS [$A(\omega)$] from ELK-TRIQS and WIEN2K-TRIQS calculated using SOC Wannier projectors constructed within the correlated energy window of [-1.22, 4.40] eV. The energy axes (ω) of the plots are with respect to the Fermi level which equals 0 here.

Calculations of Ba_2YIrO_6, which is a SOC Mott insulator with a double-perovskite structure with $a = 8.3387$ Å [147, 148], were used to test the generation of (non-collinear) spinor Wannier projectors. ELK treats spin-orbit coupling non-collinearly, whereas WIEN2K implements collinear spin-orbit coupling calculations. This means that ELK and WIEN2K uses different sets of symmetries and hence a different number of irreducible k-points for the same input k-mesh. The Ir $3d$ DFT Wannier DOS for SOC Ba_2YIrO_6 were generated using a correlated energy window of [-1.22, 4.40] eV, and a Monkhorst-Pack k-mesh of 24×24×24 corresponding to 413 and 1063 irreducible k-points used in ELK and WIEN2K, respectively. As shown in Fig. 4.3, the Wannier DOS produced by the two packages is in excellent agreement with discrepancies coming from the sources discussed previously as well as by the Brillouin zone being sampled differently due to the different irreducible k-points used in these calculations.

4.2 Electron localisation function

Section 3.7.3 has shown how to calculate the DFT+DMFT wave functions and occupation numbers without the need for analytic continuation. These can be used to calculate a quantity known as the electron localisation function (ELF) which is dependent on the occupations and wave functions of the system. The ELF is based on a same-spin pair probability density $D(\mathbf{r})$ of finding an electron close to another same-spin reference electron [149]. It has mainly been used as a tool to investigate the electron localisation in chemical bonds via Hartree-Fock [149] and DFT

[150] methods. The ELF has also been used to investigate the bond evolution in time-dependent DFT (TDDFT) [151]. The ELF $\eta(\mathbf{r})$ has the form

$$\eta(\mathbf{r}) = \frac{1}{1+\left[D(\mathbf{r})/D^0(\mathbf{r})\right]^2}, \tag{4.1}$$

where

$$D^0(\mathbf{r}) = \frac{3}{5}\left(6\pi^2\right)^{2/3}\left(\frac{\rho(\mathbf{r})}{2}\right)^{5/3} \tag{4.2}$$

is the kinetic energy density for the homogeneous electron gas as a function of the electron density ($\rho(\mathbf{r})$). The $D(\mathbf{r})$ quantity is defined as

$$D(\mathbf{r}) = \frac{1}{2}\left(\tau(\mathbf{r}) - \frac{1}{4}\frac{[\nabla\rho(\mathbf{r})]^2}{\rho(\mathbf{r})}\right), \tag{4.3}$$

with $\tau(\mathbf{r})$ being the spin-averaged kinetic energy density from the wave functions, which has the form

$$\tau(\mathbf{r}) = \sum_{\mathbf{k}i} n_{\mathbf{k}i}\left|\nabla\Psi_{\mathbf{k}i}(\mathbf{r})\right|^2. \tag{4.4}$$

The wave functions $\Psi_{\mathbf{k}i}(\mathbf{r})$ and occupation numbers $n_{\mathbf{k}i}(\mathbf{r})$ that are used to calculate an ELF can be any diagonal wave function (and occupation) set, such as those from the DFT or DFT+DMFT calculations. Hence, the index i would refer to the index ν or η for the DFT or DFT+DMFT calculation, respectively. Therefore, the effect of the electron correlation approximations on the wave functions [and consequently on $\rho(\mathbf{r})$ and $\tau(\mathbf{r})$] can be investigated by using the ELF.

It is evident from Eq. 4.1 that the ELF is a quantity which can vary from 0 to 1, with a reference value of 0.5 relating to the Pauli repulsion being equal to that from a homogeneous electron gas with the same density $\rho(\mathbf{r})$. ELF values that tend to 1 relate to a $D(\mathbf{r})$ that tends to zero with respect to the homogeneous electron gas, and therefore the electrons would be highly localised in that region of space. It should be noted, however, that a direct relationship between the ELF and the Pauli exclusion of the electrons (i.e. their localised or itinerant nature), is difficult to deduce as the ELF is dependent on $D(\mathbf{r})/D^0(\mathbf{r})$, not just the same-spin pair probability density of the material [152, 153].

The many-body effects from DMFT (encoded in the density matrix and DFT+DMFT wave functions) will change the $\rho(\mathbf{r})$ and $\tau(\mathbf{r})$ distributions, which in turn modify both the $D(\mathbf{r})$ and $D^0(\mathbf{r})$ on which the ELF depends. The extent of the changes in $\rho(\mathbf{r})$ and $\tau(\mathbf{r})$ will be material specific, so linking the ELF distribution to just one of these may not always be possible. Therefore comparing the ELF from different theoretical approaches will give insight into the interplay of the changes to the $\rho(\mathbf{r})$ and $\tau(\mathbf{r})$ distributions as well as the changes to the bonding present in the material. The charge redistribution in the materials studied here dominated the changes in the ELF.

4.3 Results

As the projector routines are shown to be working for the different types of DFT calculations, the ELK-TRIQS setup is ready to be used for DFT+DMFT calculations. To check that the DFT+DMFT one-shot (OS) and fully-charge self-consistent (FCSC) calculations have been properly implemented, the ELK-TRIQS setup has been benchmarked using the monolayer $SrVO_3$ system [154], with those results being presented in the next section. Afterwards, the rest of this chapter will then discuss the effect of electron correlations on the bonds (which are visualised by the ELF) in the monolayer $SrVO_3$ and the $CaFe_2As_2$ superconductor.

4.3.1 Monolayer $SrVO_3$

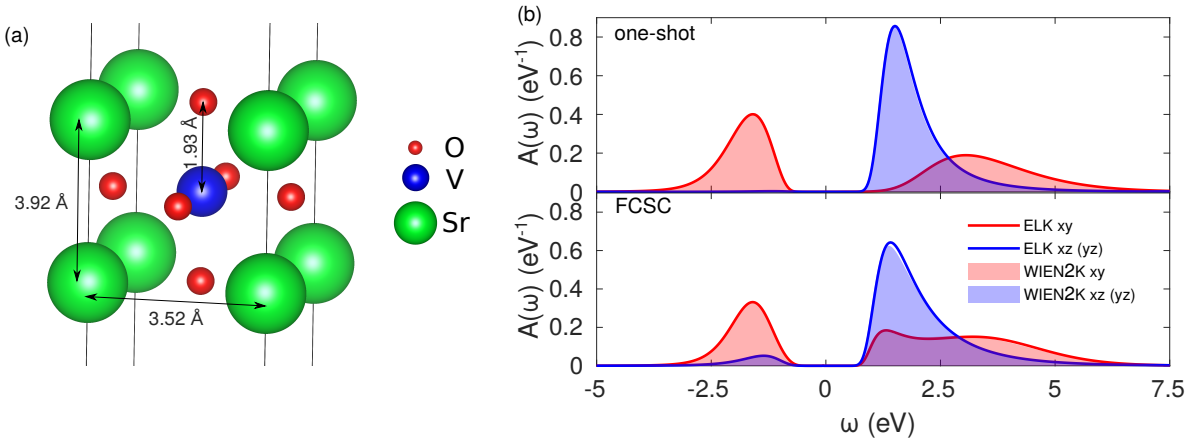

Figure 4.4: (a) The unit cell of the monolayer $SrVO_3$, where each monolayer is separated by 20 Å of vacuum. (b) The comparison of the Wannier V t_{2g} spectral functions calculated in the one-shot and fully charge self-consistent (FCSC) DFT+DMFT methods by the WIEN2K-TRIQS and ELK-TRIQS code combinations.

Monolayer $SrVO_3$ is a Mott insulator material in which the charge redistribution is significant between the OS and FCSC DFT+DMFT methods. This material has been used before to benchmark the Vienna *ab initio* simulation package (VASP)-TRIQS interface [132]. Reducing the dimensionality of bulk $SrVO_3$ to a monolayer causes a metal-insulator transition (MIT). This is seen experimentally [155, 156] and complemented by DFT+DMFT calculations [132, 157]. There are a few material-specific mechanisms which the MIT has been attributed to such as the crystal field (CF) splitting [154, 158–160] and confinement in the $SrVO_3$ layers [25].

Here, we apply both the OS and FCSC DFT+DMFT methods to the relaxed monolayer $SrVO_3$ calculations using the ELK-TRIQS and WIEN2K-TRIQS interfaces. The relaxed structure has been determined by previous GGA calculations [154]. The monolayer structure is shown in Fig. 4.4 (a). The a and c lattice parameters are 3.52 Å and 3.92 Å, respectively, where the a lattice parameter

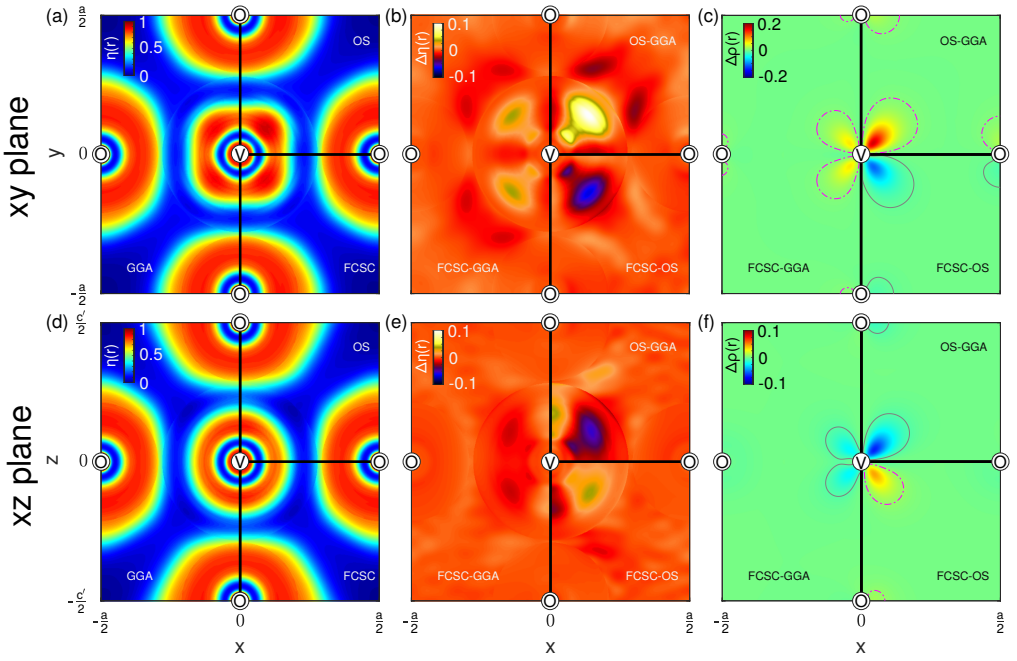

Figure 4.5: The monolayer $SrVO_3$ (a) xy and (b) xz plane ELFs, slicing through the centre of the V and O atoms. The four-fold symmetry of the planes has been exploited to show the results from the GGA (PBE), one-shot (OS) and fully charge self-consistent (FCSC) DFT+DMFT calculations. (b) and (e) are the differences [for example FCSC-GGA = $\eta^{\mathrm{FCSC}}(\mathbf{r})$ - $\eta^{\mathrm{GGA}}(\mathbf{r})$] in the ELFs from the different theoretical techniques in the xy and xz planes respectively. (c) and (f) show the charge density differences [for example FCSC-GGA = $\rho^{\mathrm{FCSC}}(\mathbf{r})$ - $\rho^{\mathrm{GGA}}(\mathbf{r})$] between the different theoretical techniques in the xy and xz planes, respectively. The grey solid and magenta dot-dashed contours in (c) and (f) show the positive and negative charge density difference isovalues of 6×10^{-3}. The charge density differences are in units of electrons per unit bohr^3.

is that of bulk $SrTiO_3$. The unit cell used in the DFT calculations has a separation of 20 Å between the monolayers. The out-of-plane V-O distance has decreased to 1.93 Å compared with $c/2$.

The WIEN2K [71] and ELK DFT calculations used a Monkhorst-Pack k-mesh of $15\times15\times1$ and the PBE [64] GGA functional, which is the same as that used in Ref. [132]. The correlated V $3d$ t_{2g} states around the Fermi level are the target of the DMFT calculations. As with the bulk, the e_g states in the monolayer are unoccupied and do not hybridise with the t_{2g} states. Therefore the e_g states were not included in DMFT, which is consistent with previous benchmarking calculations [132, 157]. The V $3d$ t_{2g} Wannier projectors were generated within a correlated energy window around the Fermi energy of [-2.0, 1.1] eV and then these projectors were interfaced to the TRIQS library [15] by the TRIQS/DFTTOOLS application [16]. The DMFT calculations used the CTQMC solver in the TRIQS/CTHYB application [161] with 4.2×10^7 Monte Carlo sweeps and the Hubbard-Kanamori interaction Hamiltonian. The double counting was approximated in the fully localised limit (FLL) which used the DMFT occupations. These DMFT calculations used previously defined [132, 157] U = 5.5 eV, J = 0.75 eV, and inverse temperature β = 40 eV^{-1}.

	GGA		OS		FCSC	
	xy	xz+yz	xy	xz+yz	xy	xz+yz
ELK / WIEN2K	0.65	0.35	0.98	0.02	0.76	0.24

Table 4.1: Comparison of the GGA (PBE), one-shot (OS), and fully charge self-consistent (FCSC) DFT+DMFT 3d t_{2g} orbital charges based on the ELK and WIEN2K DFT codes.

Figure 4.4 (b) shows the spectral function comparison between the ELK-TRIQS and WIEN2K-TRIQS DFT+DMFT calculations of both the OS and FCSC methods. These spectral functions were obtained by analytically continuing the DMFT local Green's function by the *LineFitAnalyzer* technique of the analytic continuation MEM implemented within the TRIQS/MAXENT application [125]. The ELK-TRIQS and WIEN2K-TRIQS spectral functions are in excellent agreement with each other, with both showing the incoherent Hubbard peaks. However, there are some minor discrepancies between the spectral functions which are mainly a consequence of the ill-posed problem in the analytic continuation process. Both the ELK-TRIQS and WIEN2K-TRIQS calculations produce the strong orbital charge polarisation seen in the OS calculations which is softened in the FCSC results because of charge redistribution. This redistribution occurs at the DFT level in the FCSC DFT+DMFT cycle when the correlated t_{2g} states are fed back into DFT [157]. These results agree with previous studies of this monolayer [132, 157]. The Wannier orbital charges are identical in Table 4.1 when quoted to two significant figures. There are minor discrepancies between ELK-TRIQS and WIEN2K-TRIQS present in the DFT Wannier charges when quoted to higher significant figures. These discrepancies will have propagated to the DFT+DMFT calculations. These reasonable DFT discrepancies can be explained by the different (default) set of local orbitals used, the MT radial functions being evaluated at different linearisation energies, as well as the different hard-coded approaches the DFT packages used to implement the APW+lo method. A discussion on the comparison of quantities evaluated by different DFT codes, and their discrepancies, can be found in Ref. [74]. In the DFT+DMFT calculations, on the other hand, the results from ELK-TRIQS and WIEN2K-TRIQS are the same to two decimal places. The values are quoted to this precision because of the inherent noise present from the CTQMC solver which causes the charge to fluctuate at higher decimal places. It should be noted that the OS orbital charges are slightly different here compared with the results in Ref. [132]. This is because more OS DFT+DMFT cycles were performed here for better convergence, but this discrepancy does not change the conclusions of Schuler et al. [132]. Nonetheless, the excellent agreement shown in Fig. 4.4 (b) clearly demonstrates that the ELK-TRIQS interface works.

As the ELF [$\eta(\mathbf{r})$] depends on wave-function-dependent quantities, the effect of the electron correlations from the different theoretical methods can be investigated. Fig. 4.5 shows $\eta(\mathbf{r})$, the difference in $\eta(\mathbf{r})$ [$\Delta\eta(\mathbf{r})$], and the differences in $\rho(\mathbf{r})$ [$\Delta\rho(\mathbf{r})$] between the DFT and DFT+DMFT techniques for the V-centred xy and xz planes [the $\eta(\mathbf{r})$ in the yz plane is the same as that in the xz plane due to symmetry]. The xy and xz $\eta(\mathbf{r})$, in Figs. 4.5 (a) and (d), are similar with the

greatest values located in shells around the V and O atoms. However, the xy plane $\eta(\mathbf{r})$ has the significantly filled V xy orbital nodes around the V atom, whereas the $xz(yz)$ orbital nodes are not present in the xz plane $\eta(\mathbf{r})$ as these orbitals have little charge contribution. The contribution of the V t_{2g} orbitals to $\eta(\mathbf{r})$ in the different DFT and DFT+DMFT calculations can be seen in the $\Delta\eta(\mathbf{r})$ of the xy and xz planes in Figs. 4.5 (b) and (e), respectively. For the xy (xz) orbitals, it can be seen that the OS calculation increases (reduces) significant contributions to the $\eta(\mathbf{r})$ compared with the DFT. On the other hand, the xy (xz) orbital contributions to the FCSC $\eta(\mathbf{r})$ are only slightly increased (reduced) with respect to the DFT, so that differences between the FCSC and DFT are not so significant. This follows the xy and xz $\Delta\rho(\mathbf{r})$ orbital contributions from the DFT and DFT+DMFT calculations highlighted in Figs. 4.5 (c) and (f), respectively. It should be noted that in Figs. 4.5 (b) and (e) the MT and interstitial regions are distinctly visible which is an artefact of the basis set used.

The ELF in monolayer $SrVO_3$ is sensitive to the redistribution of charge, with respect to DFT, caused by the application of both the OS and FCSC DFT+DMFT methods. In this material, the changes in the ELF can be traced to the changes in the charge distribution (primarily from the t_{2g} orbitals as expected), indicating that it is that which dominates when DMFT is included. From Figs. 4.5 (c) and (f), small changes to the charge redistribution of the O occur even though only the t_{2g} states are treated as correlated. This is because the Wannier projectors contain information about the hybridised V t_{2g} and O p states (similar to the bulk: see, for example, Ref. [128]). The changes in the charge around the O sites appear to be too small to affect the ELF significantly. The ELF here gives another means to visualise the impact of DMFT in correlation-induced changes on the electron distribution within the bonds in this material.

4.3.2 $CaFe_2As_2$

	CT	TET
P (GPa)	0.35	0.0
T (K)	50	250
a (Å)	3.9792	3.8915
c (Å)	10.6379	11.690
z_{As}	0.3687	0.372
Fe-As (Å)	2.3560	2.410
Fe-Fe (Å)	2.8137	2.7517

Table 4.2: The experimental structural parameters for the tetragonal (TET) and collapsed tetragonal (CT) structures from Ref. [162].

The $CaFe_2As_2$ compound is a member of the AFe_2As_2 (A being an alkaline metal) 122-family of Fe-pnictide superconductors. This material has been reported to have three distinct phases: the tetragonal (TET) phase which is the structure that exists at room temperature and ambient pressure; the antiferromagnetic orthorhombic phase; and the collapsed tetragonal

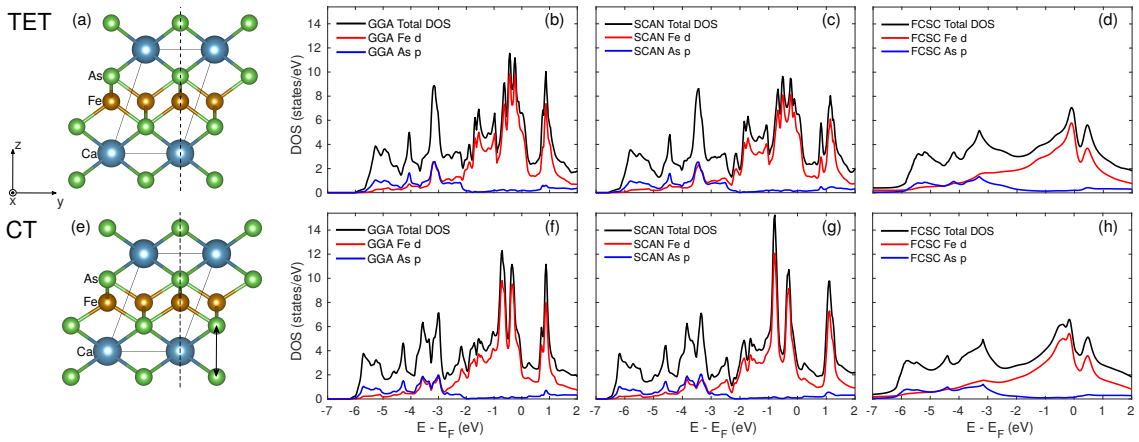

Figure 4.6: (a) and (e) show the structures of the tetragonal (TET) and collapsed tetragonal (CT) phases, respectively. The parallelepiped Wigner-Seitz unit cell is shown along with the dashed line indicating the xz plane on which the ELFs were calculated, and in (e) the interlayer As-As bond is also indicated by the double-headed arrow. (b), (c), and (d) show the total and partial density of states for the GGA (PBE), SCAN, and fully charge self-consistent (FCSC) DFT+DMFT calculations in the TET structure. (f), (g) and (h) show the same quantities as (b), (c), and (d), respectively, in the CT structure.

(CT) phase which displays superconductivity under uniaxial pressure [162, 163]. As well as superconductivity, $CaFe_2As_2$ has displayed the shape memory and superelasticity effects [164]. Chemical substitution enables the fine tuning of the properties of $CaFe_2As_2$ [165–171].

ARPES[1] studies have helped to understand the role of correlations in the TET and CT phases [172, 173]. DFT+DMFT comparisons with the experimental results [172, 174, 175] have improved agreement compared with the DFT calculations. Although DFT is able to describe some of the ARPES features well, the DFT+DMFT results capture some of the band renormalisation. However, the renormalisation is still not as significant as seen in the ARPES data which has been suggested to be attributed to both non-local correlations and/or phonon effects [174].

Previous studies on AB_2X_2 compounds (to which $CaFe_2As_2$ belongs) show that an interlayer X-X σ bond can exist from the X p states overlapping [168, 176, 177]. The bonds between the A and B_2X_2 layers are ionic, the B-B bonds are metal-metal bonds and the B-X and X-X bonds are covalent in nature. The B-X bond is associated with the hybridisation of the B d and X p states below the Fermi level [176]. X-ray diffraction and Raman spectroscopy support the existence of the X-X bond in $NaFe_2As_2$ [178]. In $CaFe_2As_2$, the As-As interlayer bond has been shown to be mediated by the Fe-As bond and the Fe spin-state [179].

As the real-space ELF and charge distribution change with respect to the inclusion of the electron correlation effects from many-body techniques, the ELF will provide information on the effect of different types of included electron correlation effects on the As-As bond. Therefore, we have calculated the ELF via GGA (PBE [64]) and meta-GGA functionals, as well as the ELK-TRIQS

[1] See Chapter 5 for further information about the ARPES experimental technique.

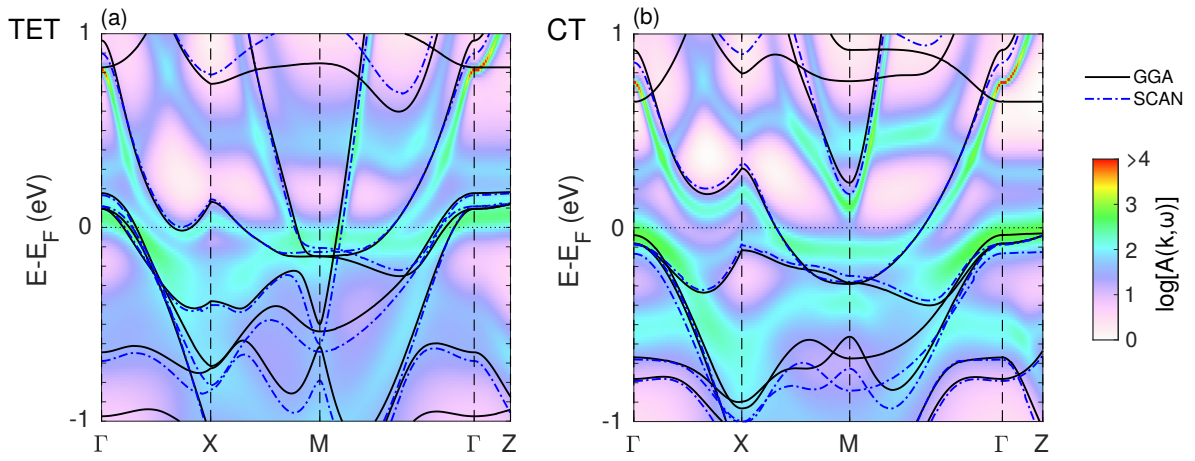

Figure 4.7: The band structures according to the GGA (PBE) and SCAN functionals and the $A(\mathbf{k},\omega)$ of the fully charge self-consistent DFT+DMFT calculations for the (a) tetragonal (TET) and (b) collapsed tetragonal (CT) structures. The high symmetry points correspond to a simple tetragonal unit cell. The natural log colour scale and range were used for clarity of the bands.

	Z			
	z^2	x^2-y^2	xy	$xz(yz)$
TET	0.57	0.53	0.60	0.54
CT	0.66	0.67	0.65	0.61

Table 4.3: The fully charge self-consistent DFT+DMFT 3d QP residues (Z) in the tetragonal (TET) and collapsed tetragonal (CT) structures.

FCSC DFT+DMFT implementation, to determine how the changes in the electron correlation effects between each method affect the ELF distribution around the As atoms in the TET and CT structures, along with the consequences this has on the interlayer As-As bond. For the meta-GGA calculations, we used the strongly constrained and appropriately normed (SCAN) functional [66] as this was constructed with consideration of $D(\mathbf{r})/D^0(\mathbf{r})$, on which the ELF is also dependent in Eq. 4.1.

Here, we considered the TET structure at 0 GPa and 250 K, and the CT structure at 0.35 GPa and 50K using the experimental structural parameters [162], summarized in Table 4.2. The TET and CT structures are shown in Figs. 4.6 (a) and (e), respectively, with both structures showing the parallelepiped Wigner-Seitz unit cell used in the calculations. Both the GGA and SCAN calculations used a 24×24×24 Monkhorst-Pack k-mesh for both structures. Whenever we discuss the GGA results, we are referring to the PBE functional. The FCSC DFT+DMFT calculations (using the PBE GGA functional) imposed DMFT on the Fe d states using Wannier projectors generated within a correlated energy window around the Fermi energy of [-5.9, 16.0] ([-6.3, 16.0]) eV to encapsulate all of these Fe d states in the TET (CT) structure. The DMFT calculations used the full multi-orbital rotationally invariant form of the interaction Hamiltonian

		GGA (PBE)	SCAN	FCSC
TET	Fe d (%)	25.2	23.4	31.8
	As p (%)	26.2	26.8	23.0
	As p limits (eV)	[-6.07, -1.93]	[-6.64, -2.15]	[-5.97, -2.03]
CT	Fe d (%)	24.5	22.5	29.7
	As p (%)	25.7	26.5	23.4
	As p limits (eV)	[-6.26, -1.99]	[-6.69, -2.15]	[-6.22, -2.33]

Table 4.4: The estimated percentage of charge associated with As p and Fe d character for each calculation and structure. These percentages were calculated from the partial and total DOS integrals within the σ bond DOS energy window. The As p estimated energy ranges, which the DOS integrals were evaluated within, are also included.

(see Section 3.3.1) with the CTQMC solver employing 2.52×10^8 Monte Carlo sweeps. These DMFT calculations were in the paramagnetic phase and used the previously defined values of U = 4.0 eV, J = 0.8 eV, inverse temperature β = 40 eV^{-1}, and the FLL double counting term [174]. Here, the FLL was calculated from the DMFT occupations.

Figs. 4.6 (b) [(f)], (c) [(g)] and (d) [(h)] show the TET [CT] total and partial As p and Fe d DOS for GGA, SCAN, and FCSC DFT+DMFT calculations, respectively. The FCSC DOS was calculated using the analytically continued DMFT self-energy via the TRIQS/MAXENT application [125]. The SCAN DOS has a similar shape to the GGA; however, the band widths have generally increased, and the band centres tend to shift away from the Fermi level for larger absolute energies. This indicates that these states are more delocalised than in GGA functional calculations. On the other hand, the FCSC DOS shows a significant renormalisation of the states around the Fermi level, as expected from the QP residue (see Table 4.3), which broadly agrees with the previous studies on this material [174, 175]. The smooth profile is a consequence of the reduced QP lifetimes relating to the imaginary part of the self-energy.

The band structures and $A(\mathbf{k},\omega)$ for the TET and CT structures are shown in Figs. 4.7 (a) and (b), respectively. The FCSC $A(\mathbf{k},\omega)$ broadly agrees with the previous studies in Refs. [172, 175], and any discrepancies with those results are likely due to the different U, J, and correlated energy window used. Even within the displayed energy window around the Fermi level, the increased bandwidths of the SCAN bands can be seen. The band renormalisation is distinct for the FCSC $A(\mathbf{k},\omega)$. The GGA and SCAN bands cross the Fermi level at similar $\mathbf{k}$ values for the CT structure whereas there are small, but observable, changes for the TET structure. However, the FCSC $A(\mathbf{k},\omega)$ have bands crossing the Fermi level at different $\mathbf{k}$ values compared with both the GGA and SCAN results for both structures.

The ELFs for the TET and CT structures are given in Figs. 4.8 (a) and (b), respectively. These ELFs are two-dimensional (2D) slices in the xz plane, which is indicated by the dashed lines in Figs. 4.6 (a) and (e), centred around the As-As bond. For the TET structure, the ELF indicates that there is a higher likelihood of finding an electron in the horseshoe shaped region between

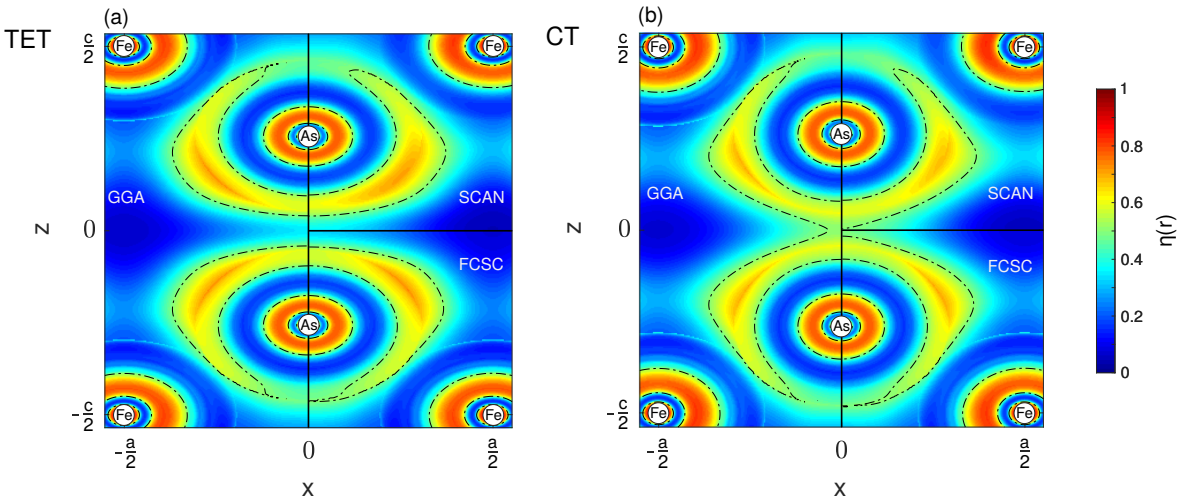

Figure 4.8: The 2D ELFs in the xz plane [as indicated in Figs. 4.6 (a) and (e)] for the (a) tetragonal (TET) and (b) collapsed tetragonal (CT) structures. The ELFs for the GGA (PBE), SCAN, and fully charge self-consistent (FCSC) DFT+DMFT calculations are shown in quadrants, as this plane is four-fold symmetric. The dot-dashed contours are of $\eta(\mathbf{r}) = 0.5$.

the interlayer As atoms. However, it is in the CT structure where these horseshoe shaped regions have coalesced to form distinct ELF weight at the centre between the atoms. This indicates that the bond has formed between these interlayer As atoms. The ELFs in these regions are robust between the different calculations as significant (hybridised) As p and Fe d states (within the energy range of [-7, -2] eV) are still fully occupied meaning that the associated As-As and As-Fe bonds still exist. Although the $\mathbf{k}_F$ of certain bands has changed between each calculation, this has not affected the ELF significantly, especially in the region around the Fe atoms as it is the states around the Fermi level which are predominantly Fe d in character. However, there are slight changes to the ELF which are highlighted by the dot-dashed contour of $\eta(\mathbf{r}) = 0.5$. Compared with GGA, the SCAN $\eta(\mathbf{r})$ redistributes weight away from the Fe-As bond and moves it into the interstitial region away from the Fe and As atoms. On the other hand, the FCSC $\eta(\mathbf{r})$ results redistribute weight (compared with GGA) to the region between the As and Fe atoms.

These results are consistent with the changes in the percentage each atom contributes to the total charge within the interlayer As-As σ bond regions (see Table 4.4). These were estimated by integrating the partial and total DOS over the energy range (see Table 4.4) in which there is significant As p partial DOS. This energy range is where the (hybridised) As p and Fe d states are associated with the As-As and As-Fe bonds. Compared with the GGA, the SCAN results indicate that charge has redistributed away from the Fe atoms, which results in greater interstitial region contributions to the ELF. This is likely due to the delocalisation of the states seen in the band widths of the SCAN DOS and band structures. However, the FCSC results have greater charge around the Fe atom and reduced contributions from the other regions with respect to the GGA results. This increases the Fe d and As p hybridisation and strengthens the Fe-As bond which

in turn weakens the As-As bond. This is similar to the effect of the Fe spin-state in Ref. [179], but here the strength of the bonds is weakly influenced by correlations. Both the SCAN and FCSC results have drawn weight away from the centre of the As-As bond. Nonetheless, these calculations give an indication that the electron correlation effects affect the As p and Fe d hybridisation (as shown in Table 4.4), which in turn influences the strength of the As-As and Fe-As bonds as seen in the ELF.

4.4 Conclusions

The newly developed ELK-TRIQS interface has been introduced. In addition to standard one-particle quantities such as spectral functions, it also allows the calculation of orthonormal DFT+DMFT wave functions and related quantities. To illustrate the effect of correlations on these wave functions and occupations, we calculated the ELF. The changes in the DFT+DMFT ELF come from the redistribution of the charge and kinetic energy density. The modifications in the charge density distribution dominated the changes in the ELF for monolayer $SrVO_3$, but it should be noted that in other materials this may not always be the case due to its dependence on the kinetic energy density. Therefore a comparison of ELFs which have been computed within DFT+DMFT and DFT, as has been demonstrated in $CaFe_2As_2$, helps to visualise the role of correlations on the ELF. This means that the ELF, which is related to the strength of the chemical bonds, could be used to investigate changes in chemical bonding due to the electron correlations from DMFT.

The ELK-TRIQS monolayer $SrVO_3$ results have excellent agreement with the WIEN2K-TRIQS results and the generated ELFs were sensitive to the charge distribution of the V $3d$ xy and $xz(yz)$ orbitals. Therefore, any factors which influence the charge redistribution such as the correlated energy window and/or double counting, will also impact the DFT+DMFT ELF. The $CaFe_2As_2$ ELFs show an excellent visualisation of the interlayer As-As bond formed in the CT phase. The Fe-As bonds (and As-As bonds present in the CT structure) are influenced by the Fe d and As p hybridisation which is weakly dependent on the different electron correlation effects beyond GGA that are present in either SCAN or FCSC DFT+DMFT calculations. This is contrary to the large effects that correlations have on the FCSC DFT+DMFT spectral functions. Correlations may have a more pronounced effect on the ELF if there is a significant charge redistribution and/or if the states affiliated with the bonds are at the Fermi level, where the additional correlations (from the many-body technique) affect the results more significantly. This could potentially be seen in other AB_2X_2 compounds, such as those investigated in Ref. [180]. We also suggest that the ELF should be used to investigate the effect of correlations on the bond-disproportionated insulating phase in rare-earth nickelates ($RNiO_3$) [181]. As well as this, the effect the MIT has on the bonds in heterostructures, such as $SrVO_3$/$SrTiO_3$ [25, 154], and at their interfaces could be investigated using the ELF. Nonetheless, these results show the

usefulness of the ELF in helping to visualise the bonds present in many other similarly correlated crystalline materials.

There is also the possibility of incorporating DMFT with other capabilities within ELK such as the out-of-equilibrium functionality using TDDFT [182], where real material TDDFT+DMFT calculations are being reported [183]. There are other wave-function-dependent quantities which can be calculated using this formalism, such as the EMD, which is experimentally probed by Compton scattering [19]. This is the subject of Chapter 5.

CHAPTER 5

COMPTON SCATTERING

In this chapter, the Compton scattering experimental technique used for measuring the electron momentum density (EMD) will be reviewed along with introducing the methodology of how to calculate the DFT+DMFT EMD. The inclusion of effects induced by DMFT within the EMD, and the (magnetic) Compton profile, will be investigated for elemental Ni and V. This chapter will contain content adapted from Ref. [24], in which the author calculated the magnetic Compton profiles and spectral functions of Ni using the ELK+TRIQS package, and was the principal author of the article. The KKR(+DMFT) Ni results presented in this chapter were calculated by M. Sekania. This chapter concludes by discussing results for V which also shows that this DFT+DMFT EMD implementation is not limited to magnetic Compton profile calculations.

5.1 Background

The Compton effect, named after A. H. Compton in 1923 [184], describes the inelastic scattering of X-ray photons by charged particles considering conservation of energy and momentum. This interaction explains the measured (Compton) shift in the wavelength of the scattered X-rays, which is also dependent on the scattering angle but independent of the intensity of the incoming X-rays. Up to this point in the early 1900s, light was thought to be a purely wave phenomena, but the explanation of the Compton effect uses the particle description of light (photons), which subsequently led onto the validation of the particle-wave nature and quantum mechanical aspects of light.

Compton scattering from a stationary electron leads to a single energy in the outgoing X-ray spectrum which has been shifted from the original energy of the incoming X-ray. This change in energy is directly related to the Compton shift. However, the Compton scattering of real electrons, interacting with a monochromatic light source, produces a Doppler broadening of the outgoing

X-ray spectrum [19, 185], where this broadening is caused by the motion of the electrons along the scattering vector. Consequently, this Doppler broadened Compton spectrum can be related to the momentum distribution of the electrons and therefore, this is used to probe the electronic structure of materials in condensed matter systems. Due to the high energy (> 100 keV) incoming X-rays used, these X-rays are deeply penetrating and measure the bulk electronic structure, as well as probing the bulk ground-state many-body electron wave function of the material [18–21]. All of the electrons in the system contribute to this Doppler-shifted distribution equally. Also, only occupied electronic states contribute to this momentum distribution meaning that the Fermi surface can be determined from the measured Compton scattered spectra.

Although this is a very promising technique, it has limitations in terms of the requirement of high energy X-ray sources (such as a synchrotron) to produce spectra with good resolution *and* count rate; all of the electrons are measured which could be considered a hindrance (from a "signal to background" point of view) when the Fermi surface electrons are the subject of study in a many-electron system; and finally, many Compton scattering measurements (with profiles measured along different crystallographic directions) are required to reconstruct the 2D or 3D Fermi surface. However, there are no other current experimental techniques which can confidently measure the ground-state many-body electron wave function which is what Compton scattering offers [18–21]. In recent years, Compton scattering has been used to reveal the electronic structure and Fermi surfaces [18] in electronically complex materials such as substitutionally disordered alloys [186, 187] and compounds with high vacancy concentrations [188]. Most relevantly, Compton scattering is able to probe the electron correlations within many complex materials [189–192]. DFT calculations are often used to complement and aid the interpretation of experimental data. DFT can reveal the origin of the many features seen in the experimental Compton scattering data. However, in order to capture all of the features and trends seen in the experimental data, there is a vital need to use theories with descriptions of the electron correlations beyond current DFT capabilities.

The 2D angular correlation of annihilation radiation (2D-ACAR) is another closely related technique to Compton scattering which uses positrons (which have thermalised in the material being studied), instead of high energy X-rays, to probe the EMD [18]. These thermal positrons annihilate the electrons resulting in the emission of two anti-parallel γ-rays in the rest frame [18, 193]. In the lab frame, the deviation from anticollinearity in the γ-rays gives information about the electron-positron pair's momentum before annihilation (the momentum being dominated by the electron because the positron is thermal); the 2D-ACAR measurements give the once projected, 2D momentum density which is often called the "two-photon momentum density" (TPMD) or the "electron-positron momentum density" (which is closely related to the electron momentum density). As a consequence of the positive charge of the positrons, they preferentially sample the electronic states closer to the Fermi level (as the Coulomb repulsion from the ion core means that the positron wave function will overlap most strongly with the most itinerant

states). The positrons, due to their positive charge, perturb the system (in fact, they will have a significant screening cloud of electrons around it) meaning that the ground-state is not measured, unlike in Compton scattering. However, this does help in Fermi surface studies, because electrons at the Fermi surface are the ones that are preferentially being sampled. The positrons can, however, be trapped in vacancies caused by defects or large open volumes in the material. This results in the delocalised Bloch states not being sampled and consequently meaning that getting information about the Fermi surface is a lot harder or potentially impossible [194]. Finally, the electron-positron correlations introduces enhancement of the momentum density around the Fermi level which is difficult to model [195]. However, a couple of advantages of this technique are that it has higher resolution compared with current Compton techniques [196] and it can be implemented in a laboratory setting rather than requiring a synchrotron.

There are two other Fermi surface determining techniques which currently are more commonly used within the condensed matter community. The angle-resolved photoemission spectroscopy (ARPES) technique directs monochromatic light of energy greater than the material's work function onto the sample [197]. This results in the photoelectric effect. Measuring the kinetic energy as a function of angle produces the energy distribution curves and momentum distribution curves, which correspond to the theoretical $\mathbf{k}$-resolved spectral function, as well as giving information on the Fermi surface. Although the momentum resolution is better than Compton, the photo-electrons originate from the surface of the sample, within $\approx$ 5 - 10 Å, for the most frequently used photon energy range of 20-200 eV [198]. Therefore, there is debate on whether this ARPES data is of the bulk. As the technique is surface sensitive, getting information about the bulk is often limited to samples which cleave easily *in situ* and whether the surface electronic structure represents the bulk. However, recent ARPES measurements used photons outside of the aforementioned energy range, which means that these photons penetrate deeper into the sample and are therefore more sensitive to the 'bulk'-like states [199, 200]. Also, the photoemission interaction involves matrix elements [200, 201] which may result in uneven sampling of electron states and potentially miss Fermi surface features.

The other Fermi surface measuring technique uses quantum oscillations which refers to oscillations in thermodynamic quantities (such as magnetisation in the de Haas-van Alphen (dHvA) effect [202]) with respect to changing magnetic field. These oscillations are a consequence of the Landau levels, which form when applying a magnetic field to the material, depopulating when the field is changed and a level passes through the Fermi energy; the oscillations are periodic with inverse field. This period is inversely related to the extremal areas of the Fermi surface which are orthogonal to the applied field direction[1], meaning that the Fermi surface can be mapped out if measurements are made with the magnetic field along different crystallographic directions. This technique yields the bulk Fermi surfaces with high resolution and accuracy and can also be used to extract the effective mass of the electron QPs. However, this technique requires the electrons

[1] or the Fermi surface plane normal is (anti-)parallel to the field direction

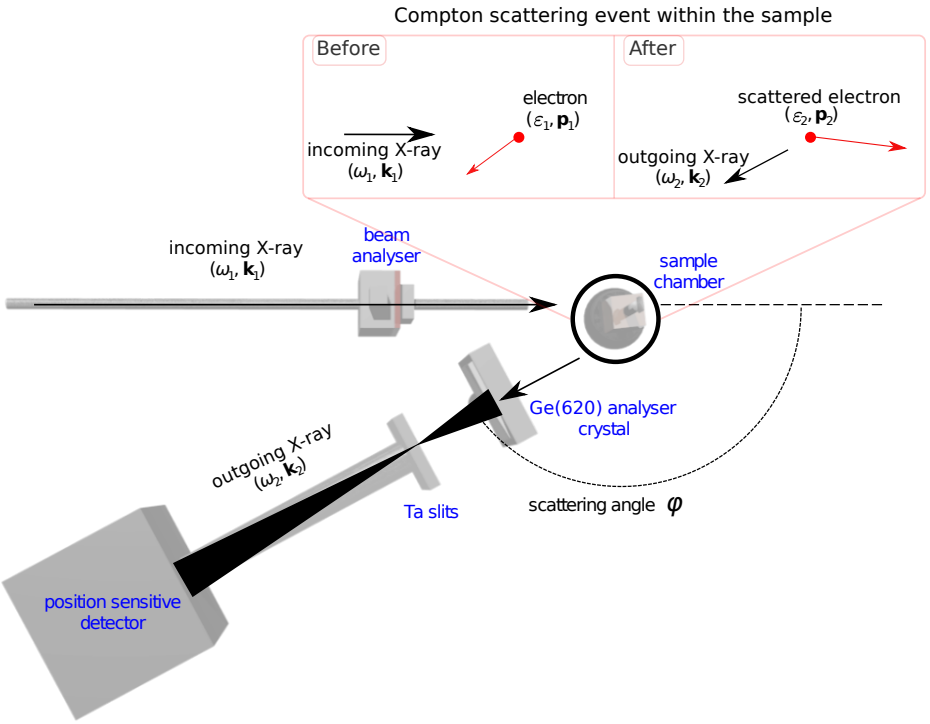

Figure 5.1: Experimental setup for the high-resolution charge Compton scattering spectrometer at beamline BL08W of SPring-8, Japan [203, 204], shown overlaid with a schematic diagram of the path of the X-ray. The inset shows the X-ray and electron states before and after the Compton scattering event within the sample. The outgoing X-ray has been scattered by an angle of φ (the scattering angle) with respect to the incoming X-ray.

to have long mean-free paths in order to complete the orbits in their Landau level. Hence, the material needs to have high purity and placed into extreme low temperatures (in the order of a few mK) and high magnetic fields. Fortunately, Compton does not suffer from this and therefore it can access other areas of the phase space and be used to measure disordered compositions. It should be noted that both ARPES and quantum oscillations are perturbing techniques and therefore, they do not measure the ground-state, in contrast to Compton scattering.

5.1.1 The Compton scattering cross-section

The core concepts associated with measuring the Compton scattering cross-section and how it can be related to the electron momentum density are discussed here. This section follows Refs. [19, 205], and further information about the derivations can be found there.

The process of Compton scattering, shown in Fig. 5.1, starts with the incoming high energy X-ray with energy ω_1 and momentum $\mathbf{k}_1$ which scatters from an electron with energy ε_1 and true momentum $\mathbf{p}_1$. This interaction involves a large momentum transfer from the incoming X-ray with respect to the electron's momentum. The measured X-ray has scattered by an angle

of φ (which is referred to as the scattering angle) and has energy ω_2 and momentum $\mathbf{k}_2$. The scattered electron, now having energy ε_2 and momentum $\mathbf{p}_2$, has 'passed on' information about its initial state to the scattered X-ray. Each inelastic scattering event is measured as a count in the experiment and this accumulation of counts relates directly to the double differential cross-section (the Compton scattering cross-section), $\frac{\mathrm{d}^2\sigma}{\mathrm{d}\Omega_s \mathrm{d}\omega_2}$, along the measured scattering vector, $\mathbf{K} = \mathbf{k}_2 - \mathbf{k}_1$. The double differential cross section is defined as the probability of measuring the scattered X-ray at solid angle Ω_s with energy ω_2.

In the first Born approximation[2], the double differential cross-section is written as

$$\frac{\mathrm{d}^2\sigma}{\mathrm{d}\Omega_s \mathrm{d}\omega_2} = \left(\frac{\mathrm{d}\sigma}{\mathrm{d}\Omega_s}\right)_{\mathrm{KN}} S(\mathbf{K},\omega). \tag{5.1}$$

Here, $\left(\frac{\mathrm{d}\sigma}{\mathrm{d}\Omega_s}\right)_{\mathrm{KN}}$ is the Klein-Nishina (KN) cross-section which describes the interaction between the photon and a free electron and it has the form

$$\left(\frac{\mathrm{d}\sigma}{\mathrm{d}\Omega_s}\right)_{\mathrm{KN}} = \frac{r_0^2}{2}\left(\frac{\omega_2}{\omega_1}\right)^2\left(\frac{\omega_2}{\omega_1} + \frac{\omega_1}{\omega_2} - \sin^2(\varphi)\right), \tag{5.2}$$

where r_0 is the classical electron radius. Information about the electron scatterer, which is missing in the KN cross-section, is described by the dynamic structure factor via Fermi's golden rule [206],

$$S(\mathbf{K},\omega) = \sum_{|i\rangle,|f\rangle} \left|\left\langle f \left| \sum_j \exp\left(i\mathbf{K}\cdot\mathbf{r}_j\right) \right| i \right\rangle\right|^2 \delta(\varepsilon_2 - \varepsilon_1 - \omega), \tag{5.3}$$

which describes the transition of the electron from the initial $|i\rangle$ to the final $|f\rangle$ electronic state, the Kronecker delta function ensures conservation of energy with respect to the energy transferred to the electron, with $\omega = \omega_1 - \omega_2$, and $\mathbf{r}_j$ is the position of the jth electron.

The desired information, which holds insight into the ground-state many-body electron wave function, comes from the initial state of the electron. Therefore, it is imperative that the potential in the electron's environment remains unchanged for the duration of the inelastic scattering interaction, so that the scattered photon contains this information. Fortunately, this is often naturally the case and it is justified within the Impulse Approximation [207]. This approximation states that after the scattered photon has left the vicinity, the target electron will then be subject to any relaxation of surrounding electrons and potentials from the recoiling target electron[3]. As long as the energy of the recoiled electron is far greater than its binding energy (meaning that high energy incident X-rays are needed), this approximation is valid [208, 209].

[2]There is only weak coupling between the incoming photon and the electron, meaning that the initial electronic state is unaltered and thus the scattering process and the target can be decoupled.

[3]The Compton scattering inelastic interaction takes far less time than that required for the electronic structure to relax after the interaction when using a high energy incoming X-ray.

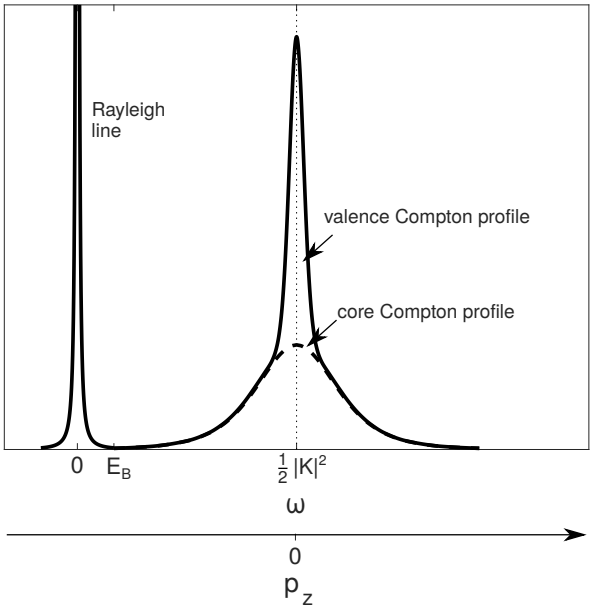

Figure 5.2: A hypothetical Compton profile measurement with the quasi-elastically scattered Rayleigh line. This has been plotted against energy loss ω and the electron momentum p_z (which is directed along the scattering vector). The Compton profile can be decomposed into a valence and core part. The valence profile is localised around the Compton peak ($p_z = 0$, or $\omega = \frac{1}{2}|\mathbf{K}|^2$) in momentum space, which is due to the valence electrons being delocalised in real space. On the other hand, the core profile is delocalised in momentum space (hence the distribution ranges over a greater range of momenta); this is because the core electrons are localised in real space. E_B marks the core-electron binding energy threshold of the core contribution below which the Impulse Approximation breaks down. This is a reimagined version of Fig. 2.2 in Ref. [19].

Using the conservation of energy (and momentum, i.e. $\mathbf{p}_2 = \mathbf{p}_1 + \mathbf{K}$) within the Impulse Approximation, the potential terms will cancel, producing

$$\begin{aligned} \omega_1 - \omega_2 &= \frac{1}{2}\mathbf{p}_2^2 - \frac{1}{2}\mathbf{p}_1^2 \\ \omega &= \frac{1}{2}(\mathbf{p}_1 + \mathbf{K})^2 - \frac{1}{2}\mathbf{p}_1^2 \\ &= \frac{1}{2}|\mathbf{K}|^2 + \mathbf{K}\cdot\mathbf{p}_1. \end{aligned} \tag{5.4}$$

The resultant two terms refer to the Compton shift and the Doppler broadening respectively (see Fig. 5.2). The Compton shift is dependent on the scattering vector of the interaction and it shifts the measured X-ray spectra to lower energies. The second term contains the desired information about the initial electron momentum projected along the scattering vector, broadening the initially monochromatic light in energy. It should be noted that from the Impulse Approximation, the momentum transfer is far greater than the initial momentum of the electron i.e. $|\mathbf{K}| \gg |\mathbf{p}_1|$. Therefore, the structure factor can be simplified to be in terms of the EMD, $\rho(\mathbf{p})$, of the material such that Eq. 5.1 can be rewritten as

$$\frac{\mathrm{d}^2\sigma}{\mathrm{d}\Omega_s \mathrm{d}\omega_2} = \frac{r_0^2}{2}\frac{1}{|\mathbf{K}|}\frac{\omega_2}{\omega_1}\left(\frac{\omega_2}{\omega_1}+\frac{\omega_1}{\omega_2}-\sin^2(\varphi)\right)\iint \rho(\mathbf{p})\mathrm{d}p_x\mathrm{d}p_y. \tag{5.5}$$

The relativistic form can be found in Refs. [205, 210].

The experiment uses fixed scattering angles and an initial monochromatic X-ray source meaning that the quantities prior to the double integral are constant. Therefore, the measured double differential cross-section depends on the Compton profile $J(p_z)$[4] which is the 1D projection of the (total) EMD,

$$J(p_z) = \iint \rho(\mathbf{p})\mathrm{d}p_x\mathrm{d}p_y, \tag{5.6}$$

in which all of the (occupied) electron states have contributed equally.

If the incident photon beam has a component of circular polarisation, the scattering cross-section contains a term which is spin dependent. This term may be isolated from the charge scattering by either flipping the direction of the sample magnetisation or the photon helicity parallel and antiparallel with respect to the scattering vector, resulting in a magnetic Compton profile (MCP), $J_{\mathrm{mag}}(p_z)$ [211]. In analogy to the Compton profile, the MCP is defined as the 1D projection of the spin-polarised electron momentum density:

$$J_{\mathrm{mag}}(p_z) = \iint \left[\rho^{\uparrow}(\mathbf{p}) - \rho^{\downarrow}(\mathbf{p})\right]\mathrm{d}p_x\mathrm{d}p_y. \tag{5.7}$$

5.1.2 The electron momentum density

As the EMD was introduced in the previous section, how this is related to the ground-state many-body electron wave function will be discussed here[5]. The EMD is analogous to the electron density in real space (which is used in DFT as discussed in Section 3.1), so the total EMD can be normalised to the total number of electrons, N, in the (primitive) unit cell,

$$N = \iiint \rho(\mathbf{p})\mathrm{d}p_x\mathrm{d}p_y\mathrm{d}p_z. \tag{5.8}$$

Therefore, the MCP can also be normalised to the spin moment (m_s),

$$m_s = \int J_{\mathrm{mag}}(p_z)\mathrm{d}p_z. \tag{5.9}$$

Starting with the independent particle model, the EMD is derived from the integral of the square modulus of the Fourier transformed real space ground-state wave function being summed over all occupied states,

[4] The 'z' axis is used as convention and it refers to the axis parallel to the scattering vector.
[5] Spin indices have been omitted here for clarity.

$$\rho(\mathbf{p}) = \sum_{\mathbf{k},j} n_{\mathbf{k},j} \left| \int_{\Omega} \exp(-i\mathbf{p}\cdot\mathbf{r}) \psi_{\mathbf{k},j}(\mathbf{r}) \mathrm{d}\mathbf{r} \right|^2 . \tag{5.10}$$

In Eq. 5.10, $\psi_{\mathbf{k},j}(\mathbf{r})$ is the real space wave function, at crystal momentum $\mathbf{k}$ and eigenstate index j, being Fourier transformed over the (primitive) unit cell volume Ω with the sum over the occupied states described by the occupation function $n_{\mathbf{k},j}$.

In a lattice, the Bloch wave function has the form (see Chapter 2)

$$\psi_{\mathbf{k},j}(\mathbf{r}) = \frac{1}{\sqrt{\Omega}} u_{\mathbf{k},j}(\mathbf{r}) \exp(i\mathbf{k}\cdot\mathbf{r}), \tag{5.11}$$

where $u_{\mathbf{k},j}(\mathbf{r})$ can be written in terms of a series of plane-waves:

$$u_{\mathbf{k},j}(\mathbf{r}) = \sum_{\mathbf{G}} a_j(\mathbf{k}+\mathbf{G}) \exp(i\mathbf{G}\cdot\mathbf{r}), \tag{5.12}$$

with the $a_j(\mathbf{k}+\mathbf{G})$ Fourier coefficients defined such that the entire wave function is normalised (e.g. $\sum_{\mathbf{G}} \left|a_j(\mathbf{k}+\mathbf{G})\right|^2 = 1$ for each spin). Including this in Eq. 5.11 produces

$$\psi_{\mathbf{k},j}(\mathbf{r}) = \frac{1}{\sqrt{\Omega}} \sum_{\mathbf{G}} a_j(\mathbf{k}+\mathbf{G}) \exp(i(\mathbf{G}+\mathbf{k})\cdot\mathbf{r}), \tag{5.13}$$

resulting in the EMD being reformulated as

$$\rho(\mathbf{p}) = \frac{1}{\Omega} \sum_{\mathbf{k},j} n_{\mathbf{k},j} \left| \sum_{\mathbf{G}} a_j(\mathbf{k}+\mathbf{G}) \int_{\Omega} \exp(-i(\mathbf{p}-\mathbf{k}-\mathbf{G})\cdot\mathbf{r}) \mathrm{d}\mathbf{r} \right|^2 . \tag{5.14}$$

This can be simplified as

$$\rho(\mathbf{p}) = \sum_{\mathbf{k},j,\mathbf{G}} n_{\mathbf{k},j} \delta(\mathbf{p}-\mathbf{k}-\mathbf{G}) \left|a_j(\mathbf{k}+\mathbf{G})\right|^2 . \tag{5.15}$$

This form of the EMD makes it easier to understand what is being calculated from the wave functions. The Kronecker delta function ensures that the crystal momentum is conserved and it redistributes the $a_j(\mathbf{k}+\mathbf{G})$ information in $\mathbf{k}$-space out into $\mathbf{p}$-space. This introduces so-called "umklapp" processes where higher BZs ($\mathbf{p} = \mathbf{k} + m\mathbf{G}$ with integer m) contribute to the EMD. Essentially, the information in the 1BZ has been 'folded outwards' into $\mathbf{p}$-space, meaning that the EMD has the point symmetry of the crystal but it does not have the translational invariance of k-space.

The Fermi surface can be determined from the EMD as shown in Fig. 5.3. If there is a fully occupied band (i.e. a band not crossing the Fermi level) [see Fig. 5.3 (a)], this results in a

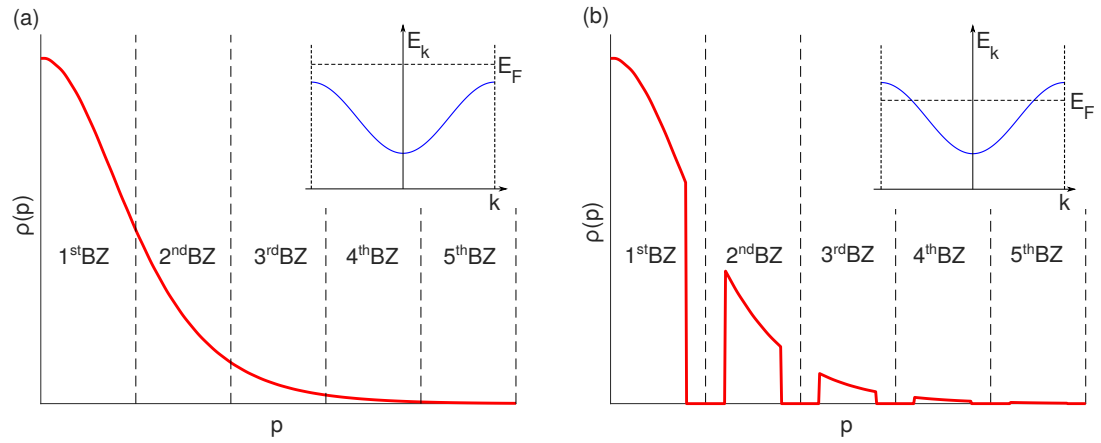

Figure 5.3: Hypothetical 1D EMD, $\rho(p)$, for two corresponding bands. (a) The band is fully occupied in the inset, so the p-space distribution is smooth and continuous. (b) The band crosses the Fermi level (see the corresponding inset) meaning that it changes its occupation in the Brillouin zone (BZ). Therefore, there are certain k states which no longer contribute to the 1D EMD resulting in a Fermi break occurring in the first and subsequent BZs. These periodic breaks in the EMD have a periodicity of the 1D lattice vector G.

continuous EMD distribution over all BZs. In the case where there is a partially occupied band crossing the Fermi level [see Fig. 5.3 (b)], there will be Fermi breaks in the EMD distribution over all of the BZs in **p**-space with the lattice periodicity (**G**). This shows how the EMD (and the Compton profile) is sensitive to the Fermi surface. For a real material, contributions to the EMD come from all of the occupied and partially occupied bands which accumulate to form a continuous distribution (from the fully occupied bands) along with contributions containing the Fermi breaks (from partially occupied bands). However, as there are likely to be far more filled bands than partially-filled bands, the Fermi breaks tend to be small and often difficult to determine from the EMD alone. To complicate matters, when smearing from temperature and electron correlations are considered[6], the sharp finite jumps in the Fermi breaks, which come from $n_{\mathbf{k},j}$, smear out making it even harder to determine the breaks. However, the smearing from these factors tend to be smaller than the contribution from the experimental resolution, which overall means that the measured Fermi breaks would be less distinguishable than those in the hypothetical 1D EMD in Fig. 5.3.

The inclusion of electron correlations has a significant effect on the $n_{\mathbf{k},j}$ occupation function, as discussed in Chapter 2. This can be understood in terms of the self-energy which can shift the bands across the Fermi level (from the real part of the self-energy) and gives a (energy-dependent) width to the states which arises from the QP lifetime (which relates to the imaginary part of the self-energy). Here, we will mainly discuss the effect the electron correlations have on $n_{\mathbf{k},j}$ and $J(p_z)$ within the Fermi-liquid regime, as this regime is able to describe many of the

[6]As well as smearing from the disorder of alloyed atoms in the crystal structure of certain materials [186].

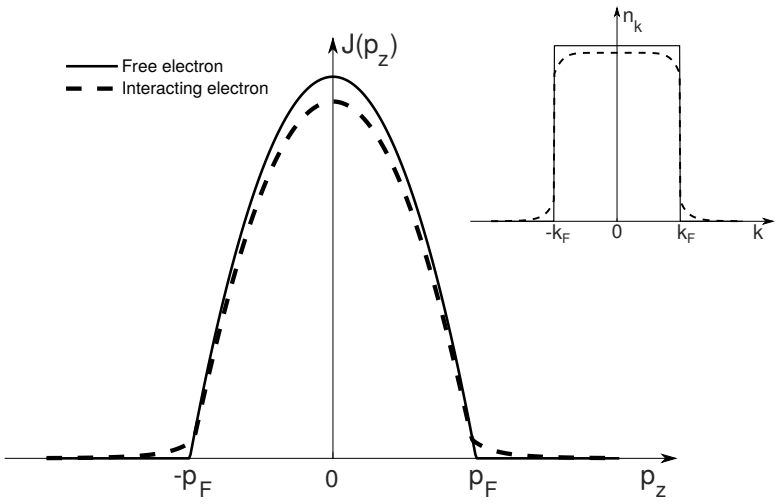

Figure 5.4: Hypothetical non-interacting and interacting free electron Compton profiles $J(p_z)$. The inset shows the corresponding occupation functions used to generate the Compton profiles. Further details about the free electron Compton profile can be found in Ref. [19]. The interacting occupation function is the empirical form proposed by Schülke *et al.* [46], using the z = 0.713 (which is the height of the discontinuity at k_F [Z_{k_F}]). The corresponding interacting electron Compton profile was derived using the Schülke occupation function.

features within the materials presented later in this chapter. The inclusion of the (Fermi-liquid) self-energy subsequently changes the occupation function from being a step (or Fermi-Dirac) function to a more smeared function (which still has a discontinuous jump at 0 K), as discussed in Chapter 2. To illustrate the influence of the occupation function, Fig. 5.4 shows the effect of adding electron correlations (which manifest in the occupation function) to the free electron Compton profile[7]. As can be seen, the height of the correlated Compton profile reduces at low momentum and also has a smoother shape around p_F. However, this change to the profile shape is highly dependent on the type of electron correlations included in the calculation. It should be noted that for a system within the Fermi-liquid regime, as well as for a non-interacting system, the volume enclosed by the Fermi surface(s) is directly proportional to the electron's density, as per Luttinger's theorem [212, 213]. Therefore, the volume of the Fermi surface(s) must be conserved if the system is subjected to any changes whilst being within this weakly correlated regime. Although, beyond this regime, Luttinger's theorem breaks down [214, 215].

Without the description of all of the electron correlations, the calculated Compton profile (from DFT or HF) has distinct discrepancies with respect to the measured one. The first step made to correct for these discrepancies was the Lam-Platzman correction [216], $\Delta\rho(\mathbf{p})$, to the

[7]The free electron Compton profiles in Fig. 5.4 were determined by solving $J(p_z) = 2\pi \int p\rho(p)\mathrm{d}p$ which is valid for an isotropic system [19]. Note that $\rho(p) = n_{k=p}$ as the free electron EMD does not have higher BZ contributions because this system does not have a periodic potential. (The j index has been dropped in n_k because the free electron model does not have distinct bands.)

calculated EMD. This $\Delta\rho(\mathbf{p})$ is derived from

$$\Delta\rho(\mathbf{p}) = \frac{\delta\hat{E}_{xc}[\rho]}{\delta\varepsilon_{\mathbf{p}}}, \tag{5.16}$$

where $\varepsilon_{\mathbf{p}}$ is the energy of an electron with real momentum $\mathbf{p}$. This correction has only been derived for the LDA exchange-correlation functionals and is isotropic by construction. However, discrepancies between calculations and experiment tend to be anisotropic [208, 217, 218]. Other attempts at correcting the anisotropies arising from correlations used approximations to generate the correlated $n_{\mathbf{k},j}$ which has had some success [46, 219–221]. On the other hand, there has been work in calculating the EMD from many-body approaches such as *GW* [222–225] and DFT+DMFT [24, 226–229], where certain electron correlation effects have been included. With the further development of many-body theories combined with DFT and the increasing computational power, calculating the EMD from these theories is becoming feasible. The effect of the correlations from DMFT on the EMD is the focus of this chapter.

As a closing remark, the Kohn-Sham wave functions have the constraint of reproducing the many-body $\rho_0(\mathbf{r})$, not the EMD. Therefore, even with the inclusion of many-body theories (along with their effect on the wave functions and occupations), there may be a limit regarding the agreement between the experimentally measured EMD and the theoretical EMD calculated from the wave functions described by a basis set of (auxiliary) single orbitals.

5.1.3 Experimental overview

Although this thesis does not present new experimentally measured Compton profiles, an understanding of the experimental procedure is required to know what information can be extracted from the experiment. This section will give a brief overview of the Compton scattering experimental procedure.

In recent years, Compton profiles are measured at a few synchrotron facilities such as the BL08W beamline at the SPring-8 synchrotron in Japan [203, 204, 230]. This beamline uses an energy dispersive spectrometer meaning that the entire scattered spectrum is collected simultaneously instead of scanning over the energy spectrum. The experimental setup is shown in Fig. 5.1. The incident monochromatic X-rays from a Si(400) monochromator (beam analyser), have an energy of 115.6 keV. These photons pass through the evacuated chamber before striking the sample. The sample environment could be subjected to magnetic fields to measure the MCPs. After the X-rays have been inelastically (Compton) scattered through a scattering angle of 165°, the photons arrive at a Ge(620) crystal analyser which disperses the photons according to their energy. The analyser has been aligned to focus the photons onto a Ta slit which is used to reduce the background signal. These photons are then spread over a position sensitive detector (PSD) which contains a charge coupled device (CCD) digital camera along with an optical image

intensifier. The PSD has been calibrated to detect the photons across a range of around 70 - 90 keV and is aligned such that the Compton peak is at the centre of this range (~ 80 keV).

5.1.3.1 The Data Analysis

The measured spectra will not only be of the desired Compton profile, but it will also include the measured photons which have not originated from the sample at all, along with contributions from the equipment as a result of the additional interactions the scattered photons have as they make their way from the sample to the CCD. Therefore, the measured spectra will (likely) include Pb fluorescence lines originating from the photons which interacted with Pb radiation shielding used in the beamline; additional Compton scattering from the equipment (from the X-ray photons making their way from the sample) as well as other background contributions; absorption effects; and multiple scattering events of the photons within the sample. These, as well as the factors which may affect the CCD image (such as image distortion, saturation, detector efficiency, and hot spots [which likely originates from cosmic radiation]), need to be corrected for. Often, these corrections (with exception of the Pb fluorescence lines) are predominately smooth and featureless. The order in which the corrections are applied is vital. The corrections are applied in reverse order of what the photons interact with during their path to the detector[8]. The following is a brief technical account of how the corrections are implemented in the order that they are applied to the raw Compton profile:

1. Calibrate the energy scale with the fluorescence lines of the reference sample of Bi and Tl (see for example Refs. [203, 230]).
2. Remove the distortion, caused by the PSD, in the measured CCD image by using a pincushion function.
3. Remove hot spots by fitting them with a Gaussian function and then removing them with this fit.
4. Integrate the 2D CCD image to produce a 1D raw Compton profile, taking any detector saturation into account.
5. Convert the the PSD x-axis (the channel numbers) into the calibrated energy scale.
6. Remove the Pb fluorescence lines.
7. Remove the background counts, see Refs. [230, 231].
8. Account for the detector efficiency [230].
9. Convert the energy scale to the electron momentum scale.

[8] I.e. corrections from the detector are applied first and so on up to and including correcting for the other photon interactions within the sample last.

10. Remove the multiple scattering which is modelled by a Monte Carlo code such as that developed by Sakai [232].

11. Remove the effects due to sample absorption.

12. The distribution now should be that of the Compton scattering cross-section. The all-electron Compton profile can be calculated by putting in the constants into (the rearranged version of) Eq. 5.5. Then remove the core electron contributions (which are well described by the free-atom HF states, tabulated in Ref. [233], due to their localisation in real space) to the Compton profile, leaving the desired valence Compton profile.

Further in depth discussions of the data analysis is found in Ref. [230] and previous theses [234–236]. The resultant corrected Compton profile signal will be of the valence electrons (within a momentum window of $\sim \pm 10$ a.u. (atomic units)[9] due to experimental restrictions).

It is imperative to be precise with the corrections so that the discrepancies between the experimental and theoretical Compton profiles can be accurately and reliably determined. The Compton profile is very sensitive to the corrections making it difficult to apply them. However, there are three criteria of the Compton profile which must be obeyed and are used to ensure the corrections have been applied correctly: (1) The profile is symmetric about the centre[10] for Compton profiles from high energy incident X-rays (which is the case for the presented Compton profiles in this thesis). Otherwise, for lower incident energies, notable asymmetries would be present in the Compton profile as a consequence of the breakdown of the Impulse Approximation [208, 209]; (2) The valence Compton profile area must be equal to the number of valence electrons within the aforementioned experimental momentum window. This condition is the same for the core Compton profile which must be normalised to the number of core electrons (within the momentum window); and (3) The high momentum "tails" of the Compton profile must smoothly tend to zero as momentum tends to $\pm\infty$. These tails are atomic-like and therefore they can be compared with the tails of the well-characterised free-atom HF Compton profiles. The corrections are optimised until these three criteria are fulfilled[11].

When we have the corrected Compton profiles, these can be compared with the calculated valence Compton profiles from DFT (or another model), along with comparing the experimental and theoretical "directional differences" (i.e. the differences in Compton profiles along different scattering vectors). The directional differences often show more distinct structures as they have prominent features due to the anisotropy in the Compton profiles along different crystal directions. These experiment-theory comparisons reveal the origin of the electronic structure

[9] "a.u." stands for atomic units in this thesis.

[10] Unless there are other physical reasons why this is not the case (such as in Ref. [237]), but these do not apply for the (symmetric) Compton profiles discussed in this thesis.

[11] As a sanity check, the corrected Compton profiles are compared with corresponding theoretical profiles to ensure that the correct direction was measured. Although, there will be differences between these Compton profiles.

features, as well as indicating what is missing from within the theory, such as the missing correlation contributions as discussed previously.

5.2 DFT+DMFT electron momentum densities

The EMD calculations for DFT have been computed using the ELK code with the tetrahedron method described in Refs. [235, 238]. This thesis builds upon the aforementioned method to calculate the DFT+DMFT EMD. These calculations evaluate the EMD by using

$$\rho^{\sigma}(\mathbf{p}) = \sum_{\mathbf{k},\nu} n^{\sigma}_{\mathbf{k},\nu} \left| \int \Psi^{\sigma}_{\mathbf{k},\nu}(\mathbf{r}) \exp(-i\mathbf{p}\cdot\mathbf{r}) \mathrm{d}\mathbf{r} \right|^2 . \tag{5.17}$$

Here, $\Psi^{\sigma}_{\mathbf{k},\nu}(\mathbf{r})$ is the single-orbital (electron) wave function at $\mathbf{k}$ with spin σ and eigenstate ν, and $n^{\sigma}_{\mathbf{k},\nu}$ is the electron occupancy. These wave functions and occupations are either from the DFT or the DFT+DMFT calculation, where the diagonal set[12] of DFT+DMFT wave functions and occupation functions are calculated using the method discussed in Section 3.7.3. Therefore, the EMD is calculated without using analytic continuation.

5.2.1 Testing the electron momentum density calculations from ELK-TRIQS

As the DFT+DMFT wave functions and occupations are stored in the same arrays in the ELK code, the EMD ELK code can be used without further modification. Therefore, only the interface needs to be tested to ensure that the required information is being passed through TRIQS correctly. This test was done by passing the DFT quantities through TRIQS (without doing any DMFT cycles) and then comparing the DFT Ni MCP calculated from these quantities with the ELK Ni MCP. The Compton profiles and MCPs were used for benchmarking to ensure that both of these quantities are being calculated correctly when using the interface. The parameters used for the Ni DFT calculation are the same as those used in Section 5.3.

Figures 5.5 (a) and (c) show that the unconvoluted Ni DFT [100] Compton profiles (normalised to the number of valence electrons) and MCPs (normalised to the DFT magnetic spin moment) for the ELK and ELK-TRIQS interface with the default maximum number of Matsubara frequencies ($\mathrm{n}_{i\omega}$)[13], and a ELK-TRIQS calculation with $4\times\mathrm{n}_{i\omega}$ (i.e. the Green's functions and self-energies have a higher Matsubara cut-off frequency). It is important to note that the exact same temperature was used in ELK-TRIQS calculations as in ELK calculation, otherwise the Fermi-Dirac occupation functions will be different resulting in further discrepancies in the Compton profiles and MCPs. From Figs. 5.5 (b) and (d), it is clear that the Compton profiles and MCPs are the same within a certain numerical error. This error can be reduced by increasing $\mathrm{n}_{i\omega}$[14], but the default value is

[12] I.e. the eigenvectors and eigenvalues of the density matrix.
[13] The default $\mathrm{n}_{i\omega}$ value of positive Matsubara frequencies is equal to 1025.
[14] As well as increasing the number of τ points used to avoid numerical issues with the Fourier transformations.

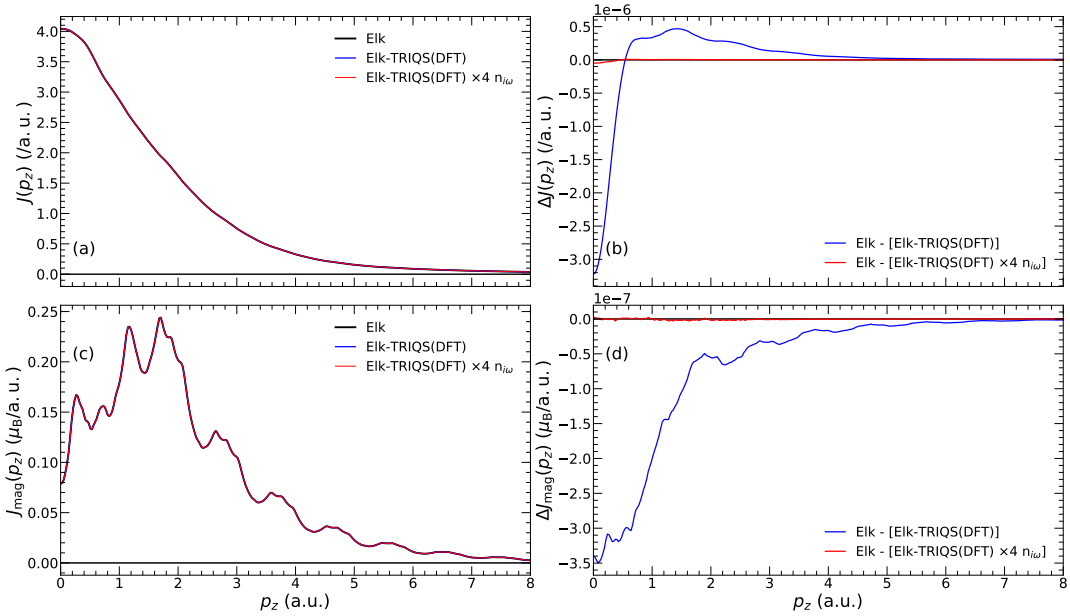

Figure 5.5: Interface tests of the DFT [100] Compton profiles and MCPs of Ni. (a) [(c)] The DFT Compton profiles [MCPs] from the ELK, ELK-TRIQS interface, and the ELK-TRIQS interface with 4 times greater Matsubara frequency cutoff $n_{i\omega}$. (b) [(d)] The differences between the Compton profiles [MCPs] generated from the ELK and the interface calculations.

more than sufficient here. It should be noted that including bands above and below the Fermi level with greater (absolute) energies within the correlated energy window may require a larger $n_{i\omega}$. Nonetheless, it is evident that the interface works for calculating Compton profiles and MCPs. Also, this code uses the same method to generate the DFT+DMFT wave functions and occupations for other wave function-dependent-quantities (as well as the rest of the ELK code remaining unchanged). Therefore, calculating the other wave function-dependent quantities will work and will also have the same parameter considerations regarding the ELK-TRIQS setup as with this example.

Lastly, relatively good Compton profiles and MCPs can be calculated from DFT+DMFT calculations based on lower statistics used in the CTQMC solver than that needed to get good spectral functions. This is because the EMD calculations do not require analytic continuation which is very sensitive to the noise in the Green's functions and self-energies. In Figs. 5.6 (a) and (c), the low statistics Ni DFT+DMFT [100] Compton profile and MCP used the same parameters as the high statistics calculation, but it used 1/20th of the Monte Carlo statistics. The parameters used for the higher statistics ELK-TRIQS DFT+DMFT calculation[15] are discussed in Section 5.3. The MCPs from the different Monte Carlo statistics calculations are in good agreement with each other. Figure 5.6 (b) and (d), on the other hand, show the difference between these DFT+DMFT Compton profiles and MCPs, and it is far greater than that in Figs. 5.5 (b) and (d), which indicates

[15]Note that this higher statistics DFT+DMFT calculation used 4.2×10^8 Monte Carlo sweeps.

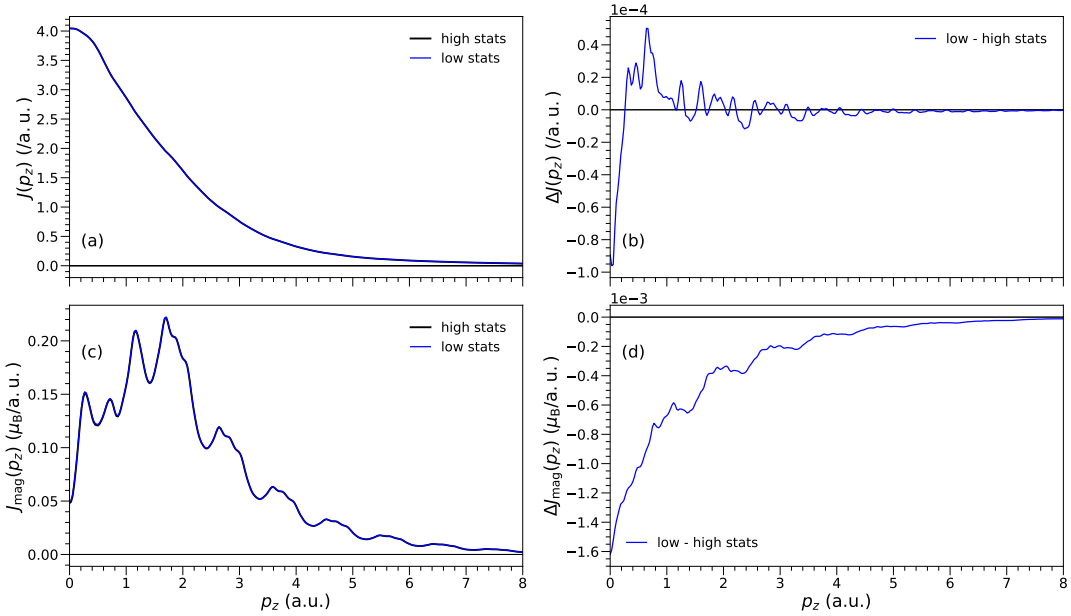

Figure 5.6: Testing the $U = 2.0$ eV DFT+DMFT [100] Ni MCP using different Monte Carlo statistics ("stats" in the legends) in the DMFT calculations. The MCP with the high Monte Carlo statistics used the parameters given in section 5.3. On the other hand, the MCP with the low Monte Carlo statistics used 1/20th of the statistics used in the high Monte Carlo statistics DMFT calculation. (a) [(c)] The [100] Ni DFT+DMFT Compton profiles [MCPs] from the different statistics. (b) [(d)] The difference between the Compton profiles [MCPs] generated from the Ni DFT+DMFT calculations using different statistics.

that the quality of the Monte Carlo statistics used is an important factor in the EMD calculations. However, the error due to the Monte Carlo noise here is less than the typical (magnetic) Compton profile experimental statistical error seen in the experimental (magnetic) Compton profiles of Ni and V presented in Sections 5.3.2 and 5.4.1. Of course, the experimental statistical error can be improved upon by measuring more counts (N), which would be possible if Ni and V were remeasured at SPring-8, as the experimental statistical error is proportional to $1/N^{1/2}$. Therefore, (magnetic) Compton profiles from (preliminary) DFT+DMFT calculations with lower statistics can give good results when comparing with the experiment, but if the experimental statistical error is small (at least on the same order of magnitude as seen here), then higher Monte Carlo statistics must be used to eliminate any potential concerns from this part of the DMFT calculation.

5.3 Nickel

One of the most studied simple metallic system that presents signatures of electronic correlations is the FCC itinerant ferromagnetic Ni. It is known that the DFT alone cannot reproduce the dispersionless feature at a binding energy of about 6 eV which is known as the "6 eV satellite" [239]. The valence band photoemission spectrum of Ni shows a $3d$ band width that is about 30% nar-

rower than the value obtained from the DFT calculations. Similarly, the exchange splitting in both the LSDA and the GGA [240] overestimates the experimental splitting by approximately 50% [241–244]. The combined DFT+DMFT describes the occupied $3d$ band width of Ni, and reproduces the exchange splitting and the 6 eV satellite structure in the valence band [245–247]. Recently, DFT+DMFT has shown the consequences of the local moment in ambient and Earth-core-like conditions [248]. Yet further information about the electronic structure of Ni can be extracted by using Compton scattering.

The MCPs of Ni have been calculated by using various DFT implementations and their extensions. Features associated with the Fermi surface (as a consequence of bands crossing the Fermi energy) seen in experiment [249] were generally reproduced with good agreement, notwithstanding the distinct discrepancy at low momenta which points towards some inaccuracies in the position of the spin-polarised bands with respect to the Fermi level. It has also been shown that the negative polarisation of the itinerant s- and p-like band electrons can be observed [250, 251] and the discrepancy with respect to the theoretical predictions were attributed to the insufficient treatment of correlations present in the standard DFT exchange-correlation functionals at low momentum [250]. The directional Compton and magnetic Compton profiles have also been computed in combination with DMFT [226–228] which facilitated a discussion of the anisotropy of the electronic correlations of Ni as a function of the on-site Coulomb interaction strength, U. Those theoretical comparisons with the experimental data led to the conclusion that the theoretical MCPs improved when the local correlations are taken into account, which also extends to the total Compton profiles.

Here, we focus on the calculation of the momentum distribution and related quantities within the framework of many-body theory for Ni. We have used two approaches on the DFT side, namely Korringa-Kohn-Rostoker (KKR) [252–254] which is a spin-polarised relativistic multiple-scattering theory implementation, and ELK[16]. The calculation scheme within the KKR method is based on the Green's function formalism of multiple-scattering theory [252]. Both the KKR and ELK self-consistent computations were performed with the same parameters for the crystal structure ($a = 3.52$ Å) and the same parametrisation for the DFT exchange-correlation potential, LSDA [60]. The ELK DFT calculations used a $20\times20\times20$ Monkhorst-Pack k-mesh, which proved to be sufficient for the k-point convergence of the self-consistent calculation. The KKR calculations within atomic sphere approximation were performed on a $57\times57\times57$ Monkhorst-Pack k-mesh, and a semicircular complex contour was used with 40 energy points enclosing the one-particle poles of the Green's function. The minor differences in the DOS and spectral functions can be attributed to the different approaches within ELK and KKR.

Sightly more significant differences are expected to appear at the DFT+DMFT level. Both approaches use a rotationally invariant form for the interacting Hamiltonian. The multi-orbital interaction has been parameterised by the average screened Coulomb interaction U and the

[16]For clarity, ELK refers to the FP APW+lo DFT calculation from the ELK code.

Hund's exchange coupling J. The values of U and J are sometimes used as fitting parameters, although recent developments allow the computation of the dynamic electron-electron interaction matrix elements exactly [255]. It was shown [256] that the static limit of the screened energy-dependent Coulomb interaction led to the U parameter being in the energy range of 2 and 4 eV for all $3d$ transition metals. The vast amount of results on the ground state properties of bulk Ni have been produced using $J = 0.9$ eV [226–228, 245, 257] with excellent agreement with experimental results. That value of J was used here. Previous DMFT calculations showed that these U and J parameters provide the best description of the ground-state properties related to the structure and different spectroscopic measurements for many of the $3d$ metals [113, 245, 258, 259]. For consistency with those and previous Ni DFT+DMFT Compton [226–228] and 2D-ACAR [257] studies, we have chosen to investigate around the previously used "U–J" parameter space of Ni here. Besides, these U and J parameters are in line with cRPA calculations of $3d$ transition metals [260, 261]. Note, however, that the multi-orbital interacting Hamiltonian is formulated in different basis sets. In KKR+DMFT, the local atomic basis set is used [254, 262], and consequently, the many-body problem is formulated within the d-block. Correlation effects are felt by other orbitals only through the self-consistency cycle. The DMFT solver used in the current KKR implementation is the relativistic version of the so-called Spin-Polarised T-Matrix (SPT-) Fluctuation Exchange approximation (FLEX) [113, 263] which is formulated on the Matsubara axis. In contrast, with the ELK+DMFT[17], the Wannier projectors are constructed such that the Ni d states, which are completely within the used correlated energy window of [-10, 3] eV, are captured. Further essential parameters for the ELK+DMFT CTHYB impurity solver [161] are the number of Monte Carlo sweeps (4.2×10^8) used and the inverse temperature β of 40 eV^{-1}. In both DFT+DMFT methods, the spin-polarised AMF double counting term [98, 264] was employed.

The ELK+DMFT spectral function presented in Section 5.3.3 was calculated by analytically continuing the DMFT self-energy using the *LineFitAnalyzer* technique of the maximum entropy analytic continuation method implemented within the TRIQS/MAXENT application [125].

The different descriptions of the potentials, full potential in ELK and the atomic sphere approximation in KKR, also lead to the difference in the calculated chemical potentials. Within the KKR+DMFT method, the self-energy is added into the Kohn-Sham-Dirac equation [254, 262], and the chemical potential is updated to conserve the number of valence electrons, similar to what is done in the DFT loop. The ELK+DMFT, using the Wannier projectors instead, updates the electron density from which a new set of Kohn-Sham eigenvalues and eigenvectors are generated and the corresponding DFT+DMFT chemical potential is obtained in the DMFT cycle (again to conserve the number of electrons). The difference in the DFT+DMFT chemical potential with respect to the DFT values is at most a few tenths of an eV. The different solvers produce slightly different values for the real parts of the self-energies at the chemical potential. An important

[17] For clarity, ELK+DMFT refers to the DFT+DMFT calculations from the ELK-TRIQS package.

factor here is the double counting and even though its functional form is the same for both KKR+DMFT and ELK+DMFT, the slightly different values in the occupation matrix produce slightly different double counting values.

Magnetism can alternatively be purely treated in DMFT cycle only and use non-magnetic (NM) DFT calculations as inputs (so the DFT part of the FCSC DFT+DMFT cycle remains non-magnetic). Here, magnetism in DMFT arises by breaking the spin degeneracy in the self-energy and allowing this non-degenerate spin calculation to converge. This introduces a local spin moment in the correlated d states treated in DMFT only. This is what was done in the ELK(NM)+DMFT calculations[18], which used the same parameters as the ELK+DMFT calculations apart from using the spin-averaged AMF double counting and non-magnetic LDA functional. The ELK(NM)+DMFT calculations are fully charge self-consistent, but the spin-averaged density matrix from the DMFT lattice Green's function was interfaced back into the DFT part of the cycle (hence keeping the DFT part non-magnetic). Although the temperature used within the KKR+DMFT, ELK(NM)+DMFT, and ELK+DMFT calculations was below that of experimental and DFT+DMFT calculated Curie temperatures [245, 248], meaning that these systems are in the ferromagnetic phase, the magnetism treated purely on the DMFT level is missing certain magnetic mean-field contributions which are captured in LSDA, such as mean-field treatment of the non-local correlations, exchange, and s and p contributions. Therefore, it is unlikely that the ELK(NM)+DMFT results would resemble those from ELK+DMFT, but information can still be extracted from them.

5.3.1 U-dependent spin and orbital magnetic moments

To identify the optimal value of U, or at least to narrow the *ab-initio* interval, we first analysed the behaviour of the Ni ferromagnetic spin magnetic moment with respect to the on-site Coulomb interaction, U and fixed Hund's rule coupling, $J = 0.9$ eV.

The magnetic spin (m_s) and orbital (m_ℓ) magnetic moments as a function of the on-site Coulomb interaction U are shown in Fig. 5.7. Both the ELK+DMFT and KKR+DMFT results show a similarly decreasing spin magnetic moment with increasing U, in quite close correspondence to each other.

Contrary to the decreasing spin moment over the entire U range, the orbital moment m_ℓ obtained in relativistic KKR+DMFT calculations, increases with the U values, passing the maximum value at $U \approx 2.3$ eV, and decreases upon further increasing the value of U. Even for the largest value of U ($U = 3.0$ eV in the presented calculations), the KKR+DMFT orbital magnetic moment is larger than the corresponding DFT value by about 30%. Similar results have also been reported previously in Ref. [265] and were interpreted as a correlation-induced orbital moment enhancement.

[18] For clarity, ELK(NM)+DMFT refers to non-magnetic DFT calculations used in the DFT+DMFT calculations from the ELK-TRIQS package, where magnetism only exists in the DMFT cycle.

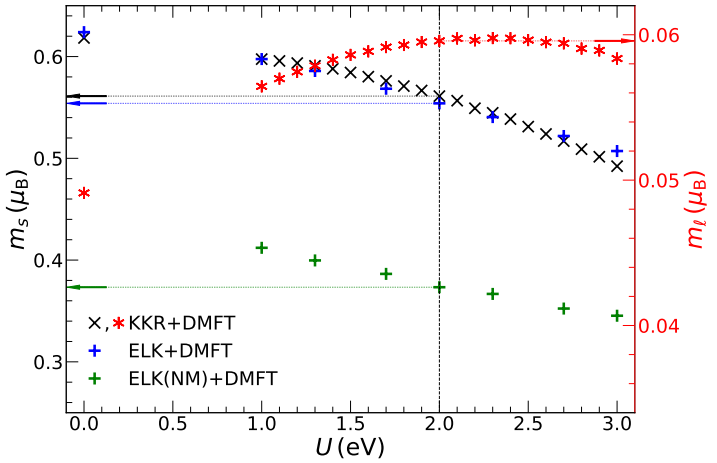

Figure 5.7: Spin $m_s(\mu_B)$ and orbital $m_\ell(\mu_B)$ magnetic moments as a function of the intra-site Coulomb potential U. Blue plus signs and black crosses represent results of ELK(+DMFT) and KKR(+DMFT) spin magnetic moment calculations, respectively. The ELK(NM)+DMFT local spin magnetic moments are shown by the green pluses. The right axis represents the KKR (red asterisks) orbital magnetic moment (m_ℓ). In all of the calculations, the Hund's rule coupling parameter $J = 0.9$ eV was used. The data points for $U = 0.0$ eV ($J = 0.0$ eV) represent the DFT (LSDA) calculations.

Despite the different descriptions, it is satisfying to see the good agreement between the results obtained with both methods. For $U = 2.0$ eV, the calculated spin moment matches best with experiment $\approx 0.56\ \mu_B$ for both DFT+DMFT methods and is within the *ab-initio* predictions for the $3d$ transition elements. These $U = 2.0$ eV and $J = 0.9$ eV values are in agreement with that used in the previous spin-polarised Ni 2D-ACAR study [257], as well as being in good agreement with other DFT+DMFT studies which focused on the spectroscopic properties [113, 259].

Turning to the ELK(NM)+DMFT results, it can be seen that they have the same reduced spin moment trend with increasing U as the ELK+DMFT, along with a similar gradient. This helps to enforce the notion that the reduction of the moment is due to the strength of the local correlations parameterised by U. The discrepancy in the magnitude of the moments between the ELK+DMFT and ELK(NM)+DMFT results is from the aforementioned missing vital mean-field electron correlations which are present in the (magnetic) LSDA functional.

The experimental value for the spin moment originates from the polarised neutron diffraction measurements by Ref. [266]. The total (spin + orbital) measured magnetic moment, which the analysis relied on, was subsequently revised by Ref. [267] to $0.616\,\mu_B$, and with which our KKR+DMFT $U = 2.0$ eV calculation has excellent agreement. Although we have this excellent agreement with the experimental moments of ferromagnetic Ni, our chosen U and J values do result in a higher J/U ratio than in previous paramagnetic (DFT+)DMFT studies (of Hund physics) [6]. Attempting to reduce this ratio by varying J also results in changes to the moments, but we did not find better agreement for both the orbital and spin moments for any other values

	$3d\ m_s(\mu_B)$	remaining $m_s(\mu_B)$	total $m_s(\mu_B)$	$3d\ m_\ell(\mu_B)$
ELK (LSDA)	0.665†	-0.041†	0.624	-
ELK+DMFT	0.591†	-0.037†	0.554	-
ELK(NM)+DMFT	0.365†	0.01†	0.375	-
Experiment	0.667	-0.107	0.560	0.056

Table 5.1: The theoretical and experimental spin $m_s(\mu_B)$ and orbital $m_\ell(\mu_B)$ moments from the $3d$ electrons and the other contributions. The presented ELK-TRIQS DFT+DMFT values are from the $U = 2.0$ eV calculation. The experimental values are from Ref. [266], but these have been corrected using the revised total moment from Ref. [267]. The presented total spin moments were obtained from the FCSC DFT+DMFT outputs. †These theoretical values were determined from the integral of the occupied total and partial $3d$ DOS, given in Eqs. 5.18 and 5.19. Therefore, the theoretical $3d$ electron spin moment is within the muffin-tin (MT) and the remaining spin moment contribution is the difference between the total spin moment and the $3d$ MT spin moment.

of U and J[19]. The revised experimental spin moment value is given in Table 5.1. Also, Table 5.1 gives the moment contributions as present in Ref. [266] (corrected with respect to the revised total moment from Ref. [267]). The theoretical values have been calculated from the occupied DFT(+DMFT) partial and total DOS (from the lattice spectral function). The occupied and partial DOS is the trace over the band indices of the product of the DFT+DMFT density matrix $N^{\mathbf{k},\sigma}_{\nu\nu}$ (the diagonal elements from Eq. 3.74) with the band resolved spectral function. Therefore, the information about the occupations within the DFT+DMFT density matrix is now included in the occupied DOS. The occupied total DOS has the form

$$A^{\mathrm{occ}}(\omega) = \int_{BZ} \mathrm{Tr}_\nu[N^{\mathbf{k}}_{\nu\nu} A_{\nu\nu}(\omega,\mathbf{k})] d\mathbf{k}, \tag{5.18}$$

and the occupied partial DOS is given by

$$A^{\mathrm{occ}}_c(\omega) = \int_{BZ} \mathrm{Tr}_\nu[N^{\mathbf{k}}_{\nu\nu} A_{c,\nu\nu}(\omega,\mathbf{k})] d\mathbf{k}, \tag{5.19}$$

where ν is the eigenstate and c is the orbital character (s, p, d, f, and interstitial). The results from Table 5.1 give an indication on how the addition of DMFT affects these contributions with respect to the experiment. It should be noted that quantitative agreement between the theory and experiment is not expected as there are slight, but noteworthy differences between the theoretical and experimental quantities, such as the $3d$ moment, which will differ as the theoretical value is of the $3d$ moment within the MT, unlike the corresponding experimental quantity (which is the $3d$ moment within the entire cell). However, as the significant contribution to the $3d$ moment is within the MT, the comparison is justifiable. Also, the theoretical values do not include

[19] There is, however, a lower bound for U: $U = J$, below which the system is not physical.

moment contributions from electron currents in the interstitial region, which may be present in the experimental results. However, trends can be established from these results.

From Table 5.1, the magnitude of the $3d$ and other spin moments underestimates the experimental values in DFT. The agreement between the experiment and the ELK+DMFT spin moment contribution values worsens with respect to the DFT results – all of the FCSC ELK+DMFT spin moment contributions have reduced in magnitude. Even though the total spin moment is close to the experimental value for the ELK+DMFT $U = 2.0$ eV calculation, the worsened agreement between spin moment contributions in Table 5.1 suggests that DMFT is missing certain correlations effects. This notion is also reinforced from the ELK(NM)+DMFT moments in Table 5.1, as these results show that the magnetism from only DMFT is insufficient to describe ferromagnetic Ni. The ELK(NM)+DMFT values do not have a negative contribution, as this is likely due to the magnetism being only treated within the correlated $3d$ electrons. The additional small positive "remaining $m_s(\mu_B)$" contribution in these results will likely be from the $3d$ electrons within the interstitial region. The negative contribution to the moment has been attributed to the negative spin polarisation which originates predominantly from the electrons that screen the $3d$ moment. Therefore, the ELK(NM)+DMFT calculation may have insignificant screening contributions which affects the spin moment.

It should be noted that magnetic Compton scattering does not directly provide information concerning the orbital moments, but when combined with a superconducting quantum interference device (SQUID) measurement of the total magnetic moment, the orbital contribution can be inferred [268].

5.3.2 Magnetic Compton profiles

In the KKR(+DMFT), the magnetic Compton profiles are calculated from the spin-resolved momentum density $\rho^\sigma(\mathbf{p})$ which in turn is obtained as a contour integral of the Green's function in the momentum representation [269]:

$$\rho^\sigma(\mathbf{p}) = -\frac{1}{\pi}\int_{-\infty}^{E_F} \mathrm{Im}\, G_\sigma(\mathbf{p},E)\mathrm{d}E. \tag{5.20}$$

In the ELK+DMFT, the electron momentum densities (and the MCPs) are computed through the wave functions and occupation functions across the Brillouin zone on the imaginary frequency axis. The method of obtaining the wave functions and occupation functions in ELK-TRIQS are described in Ref. [23] and Section 3.7. In both methods, the MCPs were calculated within a sphere of radius 16 a.u. ($|\mathbf{p}| \leqslant 16$ a.u.), and then renormalised such that their areas were equal to the corresponding spin magnetic moment.

To analyse the effects of the electron correlations on the MCPs, we calculated MCPs with the DFT+DMFT method for a series of on-site interaction values U and Hund's rule coupling $J = 0.9$ eV by employing both KKR+DMFT and ELK+DMFT. Figure 5.8 shows the Ni MCPs

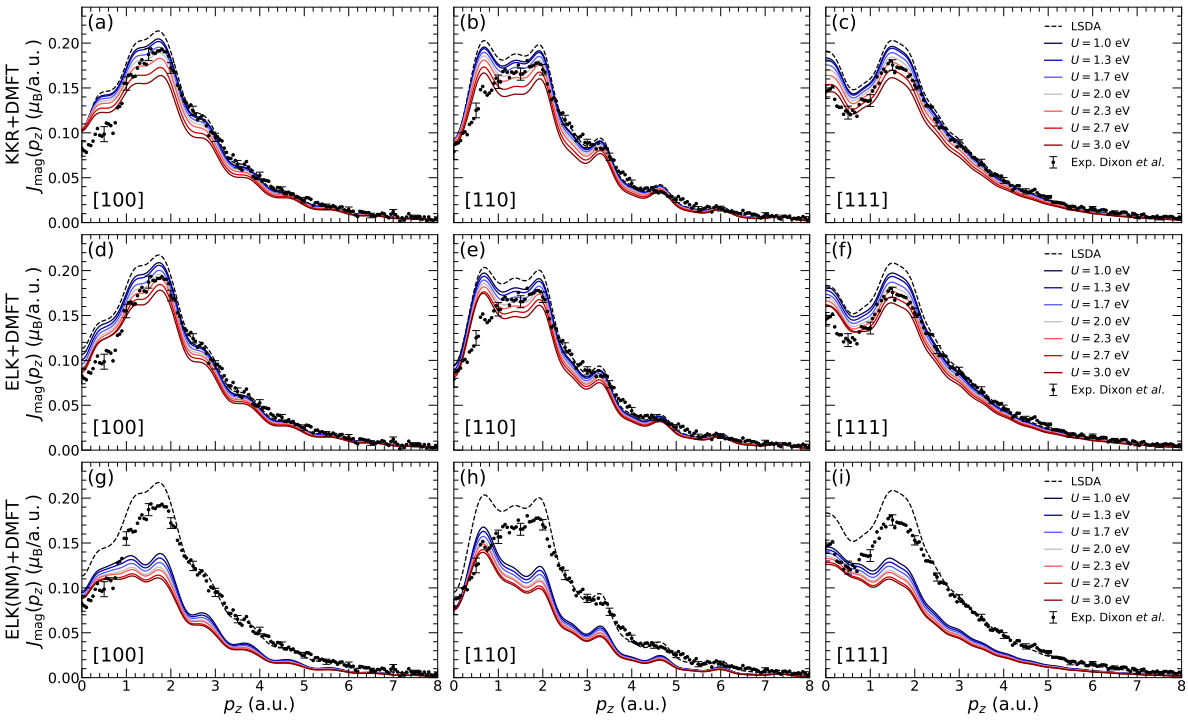

Figure 5.8: The Ni magnetic Compton profiles (MCPs) at [100], [110], and [111] high symmetry directions (indicated on each plot) for several intra-site Coulomb potential U and fixed Hund's rule coupling $J = 0.9$ eV. The KKR+DMFT MCPs results are shown in the (a), (b), and (c) panels (upper row). The ELK+DMFT MCPs are presented in the (d), (e), and (f) panels (middle row). The MCPs from the local spin ELK(NM)+DMFT calculations are shown in panels (g), (h), and (i) (lower row). The areas of each MCP have been normalised to their corresponding spin magnetic moment results given in Fig. 5.7. The DFT+DMFT results are complemented by the (magnetic) LSDA results from the respective ELK and KKR codes (dashed curves) and the experimental measurements from Dixon *et al.* (dots with error bars) [249]. For clarity, the error bars are shown for every tenth data point. The computed results have been convoluted with a Gaussian with a full-width-at-half-maximum (FWHM) of 0.43 a.u. to represent the experimental resolution.

along the cubic high symmetry directions, obtained using the KKR(+DMFT) [Figs. 5.8 (a)-(c)], and the ELK(+DMFT) [Figs. 5.8 (d)-(f)] in the momentum range $0 \leq p_z \leq 8$ a.u.. The MCPs from the ELK(NM)+DMFT calculations [Figs. 5.8 (g)-(i)] show the effect of the missing electrons correlations which are included in the LSDA calculations. The theoretical MCPs have been convoluted with a Gaussian with a full-width-at-half-maximum (FWHM) of 0.43 a.u. to represent the experimental resolution.

Starting with the presented DFT results, the MCPs show good agreement with the experiment for $p_z > 2$ a.u. but these MCPs do not match the low-momentum region for any of these high symmetry directions. Our DFT results are in good agreement with those previously presented in Ref. [249]. The MCP peak structures within the 1BZ are due to the exchange splitting, which in turn causes the majority and minority spin bands to cross the Fermi level at different $\mathbf{k}_F$ values

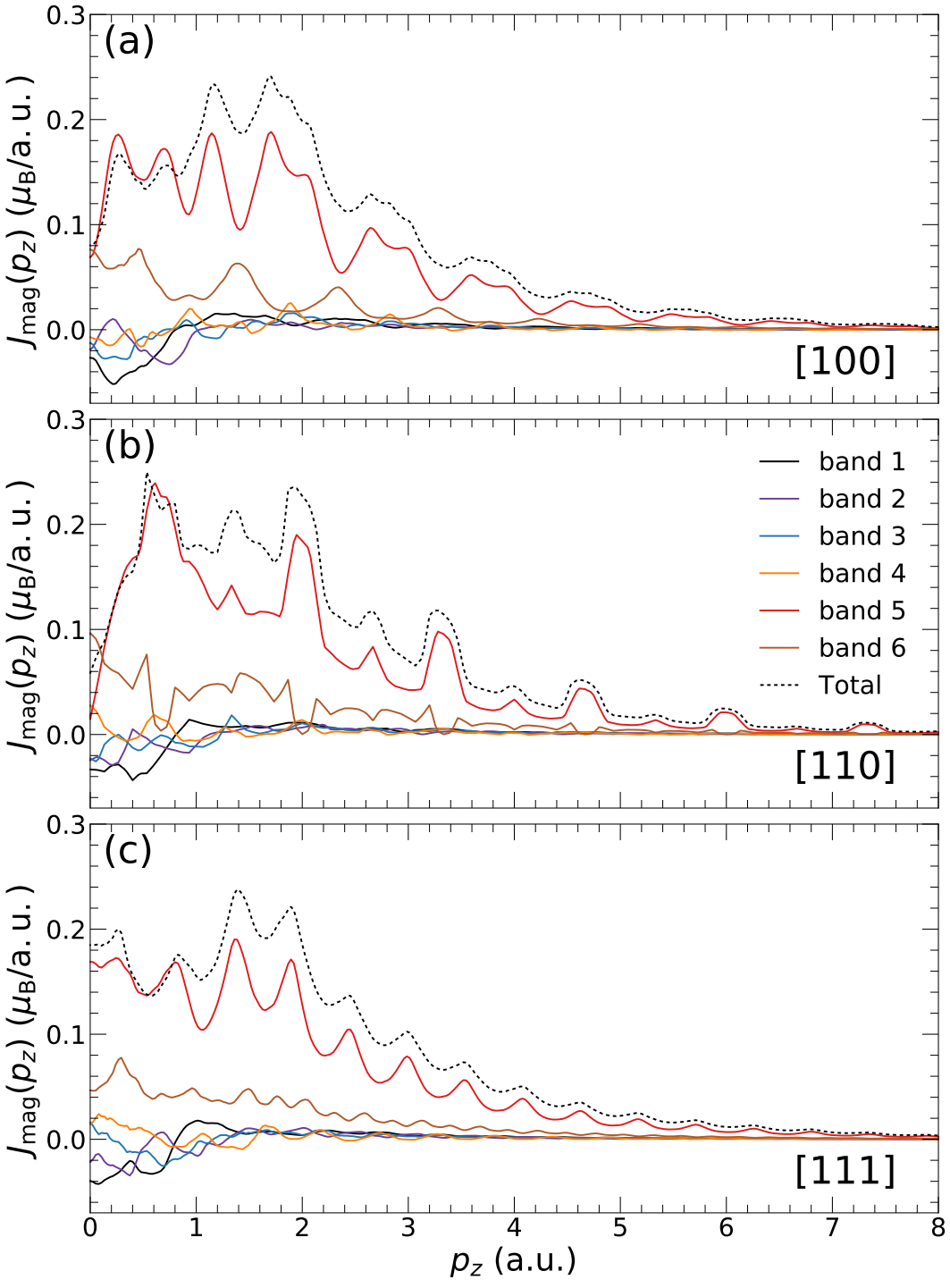

Figure 5.9: The ELK DFT unconvoluted band resolved MCPs for each high symmetry direction ([100], [110], and [111]). The DFT band contributions have been broken down in terms of their indices (using the same numbering as Dixon *et al.* [249]) for discussions about the band resolved MCPs and resemble those of Dixon *et al.*. The profiles have been normalised such that the summed area of the band resolved MCPs are equal to the ELK DFT spin moment.

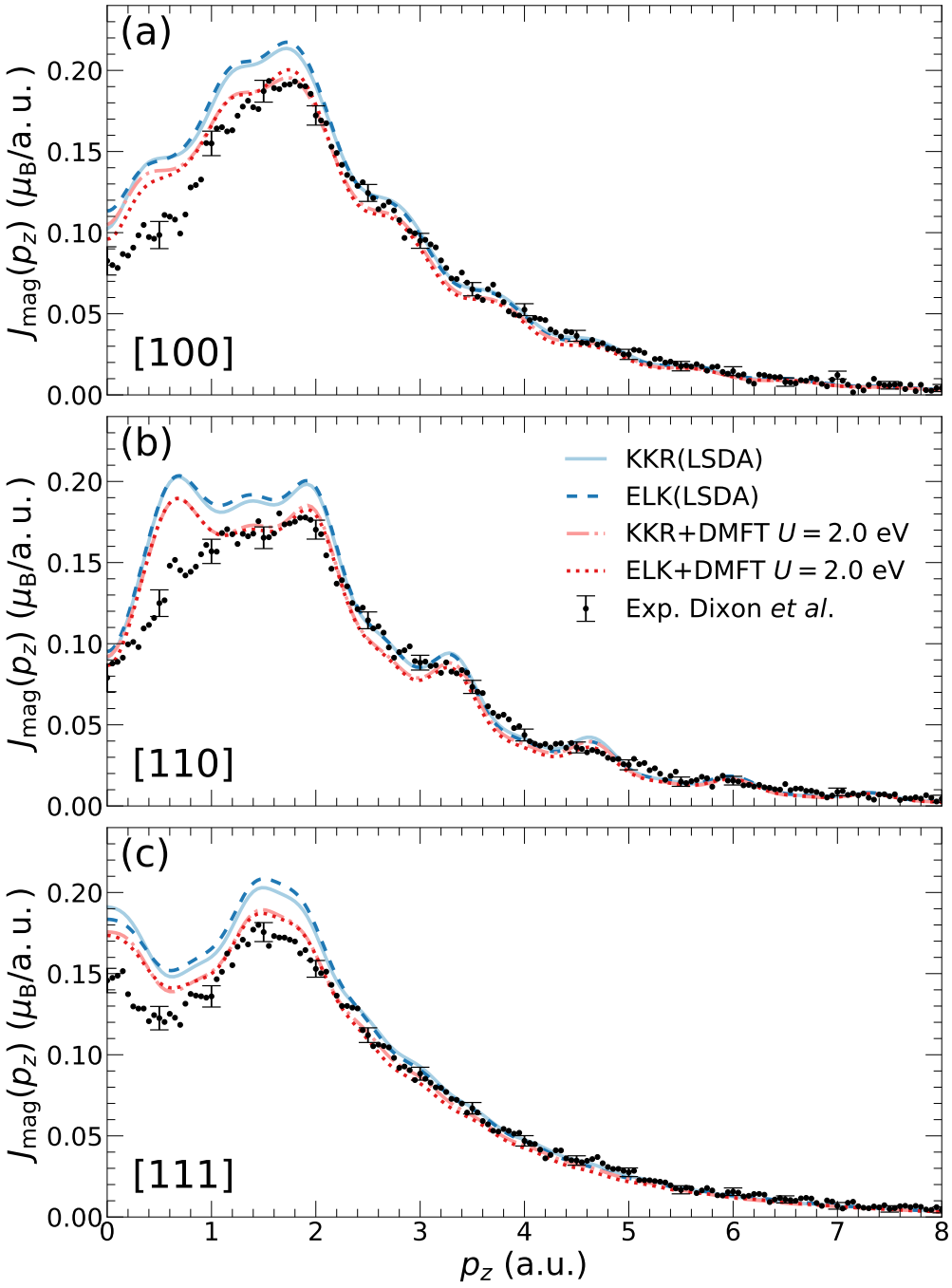

Figure 5.10: The comparison of the experimental Ni magnetic Compton profiles (MCPs) from Dixon *et al.* [249] (dots with error bars) with the DFT results (solid and dashed curves) and the DFT+DMFT results for the chosen $U = 2.0$ eV and $J = 0.9$ eV (dash-dotted and dotted curves). For clarity, the error bars are shown for every tenth data point. The (a), (b) and (c) panels show the MCPs for the [100], [110] and [111] high symmetry directions. The computed results have been convoluted with a Gaussian with a full-width-at-half-maximum (FWHM) of 0.43 a.u. to represent the experimental resolution. The areas of each MCP have been normalised to their corresponding spin magnetic moments given in Fig. 5.7.

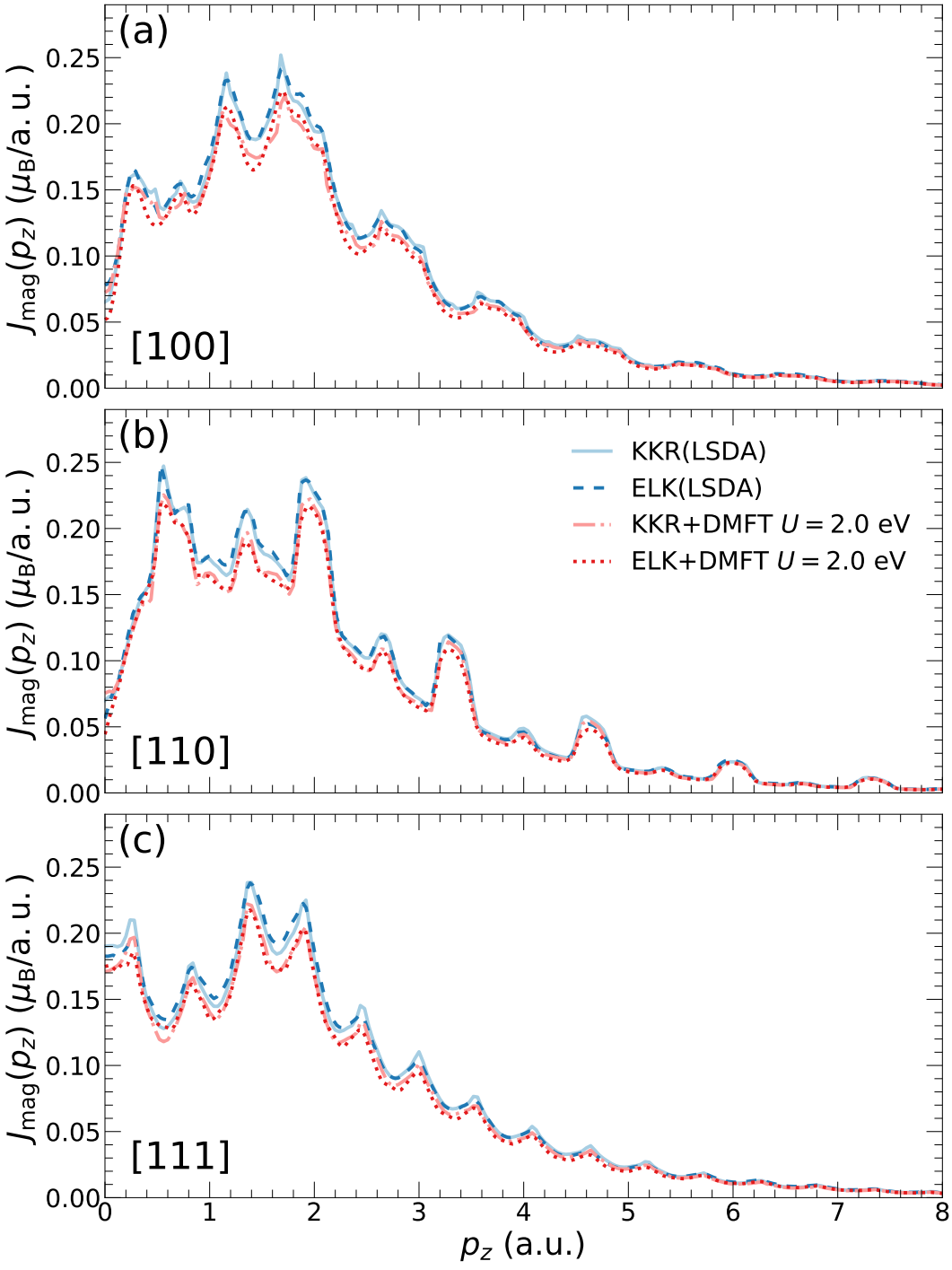

Figure 5.11: The comparison of the unconvoluted high symmetry direction ([100], [110], and [111]) MCPs from the DFT (solid and dashed curves) and the DFT+DMFT with $U = 2.0$ eV, $J = 0.9$ eV (dash-dotted and dotted curves) calculations. The profiles in this figure are the unconvoluted counterparts of the MCPs which are in Fig. 5.10.

(see Fig. 5.9, Fig. 5.11, and Fig. 5.12). This relates to the Fermi breaks discussed in Section 5.1.2. These peaks are periodically repeated in the MCPs as these are the umklapp contributions from higher zones (i.e. $\mathbf{k}+\mathbf{G}$ where $\mathbf{G}$ is the reciprocal lattice vector). One of the advantages of the effective one-particle framework of DFT calculations is the possibility to decompose the total MCP into the contributions originating from individual bands [249–251, 270]. The dip in this low-momentum region has been attributed partly to the contribution of the so-called negative polarisation of the s- and p-like bands with respect to the positive contribution of the d-bands (as seen in Fig. 5.9). At the same time, Refs. [249, 270] note that another source of discrepancy may be due to the d-like fifth band (band numbering according to Ref. [249] and Fig. 5.9), where Ref. [270] attributes the shape of the contribution of this band to the inconsistencies between the theoretical and the true Fermi surface. These interpretations, based on the DFT band structures, raise some interesting unsolved questions about the origin of the discrepancy at low momentum. From the DFT results, the predicted negative polarisation contributions are not sufficient to explain the low momentum dip seen in the experimental results. Dixon *et al.*, Ref. [249], suggested that it was the deficient representation of the d electron correlations in LSDA (and GGA), not just the negative polarisation from the s and p electrons, which was the potential cause for the low momentum experiment-theory disagreement [249]. Artificial shifts of the bands around the Fermi level [271] showed improved agreement with the low momentum MCP region. As correlation effects lead to the shift of those bands naturally, improved theoretical description of the Ni MCPs can be obtained by taking them into account. Recent studies [226–228] also demonstrated that including the local correlations through the DMFT framework reduces the discrepancy between theoretical and experimental MCPs of Ni.

Moving onto the DFT+DMFT results, the large dips near $p_z = 0$ a.u. in the high symmetry directions are better reproduced by the DFT+DMFT MCP for $U > 2.3$ eV. On the other hand, for the high-momentum ($p_z > 2$ a.u.) region, $U < 2.3$ eV is a better choice. Although we are able to produce improved agreement (with respect to the DFT MCPs) with the experiment at low momentum, $p_z < 1$ a.u., DFT+DMFT fails to reproduce the experimental MCP for the [100] and [110] directions [see Fig. 5.8 (a), (d) and (b), (e)]. Along the nearest-neighbour direction [110], no U value was found to suppress the peak at around $p_z = 0.6$ a.u.. Although the general low momentum disagreement is the case for both implementations, there are some notable differences between the ELK+DMFT and KKR+DMFT results. Along [100] direction, $J_{\mathrm{mag}}(p_z)$ for $p_z < 1$ a.u calculated with ELK+DMFT for increasing values of U matches the experimental MCP better than those obtained with KKR+DMFT. The latter visibly overestimates the $J_{\mathrm{mag}}(p_z)$ (by almost the same amount) for all U values considered. The opposite happens for the [111] direction. In this case, $J_{\mathrm{mag}}(p_z)$ obtained with KKR+DMFT matches the experimental values in $p_z \lesssim 2$ a.u. region for $U \geqslant 2.3$ eV, while ELK+DMFT results overestimate the experimental values for $p_z \lesssim 1$ a.u for all considered values of U.

Although in general the low momentum is better described with higher U values (see Fig. 5.8),

the cost of this is the poorer agreement with the experiment from 1 a.u. to about 5 a.u.. This is because the area under the MCP, which is equal to the corresponding spin moment for each U value in Fig. 5.7, reduces with increasing U and is less than the experimental value for $U > 2.0$ eV. Therefore, for the different U values, an improvement in one momentum region of the MCP causes another region to worsen in order to conserve the area.

We did not find a single U value, within the *ab-initio* range of U values, which would simultaneously match both, low- and high-momentum regions of experimental profile within its error. On the other hand, in the previous section, we identified that the DFT+DMFT calculation with $U = 2.0$ eV and $J = 0.9$ eV produces the best match between the calculated and experimental magnetic moment. To see how well the DFT+DMFT MCPs for $U = 2.0$ eV match the experimental MCPs from Ref. [249], and also to compare the results obtained by two different packages and two distinct frameworks, we show the corresponding MCPs in Fig. 5.10. Although the MCPs calculated in the DFT+DMFT framework for $U = 2.0$ eV deviate from the experimental results in the momentum range $0 < p_z < 1$ a.u., extending DFT with the DMFT framework significantly improves the description of the experiment in the range $1 < p_z < 2$ a.u.. For $U = 2.0$ eV, the structure of the MCPs is well reproduced in all three high symmetry directions in this region where the dominant contributions are made. DFT+DMFT results also stay in reasonably good agreement with the experiment for higher values of p_z, from $p_z = 2$ a.u. onwards, but they tend to slightly underestimate the tails, although they are within the experimental error. This is also a consequence of the calculations overestimating the low momentum region.

Overall, dynamic correlations improve the agreement with the experimental data beyond the LSDA results. The results including dynamic correlations also show the correct trend for low momentum region $p_z \lesssim 2$ a.u. where better MCPs are obtained in comparison to the LSDA. LSDA overestimates the MCP values for almost the entire region. As mentioned earlier, since the areas under the MCPs directly equal the spin moment (m_s), the areas reduce with increasing U as per Fig. 5.7. Nevertheless, since DFT+DMFT also overestimates the experimental MCP values in the $p_z \lesssim 1$ a.u. region, the consequence is that the high-momentum region tails are underestimated – after all, the areas beneath the MCP and $U = 2.0$ eV DFT+DMFT curves are almost equal. The current results, however, do not allow us to infer the optimal value for the on-site Coulomb interaction necessary to obtain the best agreement with the experimental measurements. Nevertheless, we see that U values in the range $[1.7, 2.3]$ eV describe the on-site Coulomb interaction reasonably well (almost exactly within the experimental error bars in the $1 \lesssim p_z \lesssim 2$ a.u. range), in agreement with positron annihilation measurements [257]. Similar conclusions have been drawn in previous papers reporting the correlation effects upon the MCP of Ni [226–228].

A direct comparison between the methods can be seen in Fig. 5.11, where we plot the theoretical MCPs which have not been convoluted with the experimental resolution. The results from the two DFT+DMFT implementations are in excellent agreement. Therefore, we are confident that

the effect of the resolution on the MCPs does not hide any glaring disagreements between the implementations.

The ELK(NM)+DMFT MCPs (Figs. 5.8 (g)-(i)) have drastically worse agreement compared with the ELK+DMFT results as the area and shape do not match with the experimental data at all. This strongly indicates that there are vital electron correlations within the ELK+DMFT results which are missing in the ELK(NM)+DMFT calculations. From Table, 5.1, there is no negative moment contribution (originating from the negative spin polarisation) to the spin moment. This explains the vastly different shape of the MCPs at low momentum $p_z \lesssim 1$ a.u. (in which region the DFT band resolved MCPs have negative contributions, as seen in Fig. 5.9). These results indicate that the ELK(NM)+DMFT results are missing the mean-field screening contributions. This screening may have an effect on the magnitude of the $3d$ moment which may explain the discrepancy between the ELK+DMFT and ELK(NM)+DMFT total spin values. However, other electron correlation contributions, such as non-local spin fluctuations and exchange, may also be significant. Because of these missing vital electron correlation contributions, the ELK(NM)+DMFT results were not investigated any further.

Finally, we conclude that neither implementation (ELK+DMFT nor KKR+DMFT) produces results (for all U values) that have a better overall agreement with the experimental data than the other (within the experimental error). The level of experiment-theory agreement between the MCPs from both implementations varies in different regions of momentum. Overall, the results from the two implementations are in good agreement with minor discrepancies due to the aforementioned differences discussed at the beginning of Section 5.3.

5.3.3 Spectral function

Features in the MCPs can be traced back to the form of the spectral function which, for the non-interacting case, is represented by the band structure. Figure 5.12 shows the DFT band structure together with the DFT+DMFT $\mathbf{k}$-resolved spectral function along the high symmetry directions in the BZ from the ELK and ELK+DMFT calculations. In the present DFT calculation, we confirm that the bands 5 and 6 of Fig. 5.12 only give a positive contribution to the MCPs whereas bands 1-4 have negative contributions to the MCPs at low momentum, see Fig. 5.9.

In a many-body picture, however, such a band-resolved interpretation is not possible. The spectral function in Fig. 5.12 shows the QP dispersion. The self-energy affects the two spin channel spectral functions differently. A significant part of the energy dependence of the self-energy is related to the different occupations of the spin-polarised d-states, on which the MCPs are also dependent. Scattering processes involving s electrons may be neglected as the corresponding orbitals are almost completely filled [272].

Within the single-site DMFT approximation, the self-energy matrix is diagonal in the angular momentum representation and is independent of $\mathbf{k}$. It is the orbital dependence of the self-energy

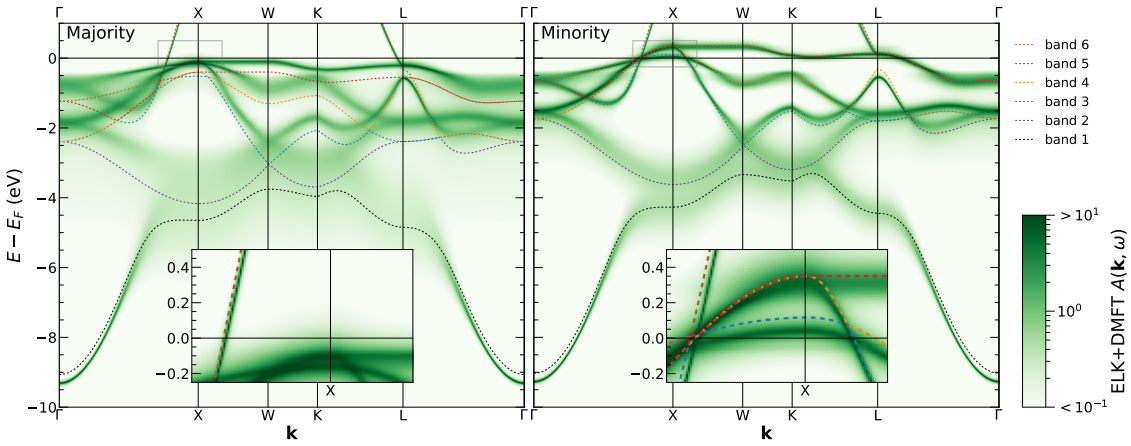

Figure 5.12: The ELK DFT band structure and ELK+DMFT, DFT+DMFT ($U = 2.0$ eV and $J = 0.9$ eV) spectral function for the majority (left) and minority (right) spin. The DFT bands have been broken down in terms of their indices (using the same numbering as Dixon *et al.* [249]) for discussions about the band contributions to the MCPs and resemble those of Dixon *et al.*. The insets are a zoomed image around the X symmetry point (indicated by the grey outline) showing the differences between the theoretical treatments.

that produces a coupling between the terms of the d^8-multiplets[20] [272], where the neglected k-dependence of the self-energy (within the single-site DMFT) amounts to disregarding the hopping processes of the two holes bound to the same Ni-site. The CTHYB impurity solver captures the self-energy contributions relevant for the strong ferromagnetic state such as repeated scattering of paired holes, hole-hole and hole-electron interactions as these processes enter in the fully rotationally invariant formulation of the Hubbard model and parameterised by the U and J parameters [259]. As Ni has a relatively large band width, the atomic multiplet structure is extended in the energy range around -6 eV. Therefore, the expected satellite in our treatment is a broad feature instead. The prominent correlation effect on the DFT+DMFT $\mathbf{k}$-resolved spectral function is to renormalise the position and width of the d-bands and significantly reduce the exchange splitting to about 0.3 eV at the L-point (which we measured as the difference between the majority and minority band centres). These are direct consequences of the presence of the real part of the DMFT self-energy having a negative slope at E_F. These features are in good agreement with experiments [243, 244] and are in line with previous studies [245, 246, 248]. We observe that the crossing of the bands at the Fermi level hardly changes for the majority spin channel (see the left panel in Fig. 5.12). In the minority bands, however, there are subtle changes around the X-point, where two X-hole pockets reside (see the inset in the right panel in Fig. 5.12). These changes are less significant for the MCPs but are relevant in other experiments such as dHvA and ARPES [273, 274]. Previous experiment-theory comparisons [273, 274] have shown that DFT predicts a second shallow minority hole pocket around X. This is referred to as the

[20]Note that in the Bloch basis, the k-dependence of the projectors also provides coupling between the multiplets, but this is likely to be less significant than that of the coupling from the orbital dependence of the self-energy.

minority X_2 hole pocket (related to minority band 3 in Fig. 5.12) but there is no strong evidence of its presence in the experiments. The present DFT+DMFT calculation with $U = 2.0$ eV shows that the size of the minority X_2 hole pocket shrinks and also becomes shallower as compared with the DFT results, but it does not vanish. These may indicate that other correlation effects are required to suppress this band below the Fermi level, or that the large effective mass of X_2 hole pocket due to the shallowness of the corresponding band around X (see the inset in the right panel in Fig. 5.12) might have made its observation more challenging.

Contrary to previous interpretations based on the one-particle description, it is not obvious that the negative polarisation contributions to the MCP (by the s and p electrons) is the cause for the disagreement between the experiment and the DFT and DFT+DMFT computations. The low momentum disagreement is likely the consequence of the other missing correlation effects beyond DFT+DMFT, such as screening. Therefore, these missing correlation effects will likely affect the low momentum contributions from the d electrons, and may influence the s and p negative contributions, to the MCPs. As screening is a genuine many-body effect, it requires methods such as QSGW. Such a calculation for Ni has been performed recently by L. Sponza *et al.* [275]. The QSGW calculation produce an enhanced value for the magnetic moment and exchange splittings. Nonetheless, in supplementing the computations with DMFT in the combined QSGW+DMFT, the values for the magnetic moment and exchange splitting are in good agreement with the experiment. The increased moment in QSGW and its subsequent reduction when including DMFT is intriguing and further investigation into their spin moment contributions, as in Table 5.1, should be explored. The ELK+DMFT and ELK(NM)+DMFT results show how important the screening and potentially other non-local effects are in Ni. Therefore, We expect that a QSGW+DMFT calculations would likely improve the MCPs, as these incorporate the non-local (screening) effects.

5.4 Vanadium

Vanadium is a body-centred cubic (BCC) $3d$ transition metal (with $a = 3.03$ Å [276]) which is a vital component of many correlated systems, for example transition metal oxides such as $SrVO_3$ and VO_2. The element V has three electrons in its $3d$ orbitals, but in oxides it tends to be in the V^{4+} state meaning that there is one electron in the $3d$ orbital. Due to the local nature of the $3d$ orbital, this may result in the electronic structure being a correlated metal or potentially an insulator due to the strong electron correlations.

Like Ni, elemental V is another weakly correlated material and DFT is able to qualitatively match the dHvA [277], ARPES [278, 279], and 2D-ACAR [195, 196, 271, 280–289] measurements. The V DFT Fermi surfaces in Fig. 5.13 reproduce the observed Fermi sheets in the dHvA experiments, but the sizes of corresponding Fermi sheets do not match, which is discussed

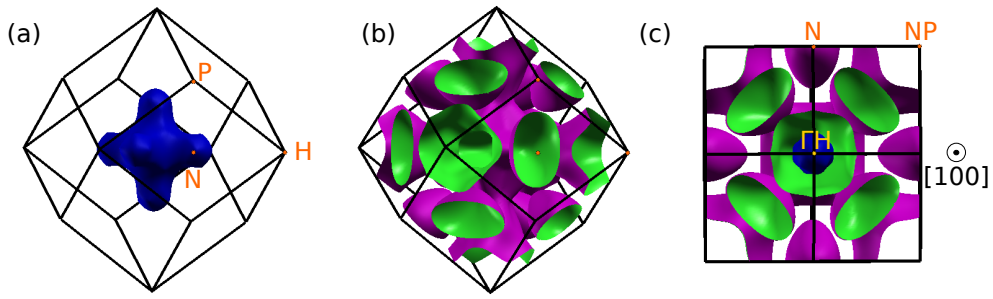

Figure 5.13: The V Fermi surfaces shown within the BCC 1BZ which has the high symmetry points indicated on its boundaries. (a) The octrahedral Fermi sheet around the Γ-point. (b) The hole ellipsoid Fermi sheet which surrounds the N-point and the "jungle gym" hole Fermi sheet which surrounds the Γ and H high symmetry points. (c) All of the V Fermi sheets as viewed along the [100] direction.

in Section 5.4.2. This indicates that there are still missing electron correlations in the DFT calculations. The high-resolution Compton profiles measured by Shiotani *et al.* [217], on the other hand, are significantly different from the corresponding DFT predictions. The large discrepancies between the calculated and measured Compton profiles in Ref. [217] were attributed to the neglected electron correlations in the theory. There has been some success in modelling the effect of the missing electron correlations within previous theoretical studies of V Compton profiles, such as incorporating the Lam-Platzmann correction [290], as well as an empirical Fermi-liquid-like occupation function [219]. In the following sections of this chapter, we show how the inclusion of DMFT changes the experiment-theory agreement of V with regards to the Compton profiles and the directional differences (in Section 5.4.1), as well as the spectral function and its corresponding experimental quantities (in Section 5.4.2).

The ELK DFT calculation used the LDA functional with a 20×20×20 Monkhorst-Pack k-mesh. For the ELK-TRIQS DFT+DMFT calculations, the DMFT cycles used the full rotationally invariant interaction Hamiltonian in the impurity problem which was solved using the CTQMC solver with 2.8×10^8 Monte Carlo sweeps, $\beta = 40$ eV^{-1}, $J = 0.9$ eV, and the AMF double counting term. The J value is the same as that used for Ni (for the reasons discussed in Section 5.3), and it has been used for another V DFT+DMFT study [289]. All five $3d$ orbitals were used in the DMFT cycle, and the corresponding $3d$ Wannier projectors were generated using the eigenstates within the correlated energy window of [-7.00, 5.01] eV. A range of U values, [2.3, 2.6, 3.0, 3.3] eV, were used to determine the profile dependence on the local d correlations. This range was determined from the upper and lower limits of previously used U values [256, 289, 292].

5.4.1 Compton profiles

The Compton profiles were calculated within a sphere of radius 16 a.u. ($|\mathbf{p}| \leqslant 16$ a.u.), and then renormalised such that their areas were equal to the number of valence electrons used by the

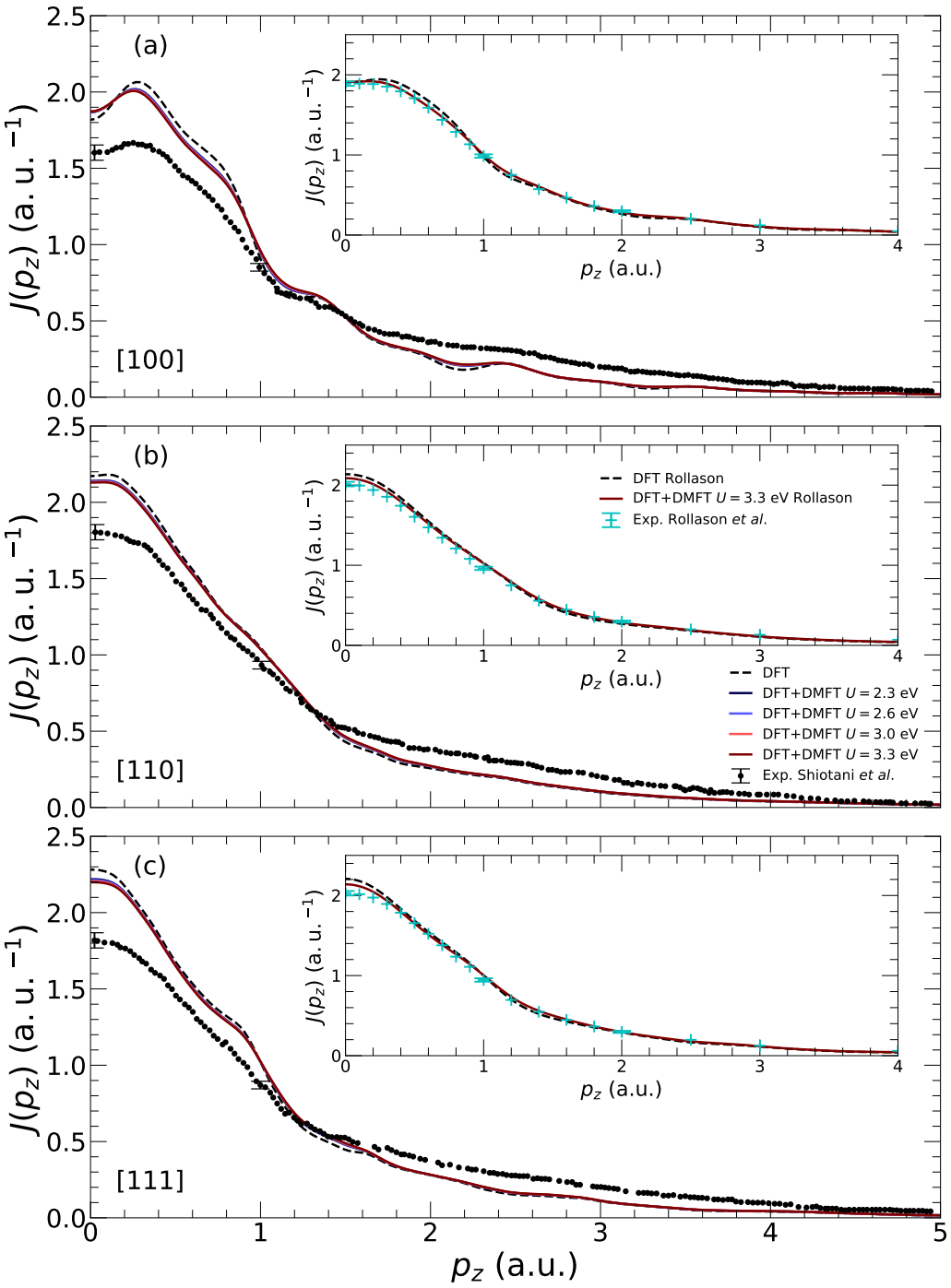

Figure 5.14: The theoretical (DFT and DFT+DMFT with several intra-site U values) and Shiotani experimental [217] Compton profiles along the (a) [100], (b) [110], and (c) [111] high symmetry directions. The theoretical Compton profiles have been convoluted with a Gaussian with a full-width-at-half-maximum (FWHM) of 0.12 a.u. to represent the Shiotani experimental resolution. The inset panels for each high symmetry direction show the comparisons of the corresponding theoretical Compton profiles to the older Rollason data [291]. The theoretical Compton profiles in the insets have been convoluted with a Gaussian with a FWHM of 0.40 a.u. to represent the Rollason experimental resolution.

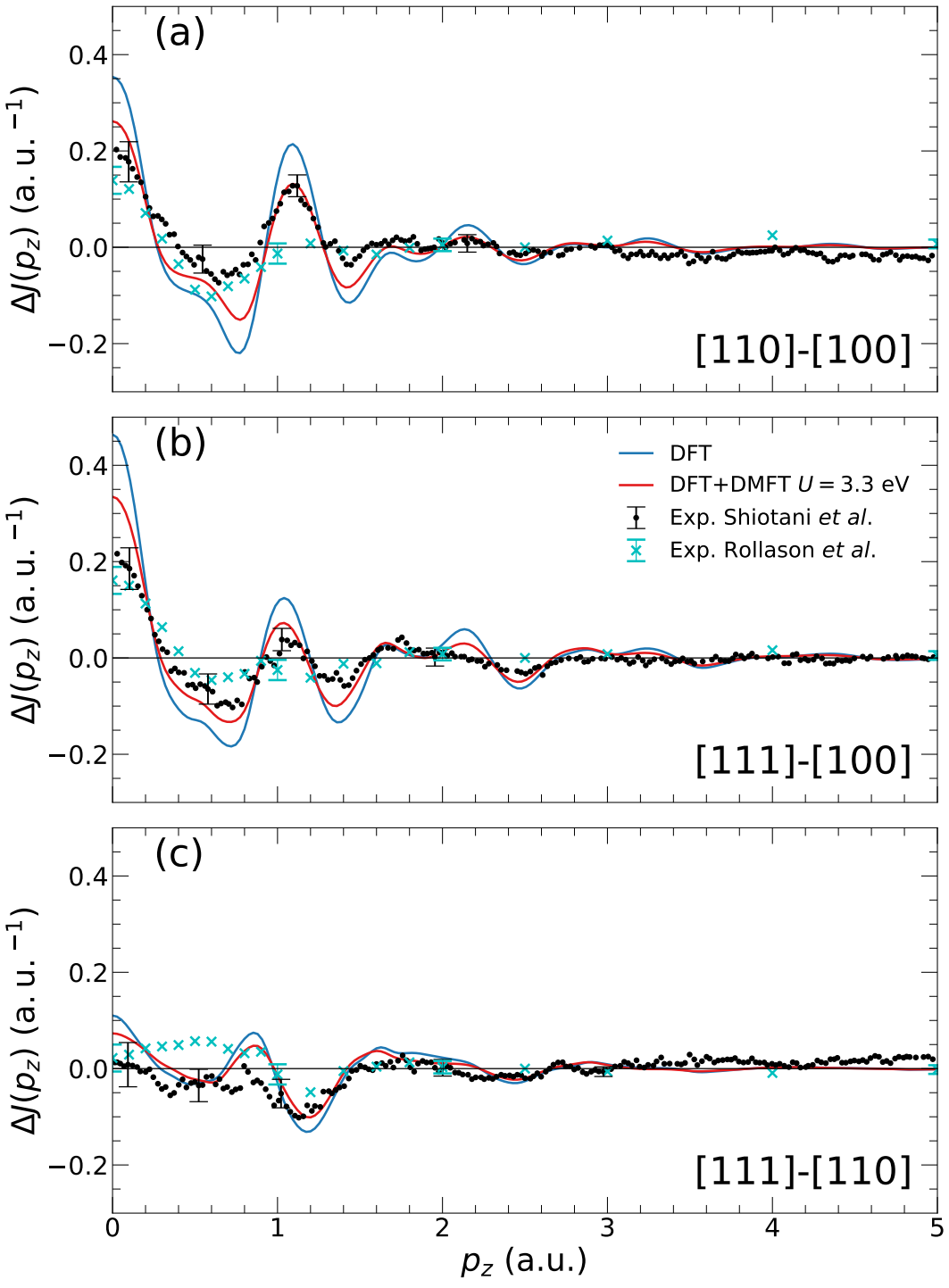

Figure 5.15: The theoretical (DFT and DFT+DMFT $U = 3.3$ eV) and experimental high symmetry directional differences of (a) [110]-[100], (b) [111]-[100], and (c) [111]-[110]. Both the Shoitani [217] and Rollason [291] experimental data have been plotted for each directional difference. The theoretical profiles have been convoluted with a Gaussian with a full-width-at-half-maximum (FWHM) of 0.12 a.u. to represent the Shiotani experimental resolution.

DFT(+DMFT) calculations. The HF Compton profiles were calculated and used to remove the isotropic semi-core states from the DFT(+DMFT) Compton profiles. This has to be done in this way as the DFT+DMFT calculations no longer have "band indices" as in DFT, meaning that a band resolved DFT+DMFT EMD is not possible. This HF Compton profile subtraction results in the theoretical and experimental valence Compton profiles relating to the same five valence electrons. Therefore, the resulting theoretical Compton profiles are normalised to the five valence electrons.

Figure 5.14 shows the Compton profiles along the high symmetry directions for the DFT and DFT+DMFT calculations as well as the experimental data of Shiotani *et al.* [217][21]. The calculated Compton profiles have been convoluted with a Gaussian with a FWHM of 0.12 a.u. to represent the experimental resolution. Firstly, our DFT Compton profiles and directional differences in Figs. 5.14 and 5.15 are in good agreement with the theoretical Compton profiles and directional differences presented in Ref. [217]. The DFT+DMFT Compton profiles have very weak dependence on U for the range of U values presented. However, there are significant changes to the Compton profiles when including DMFT compared with the DFT results. The results from the DFT+DMFT $U = 3.3$ eV calculation will be used from this point onwards as this U value agrees with previous *ab initio* results [256].

Shiotani *et al.* [217] suggested that the poor agreement between the theoretical and experimental Compton profiles, shown in Fig. 5.14, was due to the missing electron correlations in the exchange-correlation functional used in the DFT calculation. This is indeed plausible because the electron correlations produce the Fermi-liquid-like occupation function which suppresses the profile height at low momentum, as shown in Section 5.1.2. The DFT+DMFT Compton profiles changed in the way one would expect when using the Fermi-liquid-like occupation function from DMFT, but the magnitude has not been sufficiently altered to be in agreement with the Shiotani results. However, the insets of Fig. 5.14 show that the theoretical Compton profiles, especially the DFT+DMFT Compton profiles, have better agreement with the older, lower resolution Compton data measured using γ-radiation (in the laboratory) by Rollason *et al.* [291][22]. (These theoretical Compton profiles in the insets were convoluted with a Gaussian with an FWHM of 0.40 a.u. to represent the Rollason experimental resolution.) This is concerning as the difference in both sets of experimental Compton profiles is greater than can be explained by the difference in the resolution.

Interestingly, the theoretical directional differences have better agreement with the Shiotani experimental directional differences than the Rollason data in Fig. 5.15. However, there are some problems with the Shiotani directional differences highlighted by the fact that the high momentum region of the directional differences in Fig. 5.15 (a) and Fig. 5.15 (c) is not (approximately) zero. These differences should be zero within this region as this is where the profiles become

[21] This experiment used a synchrotron as the source of the X-rays.

[22] The Rollason Compton profiles in Ref. [291] were of all of the electrons. The Rollason profiles presented in this section are from the tabulated data in Ref. [291] with their core contributions removed.

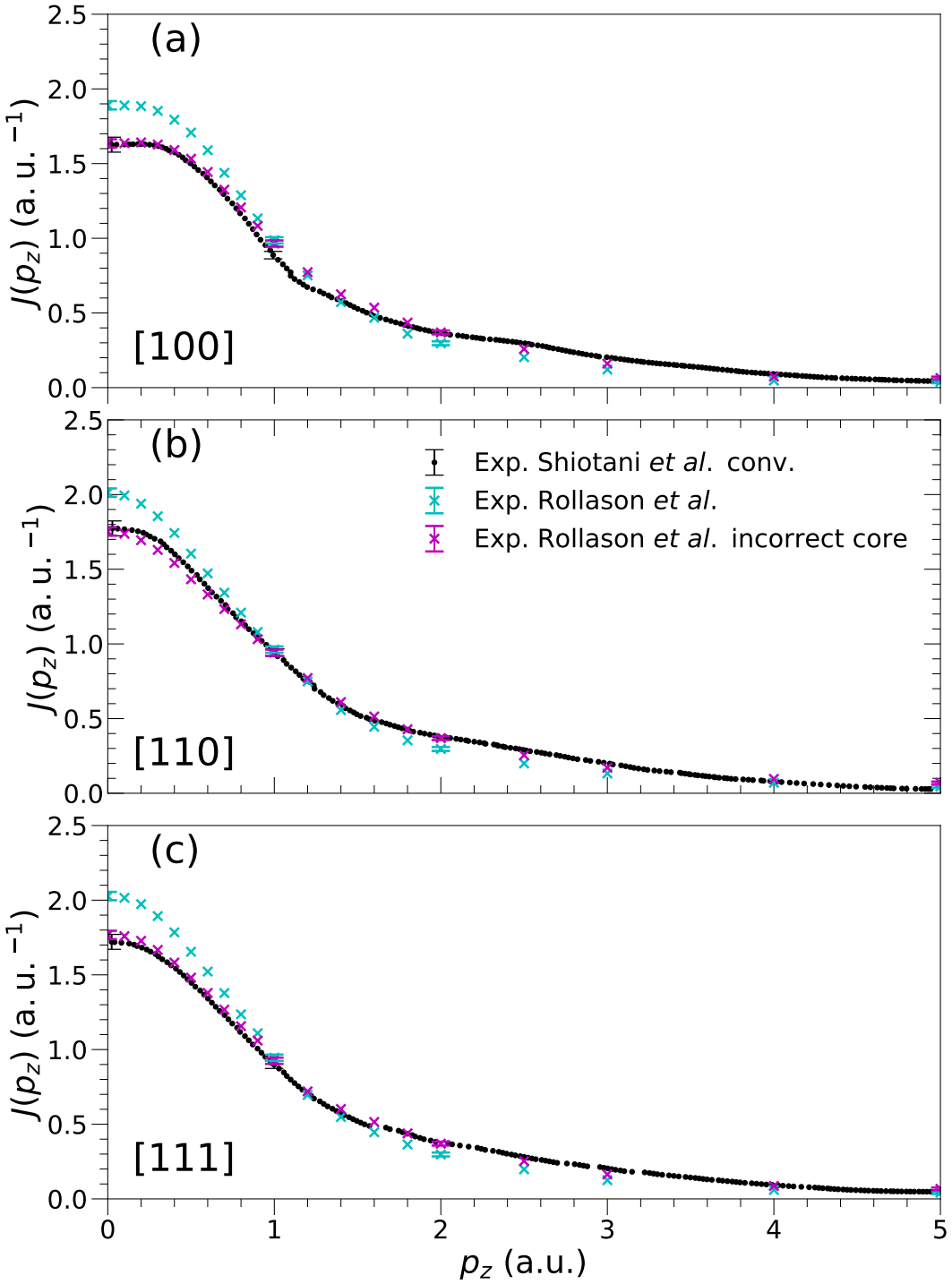

Figure 5.16: The valence Compton profiles of (a) [100], (b) [110], and (c) [111] from the Shoitani [217] and Rollason [291] experimental data. For comparison, the Shiotani data was convoluted by an additional Gaussian to simulate data with a broader 0.40 a.u. experimental resolution. There are two plots of the Rollason valence Compton profiles, one from the removal of the correct core profile (cyan) and the other is from using an incorrect core Compton profile (magenta), for reasons explained in the main text.

isotropic and HF-like (see Section 5.1.3.1). As the high momentum region of the directional differences in Fig. 5.15 (b) is approximately zero, this suggests that there is a problem with the high momentum tail of the [110] Compton profile. Therefore, the consequence of getting the correct behaviour in the high momentum region of the directional differences [for Figs. 5.15 (a) and (c)] may cause the corresponding low momentum region to be slightly shifted (upwards for [111]-[110] and downwards for [110]-[100]), which would improve the experiment-theory agreement. On the other hand, the theoretical directional differences have fairly poor agreement with the corresponding Rollason experimental data. Note that in Ref. [291], the Rollason directional differences were only shown up to 3 a.u., whereas we present their experimental data up to 5 a.u. in Fig. 5.15 (using the tabulated data in Ref. [291]). As the data in the high momentum region is sparse, this makes it difficult to ensure that these directional differences have converged to zero here. An incorrect shape in the high momentum region would affect the low momentum shape of the directional differences[23]. However, these issues have less impact on the measured Rollason Compton profiles (although they are important to resolve when doing the data analysis). Consequently, this means that the Rollason directional differences are less reliable than their Compton profiles. However, the problems in these directional differences should be easier to manage when doing the data analysis on the Shoitani Compton profiles, as this data has good momentum resolution.

The question is: how are the Shiotani Compton profiles so different, but yet the comparisons of the directional differences with the theory look fairly reasonable? The most likely explanation is that these differences are due to the image plate Shiotani *et al.* used, which had no energy resolution meaning that the authors had to approach the data analysis differently to that described in Section 5.1.3.1. Only the Compton scattered X-rays which satisfied Bragg's law[24] were properly analysed with respect to the photon energy [217]. The authors stated that the background noise was the most difficult to determine. Therefore, the error may have occurred when they accounted for the background, which involved using the HF core Compton profile (calculated from Ref. [233]), within their data analysis. Consequently, we are going to assume that the HF core Compton profile was treated incorrectly in the Shiotani data analysis to see if we can obtain their skewed Compton profile shape from the Rollason data. The core and valence Compton profiles should be describing the 18 core electrons and the 5 valence electrons (per unit cell). It is possible that certain electron orbitals were unintentionally treated as core, resulting in an incorrect core Compton profile. This incorrect core Compton profile would then be removed from the total Compton profile and the remaining incorrect valence Compton profile appears to have been renormalised to the expected 5 valence electrons (per unit cell). As this process involves an isotropic removal, the anisotropic parts of the Compton profile remain to give good experimental-theory agreement with the directional differences, whilst also giving poor looking

[23] This is a consequence of the area conservation of the Compton profile. As the area is fixed, any changes to the high momentum region during the data analysis will be compensated in the other momentum regions.

[24] $2d\sin(\theta) = n\lambda$

valence Compton profiles. This scenario is shown in Fig. 5.16 and it explains the skewed shape seen in the Shiotani Compton profiles. Fig. 5.16 shows the core Compton profile removal of the total Rollason Compton profile with the correct HF core Compton profile and an incorrect one. The core Compton profile is constructed from the HF Compton profiles of each (occupied) orbital from the tabulated results in Ref. [233]. The correct core Compton profile is constructed from the HF Compton profile contributions of the occupied $1s^2 2s^2 2p^6 3s^2 3p^6$ orbitals, and this core Compton profile is normalised to the correct 18 core electrons (per unit cell). However, using an incorrect core Compton profile composed of HF Compton profiles from the incorrectly occupied $1s^2 2s^2 2p^5 3s^3 3p^5$ orbitals, but normalised to the correct 18 core electrons (per unit cell), is able to reproduce the (convoluted[25]) Shiotani valence Compton profile. Note that this incorrect Compton profile is not necessarily the core Compton profile used by Shiotani *et al.* during their data analysis, but it illustrates that there is potentially an issue with these Shiotani valence Compton profiles, which may have occurred due to an incorrect core Compton profile subtraction process or any other incorrect treatment/removal of the isotropic part of the Compton profile in the data analysis. Unfortunately, it is not easy to check whether they used the wrong HF core Compton profile without having the total Compton profile data from the Shiotani experiment (i.e. the Compton profile prior to the core subtraction). To be sure, the V Compton profiles should be remeasured, at least for the high symmetry directions.

If the skewed shape of the Shiotani Compton profiles is due to the core subtraction (or any other isotropic treatment) issues, then the directional differences are fairly reliable (except for the other issues discussed previously). Therefore, the DFT+DMFT directional differences in Fig. 5.15 show improved agreement with the Shiotani data with respect to the corresponding DFT results. The magnitude of the DFT+DMFT directional differences have reduced by up to a factor of a half in certain momentum regions, bringing them into better correspondence with the data. These results are consistent with Ref. [294] which showed the important role local (atomic) correlations from the $3d$ states (which results in a modification of the occupation function) have in the $3d$ transition metals. On the other hand, the shape of the directional differences pretty much remains unchanged compared with the DFT, which relates to only minor changes to the Fermi surface, at least within the Compton experimental error (the effect of the bands and Fermi surface on the EMD is discussed in Section 5.1.2).

For further analysis, the V Compton profiles should to be remeasured to resolve the possible issues with the experimental data. With the current setup of Compton scattering measurements at SPring-8, the measurement of the high symmetry directions should not be too difficult or time consuming to do. As all of the electrons contribute to the Compton scattering measurement, there are only 5 out of the 23 electrons – this equates to 5/23 of the measured signal – in which we would

[25]The Shiotani data here was convoluted by a Gaussian to simulate data with a 0.40 a.u. experimental resolution, so that it can be compared more easily with the Rollason data. This simulated data approximation is possible from the successive convolution of two Gaussians being the same as the convolution with a single Gaussian of a different width (see Ref. [293] for further details).

interested in. Also, using large single crystals will mean that a larger X-ray beam can be used which will result in a greater measured count rate of the Compton spectra. Therefore, to get high quality high symmetry data for V (with comparable resolution as quoted in the Shiotani data) may take only one day of beamtime at SPring-8. This experiment proposal could be extended to extract the 3D EMD by reconstruction done by measuring the Compton profiles along certain special directions (see Ref. [18] for further information on this technique). This could mean that about a dozen Compton profiles may be measured to extract the 3D EMD, which then would be used to determine the occupation density by using the Lock-Crisp-West (LCW) method [295]. This measured occupation density would give another excellent insight into the manifestations of the many-body interactions. Similar 2D-ACAR studies have investigated the many-body electron-positron correlations effects from the measured two-photon momentum density (TPMD) and 2D projected electron-positron occupation density (see, for example Refs. [284, 285]). However, there have been little to no notable V experimental studies of the 2D/3D EMD or occupancy density.

Overall, although there are questions about the reliability of the experimental Compton data, it appears that the DMFT self-energy causes the occupation function to improve the isotropic and anisotropic distribution of the EMD, which subsequently affects, and indeed improves, the Compton experiment-theory comparison. However, the DFT+DMFT wave functions may have also contributed to the improvements, but as the occupation function implicitly depends on the wave functions, it is difficult to decouple the contributions these quantities have to the EMD.

5.4.2 Spectral function

As seen with the Ni results, changes to the Compton profiles are related to the spectral function, so looking into the spectral function addresses whether there are any significant changes at the Fermi level. It is also important to investigate the spectral function with the corresponding experimental quantities to determine whether the inclusion of DMFT has improved these experiment-theory comparisons. Fig. 5.17 compares the total DOS from the DFT and DFT+DMFT calculations, and it is evident from this that the DMFT has significantly renormalised the d band widths and smeared the spectral weight (as a consequence of the DMFT lifetime). The noise in the DFT+DMFT spectral function between [-6, -4] eV is due to the s bands having little smearing contributions from the DMFT self-energy[26]. The effect of the occupation function on the occupied total DOS, in the inset of Fig. 5.17, gives a visual indication on which eigenstates contribute (and the magnitude of their contribution), above and below the Fermi level, to the EMD calculations from the different theories.

The DFT band character plot in Fig. 5.18 (a) shows that the bands around the Fermi level are predominantly d in character apart from around the N-point (which is more p in character). It should be noted that the inclusion of DMFT, in Fig. 5.18 (b), only causes minor changes to

[26]Currently in TRIQS, this type of noise can only be reduced by either having a denser k-mesh or using a larger artificial imaginary part in the Green's function.

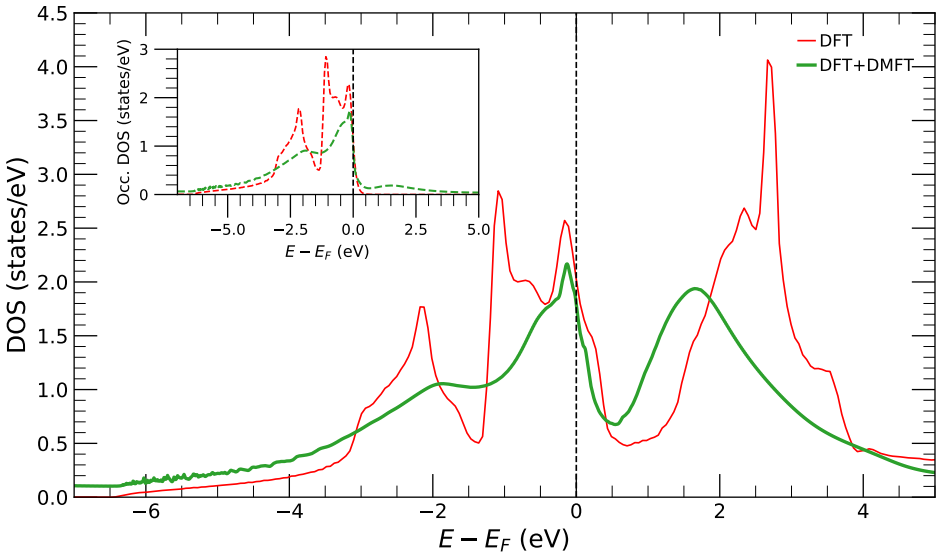

Figure 5.17: The total density of states (DOS) from the DFT and DFT+DMFT (U = 3.3 eV) calculations shown within the [-7, 5] eV energy range with respect to the Fermi energy. The inset is the occupied total DOS calculated by including the occupation function in Eq. 5.18. The DOS BZ integral was evaluated with a denser k-mesh of 40×40×40.

the bands around the N-point in the DFT+DMFT k-resolved spectral function, as these bands contain little contribution from the correlated d electrons. The smearing and renormalisation effect from DMFT within the DFT+DMFT spectral function is more visible in Fig. 5.18 (b). This renormalisation causes the DFT+DMFT k-resolved spectral function to be in excellent agreement with the ARPES and KRIPES experimental data [278, 279]. There are only minor changes at the Fermi level shown in Fig. 5.18 (b). This confirms that little change has happened to the Fermi surfaces from DFT to DFT+DMFT, and these changes appear to be too small to affect the Compton profiles. This reinforces the notion that the improvement in the Compton experiment-theory agreement using DFT+DMFT is more likely coming from the correlated occupation function than changes to the Fermi surface.

On the other hand, more sensitive information about the Fermi surface can be obtained by looking at the V dHvA data reported in Ref. [277]. The comparison of the N hole ellipsoid Fermi surface pocket dHvA data with the theory is given in Table 5.2. We see that the agreement between the theory and experiment worsens when DMFT is included for the NΓ and NP calipers (dimensions). However, The NH caliper does not change between the DFT and DFT+DMFT calculations. This worsened agreement is likely a consequence of the bands shifting at the Fermi level, which is caused by the inclusion of the real-part of the self-energy and the double counting used. A potential problem with DFT+DMFT calculations is the double counting approximation. As the true double counting is not known, the commonly used approximations may lead to incorrect shifts of the bands in the spectral function, which the dHvA would be sensitive to. The AMF

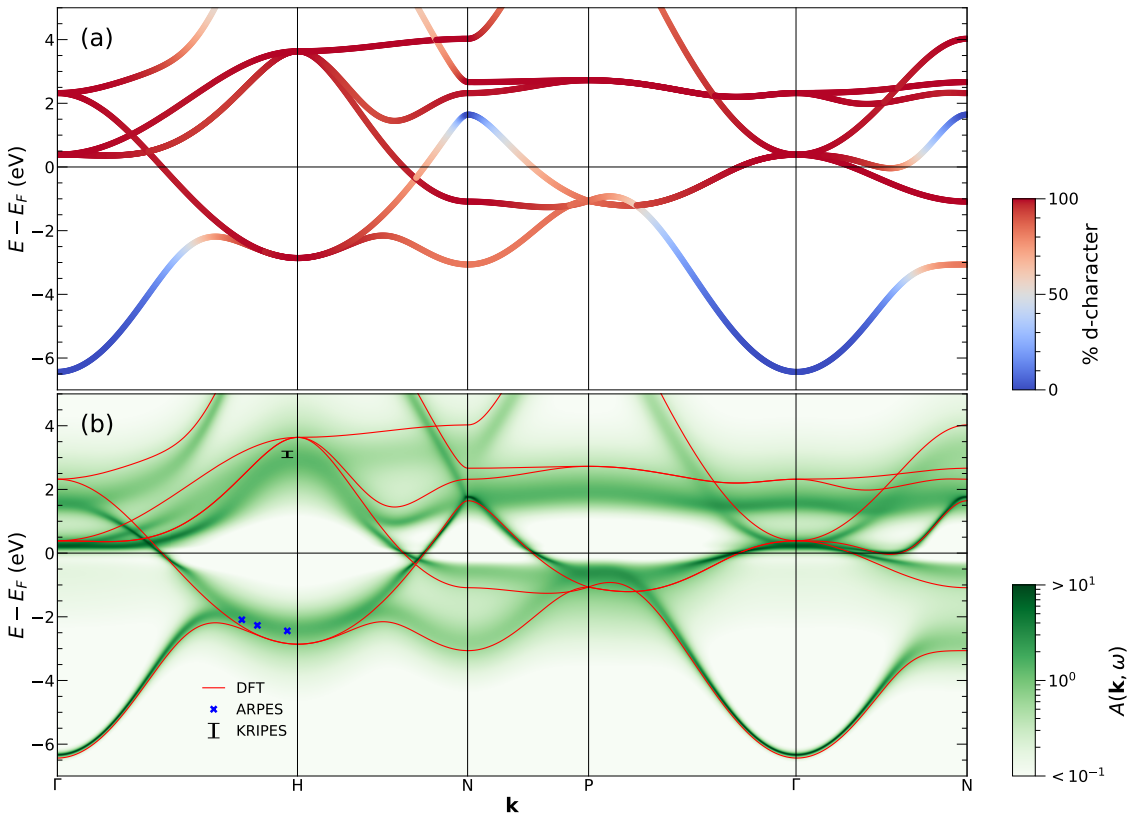

Figure 5.18: The V (a) DFT d band character plot and (b) DFT band structure and DFT+DMFT (U = 3.3 eV) k-resolved spectral function [A($\mathbf{k}$, ω)] plot. Both plots are within the [-7, 5] eV energy range with respect to the Fermi energy. The ARPES [278] and KRIPES [279] experimental data have also been plotted in (b).

double counting approximation is more appropriate to use than FLL for V as the total occupation of the V d orbitals is not an integer. This double counting problem can only be truly resolved by using the exact double counting which is still unknown. It should be noted that these DFT+DMFT N hole ellipsoid Fermi surface pocket caliper sizes are different compared with the DFT+DMFT results by Ref. [289]. This is likely due to the different solver and double counting used in those calculations. On the other hand, the N hole ellipsoid Fermi surface pocket is not truly an ellipsoid, but it is close to being one. This hole Fermi surface sheet was *approximated* as an ellipsoid in the dHvA data by Ref. [277] in order to determine the quoted dHvA caliper sizes in Table 5.2. Therefore, this approximation may have introduced errors in the reported dHvA values, but this is unlikely to fully account for the discrepancy between the experiment and theory.

The V dHvA experiment [277] also extracted the mass enhancements (m^*/m) of the N hole ellipsoid Fermi surface pocket along [100] and [110], which were 2.05 and 2.4 (with respect to their DFT (APW) mass) respectively. This enhancement was attributed to the phonon enhancement (equal to $1+\lambda$, where λ is the electron-phonon coupling constant) of the bare electrons, but this only enhances the mass by a factor of 1.6 as reported by Refs. [277, 296]. However, the experimental

	DFT	DFT+DMFT (U=3.3 eV)	Experimental
NΓ (Å^{-1})	0.57	0.60	0.4405
NH (Å^{-1})	0.37	0.37	0.3649
NP (Å^{-1})	0.56	0.57	0.4632

Table 5.2: The N hole ellipsoid Fermi surface pocket calipers (dimensions). The calculations are compared with the quoted experimental (dHvA) calipers in Ref. [277]. Due to the finite lifetime in the DFT+DMFT spectral function, there is an error associated to the quoted values. Therefore, the DFT and DFT+DMFT values have been quoted to a resolution of 0.01 Å^{-1} (which is approximately the error in the DFT+DMFT values).

value of λ from specific heat measurements by Ref. [297] showed that $\lambda = 1.0 \pm 0.2$, which therefore means that the phonon enhancement is actually 2.0 ± 0.2. This may account for the N hole ellipsoid Fermi surface pocket enhancement along [100], but this still too small for the [110] value. This may mean that the discrepancy in the mass enhancement may be due to the electron correlations. The mass enhancement due to electron correlations from DMFT can be determined from the QP residue Z, which itself is related to the DMFT Matsubara self-energy by

$$Z = \left(1 - \frac{\partial \mathrm{Im}[\Sigma(\mathrm{i}\omega_n)]}{\partial \mathrm{i}\omega_n}\Big|_{\mathrm{i}\omega_n \to 0^+}\right)^{-1}, \tag{5.21}$$

where the Z is evaluated from the differential of the imaginary part of the Matsubara self-energy at $\mathrm{i}\omega_n \to 0^+$ (close to the Fermi level). Then, from this, $m^*/m = Z^{-1}$ (for the $\mathbf{k}$-independent self-energy, as introduced in Section 2.3). Calculating the QP residue on the Matsubara axis means that this will not suffer from any potential analytic continuation difficulties. The mass enhancements due to DMFT correlations in the Wannier t_{2g} and e_g orbitals are 1.72 and 1.41, respectfully. Therefore, the mass enhancement range, including the phonon enhancement, is between $1.8 \leq m^*/m \leq 3.8$ (by taking the lower limit of the experimental phonon enhancement for the lower bound and multiplying the higher experimental phonon enhancement value with the larger DMFT electron correlation enhancement factor to estimate the upper bound). This is a crude estimate of the enhancement as there are factors which have not been consider, such as the band character for the bands around the N-point [which will have changed in the DFT+DMFT calculation compared with the band character plot in Fig. 5.18 (a)]. The important message from this estimate is that (DMFT) electron correlations are needed for a better agreement of the mass enhancement between the experiment and theory.

Theories which treat s and p (and non-local) electron correlations beyond DFT+DMFT (such as GW, GW+DMFT, and so on) should affect the bands around the N-point more significantly, which will likely lead to other changes in the Compton profiles and directional differences. Hopefully, using these theories will help reduce the other discrepancies prominent in the directional differences. The sizes of the N hole ellipsoid Fermi surface pocket improve when including these missing s and p (and non-local) electron correlations from one-shot GW, QSGW, and the SCAN

functional [298]. Also, including these missing electron correlations should bring the aforementioned theoretical mass enhancement range in line with the experimental values when accounting for the band characters. Therefore, the Compton profiles (and the other quantities discussed in this section) should be investigated with these theories, as well as with other techniques such as QSGW+DMFT if the double counting could be better accounted for in V.

5.5 Conclusions

This chapter has shown DFT+DMFT EMD calculations using the ELK-TRIQS interface. Both Ni and V calculations were used to benchmark the DFT+DMFT EMD code, along with investigating the effect of DMFT on the EMDs and spectral functions within these weakly correlated materials.

For Ni, the DFT+DMFT spin moment calculations have the same U dependence in both ELK+DMFT and KKR+DMFT, with the slight difference in magnitude likely being due to the details of the implementations. Although the spin moment improves to be comparable with the experimental value, the shape of the MCP has a weak U dependence. Features in the profile, such as umklapp peaks, remain relatively unchanged and only the MCP contributions are redistributed compared with the calculated DFT profiles. For the $U = 2.0$ eV calculation, which reproduces the experimental spin (and total) magnetic moments, the corresponding spectral function reveals that the minority X_2 pocket shrinks and gets shallower with respect to the DFT calculations, but nevertheless still survives. This small X_2 pocket could have a large effective mass and this may explain why it was not observed in the dHvA experiment. According to our combined DFT+DMFT approaches, some arguments in previous DFT studies built upon the existence of negative polarisation description [250, 251] are not sufficient to explain the discrepancy between the theoretical and experimental MCP and low-momentum region. Instead, theories including a non-local description of interaction and retardation effects (i.e., energy-dependent screening) such as cluster-DMFT, GW (QSGW), and beyond might be more suitable to deliver a better description of the MCP in ferromagnetic metals such as Ni. To truly resolve the intricacies which may arise between the aforementioned theoretical frameworks, it would be essential to remeasure the Ni MCPs with a higher resolution. This will lead to a further valuable understanding of the many-body ground-state properties probed in momentum space.

The DFT and DFT+DMFT Compton profiles were also calculated for V. There is little dependence of the Compton profiles on the different U values used, but the DMFT reduces the magnitude of the Compton profiles and directional differences to be more inline with the experimental data [217, 291]. This reduction is likely a consequence of the improved description of the occupation function calculated in the DFT+DMFT compared with the DFT. There are concerns with the Shiotani Compton profile data as shown with the comparison with the older Rollason data. The issues with the experimental Compton profiles can only be truly resolved by remeasuring them. Ideally, the 3D EMD should also be extracted (by 3D reconstruction methods),

as this will give desirable information about the electron occupation density. Our $U = 3.3$ eV DFT+DMFT spectral function has excellent agreement with the ARPES and KRIPES data along with improved mass enhancements around the N hole ellipsoid Fermi surface pockets. There are small changes to the Fermi surface when including DMFT, but these changes worsened the theoretical agreement with the dHvA data. This could be a consequence of not using the true double counting. However, these N hole ellipsoid Fermi surface pocket caliper sizes improve when including the missing electron correlations beyond the DFT+DMFT picture [298]. As there are a lot of 2D-ACAR measurements on V [195, 196, 271, 280–289], a future direction for this work is to do DFT+DMFT TPMD calculations. The ELK Compton code used in this thesis has TPMD capabilities (discussed in Ref. [235]) for DFT calculations. Doing DFT+DMFT TPMD calculations are potentially possible with the setup outlined in this thesis. This has been left for future work as benchmarking this code for the DFT+DMFT calculations is required, as well as other factors, such as treatment of the electron-positron enhancement, would also need to be considered.

The results presented for both Ni and V show that electron correlations beyond DFT are vital for better agreement between experiment and theory in these weakly correlated materials. Although we have seen significant improvements when including DMFT, there are still discrepancies with the experiments which indicate that the electron correlations which are not included in DFT+DMFT are important. Recently, results from GW, QSGW, and the SCAN functional improve upon the discrepancies in V which DFT+DMFT does not improve upon [298]. Therefore, theories, such as QSGW+DMFT (with better a treatment of the double counting) should be used on these materials to investigate whether they improve upon the discrepancies with the experimental quantities.

CHAPTER 6

CONFINEMENT INDUCED METAL INSULATOR TRANSITION IN $SrVO_3$ SUPERLATTICES

This chapter discusses, and has adapted, the content from Ref. [25] where the author is the principal author of that article. The focus of the chapter will be on the substantial contributions the author has made to the article, namely the ELK DFT, ELK-TRIQS DFT+DMFT and (ELK) one-shot GW ($G0W0$) calculations. The tight-binding (TB) models and pseudo-potential calculations were done by J. Laverock, and are included here for context.

6.1 Introduction

Many of the bulk properties of a material can be manipulated just by reducing the length scales of the crystal to be on the scale of the electron's de Broglie wavelength (a few lattice constants). Consequently, this means that the crystal is no longer bulk. These reduced length scales, along one or more dimensions, results in a reduction in the degrees of freedom of the carrier particles, implying a reduction in the allowed phase space [299]. This defines the quantum confinement effect. This confinement reduces the propagation of the electron wave function along those reduced dimensions[1]. A (relevant) confined system is a material in which the length scale of one of the dimensions has been reduced such that the material's properties have subsequently changed from being 3D to being described by a 2D system. This example 2D system here is a quantum well (QW). The QW region is where the quantum-confined electrons exists and its boundaries (along the confined dimension) are of an interface to another material or the vacuum. Quantum confinement is an established mechanism which has been used in device manufacture

[1]The "particle in a box" solution to the Schrödinger equations (of appropriate length scales) from undergraduate studies is a nice illustration of quantum confinement [300].

with semiconductors, nanomaterials, and so on [1, 299, 300].

Although QW structures are well-known in semiconducting [1, 301] and free electron-like [302] materials, using correlated $3d$ metals within these structures has only recently been utilised with a select few transition metal oxides [303–305], as well as in few-layer $SrVO_3$ thin films [306]. Recently, substantial advances in the quality and control of layer-by-layer growth methods have facilitated designed transition metal oxide heterostructures and superlattices (SLs) [which are multiple layers of QWs], often focusing on emergence at interfaces and/or surfaces [307–310]. However, the nature of the correlated properties they exhibit, such as their unusual subband renormalisation [306, 311], is not yet well understood. This understanding is essential in order to exploit their properties. Therefore, these correlated heterostructures and SLs have been the subject of a plethora of DFT+DMFT studies [25, 132, 154, 157–160, 312]. DFT+DMFT is ideal to be able to get an insight into the strong correlations present in these systems comprised of transition metal oxides. The "strength" of the electron correlations present in these systems can be gauged by the U/W ratio, where W is the band width (see Fig. 3.2 for example). The electron correlations may be attributed to other effects occurring in the system. For example, the U/W ratio is known to be significantly enhanced at the $SrVO_3$ surface [313–316], and in few layer systems [154, 155]. The reduced coordination at the surface of such systems is often complicated by reconstruction and relaxation [316]. A dimensional crossover due to reduced coordination has been attributed to the observed insulating state of thin films of $SrVO_3$ with a thicknesses below about six unit cells [155, 156]. These systems have been the focus of recent DFT+DMFT studies, such as the emergence of the Mott insulating state due to crystal field (CF) effects in bilayer $SrVO_3$ [154]. The Mott insulating state has also been attributed to CF effects in other vanadates [132, 157–160]. However, it is important to investigate the effect of the electron correlations in a bulk-like heterostructure system which also has a simple structure to help reduce the complexity. This will help to reveal the underlying effect the electron correlations have without needing to disentangle the influence from other factors, such as those from a surface. With this in mind, Ref. [22] measured the spectroscoptic properties of the structurally simple bulk-like $SrVO_3/SrTiO_3$ SLs to investigate tuning the "strength" of the electron correlations. Bulk $SrVO_3$ is a correlated metal which becomes a (Mott) insulator when reducing the dimensionality to a monolayer, see Chapter 4. On the other hand, $SrTiO_3$ is a band insulator and its purpose is to be an inert spacer in these SLs. These $SrVO_3/SrTiO_3$ SLs were either metallic or insulating depending on the number of layers of $SrVO_3$. To better understand these experimental observations for the measured SLs, this led to the DFT+DMFT study in Ref. [25].

This chapter is based around the content in Ref. [25], where we showed that the correlated electronic behaviour in experimentally measured $SrVO_3/SrTiO_3$ SLs is tuned by quantum confinement, which narrows the effective band width of the correlated QW subbands. The employed DFT+DMFT calculations shows that by driving the $SrVO_3$ through an MIT to a Mott insulating phase, excellent quantitative agreement is achieved with the experimental spectral function

extracted from the corresponding spectroscopic measurements [22]. The microscopic mechanism involved is revealed by using a combination of DFT; DFT+DMFT; $G0W0$; and tight-binding models applied to the $SrVO_3/SrTiO_3$ SLs (as well as the bulk, monolayer, and strained $SrVO_3$) for direct comparison with the corresponding experimental results. These DFT+DMFT results reproduce the trends of the experimental data, and reveal that the microscopic mechanism for the MIT in the $SrVO_3/SrTiO_3$ SLs is due to quantum confinement. Also, these results shed light on previous observations of the anomalous mass enhancement in $SrVO_3$ QWs [306, 311], which can be naturally explained as consequences of quantization (i.e. the electrons' quasi-continuous properties, such as its energy and momentum, become discretised along the quantum-confined dimension).

6.1.1 Experimental quantities

This section will briefly explain the results from Ref. [22] for the context of this chapter. These experiments measured $(SrVO_3)_p/(SrTiO_3)_q$ SLs which were grown epitaxially on (001)-oriented $(LaAlO_3)_{0.3}(Sr_2TaAlO_6)_{0.7}$ (LSAT) substrates. Two series of SLs were measured; the first series of SLs is of different repetitions of the $(SrVO_3)_p/(SrTiO_3)_q$ heterostructure for fixed $p = 7$ and $q = 4$ layers. These results showed another avenue to tuning the electron correlations in the SLs, but modelling these within DFT and DFT+DMFT would be too computationally demanding as they require large unit cells to simulate the repetitions. Therefore, these results were not modelled, but are left as a possible future study. The second data series investigated the ratio of p to q layers for four structures of the $(SrVO_3)_p/(SrTiO_3)_q$ SLs, with p:q = 2:7, 3:6, 6:5, and 13:4, each with nine repetitions. These results are the focus of the study here and in Ref. [25]. Transport measurements (via the van der Pauw method [317]) established that the 2:7 and 3:6 SLs were insulating, whereas the 13:4 SL was metallic. The 6:5 SL is metallic at room temperature, with an MIT at a low temperature. The experimental results (performed at room temperature) show the evolution in correlated electron behaviour extracted from soft X-ray absorption spectroscopy (XAS) [318] and soft resonant inelastic X-ray spectroscopy (RIXS) [319], as these experimental probes give access to both the unoccupied and occupied states respectively.

In XAS, the X-ray absorption spectra of a material will show sharp features at specific X-ray photon energies which are unique for each element. These absorption features are referred to as absorption edges, and they correspond to the energy required to eject a core electron into a unoccupied state (or out of the material to produce a photoelectron) [318]. The different types of absorption edges refer to which core electron is being ejected – for example, the K-edge refers to the ejection of the $1s$ core electron. The unoccupied partial density of states of transition metal oxides is closely related to the O K-edge ($1s \rightarrow 2p$) XAS, due to the $2p$–$3d$ hybridisation [320]. Therefore, this O K-edge was measured by Ref. [22] to get the correlated excited spectra of the V and Ti $3d$ states within the SLs. The occupied states, however, are not accessible in O K-edge XAS. Ref. [22] used two different methods to obtain the XAS spectra: total electron yield (TEY)

and total fluorescent yield (TFY). These TEY and TFY methods measure the total number of electrons and fluorescence photons per incident photon (respectively) emitted from the sample as a function of photon energy. The main difference between these methods is the sampling depth, see for example [321]. In Ref. [22], the presented XAS spectra were from the TEY method (which had a sampling depth of 4.1 nm), but these results were also checked with the TFY method (with sampling depth of 70.2 nm) to ensure that the TEY results were representative of the buried layers, which they were. Therefore, the XAS results should be representative of the bulk of the SLs. The XAS experimental energy resolution was 0.2 eV.

RIXS can be explained in terms of a two-step process. The absorption of an incident photon leads to the a very unstable system with a core hole. This intermediate state quickly decays (typically within 1–2 fs) by an electron filling the core state with the simultaneous emission of a photon. The decay of the intermediate state can happen via a number of different ways [319]. The energy of the incident photons are chosen such that they coincide (resonate) with one of the atomic X-ray transitions (one of the absorption edges), meaning that RIXS is capable of providing element-specific information of the local electronic structure. The measured photons contain information about the intrinsic excitations of the material, which relate to many of its physical properties. Therefore, many excitations due to strong correlations, ranging from plasmons and charge-transfer excitations [319], can be measured from this technique. For soft RIXS, incident photons have energies on the order of ~ 1 keV (~ 10 keV for hard RIXS). RIXS is a bulk probe meaning that the RIXS results from Ref. [22] is also representative of the bulk of the SLs. Ref. [22] measured the V L-edge (the $2p \rightarrow 3d$ scattering process here) via (soft) RIXS, which relates to the occupied states of the $SrVO_3$ layers in the SLs. The sampling depth of the RIXS measurements was estimated to be about ~ 70.5 nm. The RIXS experimental resolution was 0.35 eV at FWHM.

Figure 6.1 illustrates the main experimental spectroscopic results on the SLs [22, 322] for the different p:q ratios. The metallicity[2] [Fig. 6.1(a)] was extracted from both XAS and RIXS as the leading edge of the O K-edge XAS (which represents the conduction band minimum for insulators and E_F for metals) and from the intensity of the quasi-elastic[3] peak in V L-edge RIXS (which reflects the delocalisation of the intermediate RIXS state). Insulating SLs show large values of these quantities, whereas metallic SLs saturate at a lower value. The QP band width [Fig. 6.1(b)] was extracted from the $SrVO_3$ layer contribution to the O K-edge XAS as the FWHM of the QP peak. This quantity almost halves from the thick metallic SL to the thinnest insulating SL. The QP spectral weight [Fig. 6.1(c)] was also extracted from the $SrVO_3$ layer contribution to the O K-edge XAS as the ratio of the area under the QP peak to the total area under unoccupied V $3d$ states (i.e. the sum of QP, upper Hubbard band (UHB), and e_g spectral weights). This quantity rapidly drops in the insulating SLs, leaving a small remnant $\approx 10\%$ for the 2:7 SL. Finally, the UHB energy [Fig. 6.1(d)] is accessible to both XAS and RIXS. From O K-edge XAS, the UHB

[2]The metallicity is an experimental indication of how metallic the system is from a spectroscopic point of view (meaning it is not sensitive to macroscopic connectivity). There is no theoretical equivalent to this.

[3]This is the limiting case of inelastic scattering which is close to elastic scattering.

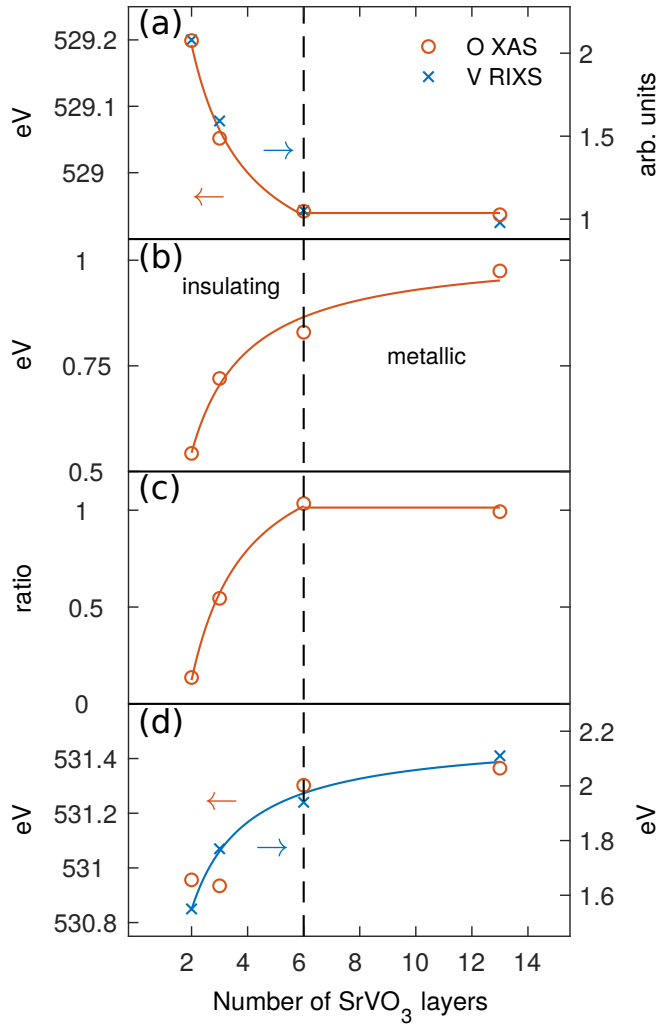

Figure 6.1: Evolution of correlated electron behaviour from experimental XAS and RIXS measurements of $SrVO_3/SrTiO_3$ SLs, reproduced from Ref. [22]. From top to bottom, evolution in (a) metallicity of SLs, (b) QP band width, (c) QP spectral weight and (d) the energy of the UHB are shown.

peak is directly observed, and its centre is shown here. From V L-edge RIXS, the UHB energy is available from transitions from occupied QP states to the unoccupied UHB. Both show equivalent evolution with SL structure, exhibiting a shift to lower energies of over 0.5 eV from the thickest SL to the thinnest.

6.2 Density functional theory calculations

The ELK DFT calculations were performed with the LDA functional. Self-consistency was achieved on a $12 \times 12 \times 4$ Monkhorst-Pack k-mesh, for relatively low computational cost with sufficient sampling, corresponding to 84 k-points in the IBZ. To stabilise the DFT self-consistent cycles,

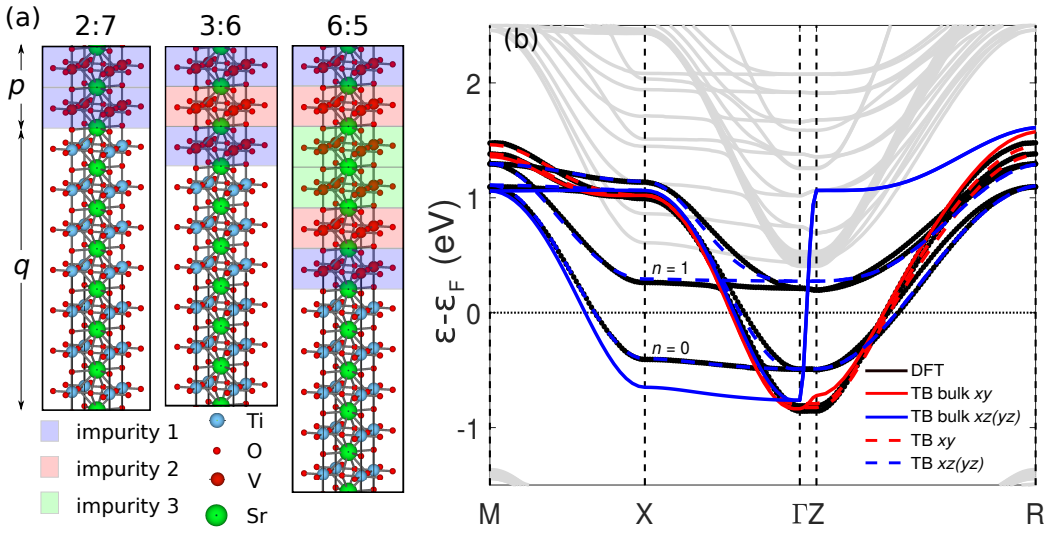

Figure 6.2: (a) Schematic diagram of the SL structures, where p and q represent the number of $SrVO_3$ and $SrTiO_3$ layers, respectively. The SL unit cells used in the DFT are indicated by the black boxes. The colour coded layers illustrate the impurities used in the DMFT calculation. (b) Quantized tight-binding bands for the 2:7 SL. The coloured dashed lines indicate the intrinsic bulk bands from which the quantized bands are derived (see text). The discrete energies from the DFT calculation are shown for comparison (both V and Ti t_{2g} bands are given). The grey bands are non-V t_{2g}.

small values of mixing of the new potentials were used, at the cost of computational time. For bulk $SrVO_3$, a Monkhorst-Pack k-mesh of $12 \times 12 \times 12$ was used (i.e., 84 k-points in the IBZ). The results are in excellent agreement with previous pseudopotential calculations within the generalised gradient approximation (GGA) of the same SLs [22]. The structures of the simple cubic $(SrVO_3)_p/(SrTiO_3)_q$ SLs are shown in Fig. 6.2 (a) for the three SLs investigated here, with p:q = 2:7, 3:6 and 6:5. These were chosen for direct comparison with previous experimental results [22, 322]. The experimental lattice parameters were used: the in-plane parameters were those of the LSAT substrate, $a = b = 3.868$ Å, and out-of-plane parameters were $c_{2:7} = 4.00$ Å, $c_{3:6} = 3.97$ Å and $c_{6:5} = 3.92$ Å. Even in the absence of the SL heterostructure, the different in- and out-of-plane lattice parameters weakly break the V t_{2g} degeneracy into $3d$ xy and $xz(yz)$ orbitals. Previous photo-emission spectroscopy work [155] shows how the dimensionality of $SrVO_3$ influences the MIT. In their results, ten $SrVO_3$ layers closely resemble bulk behaviour. From this, we approximate the 13:4 SL in Ref. [22] with bulk DFT(+DMFT) calculations.

The quantization nature of the 2:7 DFT SL is shown in the band structure of Fig. 6.2 (b). The other calculated SLs have a similar quantized nature in their band structures. The quantized and intrinsic TB fits are also shown, which are discussed in more depth in Section 6.3. The effect of quantization is also seen in the (partial) DOS. The partial DOS of t_{2g} orbitals are shown in Fig. 6.3 for the bulk and 2:7, 3:6, and 6:5 SLs. Sharp peaks in the partial DOS (highlighted by the arrows in Fig. 6.3) reflect the quantized electronic structure along c. These peaks originate from

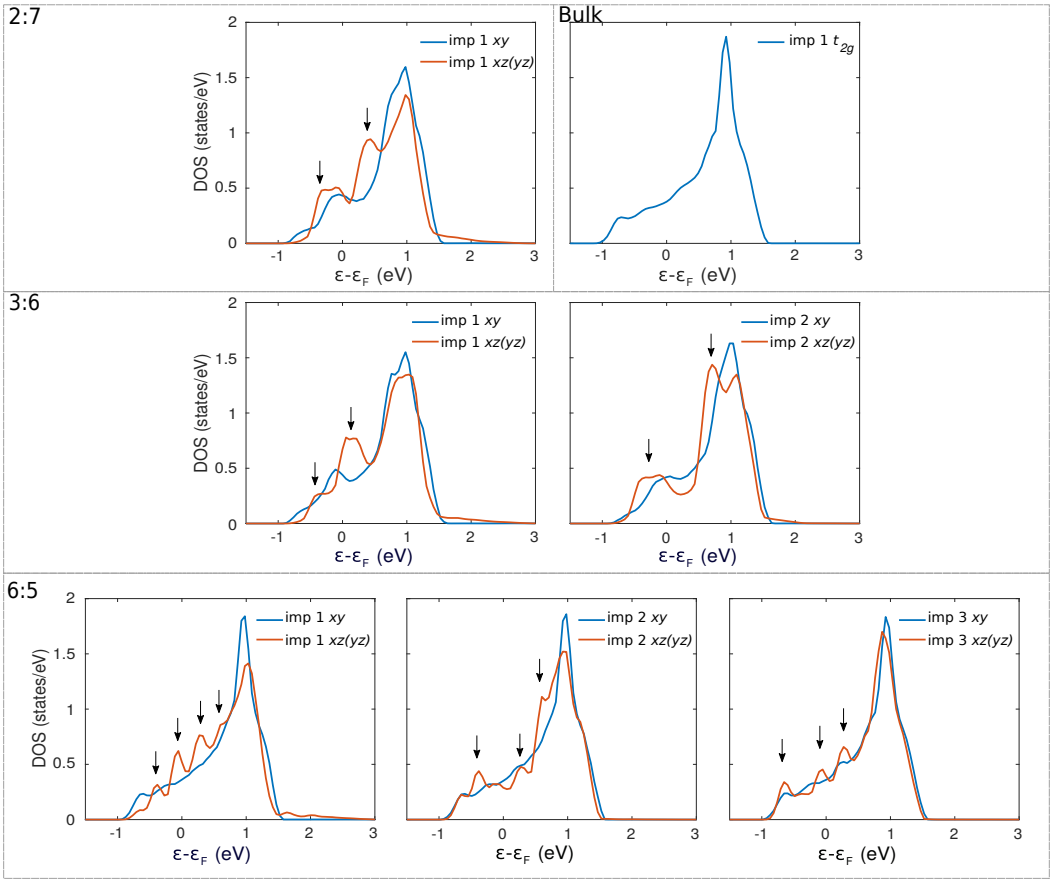

Figure 6.3: The DFT V t_{2g} partial DOS of the bulk $SrVO_3$, 2:7, 3:6 and 6:5 SLs. The dashed borders outline which plots belong to the corresponding structure. Each panel shows the partial DOS of the inequivalent V atoms in each structure, labelled by their impurity number in the DMFT cycles (imp 1 refers to the interface). The arrows indicate the contributions of quantized states to each inequivalent V atom. The greatest contribution is from the relatively flat bands along Γ-X.

the flat quantized bands, as seen in Fig. 6.2 (b) for the 2:7. For the inner layers of the thicker SLs, the partial DOS more closely resembles that of bulk $SrVO_3$, e.g. impurity 3 of the 6:5 SL. This helps the justification of approximating the 13:4 SL with the bulk structure. Near the interface, the $xz(yz)$ partial DOS extends to higher energies as a result of mixing of these states with Ti states in the $SrTiO_3$ layer.

6.2.1 Effects of structural relaxation

We looked into structural relaxation calculations (using GGA [PBE] in QUANTUM ESPRESSO), which did change the bond lengths. The relaxation resulted in the interface V-Ti distance to decrease and the V-V and Ti-Ti lengths tends towards the bulk $SrVO_3$ and $SrTiO_3$ values, respectively, for the atoms away from the interface. There were no significant octahedral tilts in

the structures, which keeps the structure of these systems relatively simple. The effect of the interface and the relaxation is too involved for the current study and has been left for a further in depth investigation. However, an initial relaxation study with (ELK) DFT and OS DFT+DMFT calculations of these relaxed systems are given in Appendix Section 6.6.1. The results in that section show that the interface influences the U_{MIT}, but the underlying MIT mechanism remains unaffected.

6.2.2 Strain calculations

We have performed volume conserving strain calculations on bulk $SrVO_3$ to investigate the effect CF splitting has on the MIT while the band widths of the t_{2g} orbitals are approximately unchanged. Compressive strain of 1% was applied along the c-axis; the other axes were tensively strained to conserve volume compared with the bulk. This strain was chosen to yield a CF splitting of 53 meV, slightly larger than, but comparable with, the CF splitting of the 2:7 SL (shown in Table 6.1).

6.3 Quantized tight-binding model

6.3.1 Bulk tight-binding bands

The (ELK) LDA results for each SL were fitted using a quantized Bohr-Sommerfeld tight-binding (QTB) model [302] to obtain a deeper understanding. The QTB model was constructed using up to the 12^{th} nearest neighbours, consisting of 24 hopping terms (t_i) up to $[l,m,n]=[2,2,2]$. From this model, we are interested in extracting the CF splitting and the band narrowing between xy and $xz(yz)$ orbitals. In order to do this, we fixed the shape of the QTB bands to that of the bulk, which therefore allowed the free parameters in the fit to represent the band centres, band widths, and the quantization parameters. We determined the "intrinsic" TB bands which correspond to bulk-like bands before the quantization conditions are applied, so it therefore represents the intrinsic 3D electronic structure from which the QW states emerge from. We do not analyse the individual parameters, as has been done before [314], as we only care about accurately describing the bulk 3D DFT band structure.

The TB dispersion, $E_n(k_x,k_y,k_z)$, has the form

$$E_n(k_x,k_y,k_z)=\varepsilon_{xy}(k_x,k_y,k_z)+\varepsilon_{xz}(k_x,k_y,k_z)+\varepsilon_{yz}(k_x,k_y,k_z), \tag{6.1}$$

where $\varepsilon_i(k_x,k_y,k_z)$ represents the band energies for the $i=[xy,xz,yz]$ planes. These band energies are given by

$$\varepsilon_i(k_x,k_y,k_z)=E_i^0+\sum_{lmn} t_i^{lmn}\cos\left(lk_x+mk_y+nk_z\right), \tag{6.2}$$

where the band energy, E_i^0, corresponds to the CF energy. The terms in the (Q)TB fits representing the 5^{th} nearest neighbour and higher were necessary to describe the band structure, even though

SL	CF splitting	Intrinsic			Quantized bands		
	(meV)	W_{xy}	W_{yz}	anis.	W_{xy}	W_{yz}	anis.
6:5	33	0.966	0.959	0.993	0.950	0.900	0.948
3:6	40	0.971	0.960	0.989	0.935	0.798	0.853
2:7	51	0.963	0.952	0.988	0.911	0.713	0.782

Table 6.1: Results of fitting the ELK DFT bands to a quantized tight-binding model. The CF splitting is the energy difference, $E^0_{yz} - E^0_{xy}$. The band width (relative to bulk $SrVO_3$), W_i, of the xy and yz bands are shown for both intrinsic bands (before quantization) and for the quantized bands, alongside their anisotropy (W_{yz}/W_{xy}).

they had a magnitude of less than 10 meV. After fitting the model to the bulk LDA band structure in the full cubic BZ, we find the root mean square difference is less than 11 meV, with a maximum difference of 70 meV.

6.3.2 Quantum confinement

The effects of quantum confinement of the V $3d$ electrons in the $SrVO_3$ layers were modelled by using the Bohr-Sommerfeld phase accumulation model [302],

$$2k_z^n(E)L + \delta(E) = 2\pi n, \tag{6.3}$$

where $k_z^n(E)$ is the quantized out-of-plane wavevector, $L = mc$ is the $SrVO_3$ layer thickness (m and c are the number of $SrVO_3$ layers and c-axis lattice parameter of the $SrVO_3$ layers, respectively), n is the quantum number, $2k_z^n(E)L$ is the total phase accumulated in travelling through the $SrVO_3$ layer and back, and $\delta(E)$ is the total phase change due to reflection at both $SrVO_3/SrTiO_3$ interfaces. Typically, the total phase change is dependent on the energy of the confined state. However, in order to simplify the fitting, and avoid unnecessary degrees of freedom, we instead implicitly include the energy dependence through different phases for each quantum number, $\delta(E) = \delta_n$. For asymmetric QWs, e.g. thin overlayers with a vacuum interface, $\delta_n = \phi_1^n + \phi_2^n$ is composed of different individual phase shifts at each reflection. In our case of symmetric barriers, $\delta_n = 2\phi$, where ϕ is the phase at a single $SrVO_3/SrTiO_3$ interface. With all of this, the quantization condition reduces to,

$$k_z^n = \frac{2\pi n - \delta_n}{2mc}, \tag{6.4}$$

from which the QTB dispersion, $E_n(k_x, k_y, k_z^n)$[4], may be evaluated.

6.3.3 Full quantization parameters

For each SL, four parameters were fitted to describe the "intrinsic" band structure, and n parameters described the confined bands. The QTB dispersion was fitted to the DFT band

[4]Here, $E_n(k_x, k_y, k_z^n)$ has the same form as Eq. 6.1, but it will have the additional constraint given in Eq. 6.4.

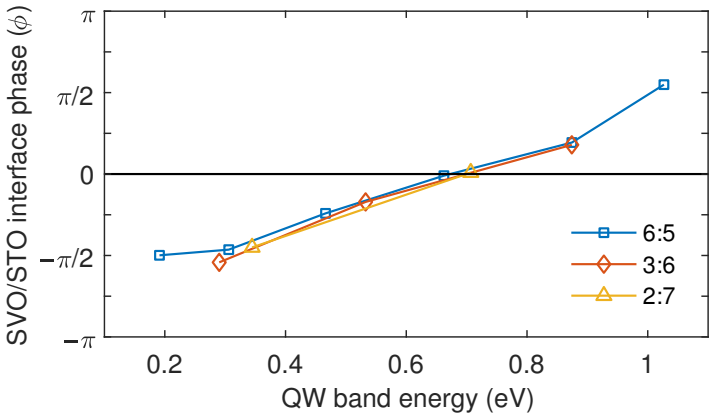

Figure 6.4: The phase shift at the $SrVO_3/SrTiO_3$ interface for each quantized state in the SLs (note $\phi_n = \delta_n/2$ is shown), shown against the mean band energy.

structure of the SLs. The four intrinsic parameters consist of band centres (E_i^0 in Eq. 6.2) and band widths for the xy and $xz(yz)$ bands. The band width parameter, W_i, is a multiplicative factor to the hopping terms, t_i[5]. In addition to the intrinsic parameters, the phase shifts for each confined state, δ_n, were also fitted. The fitted phases are shown in Fig. 6.4 against the mean energy of each state, and closely follow the same roughly linear relationship with energy for all SLs.

The results of fitting the DFT bands to the QTB model are shown in Table 6.1, separated into contributions from the underlying bulk "intrinsic" bands and after quantizing these bands. We present an example of one of our QTB fits to the LDA results of the 2:7 SL in Fig. 6.2 (b), which illustrates the agreement between them. This figure clearly displays the quantized nature of the V $xz(yz)$ orbitals, as well as showing the two subbands ($n = 0, 1$) originating from the two $SrVO_3$ layers. The xy band width is hardly affected by confinement as its wave function is perpendicular to the quantization axis. It is clear that the $xz(yz)$ bands have significantly narrowed compared with their intrinsic (bulk-like) counterparts. The confinement leads to the preferable filling of the quantized $xz(yz)$ out-of-plane bands as their k_z dispersion is suppressed and they become 1D-like, which also pulls the Fermi level down (slightly).

From our fits, confinement alone is capable of reproducing the (LDA) SL band structure almost exactly; it correctly describes the narrowing of the quantized band width and its variation with $SrVO_3$ layer thickness.

6.4 Dynamical mean-field theory calculations

In the DMFT cycle of the DFT+DMFT calculations, the CTHYB solver [161] with the Hubbard–Kanamori interaction Hamiltonian, $\beta = 40$ eV^{-1} ($\sim$ 290 K), $J = 0.75$ eV, and the FLL double

[5]The hopping terms themselves were fixed to the cubic bulk parameters determined above, effectively fixing the shape of the band.

counting term were used as in previous studies [132, 154, 157]. Each DMFT cycle calculation used 84×10^6 Monte Carlo sweeps per impurity. The DMFT cycle requires multiple impurities depending on the SL structure, as illustrated schematically in Fig. 6.2 (a), where each $SrVO_3$ layer has one impurity. However, the DMFT cycle utilises the inversion symmetry of the SLs to reduce the number of impurities used in the calculation. The systems investigated correspond to a single impurity for the 2:7 SL and bulk calculations, and two and three impurities for the 3:6 and 6:5 SLs, respectively. In each case, the impurities are considered to be independent of one another. The results presented here use the (OS and) FCSC DFT+DMFT technique as implemented in the TRIQS/DFTTOOLS library [16, 134]. The FCSC DFT+DMFT calculations on complex oxides have been used in recent studies [312]. As in the literature [132, 154, 157], only the V t_{2g} bands were projected (using Wannier projectors [130]) to construct the LDA Hamiltonian in Wannier space to be used in the DMFT calculation. These projectors were constructed in the following correlated energy windows: 2:7 SL, $[-1.36, 2.0]$ eV; 3:6 SL, $[-1.29, 2.0]$ eV; 6:5 SL, $[-1.29, 2.0]$ eV; and bulk, $[-1.50, 1.90]$ eV. These windows were constructed such that all of the V t_{2g} bands were included and the valence charge within the windows, corresponding to the charge in the V t_{2g} orbitals, was (approximately) equal to 1 per V impurity.

In order to avoid potential complications from the ill-posed problem of analytic continuation, certain quantities were determined from the Green's function and self-energy on the imaginary time or Matsubara frequency axis. The charge of each orbital (n_e) was determined by

$$n_e = \frac{1}{\beta} \sum_n G(i\omega_n) e^{i\omega_n 0^+}. \tag{6.5}$$

As there is negligible orbital-orbital overlap on the impurity, the matrix of n_e values is diagonal. The spectral function at the Fermi level, $A(\omega = 0)$, presented in this chapter was determined directly from the imaginary time Green's function by

$$A(\omega = 0) = \frac{\beta G(\tau = \frac{1}{2}\beta)}{\pi}. \tag{6.6}$$

This $A(\omega = 0)$ is an averaged quantity over a frequency window approximately equal to β^{-1} [154]. The value of the Wannier QP residue Z for each orbital was determined by

$$Z = \left(1 - \frac{\partial \mathrm{Im}[\Sigma(\mathrm{i}\omega_n)]}{\partial \mathrm{i}\omega_n}\Big|_{\mathrm{i}\omega_n \to 0^+}\right)^{-1}, \tag{6.7}$$

where the Z is evaluated from the differential of the imaginary part of the Matsubara self-energy at $\mathrm{i}\omega_n \to 0^+$ (close to the Fermi level). For U values far from the Fermi-liquid regime (namely for the presented 6:5 Z values close to the MIT), the Z values were approximated by using the differential of the interpolated self-energies at $\mathrm{i}\omega_n = 0$. There are two ways to realise the insulating solution: first, by a divergence in $\mathrm{Im}[\Sigma(\mathrm{i}\omega_n)]$, which comes naturally with $Z = 0$. Second,

the combination of the $\mathrm{Re}[\Sigma(i\omega_n)]$ and the chemical potential might move the pole position outside of the non-interacting band width, meaning that no QP peak is possible in the Green's function. In the latter case, we have $A(\omega = 0)$ vanishing with non-diverging $\mathrm{Im}[\Sigma(i\omega_n)]$. In that case, which we saw in our results, we set Z to zero manually. From this, the MIT U value (U_{MIT}) is defined as the lowest U value in which $A(\omega = 0) = 0$.

The spectral functions, $A(\omega)$, for each impurity were calculated from $G(\tau)$ using the *LineFitAnalyzer* maximum entropy analytic continuation technique implemented within the TRIQS/MAXENT application [125]. The $\mathbf{k}$-resolved spectral functions $A(\mathbf{k}, \omega)$ were calculated from the analytically continued self-energy.

The effective and correlation subband mass enhancement factors, $1/Z_\nu$ and $1/Z^{\mathrm{c}}_\nu$, in Section 6.4.3 were calculated from the ratios of the Fermi velocities using

$$Z^{\mathrm{c}}_\nu = \frac{v^c_F}{v^{QTB}_F}, \tag{6.8}$$

and

$$Z_\nu = \frac{v^c_F}{v^i_F}. \tag{6.9}$$

Here, the Fermi velocities were determined from the gradient of the linearly expanded band dispersions along M-X around $\mathbf{k}_F$ of the DFT+DMFT subbands (v^c_F), the quantized bands from QTB (v^{QTB}_F) and the intrinsic (bulk-like) TB bands (v^i_F). The intrinsic bands were used as they incorporate the effect of renormalisation due to strain. Therefore, Z^{c}_ν and Z_ν describe the effect of renormalisation from correlations, and the combination of correlations and confinement (band) effects, respectively. The DFT+DMFT subband energy centres, $E_{\nu,\mathbf{k}}$, were calculated by using

$$E_{\nu,\mathbf{k}} = \epsilon_{\nu,\mathbf{k}} - \mu + \mathrm{Re}[\Sigma_\nu(\mathbf{k}, \omega = E_{\nu,\mathbf{k}})], \tag{6.10}$$

where $\epsilon_{\nu,\mathbf{k}}$ is the DFT energy, μ is the chemical potential and $\mathrm{Re}[\Sigma_\nu(\mathbf{k}, \omega)]$ is the real part of the diagonal upfolded self-energy elements on the real frequency axis. The QP lifetime in the inset of Fig. 6.11 in Section 6.4.3 was determined from the inverse imaginary part of the analytically continued upfolded self-energy. Finally, the subband energies at the Γ high symmetry point in Fig. 6.11 of Section 6.4.3 were determined from Eq. 6.10.

6.4.1 One-shot and FCSC DFT+DMFT results

Here, we present the U-dependent MIT for each SL and different DFT+DMFT methods in Fig. 6.5. For each SL structure, U was varied in the range 5.5 to 6.25 eV, and U_{MIT} was located, which corresponds to the U at which the SL becomes insulating. The behaviour of the OS and FCSC calculations is very similar, exhibiting a similar U_{MIT} with similar characteristics, e.g. $A(\omega = 0)$

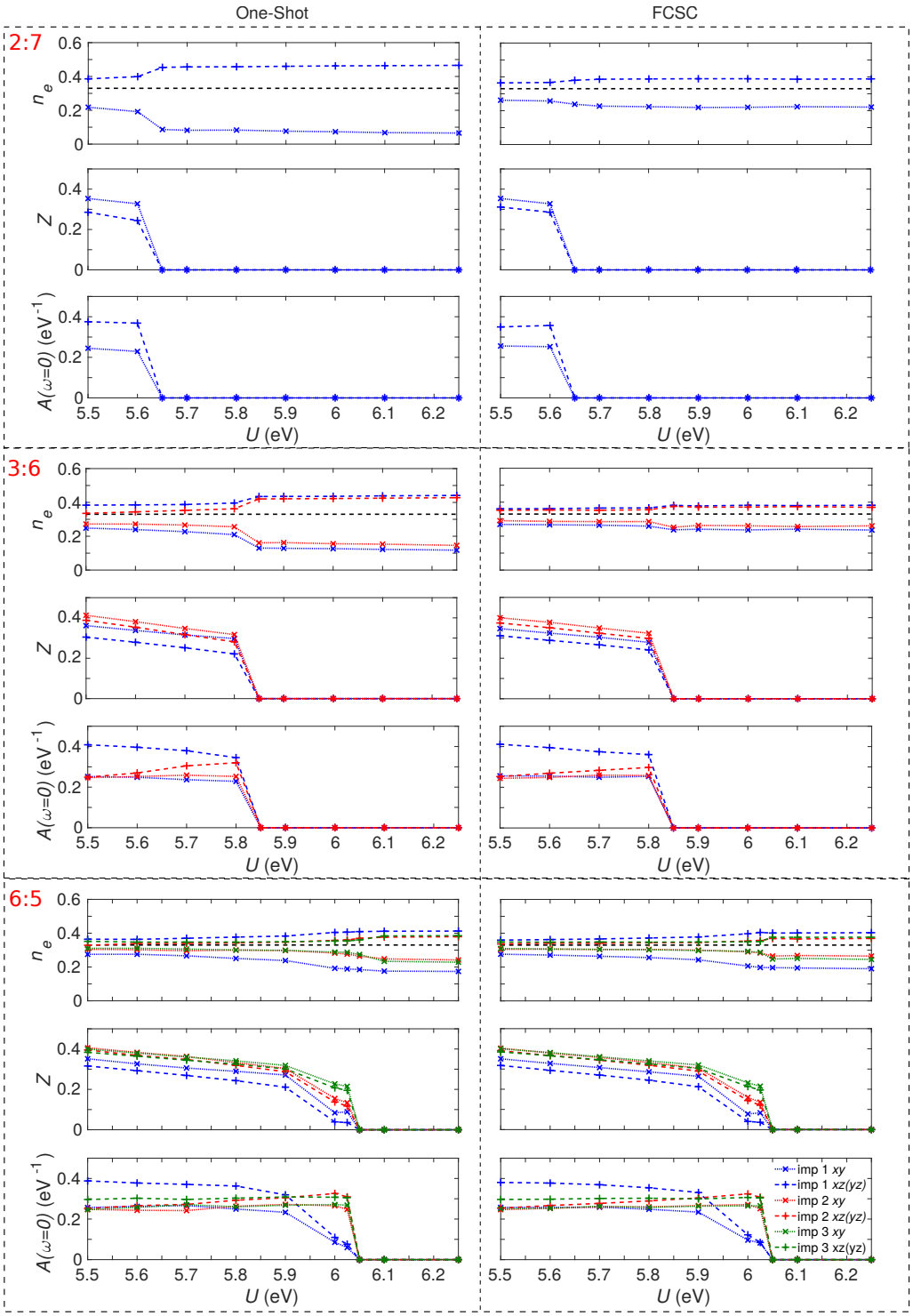

Figure 6.5: The effect of U on the orbital charge n_e (top), QP residue Z (middle) and the spectral function around the Fermi level (bottom) for each one-shot and fully charge self-consistent (FCSC) DFT+DMFT SL calculation. These quantities were extracted from the corresponding Green's functions and self-energies on either the imaginary time or Matsubara frequency axis. The dashed line represents the bulk degenerate orbital charge.

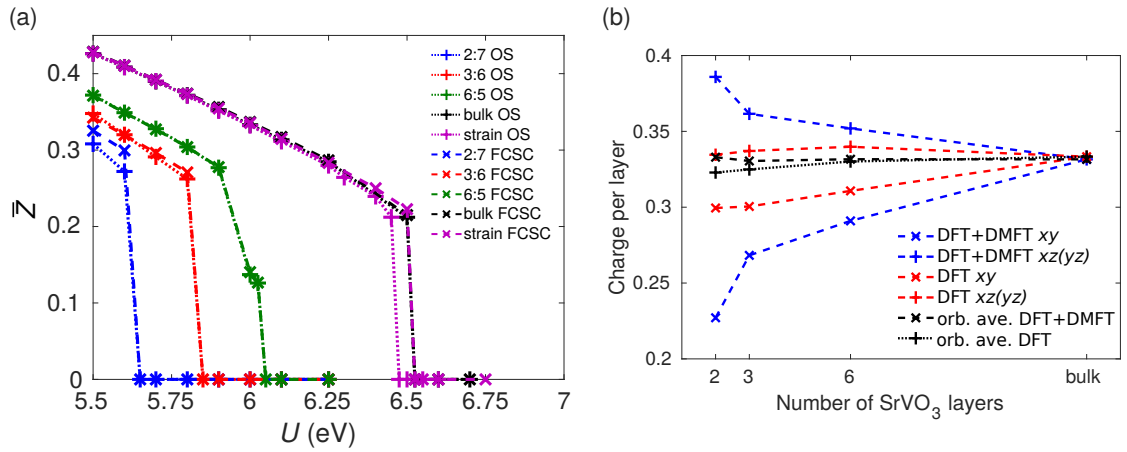

Figure 6.6: (a) The comparison of the orbitally-averaged QP residue, $\bar{Z}$, between the one-shot (OS) and fully charge self-consistent (FCSC) DFT+DMFT methods. (b) The averaged Wanner orbital charge over all layers from the DFT and ($U = 5.7$ eV FCSC) DFT+DMFT Wannier V xy and $xz(yz)$ orbitals for each SL and bulk. This includes charges from DFT, DFT+DMFT and average Wannier orbital charge per layer (orb. ave.) for each SL and bulk. The plot lines are guides to the eye.

and Z. Some differences are observed in the orbital polarisation between the two methods, whereby the polarisation is somewhat suppressed in the FCSC calculation compared with OS. This behaviour, most notable for the 2:7 SL, is consistent with other studies [132, 157, 158], and is caused by the charge redistribution with the rest of the system at the DFT stage. This trend from 2:7 to bulk, where the U_{MIT} increases by ~ 0.2 eV for each SL, is also seen in Fig. 6.6 (a) for the orbitally-averaged QP residue, $\bar{Z} = (\Sigma_i Z_i)/N$,[6] where there are some differences in $\bar{Z}$ for the 2:7 SL between OS and FCSC, but the bulk values are very similar. The biggest discrepancy between the OS and FCSC $\bar{Z}$ values are in the strain calculations; the charge redistribution in the strain FCSC DFT+DMFT calculations causes its U_{MIT} value to be inline with the bulk value. Here we see a sharp decrease at U_{MIT} in $\bar{Z}$ for each SL. This likely indicates a first order transition which would involve a U_{MIT} coexistence region. This means that there would be two values for the U_{MIT} depending on whether the initial starting point for the DMFT calculation was in the metallic or insulating phase. For this study, our calculations only started from the DFT metallic phase; we did not investigate the coexistence region in our SLs. On the other hand, the coexistence region was observed in the bilayer $SrVO_3$ on $SrTiO_3$ system in Ref. [154]. An important note to make about Fig. 6.5 is that Z at the interface (impurity 1) for the $xz(yz)$ orbitals tends to zero first for each SL. This suggests that the weight from the $xz(yz)$ QP peak depletes first. Therefore, when the interface $xz(yz)$ QP state has been fully depleted, this causes the SL to transition into the insulating state. From this, the interface between the oxides has a strong influence on the MIT. The $A(\omega = 0)$ for impurity 1 of the 6:5 also tends to zero first which strengthens the argument for at least that SL. Overall, charge self-consistency slightly adjusts some details of the results, but

[6] Here, Z_i was determined from the ith orbital self-energy on the Matsubara frequency axis.

SL	Interstitial	Sr	V	O	Ti	Ti interface
2:7	19.1	0.6	66.6	10.8	2.9	2.7 (= 0.027 e-/ Ti)
3:6	18.9	0.6	67.3	10.9	2.3	2.1 (= 0.0315 e-/ Ti)
6:5	18.9	0.6	68.5	10.8	1.2	1.1 (= 0.033 e-/ Ti)
Bulk	19.2	0.7	69.1	11.0	-	-

Table 6.2: The DFT integrated DOS percentages (%) of the total charge within the correlated energy window. The charge per interface Ti atom is given to show how much charge has leaked to the Ti interface.

the main conclusions of our study are already present in OS DFT+DMFT calculations. From this point, only the FCSC DFT+DMFT result will be discussed.

The trends across the SLs give further insight into the physical phenomena. The splitting of the orbital degeneracy strongly affects the polarisation of the orbital charge, which is shown by the averaged Wannier orbital charge in Fig. 6.6 (b). The reduction of the number of layers significantly increases the charge in the $xz(yz)$ orbitals, which appear to tend to half filling (whereas the xy orbitals are tending towards zero charge). This is a likely consequence of these orbitals trying to reduce the potential energy, analogous to what is seen in the previous monolayer calculations.

Interestingly, the DFT averaged V Wanner orbital charge over all the $SrVO_3$ layers for the decreasing number of $SrVO_3$ SLs is slightly (but noteworthy) lower than 1/3 (the sum of all of these averaged Wanner t_{2g} orbitals is equal to ~1, as expected). The Ti states have a small amount of charge as shown in Table 6.2. This table shows the DFT MT (of each species) and interstitial charge percentages calculated from integrated DOS within the correlated energy windows (used for the DMFT calculations). The total charge equals the number of V atoms (which each contribute one valence electron) in the unit cell (e.g. for the 3:6 SL, the total charge in the correlated energy window is three). As can be seen in Table 6.2, the Ti charge percentage contribution decreases with increasing number of $SrVO_3$ layers. The greatest contribution to the Ti charge is from the interface Ti [$3d$ $xz(yz)$ states] shown in Table 6.2. The difference in the total and interface Ti contributions corresponds to the charge in the other $SrTiO_3$ layers, which is small compared with the interface Ti charge. Therefore, the charge is likely to be primarily leaking from the V to the Ti atoms at the interface (due to hybridisation between the V t_{2g} and Ti t_{2g} at the interface), as indicated by the increasing V charge contribution with the number of $SrVO_3$ layers. However, the amount of charge on the (interface) Ti atoms is small and only a few percent of the total charge [which consistent with the small DFT Wanner charge deviation in Fig. 6.6 (b)], which is quite small. For this reason the Ti states were not treated within DMFT.

Finally, Fig. 6.7 shows the spectral function [A(ω)] of the correlated impurity orbitals in each $U = 5.7$ eV DFT+DMFT SL calculation (this value is used in the experiment-theory comparisons in Section 6.4.2). It is evident that the 2:7 is insulating and the 3:6 and 6:5 are metallic from the absence/presence of the QP peak at the Fermi level. There are sharp features in the QP peaks

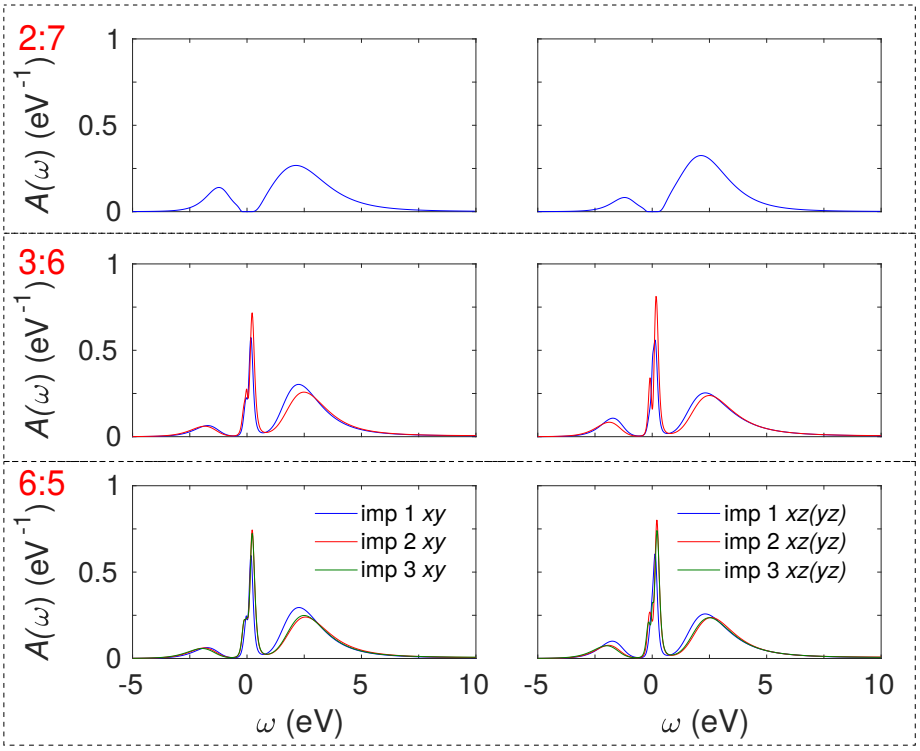

Figure 6.7: Spectral functions of the 2:7 (top), 3:6 (middle) and 6:5 (bottom) SLs from fully charge self-consistent calculations, showing xy (left) and $xz(yz)$ (right) orbitals. The spectra of the insulating 2:7 SL have been slightly shifted such that the Fermi level lies at the centre of the band gap of the xy spectrum.

around the Fermi level for the 3:6 and 6:5 SLs. These features are often attributed to spurious noise from the analytic continuation procedure, however, that may not be the case here due to the quantized bands being present around the Fermi level. The peak position of the Hubbard bands (notably the UHB) are closer in energy to the Fermi level for the interface layer (impurity 1) than the other layers for the 3:6 and 6:5. This is another indication that the interface layer is more correlated than the other layers.

6.4.2 The experiment-theory comparisons and MIT mechanism

From the established results in the previous sections, we begin here by ensuring that our DFT+DMFT calculations accurately describe the experimental system. In Figs. 6.8(b-d), we compare quantities extracted from XAS and RIXS experiments [22] with the corresponding theoretical quantities (see Appendix Section 6.6.2) from our DFT+DMFT calculations for $U = 5.7$ eV which was chosen to reproduce the phenomenological behaviour of the experiments. As demonstrated by Figs. 6.8 (b-d), our DFT+DMFT calculations not only capture the qualitative behaviour, but also yield excellent quantitative agreement with the experiment trends. We note that, although

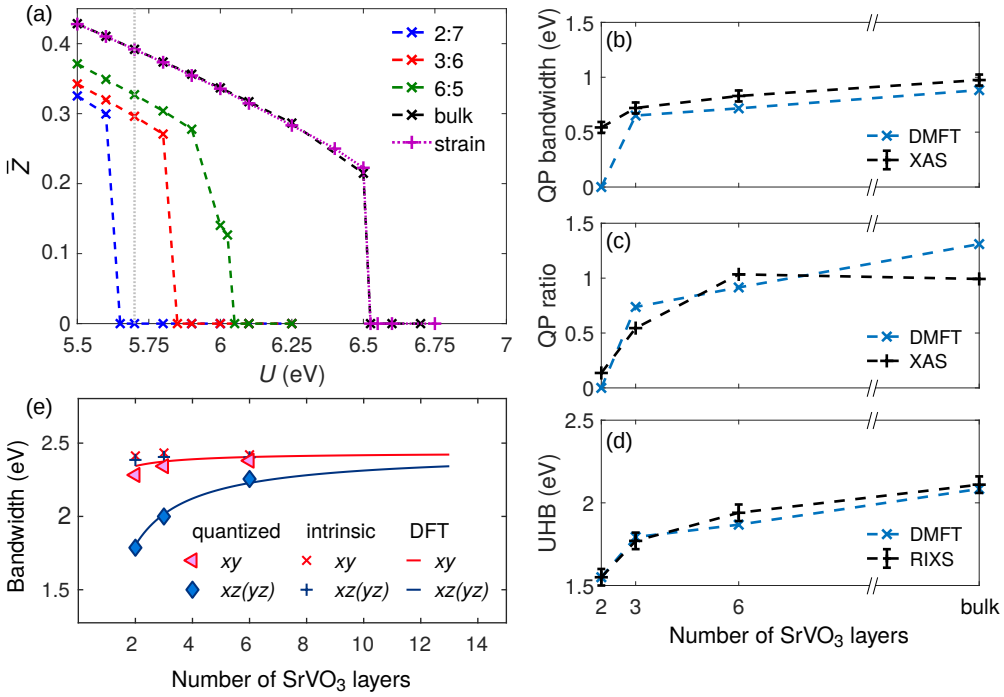

Figure 6.8: (a) The orbitally-averaged QP residue, $\bar{Z}$, for each of the p:q SLs. Also shown are the results of bulk and 1% strained calculations (see text). The grey dotted line indicates the value of $U = 5.7$ eV used for subsequent calculations. (b-d) Comparison with experimental quantities from X-ray absorption spectroscopy (XAS) and resonant inelastic X-ray scattering (RIXS) data [22]: (b) QP band width; (c) spectral weight within QP states compared with upper Hubbard band (UHB) states; (d) energy of UHB (the DMFT results have been rigidly shifted to match at the 2:7 SL). (e) The band widths of the SLs from the DFT calculation and QTB model. Also shown are the intrinsic (bulk) band widths of the QTB model.

the 2:7 SL is macroscopically insulating, it has a small QP spectral weight in the spectroscopic experiments due to properties of the sample. The sample is globally insulating from the transport measurements, but the spectroscopic experiments *may* have measured spatially disconnected puddles of metallic $SrVO_3$ in an insulating background (as seen in other correlated oxides near their MIT [323]). On the other hand, this spectral weight may be due to other (extrinsic) factors such as imperfect interfaces leading to metallic regions, defects or off-stoichiometry leading to metallicity or in-gap states that resemble QPs spectroscopically. It should be noted that the $G0W0$ results of the $SrVO_3$ monolayer (which can be thought of as the extreme limit of reducing the dimensionality in $SrVO_3$) in Appendix Section 6.6.3 do not produce the insulating state seen experimentally. This suggests that the insulating state in previous experimental results is from Mott physics which (currently) only DMFT is able to capture.

We see excellent experiment-theory comparisons for $U = 5.7$ eV, and this value is fairly consistent with the similar bilayer system [154]. Note that as U (and J) are truly frequency dependent, this adds to the difficulty of approximating these parameters as being static for

the DMFT calculation. The previously calculated cRPA U values in Ref. [154] show that the free-standing $SrVO_3$ monolayer, bilayer, and trilayer slabs have U values of approximately 5.5, 5.3, and 5.1 eV respectively. Therefore, we would expect the U value in our SL experiment-theory comparisons to be similar. Note that the cRPA only gives an estimate of the U (and J) parameters, so it is not unreasonable to use values which (slightly) deviate from the cRPA ones. The $U = 5.7$ eV value is justifiable as it is reasonable close to the cRPA U values, and the discrepancy between our U value with them will likely be down to certain factors, such as the different internal coordination of the atoms and the lattice parameters used, as well as the inclusion of the Ti t_{2g} states in the Wannier projector construction (the Ti t_{2g} state could potentially be providing a small screening channel [for example, this is seen in the bulk $SrVO_3$ $d+p$ model]). Also, the small charge contributions the (interface) Ti atoms have in the correlated window influences the U value required for experiment-theory comparisons. Therefore, the U value may also be impacted by the (interface) Ti states being treated as inert in DMFT. In Appendix Section 6.6.1, we see that the interface does influence the U_{MIT} value and that this change is due to the hybridisation of the V t_{2g} with the Ti t_{2g} states at the interface, but the underlying physical phenomena remains unchanged. Also, from the results of the relaxed structures, the changes in the lattice parameter consequently changes the phase in which the SL is in at a particular U value, which is a consequence of the V-Ti hybridisation. Therefore, the interface has a great influence on the strength of the local correlations which affects the magnitude of experiment-theory U value and U_{MIT} – this could be controlled by an external parameter (such as pressure and so on). Note that these U values would likely change if the Ti states were treated as correlated in DMFT.

Insight into the microscopic mechanism for the MIT can be obtained by analysing the QTB model for each SL. In Fig. 6.8 (e), the band widths of the SLs from the DFT calculations are shown alongside those from the QTB model. While the in-plane xy orbitals experience a slight narrowing for thinner $SrVO_3$ SLs, the overall band narrowing of the (quantized) out-of-plane $xz(yz)$ orbitals is substantial, leading to a band width reduction of $\sim 70\%$ for the 2:7 SL [22]. As expected from the quality of the fits in Fig. 6.2 (b), good agreement is observed between the QTB and DFT results. However, this behaviour is not captured at all by the "intrinsic" band widths, which correspond to the effective 3D bands of the QTB model before quantization. These results demonstrate that the band narrowing in Fig. 6.8 (e) is due to quantization of the $xz(yz)$ orbitals, which has a more pronounced impact for thinner $SrVO_3$ layers. The band narrowing of the thinner SLs leads to a greater U/W ratio, which results in stabilisation of the insulating phase, as illustrated by the DFT+DMFT calculations shown in Fig. 6.8 (a).

A previous DMFT study has attributed CF effects as being the principle factor driving the MIT in bilayer $SrVO_3$ on $SrTiO_3$ [154], and it is pertinent to ask what role, if any, the CF plays in our system. In Ref. [154], strain induced by the $SrTiO_3$ substrate led to a lowering of the xy orbitals by 180 meV due to the CF. In contrast, we find a CF splitting of ≤ 51 meV in favour of the V $xz(yz)$ bands in our SLs (see Table 6.1), in part owing to the lower strain imparted

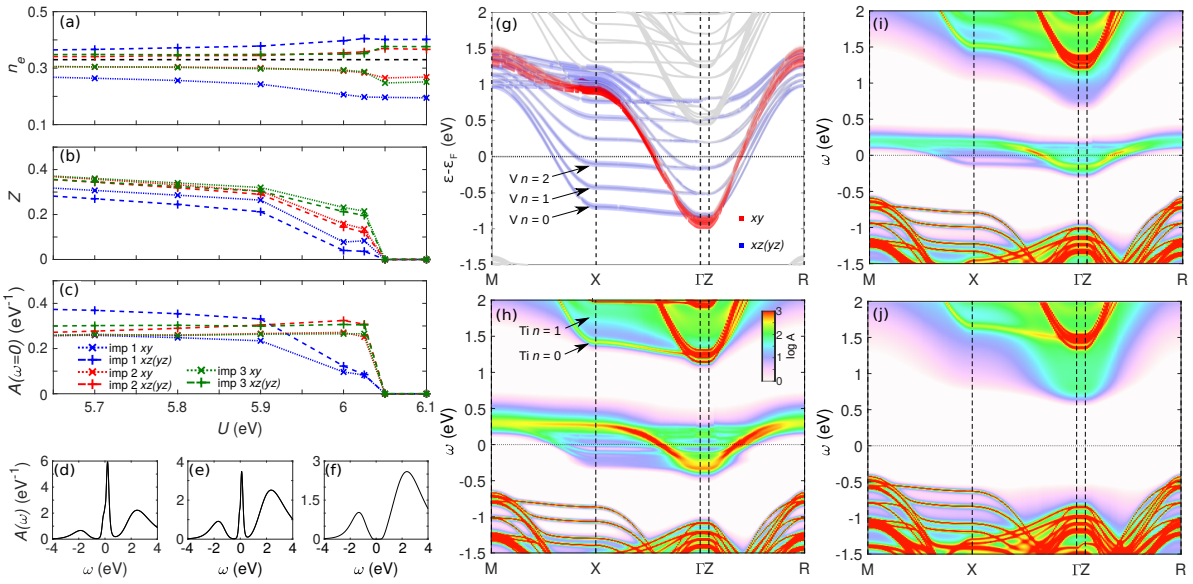

Figure 6.9: Correlated QW electronic structure. (a) Occupation number, n_e, (b) QP residue, Z, and (c) spectral function at the Fermi level [$A(\omega = 0)$], determined directly from the imaginary time Green's function, of all impurity (imp) correlated orbitals from DFT+DMFT across the MIT for the 6:5 SL. (d-f) The momentum-integrated V t_{2g} spectral function, $A(\omega)$, for $U = 5.7$, 6.025 and 6.05 eV respectively. (g) DFT band structure of the 6:5 SL, with V t_{2g} band characters shown. (h) DFT+DMFT momentum-resolved spectral function, $A(\mathbf{k},\omega)$, of the 6:5 SL for $U = 5.7$ eV, showing directly the renormalisation of the correlated bands. (i-j) DFT+DMFT spectral function close to the MIT for $U = 6.025$ and 6.05 eV, respectively.

by the LSAT substrate. To reproduce the effects of this CF, we have calculated strained $SrVO_3$ with a volume-conserving strain of 1%, which leads to similar CF splitting of 53 meV. This 3D system, which reproduces the CF levels of our SLs but without the quantization effects, is shown in Fig. 6.8 (a), and shows very similar behaviour to the bulk cubic system. The strained FCSC U_{MIT} is approximately 6.525 eV, the same as for the bulk. As shown previously, the OS strained calculation had a slightly lower U_{MIT} of 6.475 eV. Due to the small change on U_{MIT}, the CF splitting is insufficient to cause the MIT in these SLs. Therefore, we confidently rule out CF effects as a dominant factor in our SLs.

Next, we discuss the correlated behaviour of the quantized electron states, taking the 6:5 SL as an example. Fig. 6.9 (a-c) shows the orbital- and layer-resolved occupation number, n_e, QP residue, Z, and spectral weight at the Fermi level, $A(\omega = 0)$, as a function of U, illustrating the transition to the insulating phase at $U = 6.05$ eV for this SL. As presented in Fig. 6.9 (a), each layer (impurity) exhibits a sizeable orbital polarisation in favour of the xy orbitals, which is exaggerated both at the outer (interface) layer and in the insulating phase. This behaviour is consistent across all SLs (seen in the previous section), and originates from a small polarisation in the DFT calculations due to the local CF, which is subsequently amplified in the DMFT cycle. The outer layer (impurity 1) is significantly "more correlated", experiencing a smaller QP residue

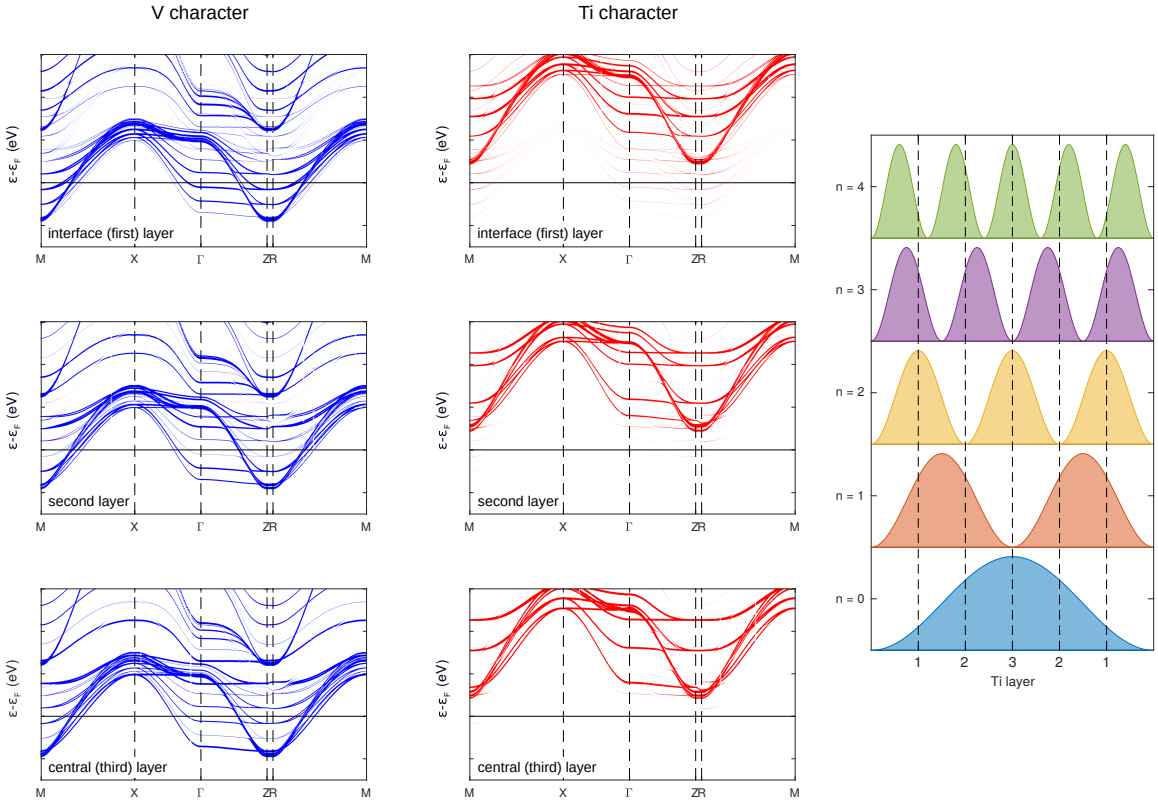

Figure 6.10: The DFT V and Ti t_{2g} band characters of the 6:5 SL. The thickness of the lines indicates the total character of each V (left) and Ti (right) site. The top row shows the band characters at the interface, while the bottom row shows the character in the centre of each layer. On the right, a schematic illustration of the real-space probability distribution of the quantized subbands in the out-of-plane direction of the $SrTiO_3$ layers is shown. The edge of the box does not coincide with the interface Ti ion or its neighbouring SrO layer due to the finite phase accumulated at the interface.

Z than the other layers [Fig. 6.9 (b)], corresponding to a greater renormalisation factor, $1/Z$. Near the MIT, this leads to a collapse in the spectral weight at $\omega = 0$ of the interface layer [Fig. 6.9 (c)]. In this sense, the more correlated interface layer simultaneously triggers the MIT in the remaining layers, in much the same way as suggested for $SrVO_3$ bilayers in Ref. [154].

The DMFT spectral functions, $A(\omega)$ and $A(\mathbf{k},\omega)$, are shown in Fig. 6.9 (d-f) and Fig. 6.9 (h-j) for $U = 5.7$, 6.025 and 6.05 eV, respectively. The renormalisation of the V bands increases from a factor of $1/\bar{Z} \approx 3.5$ at $U = 5.7$ eV to ≈ 8 just below the MIT ($U_{\mathrm{MIT}} = 6.05$ eV) before the QP spectral weight vanishes in the insulating phase [Fig. 6.9 (f)]. The renormalisation of the V bands is accompanied by a lowering in their energy with respect to O and Ti bands, leading to pronounced energy separation of O/Ti bands and metallic V t_{2g} QPs. Nevertheless, the quantized subband structure remains clear in the metallic solutions, leading to genuinely strongly correlated QWs. At $U = 5.7$ eV, the lowest three yz subbands are occupied at X and Γ, similar to the DFT, however

by $U = 6.025$ eV only the lowest subband is occupied, indicating the quantized system undergoes a correlation-induced Lifshitz transition prior to the MIT. Although the correlated orbitals remain relatively sharp throughout near $\omega = 0$, implying long-lived QPs with a well-defined Fermi surface, the lifetime rapidly broadens away from the Fermi level, in line with a strongly correlated Fermi-liquid (see inset of Fig. 6.11). We also note that the incoherent UHB, visible above 1 eV in [Fig. 6.9 (j)], exhibits rather strong momentum dependence, visible in previous bulk DMFT calculations [139, 324]. Unexpectedly, certain (uncorrelated) Ti states also show pronounced broadening, e.g. the $n = 1$ Ti yz orbital indicated in Fig. 6.9 (h), which is almost completely smeared out at $U = 6.025$ eV [Fig. 6.9 (i)]. This effect on the Ti states can be discussed in terms of the DFT band characters. The DFT characters of the 6:5 SL subbands are shown in Fig. 6.10 for each of the different V and Ti sites. As expected, the V bands dominate the character at the Fermi level, with weak contribution from interfacial Ti ions. The spatial distribution of the subband wave functions of the $SrVO_3$ QWs can be seen directly in the characters. The V $n = 0$ subband, with greatest amplitude in the centre of the well, has strong character in the central V ion and weak character at the interface. Correspondingly, the V $n = 2$ subband has strongest character at the interface and is almost absent in the second layer close to where a node is expected in the QW wave function. At higher energies, the quantized V e_g subbands appear above 1 eV. As above, the central Ti ion contributes strongly to the Ti $n = 0$ and $n = 2$ subbands. On the other hand, the interfacial Ti ion contributes significantly to the Ti $n = 1$, 2, and 3 subbands, with the largest contribution to the Ti $n = 2$ subband. The interfacial Ti ion mixes most strongly with the V orbitals, which are the correlated orbitals in the subsequent DMFT cycle. This demonstrates how the spatial penetration of the Ti $n = 1$ and $n = 2$ subbands into the correlated $SrVO_3$ layers leads to substantial broadening of these subbands in the subsequent DMFT cycle. In contrast, the Ti $n = 0$ subband is spatially deep within the $SrTiO_3$ layer and does not feel the effects of the correlated $SrVO_3$ orbitals very strongly, remaining reasonably sharp even in the insulating phase shown in Fig.6.9 (j). This surprising sensitivity of the Ti states may help to explain recent RIXS results of the $SrTiO_3$ layers of $SrVO_3/SrTiO_3$ SLs, where a sudden change in the delocalised Ti $3d$ carrier density was observed coincident with the MIT of the $SrVO_3$ layers [325].

6.4.3 Anomalous mass enhancement

We finish by discussing some important implications of our results. Anomalous mass enhancement has been reported in $SrVO_3$ QWs, whereby shallower occupied subbands were found to have a larger mass enhancement ($m^* = m/Z_\nu$) than subbands at deeper energies [306]. Subsequent theoretical [326] and experimental [311] studies argued the anomalous enhancement was a consequence of a combination of electron correlation effects and the reduced dimensionality of the surface. To address this, in Fig 6.11, we compare the total mass enhancement of a particular quantized subband, $1/Z_\nu$, with that due solely to electron correlation, $1/Z_\nu^c$, both of which are obtained through analysis of the Fermi velocities. The trend in the total mass enhancement factor,

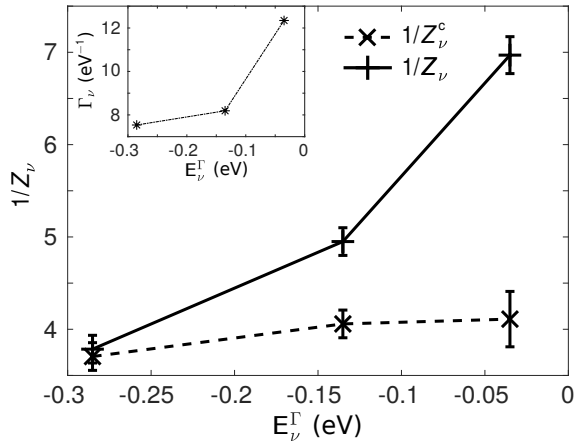

Figure 6.11: The total mass enhancement factor of each subband, $1/Z_\nu$, of the 6:5 SL at $U = 5.7$ eV shown alongside the correlation-only mass enhancement factor $1/Z^c_\nu$, evaluated along X-M. The abscissa represents the bottom energy of the subband. Error bars indicate the estimated error in determining these quantities. The inset shows the subband lifetime Γ_ν. All lines are guides to the eye.

$1/Z_\nu$, which includes both correlation effects and band effects due to quantization, qualitatively reproduces the experimental data [306] rather well, but this behaviour is only very weakly present in $1/Z^c_\nu$. Therefore, in our SLs the origin of the mass enhancement is firmly due to k_z sampling introduced by quantization, as has been observed in other systems [305]. While reduced coordination at the surface [316, 326], surface reconstruction [327, 328], or specific k_z sampling due to an asymmetric phase shift at the vacuum [305, 329, 330] may play additional roles in specific surface-terminated systems, our results reveal quantization as the primary source of anomalous mass enhancement in embedded (or capped) few-layer $SrVO_3$.

6.5 Conclusion

Our results establish quantum confinement engineering as a sensitive method to tune the correlated electron behaviour of $3d$ electron systems. We demonstrate that using SLs of few-layer $SrVO_3$ embedded in $SrTiO_3$ exhibit an MIT due to a reduction in band width by varying the number of $SrVO_3$ layers. The microscopic mechanism we reveal is a direct consequence of quantum confinement, and is distinct from previous studies invoking CF effects [154] or dimensionality [155], demonstrating the excellent versatility of the MIT in $SrVO_3$ with respect to different control parameters. Similar to Ref. [154], we find that the outer layers at the interface of the QW are more strongly correlated and trigger the transition in the rest of the layer. Our interpretation is also able to naturally explain the anomalous mass enhancement previously reported in ARPES measurements [306, 311]. Together, these results demonstrate the potency of employing quantum confinement as a tuning parameter for correlated electron behaviour in

engineered SLs. This approach also has the significant benefits that surface effects are avoided and that large (bulk-like) volumes of the system may respond to external stimuli. Aside from the expected improved performance of such a $SrVO_3$ device as a Mott transistor [154], quantized SLs made of other correlated materials are likely to show improved properties, e.g. superconducting devices in cuprate SLs [331], conductivity in nickelate SLs [332] or spintronic devices [333].

6.6 Appendix

6.6.1 DFT relaxed SLs with subsequent one-shot DFT+DMFT calculations

superlattice	2:7	3:6	6:5
mean *M*-*M* BL	4.00 Å	3.97 Å	3.92 Å
mean V-V BL	3.857 Å	3.878 Å	3.859 Å
mean Ti-Ti BL	4.028 Å	4.011 Å	3.987 Å
V-O buckling at IF	0.012 Å	0.004 Å	0.001 Å
Ti-O buckling at IF	0.006 Å	−0.003 Å	−0.012 Å
Sr-O buckling at IF	−0.029 Å	−0.029 Å	−0.037 Å

Table 6.3: Results of relaxing the atomic positions of the SLs within PP GGA. The mean *M*-*M* (*M* = V, Ti) bond lengths (BL) of the entire cell (fixed to the experimental diffraction values), $SrVO_3$ layers and $SrTiO_3$ layers are shown for comparison. The buckling of the VO_2, TiO_2 and SrO planes at the interface (IF) is also shown; these correspond to V-O, Ti-O and Sr-O bond angles of $< 1°$. Positive buckling indicates the metal ion is closer to the centre of the $SrVO_3$ layer than the oxygen.

superlattice	2:7	3:6	6:5
mean *M*-*M* BL	3.933 Å	3.921 Å	3.895 Å
mean V-V BL	3.798 Å	3.829 Å	3.835 Å
mean Ti-Ti BL	3.961 Å	3.961 Å	3.962 Å
V-O buckling at IF	0.010 Å	0.004 Å	0.001 Å
Ti-O buckling at IF	0.005 Å	−0.003 Å	−0.012 Å
Sr-O buckling at IF	−0.030 Å	−0.029 Å	−0.036 Å

Table 6.4: Results of relaxing the atomic positions and *c*-axis of the SLs within PP GGA. For comparison, the relaxed lattice parameters of bulk cubic $SrVO_3$ and $SrTiO_3$ within PP GGA are 3.855 Å and 3.932 Å. The PP GGA *c*-axis lattice parameters of $SrVO_3$ and $SrTiO_3$, with the ab plane constrained to the substrate (LSAT) lattice parameter (3.868 Å), are 3.845 Å and 3.970 Å, respectively. The parameters and acronyms here have the same definitions as in Table 6.3.

Relaxed atomic positions for the SL were obtained within the pseudo potential (PP) QUANTUM ESPRESSO code [334]. Ultrasoft potentials within the GGA [PBE] were used, with cutoffs of 40 and 400 Ry for the kinetic energy of the wave functions and charge density, respectively; these were the same as those used for the self-consistent ground-state in Ref. [22]. PP GGA was chosen

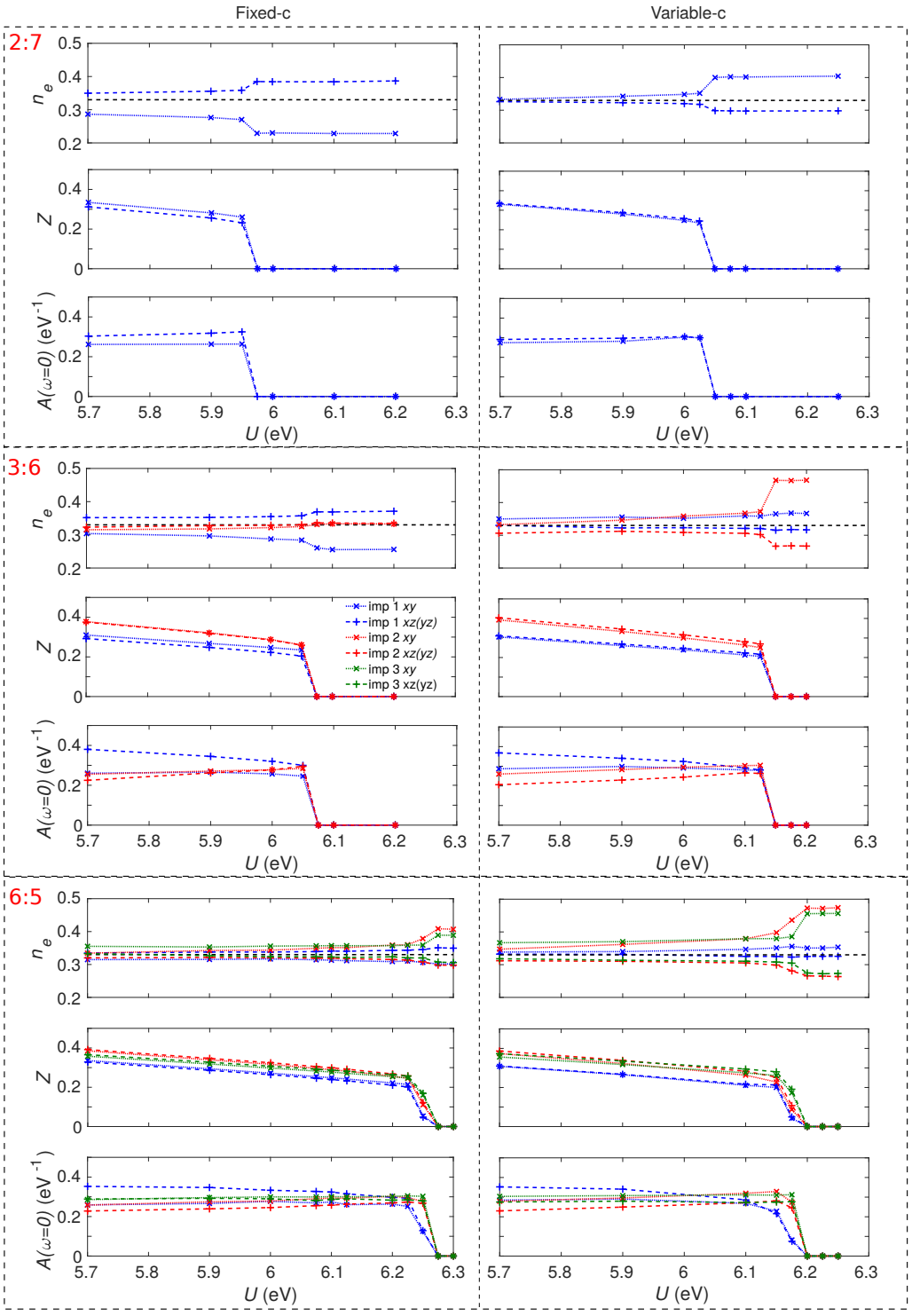

Figure 6.12: The effect of U on the orbital charge n_e (top), QP residue Z (middle) and the spectral function around the Fermi level (bottom) for the fixed c-axis and variable c-axis OS DFT+DMFT calculations. These quantities were extracted from the corresponding Green's functions and self-energies on either the imaginary time or Matsubara frequency axis. The dashed line represents the bulk degenerate orbital charge.

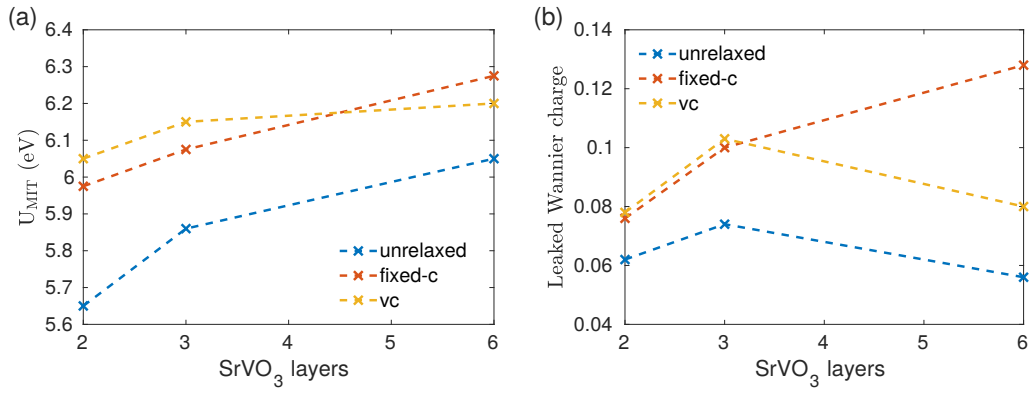

Figure 6.13: The (a) U_{MIT} and (b) total leaked Wannier charge from the V t_{2g} orbitals for each SL in the unrelaxed, fixed total c-axis length (fixed-c) relaxed, and varying total c-axis length (vc) relaxed calculations. The leaked charge was calculated by assuming that each V atom would have one electron in the t_{2g} orbitals if there were no interface effects, which is the case for bulk $SrVO_3$.

superlattice	CF splitting (meV)		
	unrelaxed	fixed c-axis	variable c-axis
6:5	33	79	35
3:6	40	40	45
2:7	51	48	57

Table 6.5: The results of fitting the QTB model to the LDA ELK SL calculations of the relaxed and unrelaxed structures. The crystal field (CF) splitting is the energy difference, $E^0_{yz} - E^0_{xy}$.

for the relaxation in order to account for some effects of electron correlation within a reasonable computational time frame. Only out-of-plane (z) atomic displacements were considered, imposed by the symmetry of the single unit cell, which was constrained to the experimental lattice parameters. This allows for different c-axis parameters for the $SrTiO_3$ and $SrVO_3$ layers, as well as out-of-plane relaxation at the $SrVO_3$-$SrTiO_3$ interface.

First, relaxation calculations were performed where the total length of the c-axis was fixed, as this length is experimentally known (this set of calculations will be referred to as fixed-c). The results are summarised in Table 6.3, showing the tendency of the $SrVO_3$ and $SrTiO_3$ layers towards the bulk parameters (a_{SrVO_3} = 3.84 Å and a_{SrTiO_3} = 3.97 Å). At the interface, a small buckling of the VO_2, TiO_2, and SrO layers is found, of the order of $< 1\%$ of the in-plane lattice parameter and corresponding to respective bond angles of $< 1°$.

For comparison, we have also allowed the c-axis to vary during the relaxation (and this relaxation set of calculations will be referred to as variable c-axis [vc]), yielding the atomic positions shown in Table 6.4. The $SrTiO_3$ layer thickness is stable at 3.96 Å, which is very close to the relaxed c-axis lattice parameter (3.970 Å) of epitaxially strained bulk $SrTiO_3$/LSAT within PP GGA. There is a small variation in $SrVO_3$ layer thickness, tending towards 3.83 Å for larger $SrVO_3$ layers, similar to the $SrVO_3$/LSAT c-axis parameter from PP-GGA of 3.845 Å. Buckling at

superlattice			DFT Wannier charge unrelaxed	fixed-c	vc
2:7	Imp 1	xy	0.299	0.302	0.311
		$xz(yz)$	0.335	0.330	0.325
	$\sum$ Imp	total	1.938	1.924	1.922
3:6	Imp 1	xy	0.303	0.319	0.331
		$xz(yz)$	0.328	0.312	0.304
	Imp 2	xy	0.296	0.306	0.315
		$xz(yz)$	0.356	0.354	0.352
	$\sum$ Imp	total	2.926	2.900	2.897
6:5	Imp 1	xy	0.307	0.307	0.318
		$xz(yz)$	0.335	0.321	0.330
	Imp 2	xy	0.310	0.317	0.319
		$xz(yz)$	0.345	0.338	0.340
	Imp 3	xy	0.315	0.326	0.329
		$xz(yz)$	0.340	0.334	0.327
	$\sum$ Imp	total	5.944	5.872	5.920

Table 6.6: The unrelaxed, fixed-c relaxed, and variable c-axis (vc) relaxed xy and $xz(yz)$ DFT Wannier orbital charges for each impurity (Imp). The total charge for each SL is calculated from all of the orbitals and $SrVO_3$ layers.

the interfaces is almost the same as in the previous relaxation results.

The resulting occupied V bands are only weakly affected; the main consequences of relaxation are (i) some high-n QW bands move to higher energy, implying the energetics of the interface are modified, (ii) the energy difference between V and Ti t_{2g} states is reduced, (iii) the O $2p$ states lower in energy. The buckling of the atomic positions are not significant considering that they do not vary significantly between both relaxed calculations. From (i) and (ii), the interface has changed in these relaxation calculations which may have consequences on the MIT, as it was shown in Fig. 6.5 of Section 6.4.1 that the interface plays a role in the MIT. Overall, the net effect of the relaxation is to decrease V-O hybridisation; band widths and CF energies (in Table 6.5) are only marginally affected. Therefore, confinement is still the mechanism for the MIT in these SLs (see the discussion in Section 6.4.2 for details about the mechanism).

The relaxed atomic positions were used as an input into the DFT+DMFT cycle, beginning with the self-consistent LDA ground-state calculations (with the same DFT input parameters as described in Section 6.2) in the ELK code. The preliminary OS DFT+DMFT results (which used the same parameters as described in Section 6.4) of both the fixed-c and vc are shown in Figs. 6.12 and 6.13. As the FCSC DFT+DMFT method mainly affects the polarisation of the orbital charges in the unrelated results, conclusions can be made from the presented OS DFT+DMFT results.

In Fig. 6.12, the Z and $A(\omega = 0)$ results follow the same trends as in the unrelaxed SLs. Across all of the SLs, it is the interface [$xz(yz)$] orbitals which lose spectral weight first and reduce in QP band width as the U value approaches U_{MIT}. This strongly reinforces the significance that interface plays in the MIT. The intriguing result from these OS DFT+DMFT calculations of the relaxed systems is the change in the U_{MIT} values for each SL compared with the unrelaxed counterparts, as shown in Fig. 6.13 (a). It can be seen from Figs. 6.13 (a) and (b) that the changes in U_{MIT} can be associated to the total DFT Wannier charge leakage from the V atoms of the SLs' QWs (which are also given in Table 6.6). Therefore, an increased DFT Wanner charge leakage from the V layers, which mostly occurs at the V-Ti interface (see Section 6.4.1), correlates to a greater U_{MIT} value in the SL. This reinforces the notion that the interface influences the strength of the local electron correlations required to cause the MIT. Therefore, the MIT could be tuned by influencing the interface (by strain, using different materials, and so on). It should be noted that although the U_{MIT} values vary between the relaxed and unrelaxed calculations for each SL, these values are still significantly less than the bulk and strain U_{MIT} values. The CF splitting of the relaxed and unrelaxed SLs in Table 6.5 show that the splitting is uncorrelated with U_{MIT}, which indicates that confinement is still the main mechanism behind the MIT in these SL systems.

The orbital occupations of the inner $SrVO_3$ layer(s) in Fig. 6.12 become more polarised compared with the interface for all multiple impurity relaxed SL calculations except for the fixed-c 3:6 SL. Intriguingly, the orbital occupation flips in the vc results compared with the fixed-c and unrelaxed calculations. All of these changes in the occupations do not correspond to the DFT occupation counterparts in Table 6.6 which suggests that other factors in the DFT+DMFT calculations influence these charges. Ref. [335] has shown that the local Coulomb interactions from DMFT can significantly change the orbital dependence on the CF splitting. Our preliminary results are reminiscent of this, so further work (and FCSC DFT+DMFT calculations) needs to be done on these systems to determine if the CF splitting or confinement is responsible for these changes to the orbital occupancy.

6.6.2 Experiment-theory quantities

Figure 6.14 shows a schematic illustration comparing the extracted experimental quantities with their DFT+DMFT definitions. The QP band width has been extracted from the DMFT spectral function by obtaining the width defined by the minima around the central QP peak. The QP ratio was determined by taking the ratio of the the QP weight (labelled Q in Fig. 6.14) and the UHB weight (labelled U). Finally, the energy of the UHB was obtained by locating the peak in the DMFT spectral function, with respect to $\omega = 0$. In the experimental RIXS process, the UHB peak energy represents the peak in the joint QP and UHB density of states, and therefore is referenced to an energy $\omega < 0$. To compare the theoretical and experimental UHB energies, we therefore apply a constant shift to all of the theoretical UHBs so that the 2:7 SLs match (the shift is -0.584 eV).

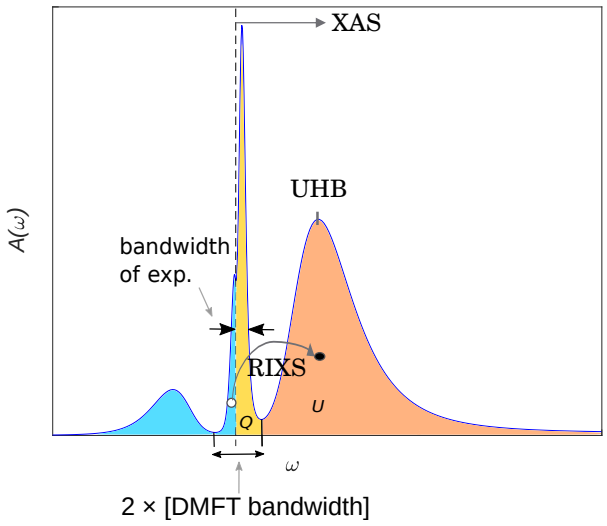

Figure 6.14: A schematic illustration of how the variables in the theory-experimental comparison were determined, see the text.

6.6.3 G0W0 bulk and monolayer $SrVO_3$

Non-local electron correlations have significant effects in bulk $SrVO_3$ as shown by previous GW and GW+DMFT studies [141, 146, 336]. This has been discussed in Section 4.1.1. The important question for this section is whether the insulating state in the presented $SrVO_3$ SLs can be described by the non-local correlations from $G0W0$. First we will look at $G0W0$ calculations for bulk, and then apply $G0W0$ on monolayer $SrVO_3$ (which has been discussed in Section 4.3.1). Unfortunately, the SLs cannot be investigated with $G0W0$ as these calculations are too computationally demanding. However, the bulk and monolayer results will give the effect of changing the dimensionality in $SrVO_3$ at the different extreme dimensional limits. The electron correlations in the monolayer are expected to be the greatest out of all systems studied in this chapter. If these $G0W0$ calculations remain metallic, it would imply that the SLs would unlikely be insulating as a consequence of non-local electron correlations.

Bulk $G0W0$ started from the converged LDA electronic structure with a Monkhorst-Pack k-mesh of 12×12×12 (as in Section 4.1.1). The $G0W0$ q-mesh used was 3×3×1 with a maximum Matsubara frequency cutoff of 272.11 eV and β = 7.74 eV^{-1}. For monolayer $SrVO_3$, a 15×15×1 Monkhorst-Pack k-mesh with the GGA (PEB) functional was used (as in Section 4.3.1). The $G0W0$ monolayer calculations used a q-mesh of 5×5×1, a maximum Matsubara frequency cutoff of 272.11 eV, and β = 7.74 eV^{-1}.

The results of the bulk $SrVO_3$ $G0W0$ and DFT DOS are shown in Fig. 6.15 (a), where these are also compared with the $G0W0$ V t_{2g} spectral functions from Refs. [146, 336]. Note that the ELK results show the total DOS, whereas the literature presented the t_{2g} DOS. The $G0W0$ QP widths are comparable with the literature showing that the ELK $G0W0$ results are producing the expected renormalisation. Interestingly, the position of the $G0W0$ Fermi level in the QP

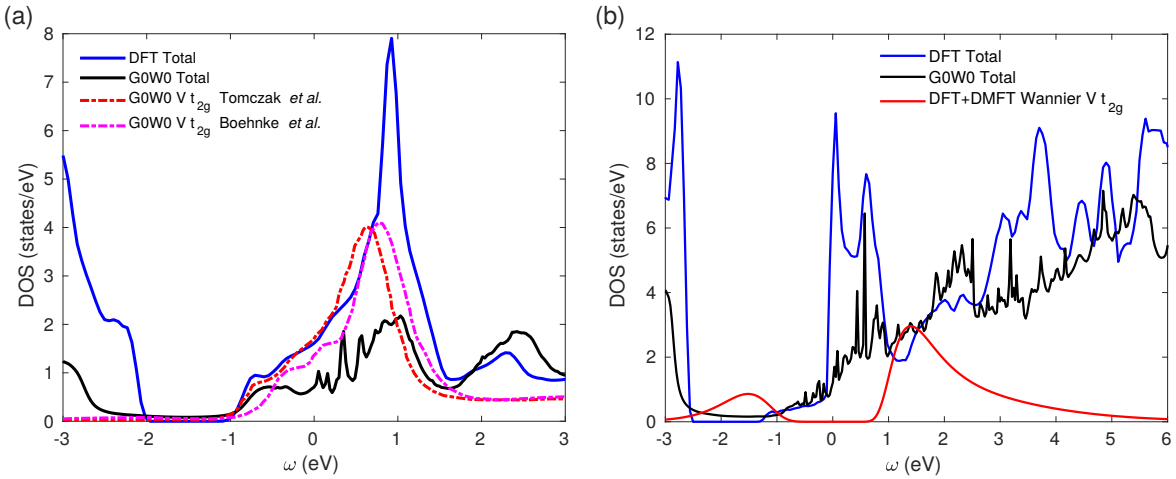

Figure 6.15: (a) Comparison of the total $G0W0$ spectral function of bulk $SrVO_3$ with the DFT DOS and the $G0W0$ V t_{2g} partial spectral function results from J. M. Tomczak *et al.* [336] and L. Boehnke *et al.* [146]. (b) The comparison of the monolayer DFT total DOS, $G0W0$ total spectral function and the fully charge self-consistent DFT+DMFT Wannier V t_{2g} spectral function.

peak are different between the literature results. The striking difference between the presented results is the noise in the QP peak of the ELK $G0W0$ results. The additional noise in our $G0W0$ calculations is due to the method in which the BZ is integrated in ELK $G0W0$ calculations, as well as our inclusion of all states (Sr, V, O and interstitial DOS) compared with the V t_{2g} partial spectral function presented by the literature references. Interpolation methods cannot be used for a $G0W0$ BZ integration (due to the non-local nature of GW), so ELK can only integrate over the k-mesh used in the $G0W0$ calculation (which causes this a well known noise problem in the bulk $SrVO_3$, see the discussion in Section 4.1.1). Overall, these results show that bulk $SrVO_3$ is metallic with a QP band width renormalisation in $G0W0$, which is in agreement with literature, and the sources of the discrepancies in the results are known.

In the monolayer dimensionality limit, Fig. 6.15 (b) shows that both DFT and $G0W0$ predict the monolayer system to be metallic, whereas the DFT+DMFT calculations (from Section 4.1.1) produce an insulator. Therefore, the DFT+DMFT results are more inline with the experimental results, as expected for this Mott insulator system. The more subtle sharp features seen in the DFT has likely been smeared out in $G0W0$ and the noise in the $G0W0$ DOS is likely coming from the small number of k-points used for the BZ integration. From these results, we assert that the inclusion of non-local correlations from the $G0W0$ calculations are unable to produce the experimentally observed insulating state in the monolayer – this Mott insulating state can only be described by (DFT+)DMFT. Therefore, it is very unlikely that the insulating state in the SLs would be described by non-local correlations.

CHAPTER 7

SUMMARY AND OUTLOOK

The work presented in this thesis shows a comprehensive interface between the ELK code and TRIQS library, both being open source. This not only enables the DFT+DMFT calculations within the ELK-TRIQS package along with the spectral functions, but facilitates the calculation of DFT+DMFT quantities which are solely dependent on the wave functions (and occupations). These quantities have the advantage of being calculable without the need of analytic continuation. In Chapter 4, the ELK-TRIQS interface has been shown to work for different systems and the DFT+DMFT ELF wave-function-dependent quantity was presented. These results show the significance this work has for the wider DFT+DMFT community.

The ELF does give further insight into the electronic structure, but it does not have a corresponding experimental measurement. However, Chapter 5 presents the DFT+DMFT EMD wave-function-dependent quantity which can be experimentally verified by Compton scattering experiments. This chapter validates the results from ELK-TRIQS with respect to the established KKR+DMFT MCPs setup, as well as giving further insight into DMFT induced changes to the Ni MCPs and the Fermi surface. The Ni MCPs cannot be fully described by DFT+DMFT meaning that there are missing electron correlations which will require other many-body theories (such as GW, GW+DMFT, and so on) to predict them. This chapter also introduces the DFT+DMFT Compton profile calculations, and the directional differences, of V. The DFT+DMFT V results improves the agreement with the majority of the experimental quantities, although there are questions about the reliability of the experimental Compton data. However, there are still significant discrepancies with the experimental data which require further investigation using theories which include electron correlations missing in the DFT+DMFT method (such as GW, GW+DMFT, and so on). This work with the DFT+DMFT EMDs could be extended to DFT+DMFT TPMD calculations for comparisons with the V 2D-ACAR experimental data.

Finally, in Chaper 6, the DFT+DMFT results of $SrVO_3/SrTiO_3$ SLs are able to reproduce the corresponding experimental quantities, as well as reveal the MIT mechanism in these systems: quantum confinement. The MIT in these systems are also influenced by the interface in the SLs, which affects the strength of the local correlations at the interface. The experimentally observed anomalous mass enhancement is predicted in these SLs and is a consequence of confinement here. These results show that there is another tunable parameter (quantum confinement) which can be used to control the electron correlations for device engineering with not only these $SrVO_3/SrTiO_3$ SLs, but SLs comprised with other transition metal oxides. Notably, these systems avoid the need of surface effects.

Overall, the DFT+DMFT method employed in the materials in this thesis provide vital insight and improved agreement with corresponding experimental quantities. However, there is still a requirement to go beyond the DFT+DMFT picture, in many of the presented materials, to include vital missing electron correlations.

There are other many-body theories which could be used to extend the work presented in this thesis, especially for the calculation of the EMD. Recently, there has been work to include the dynamic interaction matrix $U_{m,m',m'',m'''}(z)$ which is currently being used for density-density interaction Hamiltonians [81]. Also, DMFT has been extended to include a cluster of impurity sites (see Ref. [337] and the references therein). Nonetheless, other many-body techniques must be looked into to include the missing electron correlations when modelling real systems. Another established many-body technique used with DFT is GW, which is an approximation to the Hedin's equations [78]. This technique calculates the dynamical self-energy from the screened non-local Coulomb charge within the system, meaning that non-local electron correlations from charge fluctuations can be investigated. This technique has been developed further to update the DFT description in a self-consistent manner between DFT and GW. Although there are many different implementations of this self-consistency, the most notable technique is QP self-consistent GW (QSGW) [338]. As DMFT includes the local electron correlation effects, DMFT has been combined with GW to describe the different physical phenomena which arise in both techniques. This leads to the GW+DMFT [81] and the QSGW+DMFT methods [339].

There is current work to extend the DMFT formalism to include the non-local vertices which should go beyond the physical description provided by GW+DMFT (and the QSGW+DMFT variant). Techniques such as dynamic vertex approximation (DΓA), dual fermion, and Trilex are examples of this, and further details can be found in Ref. [337]. However, these techniques are currently in their infancy for real material calculations, but real material results from the DΓA technique [340] are starting to emerge. With these techniques and the continual improvement of computational resources, capturing the complex physics in real material models is ever getting closer.

BIBLIOGRAPHY

[1] Z. I. Alferov, "The semiconductor revolution in the 20th century," Russian Chemical Reviews **82**, 587–596 (2013).

[2] H. Wong and H. Iwai, "The road to miniaturization," Physics World **18**, 40–44 (2005).

[3] M. Sato and Y. Ando, "Topological superconductors: a review," Reports on Progress in Physics **80**, 076501 (2017).

[4] G. R. Stewart, "Unconventional superconductivity," Advances in Physics **66**, 75–196 (2017).

[5] L. de' Medici, R. Eder, M. Fabrizio, F. Gebhard, R. Heid, V. Janiš, H. Kroha, A. Lichtenstein, A. Oleś, P. Prelovsek, R. Resta, A. Sanna, E. Pavarini, E. Koch, R. Scalettar, and R. Martin, *The Physics of Correlated Insulators, Metals, and Superconductors* (2017).

[6] A. Georges, L. d. Medici, and J. Mravlje, "Strong correlations from hund's coupling," Annual Review of Condensed Matter Physics **4**, 137–178 (2013).

[7] K. Stadler, G. Kotliar, A. Weichselbaum, and J. von Delft, "Hundness versus mottness in a three-band hubbard-hund model: On the origin of strong correlations in hund metals," Annals of Physics **405**, 365–409 (2019).

[8] M. A. Continentino, "Quantum critical point in heavy fermions," Brazilian Journal of Physics **35**, 197 – 203 (2005).

[9] E. Snider, N. Dasenbrock-Gammon, R. McBride, M. Debessai, H. Vindana, K. Vencatasamy, K. V. Lawler, A. Salamat, and R. P. Dias, "Room-temperature superconductivity in a carbonaceous sulfur hydride," Nature **586**, 373–377 (2020).

[10] Y. Tokura, M. Kawasaki, and N. Nagaosa, "Emergent functions of quantum materials," Nature Phys. **13**, 1056 (2017).

[11] M. Brahlek, L. Zhang, J. Lapano, H.-T. Zhang, R. Engel-Herbert, N. Shukla, S. Datta, H. Paik, and D. Schlom, "Opportunities in vanadium-based strongly correlated electron systems," MRS Commun. **7**, 27 (2017).

[12] J. Mannhart and D. G. Schlom, "Oxide interfaces — an opportunity for electronics," Science **327**, 1607 (2010).

[13] G. Kotliar, S. Y. Savrasov, K. Haule, V. S. Oudovenko, O. Parcollet, and C. A. Marianetti, "Electronic structure calculations with dynamical mean-field theory," Rev. Mod. Phys. **78**, 865 (2006).

[14] J. K. Dewhurst, S. Sharma, L. Nordström, F. Cricchio, O. Granas, and E. K. U. Gross, http://elk.sourceforge.net/.

[15] O. Parcollet, M. Ferrero, T. Ayral, H. Hafermann, I. Krivenko, L. Messio, and P. Seth, "TRIQS: A toolbox for research on interacting quantum systems," Comp. Phys. Commun. **196**, 398 (2015).

[16] M. Aichhorn, L. Pourovskii, P. Seth, V. Vildosola, M. Zingl, O. E. Peil, X. Deng, J. Mravlje, G. J. Kraberger, C. Martins, M. Ferrero, and O. Parcollet, "TRIQS/DFTTools: A TRIQS application for ab initio calculations of correlated materials," Comp. Phys. Commun. **204**, 200 (2016).

[17] S. B. Dugdale, "Life on the edge: a beginner's guide to the Fermi surface," Physica Scripta **91**, 053009 (2016).

[18] S. B. Dugdale, "Probing the Fermi surface by positron annihilation and Compton scattering," Low Temperature Physics **40**, 328–338 (2014).

[19] M. J. Cooper, B. Barbiellini, P. Mijnarends, N. Shiotani, N. Sakai, and A. Bansil, *X-Ray Compton Scattering*, Oxford Series on Synchrotron Radiation (OUP Oxford, 2004).

[20] B. Barbiellini, "High-temperature cuprate superconductors studied by x-ray Compton scattering and positron annihilation spectroscopies," Journal of Physics: Conference Series **443**, 012009 (2013).

[21] I. G. Kaplan, B. Barbiellini, and A. Bansil, "Compton scattering beyond the impulse approximation," Phys. Rev. B **68**, 235104 (2003).

[22] J. Laverock, M. Gu, V. Jovic, J. W. Lu, S. Wolf, R. M. Qiao, W. Yang, and K. Smith, "Nano-engineering of electron correlation in oxide superlattices," Nano Futures **1**, 031001 (2017).

[23] A. D. N. James, E. I. Harris-Lee, A. Hampel, M. Aichhorn, and S. B. Dugdale, "Wave functions, electronic localization, and bonding properties for correlated materials beyond the Kohn-Sham formalism," Phys. Rev. B **103**, 035106 (2021).

[24] A. D. N. James, M. Sekania, S. B. Dugdale, and L. Chioncel, "Magnetic Compton profiles of Ni beyond the one-particle picture: Numerically exact and perturbative solvers of dynamical mean-field theory," Phys. Rev. B **103**, 115144 (2021).

[25] A. D. N. James, M. Aichhorn, and J. Laverock, "Quantum confinement induced metal-insulator transition in strongly correlated quantum wells of $SrVO_3$ superlattices," Phys. Rev. Research **3**, 023149 (2021).

[26] http://bris.ac.uk/acrc/.

[27] K. Momma and F. Izumi, "VESTA 3 for three-dimensional visualization of crystal, volumetric and morphology data," Journal of applied crystallography **44**, 1272–1276 (2011).

[28] J. J. Thomson M.A. F.R.S., "XL. Cathode Rays," The London, Edinburgh, and Dublin Philosophical Magazine and Journal of Science **44**, 293–316 (1897).

[29] I. Falconer, "J J Thomson and the discovery of the electron," Physics Education **32**, 226–231 (1997).

[30] P. Drude, "Zur Elektronentheorie der Metalle," Annalen der Physik **306**, 566–613 (1900).

[31] P. Drude, "Zur Elektronentheorie der Metalle; II. Teil. Galvanomagnetische und thermomagnetische Effecte," Annalen der Physik **308**, 369–402 (1900).

[32] N. Ashcroft and N. Mermin, *Solid State Physics* (Cengage Learning, 2011).

[33] C. Kittel, *Introduction to Solid State Physics*, 8th ed. (Wiley, New York, 2004).

[34] P. Hofmann, *Solid state physics: an introduction*, 2nd ed. (John Wiley & Sons, 2015).

[35] G. D. Mahan, *Condensed matter in a nutshell*, Vol. 8 (Princeton University Press, 2011).

[36] J. M. Ziman, *Principles of the Theory of Solids* (Cambridge University Press, 1972).

[37] C. Kittel, *Quantum Theory of Solids* (Wiley, 1987).

[38] R. Mattuck, *A Guide to Feynman Diagrams in the Many-Body Problem: Second Edition*, 2nd ed., Dover Books on Physics (Dover Publications, 2012).

[39] H. Bruus and K. Flensberg, *Many-body quantum theory in condensed matter physics - an introduction* (Oxford University Press, United States, 2004).

[40] G. D. Mahan, *Many-Particle Physics*, 3rd ed. (Plenum, New York, N.Y., 2000).

[41] D. Pines and P. Nozieres, *Theory of Quantum Liquids*, Vol. 1 and 2 (CRC Press, 2018).

[42] G. Giuliani and G. Vignale, "The normal Fermi liquid," in *Quantum Theory of the Electron Liquid* (Cambridge University Press, 2005) p. 405–500.

[43] A. Anderson, "Canonical transformations in quantum mechanics," Annals of Physics **232**, 292–331 (1994).

[44] J. Lacki, "The puzzle of canonical transformations in early quantum mechanics," Studies in History and Philosophy of Science Part B: Studies in History and Philosophy of Modern Physics **35**, 317–344 (2004).

[45] R. P. Feynman, "Space-Time Approach to Quantum Electrodynamics," Phys. Rev. **76**, 769–789 (1949).

[46] W. Schülke, G. Stutz, F. Wohlert, and A. Kaprolat, "Electron momentum-space densities of Li metal: A high-resolution Compton-scattering study," Phys. Rev. B **54**, 14381–14395 (1996).

[47] F. Bechstedt, *Many-Body Approach to Electronic Excitations* (Springer, 2016).

[48] R. M. Martin, *Electronic structure: basic theory and practical methods* (Cambridge university press, 2004).

[49] M. Born and R. Oppenheimer, "Zur quantentheorie der molekeln," Annalen der Physik **389**, 457–484 (1927).

[50] M. Born and K. Huang, *Dynamic Theory of Crystal Lattice* (Oxford University Press, 1954).

[51] D. R. Hartree, "The Wave Mechanics of an Atom with a Non-Coulomb Central Field. Part I. Theory and Methods," Mathematical Proceedings of the Cambridge Philosophical Society **24**, 89–110 (1928).

[52] V. Fock, "Konfigurationsraum und zweite Quantelung," Zeitschrift für Physik **75**, 622–647 (1932).

[53] J. C. Slater, "Note on Hartree's Method," Phys. Rev. **35**, 210–211 (1930).

[54] H. Eschrig, *The fundamentals of density functional theory*, Vol. 32 (Springer, 1996).

[55] K. Capelle, "A bird's-eye view of density-functional theory," Brazilian Journal of Physics **36**, 1318–1343 (2006).

[56] J. C. Slater, "The Theory of Complex Spectra," Phys. Rev. **34**, 1293–1322 (1929).

[57] P. Hohenberg and W. Kohn, "Inhomogeneous Electron Gas," Phys. Rev. **136**, B864–B871 (1964).

[58] W. Kohn and L. J. Sham, "Self-Consistent Equations Including Exchange and Correlation Effects," Phys. Rev. **140**, A1133–A1138 (1965).

[59] D. M. Ceperley and B. J. Alder, "Ground State of the Electron Gas by a Stochastic Method," Phys. Rev. Lett. **45**, 566–569 (1980).

[60] J. P. Perdew and Y. Wang, "Accurate and simple analytic representation of the electron-gas correlation energy," Phys. Rev. B **45**, 13244–13249 (1992).

[61] C. S. Wang, B. M. Klein, and H. Krakauer, "Theory of Magnetic and Structural Ordering in Iron," Phys. Rev. Lett. **54**, 1852–1855 (1985).

[62] T. Asada and K. Terakura, "Cohesive properties of iron obtained by use of the generalized gradient approximation," Phys. Rev. B **46**, 13599–13602 (1992).

[63] D. Langreth and J. Perdew, "Theory of nonuniform electronic systems. I. Analysis of the gradient approximation and a generalization that works," Phys. Rev. B **21**, 5469–5493 (1980).

[64] J. P. Perdew, K. Burke, and Y. Wang, "Generalized gradient approximation for the exchange-correlation hole of a many-electron system," Phys. Rev. B **54**, 16533–16539 (1996).

[65] K. Burke, J. P. Perdew, and M. Ernzerhof, "Why the generalized gradient approximation works and how to go beyond it," International Journal of Quantum Chemistry **61**, 287–293 (1997).

[66] J. Sun, A. Ruzsinszky, and J. P. Perdew, "Strongly Constrained and Appropriately Normed Semilocal Density Functional," Phys. Rev. Lett. **115**, 036402 (2015).

[67] Y. Fu and D. J. Singh, "Density functional methods for the magnetism of transition metals: SCAN in relation to other functionals," Phys. Rev. B **100**, 045126 (2019).

[68] F. Tran, G. Baudesson, J. Carrete, G. K. H. Madsen, P. Blaha, K. Schwarz, and D. J. Singh, "Shortcomings of meta-GGA functionals when describing magnetism," Phys. Rev. B **102**, 024407 (2020).

[69] D. J. Singh and L. Nordstrom, *Planewaves, Pseudopotentials, and the LAPW method* (Springer Science & Business Media, 2006).

[70] J. Zabloudil, R. Hammerling, L. Szunyogh, and P. Weinberger, *Electron Scattering in Solid Matter: A Theoretical and Computational Treatise* (Springer Berlin Heidelberg, 2006).

[71] P. Blaha, K. Schwarz, F. Tran, R. Laskowski, G. K. H. Madsen, and L. D. Marks, "WIEN2k: An APW+lo program for calculating the properties of solids," The Journal of Chemical Physics **152**, 074101 (2020).

[72] O. K. Andersen, "Linear methods in band theory," Phys. Rev. B **12**, 3060–3083 (1975).

[73] P. Kurz, F. Förster, L. Nordström, G. Bihlmayer, and S. Blügel, "Ab initio treatment of noncollinear magnets with the full-potential linearized augmented plane wave method," Phys. Rev. B **69**, 024415 (2004).

[74] K. Lejaeghere, G. Bihlmayer, T. Björkman, P. Blaha, S. Blügel, V. Blum, D. Caliste, I. E. Castelli, S. J. Clark, A. Dal Corso, *et al.*, "Reproducibility in density functional theory calculations of solids," Science **351**, aad3000 (2016).

[75] A. Auerbach, *Interacting Electrons and Quantum Magnetism* (Springer New York, 2012).

[76] A. Altland and B. Simons, *Condensed Matter Field Theory* (Cambridge University Press, 2010).

[77] F. Essler, H. Frahm, F. Göhmann, A. Klümper, and V. Korepin, *The One-Dimensional Hubbard Model* (Cambridge University Press, 2005).

[78] L. Hedin, "New Method for Calculating the One-Particle Green's Function with Application to the Electron-Gas Problem," Phys. Rev. **139**, A796–A823 (1965).

[79] L. Vaugier, H. Jiang, and S. Biermann, "Hubbard U and Hund exchange J in transition metal oxides: Screening versus localization trends from constrained random phase approximation," Phys. Rev. B **86**, 165105 (2012).

[80] F. Aryasetiawan, K. Karlsson, O. Jepsen, and U. Schönberger, "Calculations of Hubbard U from first-principles," Phys. Rev. B **74**, 125106 (2006).

[81] S. Biermann, "Dynamical screening effects in correlated electron materials — a progress report on combined many-body perturbation and dynamical mean field theory: 'GW+DMFT'," Journal of Physics: Condensed Matter **26**, 173202 (2014).

[82] J. Hubbard, "Electron correlations in narrow energy bands," Proceedings of the Royal Society of London. Series A. Mathematical and Physical Sciences **276**, 238–257 (1963).

[83] J. Hubbard, "Electron correlations in narrow energy bands. II. The degenerate band case," Proceedings of the Royal Society of London. Series A. Mathematical and Physical Sciences **277**, 237–259 (1964).

[84] J. Hubbard, "Electron correlations in narrow energy bands III. An improved solution," Proceedings of the Royal Society of London. Series A. Mathematical and Physical Sciences **281**, 401–419 (1964).

[85] A. Georges and W. Krauth, "Physical properties of the half-filled Hubbard model in infinite dimensions," Phys. Rev. B **48**, 7167–7182 (1993).

[86] A. Georges, G. Kotliar, W. Krauth, and M. J. Rozenberg, "Dynamical mean-field theory of strongly correlated fermion systems and the limit of infinite dimensions," Rev. Mod. Phys. **68**, 13–125 (1996).

[87] G. Kotliar and D. Vollhardt, "Strongly correlated materials: Insights from dynamical mean-field theory," Physics today **57**, 53–60 (2004).

[88] R. O. Zaitsev, "On the Phase Diagram of the 1D Hubbard Model," Journal of Experimental and Theoretical Physics **129**, 1079–1085 (2019).

[89] M. Karbach and G. Muller, "Introduction to the Bethe ansatz I," (1998), arXiv:cond-mat/9809162 [cond-mat.stat-mech] .

[90] M. Imada, A. Fujimori, and Y. Tokura, "Metal-insulator transitions," Rev. Mod. Phys. **70**, 1039–1263 (1998).

[91] A. I. Liechtenstein, V. I. Anisimov, and J. Zaanen, "Density-functional theory and strong interactions: Orbital ordering in Mott-Hubbard insulators," Phys. Rev. B **52**, R5467–R5470 (1995).

[92] V. I. Anisimov, F. Aryasetiawan, and A. I. Lichtenstein, "First-principles calculations of the electronic structure and spectra of strongly correlated systems: the LDA+U method," Journal of Physics: Condensed Matter **9**, 767–808 (1997).

[93] A. B. Shick, A. I. Liechtenstein, and W. E. Pickett, "Implementation of the LDA+U method using the full-potential linearized augmented plane-wave basis," Phys. Rev. B **60**, 10763–10769 (1999).

[94] B. Himmetoglu, A. Floris, S. de Gironcoli, and M. Cococcioni, "Hubbard-corrected DFT energy functionals: The LDA+U description of correlated systems," International Journal of Quantum Chemistry **114**, 14–49 (2014).

[95] M. Cococcioni and S. de Gironcoli, "Linear response approach to the calculation of the effective interaction parameters in the LDA + U method," Phys. Rev. B **71**, 035105 (2005).

[96] T. Ribic, E. Assmann, A. Tóth, and K. Held, "Cubic interaction parameters for t_{2g} Wannier orbitals," Phys. Rev. B **90**, 165105 (2014).

[97] J. Kanamori, "Electron Correlation and Ferromagnetism of Transition Metals," Progress of Theoretical Physics **30**, 275–289 (1963).

[98] A. G. Petukhov, I. I. Mazin, L. Chioncel, and A. I. Lichtenstein, "Correlated metals and the LDA + U method," Phys. Rev. B **67**, 153106 (2003).

[99] M. B. Zölfl, T. Pruschke, J. Keller, A. I. Poteryaev, I. A. Nekrasov, and V. I. Anisimov, "Combining density-functional and dynamical-mean-field theory for $La_{1-x}Sr_xTiO_3$," Phys. Rev. B **61**, 12810–12815 (2000).

[100] K. Held, I. A. Nekrasov, G. Keller, V. Eyert, N. Blümer, A. K. McMahan, R. T. Scalettar, T. Pruschke, V. I. Anisimov, and D. Vollhardt, "The LDA+DMFT approach to materials with strong electronic correlations," (1998), arXiv:cond-mat/0112079 [cond-mat.str-el] .

[101] K. Held, "Electronic structure calculations using dynamical mean field theory," Advances in Physics **56**, 829–926 (2007).

[102] P. W. Anderson, "Localized Magnetic States in Metals," Phys. Rev. **124**, 41–53 (1961).

[103] P. A. Wolff, "Localized Moments in Metals," Phys. Rev. **124**, 1030–1035 (1961).

[104] A. Georges, "Strongly Correlated Electron Materials: Dynamical Mean-Field Theory and Electronic Structure," AIP Conference Proceedings **715**, 3–74 (2004).

[105] J. Kondo, "Resistance Minimum in Dilute Magnetic Alloys," Progress of Theoretical Physics **32**, 37–49 (1964).

[106] W. J. de Haas, J. de Boer, and G. J. van dën Berg, "The electrical resistance of gold, copper and lead at low temperatures," Physica **1**, 1115–1124 (1934).

[107] N. Andrei, K. Furuya, and J. H. Lowenstein, "Solution of the Kondo problem," Rev. Mod. Phys. **55**, 331–402 (1983).

[108] J. R. Schrieffer and P. A. Wolff, "Relation between the Anderson and Kondo Hamiltonians," Phys. Rev. **149**, 491–492 (1966).

[109] P. W. Anderson, "A poor man's derivation of scaling laws for the Kondo problem," Journal of Physics C: Solid State Physics **3**, 2436–2441 (1970).

[110] E. Gull, A. J. Millis, A. I. Lichtenstein, A. N. Rubtsov, M. Troyer, and P. Werner, "Continuous-time Monte Carlo methods for quantum impurity models," Rev. Mod. Phys. **83**, 349–404 (2011).

[111] Y. Lu and M. W. Haverkort, "Exact diagonalization as an impurity solver in dynamical mean field theory," The European Physical Journal Special Topics **226**, 2549–2564 (2017).

[112] D. Bauernfeind, M. Zingl, R. Triebl, M. Aichhorn, and H. G. Evertz, "Fork Tensor-Product States: Efficient Multiorbital Real-Time DMFT Solver," Phys. Rev. X **7**, 031013 (2017).

[113] M. I. Katsnelson and A. I. Lichtenstein, "Electronic structure and magnetic properties of correlated metals," The European Physical Journal B-Condensed Matter and Complex Systems **30**, 9–15 (2002).

[114] A. N. Rubtsov, V. V. Savkin, and A. I. Lichtenstein, "Continuous-time quantum Monte Carlo method for fermions," Phys. Rev. B **72**, 035122 (2005).

[115] E. Gull, P. Werner, O. Parcollet, and M. Troyer, "Continuous-time auxiliary-field Monte Carlo for quantum impurity models," Europhys. Lett. **82**, 57003 (2008).

[116] P. Werner, A. Comanac, L. de' Medici, M. Troyer, and A. J. Millis, "Continuous-Time Solver for Quantum Impurity Models," Phys. Rev. Lett. **97**, 076405 (2006).

[117] N. Metropolis, A. W. Rosenbluth, M. N. Rosenbluth, A. H. Teller, and E. Teller, "Equation of State Calculations by Fast Computing Machines," The Journal of Chemical Physics **21**, 1087–1092 (1953).

[118] W. K. Hastings, "Monte Carlo sampling methods using Markov chains and their applications," Biometrika **57**, 97–109 (1970).

[119] K. S. D. Beach, R. J. Gooding, and F. Marsiglio, "Reliable Padé analytical continuation method based on a high-accuracy symbolic computation algorithm," Phys. Rev. B **61**, 5147–5157 (2000).

[120] M. Jarrell and J. Gubernatis, "Bayesian inference and the analytic continuation of imaginary-time quantum Monte Carlo data," Physics Reports **269**, 133–195 (1996).

[121] S. Fuchs, T. Pruschke, and M. Jarrell, "Analytic continuation of quantum Monte Carlo data by stochastic analytical inference," Phys. Rev. E **81**, 056701 (2010).

[122] R. Levy, J. LeBlanc, and E. Gull, "Implementation of the maximum entropy method for analytic continuation," Computer Physics Communications **215**, 149–155 (2017).

[123] G. J. Kraberger, R. Triebl, M. Zingl, and M. Aichhorn, "Maximum entropy formalism for the analytic continuation of matrix-valued Green's functions," Phys. Rev. B **96**, 155128 (2017).

[124] G. Kraberger, *Development of a full matrix ab-initio scheme for materials with strong spin-orbit coupling and Coulomb interactions, Application to selected iridates and osmates*, PhD Thesis, Graz University of Technology (2019).

[125] G. J. Kraberger and M. Zingl, `https://github.com/TRIQS/maxent`.

[126] R. N. Silver, D. S. Sivia, and J. E. Gubernatis, "Maximum-entropy method for analytic continuation of quantum Monte Carlo data," Phys. Rev. B **41**, 2380–2389 (1990).

[127] N. Marzari, A. A. Mostofi, J. R. Yates, I. Souza, and D. Vanderbilt, "Maximally localized Wannier functions: Theory and applications," Rev. Mod. Phys. **84**, 1419–1475 (2012).

[128] F. Lechermann, A. Georges, A. Poteryaev, S. Biermann, M. Posternak, A. Yamasaki, and O. K. Andersen, "Dynamical mean-field theory using Wannier functions: A flexible route to electronic structure calculations of strongly correlated materials," Phys. Rev. B **74**, 125120 (2006).

[129] B. Amadon, F. Lechermann, A. Georges, F. Jollet, T. O. Wehling, and A. I. Lichtenstein, "Plane-wave based electronic structure calculations for correlated materials using dynamical mean-field theory and projected local orbitals," Phys. Rev. B **77**, 205112 (2008).

[130] M. Aichhorn, L. Pourovskii, V. Vildosola, M. Ferrero, O. Parcollet, T. Miyake, A. Georges, and S. Biermann, "Dynamical mean-field theory within an augmented plane-wave framework: Assessing electronic correlations in the iron pnictide LaFeAsO," Phys. Rev. B **80**, 085101 (2009).

[131] K. Haule, C.-H. Yee, and K. Kim, "Dynamical mean-field theory within the full-potential methods: Electronic structure of $CeIrIn_5$, $CeCoIn_5$, and $CeRhIn_5$," Phys. Rev. B **81**, 195107 (2010).

[132] M. Schüler, O. E. Peil, G. J. Kraberger, R. Pordzik, M. Marsman, G. Kresse, T. O. Wehling, and M. Aichhorn, "Charge self-consistent many-body corrections using optimized projected localized orbitals," J. Phys.: Conden. Matter **30**, 475901 (2018).

[133] V. M. Galitskii and A. B. Migdal, "Application of quantum field theory methods to the many body problem," Sov. Phys. JETP **7** (1958).

[134] M. Aichhorn, L. Pourovskii, and A. Georges, "Importance of electronic correlations for structural and magnetic properties of the iron pnictide superconductor LaFeAsO," Phys. Rev. B **84**, 054529 (2011).

[135] C. Martin, *Interplay of Spin-Orbit Coupling and Electronic Coulomb Interactions in Strontium Iridate* Sr_2IrO_4, PhD Thesis, Centre de Physique Théorique [CPhT] (2010).

[136] L. M. Sandratskii and P. G. Guletskii, "Symmetrised method for the calculation of the band structure of noncollinear magnets," Journal of Physics F: Metal Physics **16**, L43–L48 (1986).

[137] I. A. Nekrasov, G. Keller, D. E. Kondakov, A. V. Kozhevnikov, T. Pruschke, K. Held, D. Vollhardt, and V. I. Anisimov, "Comparative study of correlation effects in $CaVO_3$ and $SrVO_3$," Phys. Rev. B **72**, 155106 (2005).

[138] A. Sekiyama, H. Fujiwara, S. Imada, S. Suga, H. Eisaki, S. I. Uchida, K. Takegahara, H. Harima, Y. Saitoh, I. A. Nekrasov, G. Keller, D. E. Kondakov, A. V. Kozhevnikov, T. Pruschke, K. Held, D. Vollhardt, and V. I. Anisimov, "Mutual Experimental and Theoretical Validation of Bulk Photoemission Spectra of $Sr_{1-x}Ca_xVO_3$," Phys. Rev. Lett. **93**, 156402 (2004).

[139] I. A. Nekrasov, K. Held, G. Keller, D. E. Kondakov, T. Pruschke, M. Kollar, O. K. Andersen, V. I. Anisimov, and D. Vollhardt, "Momentum-resolved spectral functions of $SrVO_3$ calculated by LDA+DMFT," Phys. Rev. B **73**, 155112 (2006).

[140] K. Byczuk, M. Kollar, K. Held, Y.-F. Yang, I. A. Nekrasov, T. Pruschke, and D. Vollhardt, "Kinks in the dispersion of strongly correlated electrons," Nat. Phys. **3**, 168 (2007).

[141] J. M. Tomczak, M. Casula, T. Miyake, F. Aryasetiawan, and S. Biermann, "Combined GW and dynamical mean-field theory: Dynamical screening effects in transition metal oxides," Europhys. Lett. **100**, 67001 (2012).

[142] T. Yoshida, M. Hashimoto, T. Takizawa, A. Fujimori, M. Kubota, K. Ono, and H. Eisaki, "Mass renormalization in the bandwidth-controlled Mott-Hubbard systems $SrVO_3$ and $CaVO_3$ studied by angle-resolved photoemission spectroscopy," Phys. Rev. B **82**, 085119 (2010).

[143] S. Aizaki, T. Yoshida, K. Yoshimatsu, M. Takizawa, M. Minohara, S. Ideta, A. Fujimori, K. Gupta, P. Mahadevan, K. Horiba, H. Kumigashira, and M. Oshima, "Self-Energy on the Low- to High-Energy Electronic Structure of Correlated Metal $SrVO_3$," Phys. Rev. Lett. **109**, 056401 (2012).

[144] H. F. Pen, M. Abbate, A. Fuijmori, Y. Tokura, H. Eisaki, S. Uchida, and G. A. Sawatzky, "Electronic structure of $Y_{1-x}Ca_xVO_3$ studied by high-energy spectroscopies," Phys. Rev. B **59**, 7422–7432 (1999).

[145] J. Laverock, B. Chen, K. E. Smith, R. P. Singh, G. Balakrishnan, M. Gu, J. W. Lu, S. A. Wolf, R. M. Qiao, W. Yang, and J. Adell, "Resonant Soft-X-Ray Emission as a Bulk Probe of Correlated Electron Behavior in Metallic $Sr_xCa_{1-x}VO_3$," Phys. Rev. Lett. **111**, 047402 (2013).

[146] L. Boehnke, F. Nilsson, F. Aryasetiawan, and P. Werner, "When strong correlations become weak: Consistent merging of *GW* and DMFT," Phys. Rev. B **94**, 201106 (2016).

[147] T. Dey, A. Maljuk, D. V. Efremov, O. Kataeva, S. Gass, C. G. F. Blum, F. Steckel, D. Gruner, T. Ritschel, A. U. B. Wolter, J. Geck, C. Hess, K. Koepernik, J. van den Brink, S. Wurmehl, and B. Büchner, "Ba_2YIrO_6: A cubic double perovskite material with Ir^{5+} ions," Phys. Rev. B **93**, 014434 (2016).

[148] C. Martins, M. Aichhorn, and S. Biermann, "Coulomb correlations in 4d and 5d oxides from first principles—or how spin–orbit materials choose their effective orbital degeneracies," Journal of Physics: Condensed Matter **29**, 263001 (2017).

[149] A. D. Becke and K. E. Edgecombe, "A simple measure of electron localization in atomic and molecular systems," The Journal of chemical physics **92**, 5397–5403 (1990).

[150] A. Savin, O. Jepsen, J. Flad, O. K. Andersen, H. Preuss, and H. G. von Schnering, "electron localization in solid-state structures of the elements: the diamond structure," .

[151] T. Burnus, M. A. L. Marques, and E. K. U. Gross, "Time-dependent electron localization function," Phys. Rev. A **71**, 010501 (2005).

[152] M. Kohout and A. Savin, "Influence of core–valence separation of electron localization function," Journal of Computational Chemistry **18**, 1431–1439 (1997).

[153] M. Kohout, F. R. Wagner, and Y. Grin, "Electron localization function for transition-metal compounds," Theoretical Chemistry Accounts **108**, 150–156 (2002).

[154] Z. Zhong, M. Wallerberger, J. M. Tomczak, C. Taranto, N. Parragh, A. Toschi, G. Sangiovanni, and K. Held, "Electronics with Correlated Oxides: $SrVO_3$/$SrTiO_3$ as a Mott Transistor," Phys. Rev. Lett. **114**, 246401 (2015).

[155] K. Yoshimatsu, T. Okabe, H. Kumigashira, S. Okamoto, S. Aizaki, A. Fujimori, and M. Oshima, "Dimensional-crossover-driven metal-insulator transition in $SrVO_3$ ultrathin films," Phys. Rev. Lett. **104**, 147601 (2010).

[156] M. Gu, S. A. Wolf, and J. Lu, "Two-dimensional Mott insulators in $SrVO_3$ ultrathin films," Adv. Mater. Interfaces **1**, 1300126 (2014).

[157] S. Bhandary, E. Assmann, M. Aichhorn, and K. Held, "Charge self-consistency in density functional theory combined with dynamical mean field theory: k-space reoccupation and orbital order," Phys. Rev. B **94**, 155131 (2016).

[158] A. Hampel, S. Beck, and C. Ederer, "Effect of charge self-consistency in DFT + DMFT calculations for complex transition metal oxides," Phys. Rev. Research **2**, 033088 (2020).

[159] S. Beck, G. Sclauzero, U. Chopra, and C. Ederer, "Metal-insulator transition in $CaVO_3$ thin films: Interplay between epitaxial strain, dimensional confinement, and surface effects," Phys. Rev. B **97**, 075107 (2018).

[160] G. Sclauzero, K. Dymkowski, and C. Ederer, "Tuning the metal-insulator transition in d^1 and d^2 perovskites by epitaxial strain: A first-principles-based study," Phys. Rev. B **94**, 245109 (2016).

[161] P. Seth, I. Krivenko, M. Ferrero, and O. Parcollet, "TRIQS/CTHYB: A continuous-time quantum Monte Carlo hybridisation expansion solver for quantum impurity problems," Comp. Phys. Commun. **200**, 274 (2016).

[162] A. Kreyssig, M. A. Green, Y. Lee, G. D. Samolyuk, P. Zajdel, J. W. Lynn, S. L. Bud'ko, M. S. Torikachvili, N. Ni, S. Nandi, J. B. Leão, S. J. Poulton, D. N. Argyriou, B. N. Harmon, R. J. McQueeney, P. C. Canfield, and A. I. Goldman, "Pressure-induced volume-collapsed tetragonal phase of $CaFe_2As_2$ as seen via neutron scattering," Phys. Rev. B **78**, 184517 (2008).

[163] S. L. Bud'ko, X. Ma, M. Tomić, S. Ran, R. Valentí, and P. C. Canfield, "Transition to collapsed tetragonal phase in $CaFe_2As_2$ single crystals as seen by ^{57}Fe Mössbauer spectroscopy," Phys. Rev. B **93**, 024516 (2016).

[164] J. T. Sypek, H. Yu, K. J. Dusoe, G. Drachuck, H. Patel, A. M. Giroux, A. I. Goldman, A. Kreyssig, P. C. Canfield, S. L. Bud'ko, *et al.*, "Superelasticity and cryogenic linear shape memory effects of $CaFe_2As_2$," Nature Communications **8**, 1–9 (2017).

[165] S. R. Saha, N. P. Butch, T. Drye, J. Magill, S. Ziemak, K. Kirshenbaum, P. Y. Zavalij, J. W. Lynn, and J. Paglione, "Structural collapse and superconductivity in rare-earth-doped $CaFe_2As_2$," Phys. Rev. B **85**, 024525 (2012).

[166] S. Knöner, E. Gati, S. Köhler, B. Wolf, U. Tutsch, S. Ran, M. S. Torikachvili, S. L. Bud'ko, P. C. Canfield, and M. Lang, "Combined effects of Sr substitution and pressure on the ground states in $CaFe_2As_2$," Phys. Rev. B **94**, 144513 (2016).

[167] S. Ran, S. L. Bud'ko, W. E. Straszheim, and P. C. Canfield, "Combined effects of transition metal (Ni and Rh) substitution and annealing/quenching on the physical properties of $CaFe_2As_2$," Phys. Rev. B **90**, 054501 (2014).

[168] M. Nohara and K. Kudo, "Arsenic chemistry of iron-based superconductors and strategy for novel superconducting materials," Advances in Physics: X **2**, 450–461 (2017).

[169] R. Pobel, R. Frankovsky, and D. Johrendt, "Ferromagnetism and the Formation of Interlayer As2 Dimers in $Ca(Fe_{1-x}Ni_x)2As_2$," Zeitschrift für Naturforschung B **68**, 581–586 (2013).

[170] L. Ortenzi, H. Gretarsson, S. Kasahara, Y. Matsuda, T. Shibauchi, K. D. Finkelstein, W. Wu, S. R. Julian, Y.-J. Kim, I. I. Mazin, and L. Boeri, "Structural Origin of the Anomalous Temperature Dependence of the Local Magnetic Moments in the $CaFe_2As_2$ Family of Materials," Phys. Rev. Lett. **114**, 047001 (2015).

[171] R. Yang, C. Le, L. Zhang, B. Xu, W. Zhang, K. Nadeem, H. Xiao, J. Hu, and X. Qiu, "Formation of As-As bond and its effect on absence of superconductivity in the collapsed tetragonal phase of $Ca_{0.86}Pr_{0.14}Fe_2As_2$: An optical spectroscopy study," Phys. Rev. B **91**, 224507 (2015).

[172] A. van Roekeghem, P. Richard, X. Shi, S. Wu, L. Zeng, B. Saparov, Y. Ohtsubo, T. Qian, A. S. Sefat, S. Biermann, and H. Ding, "Tetragonal and collapsed-tetragonal phases of $CaFe_2As_2$: A view from angle-resolved photoemission and dynamical mean-field theory," Phys. Rev. B **93**, 245139 (2016).

[173] R. S. Dhaka, R. Jiang, S. Ran, S. L. Bud'ko, P. C. Canfield, B. N. Harmon, A. Kaminski, M. Tomić, R. Valentí, and Y. Lee, "Dramatic changes in the electronic structure upon transition to the collapsed tetragonal phase in $CaFe_2As_2$," Phys. Rev. B **89**, 020511 (2014).

[174] J. Diehl, S. Backes, D. Guterding, H. O. Jeschke, and R. Valentí, "Correlation effects in the tetragonal and collapsed-tetragonal phase of $CaFe_2As_2$," Phys. Rev. B **90**, 085110 (2014).

[175] S. Mandal, R. E. Cohen, and K. Haule, "Pressure suppression of electron correlation in the collapsed tetragonal phase of $CaFe_2As_2$: A DFT-DMFT investigation," Phys. Rev. B **90**, 060501 (2014).

[176] R. Hoffmann and C. Zheng, "Making and breaking bonds in the solid state: the $ThCr_2Si_2$ structure," The Journal of Physical Chemistry **89**, 4175–4181 (1985).

[177] C. Zheng and R. Hoffmann, "Complementary local and extended views of bonding in the $ThCr_2Si_2$ and $CaAl_2Si_2$ structures," Journal of Solid State Chemistry **72**, 58–71 (1988).

[178] E. Stavrou, X. Chen, A. R. Oganov, A. F. Wang, Y. J. Yan, X. G. Luo, X. H. Chen, and A. F. Goncharov, "Formation of As-As Interlayer Bonding in the collapsed tetragonal phase of $NaFe_2As_2$ under pressure," Scientific Reports **5**, 9868 (2015).

[179] T. Yildirim, "Strong Coupling of the Fe-Spin State and the As-As Hybridization in Iron-Pnictide Superconductors from First-Principle Calculations," Phys. Rev. Lett. **102**, 037003 (2009).

[180] E. Cuervo-Reyes and R. Nesper, "Interlayer bonding in compounds with the $\mathbf{ThCr_2Si_2}$-type structure: Insight on the ferromagnetism of $\mathbf{SrCo_2(Ge_{1-x}P}_x)_2$ from electronic structure calculations," Phys. Rev. B **90**, 064416 (2014).

[181] O. E. Peil, A. Hampel, C. Ederer, and A. Georges, "Mechanism and control parameters of the coupled structural and metal-insulator transition in nickelates," Phys. Rev. B **99**, 245127 (2019).

[182] S. Sharma, J. K. Dewhurst, and E. K. U. Gross, "Optical response of extended systems using time-dependent density functional theory," Topics in Current Chemistry **347**, 235—257 (2014).

[183] J. M. Galicia-Hernandez, V. Turkowski, G. Hernandez-Cocoletzi, and T. S. Rahman, "Electron correlations and memory effects in ultrafast electron and hole dynamics in VO_2," Journal of Physics: Condensed Matter **32**, 20LT01 (2020).

[184] A. H. Compton, "A Quantum Theory of the Scattering of X-rays by Light Elements," Phys. Rev. **21**, 483–502 (1923).

[185] J. W. M. Du Mond, "Compton Modified Line Structure and its Relation to the Electron Theory of Solid Bodies," Phys. Rev. **33**, 643–658 (1929).

[186] H. C. Robarts, T. E. Millichamp, D. A. Lagos, J. Laverock, D. Billington, J. A. Duffy, D. O'Neill, S. R. Giblin, J. W. Taylor, G. Kontrym-Sznajd, M. Samsel-Czekała, H. Bei, S. Mu, G. D. Samolyuk, G. M. Stocks, and S. B. Dugdale, "Extreme Fermi Surface Smearing in a Maximally Disordered Concentrated Solid Solution," Phys. Rev. Lett. **124**, 046402 (2020).

[187] D. Billington, A. D. N. James, E. I. Harris-Lee, D. A. Lagos, D. O'Neill, N. Tsuda, K. Toyoki, Y. Kotani, T. Nakamura, H. Bei, S. Mu, G. D. Samolyuk, G. M. Stocks, J. A. Duffy, J. W. Taylor, S. R. Giblin, and S. B. Dugdale, "Bulk and element-specific magnetism of medium-entropy and high-entropy Cantor-Wu alloys," Phys. Rev. B **102**, 174405 (2020).

[188] D. Ernsting, D. Billington, T. E. Millichamp, R. A. Edwards, H. A. Sparkes, N. D. Zhigadlo, S. R. Giblin, J. W. Taylor, J. A. Duffy, and S. B. Dugdale, "Vacancies, disorder-induced smearing of the electronic structure, and its implications for the superconductivity of anti-perovskite $MgC_{0.93}Ni_{2.85}$," Scientific Reports **7**, 1–9 (2017).

[189] Y. Sakurai, Y. Tanaka, A. Bansil, S. Kaprzyk, A. T. Stewart, Y. Nagashima, T. Hyodo, S. Nanao, H. Kawata, and N. Shiotani, "High-Resolution Compton Scattering Study of Li: Asphericity of the Fermi Surface and Electron Correlation Effects," Phys. Rev. Lett. **74**, 2252–2255 (1995).

[190] W. Schülke, C. Sternemann, A. Kaprolat, and G. Döring, "Ultra-high Resolution Compton Scattering of Li Metal: Evaluation with Respect to the Correlation Corrected Occupation Number Density," Zeitschrift für Physikalische Chemie **215**, 1353 (2001).

[191] K. O. Ruotsalainen, J. Inkinen, T. Pylkkänen, T. Buslaps, M. Hakala, K. Hämäläinen, and S. Huotari, "The isotropic Compton profile difference across the phase transition of VO_2," The European Physical Journal B **91**, 225 (2018).

[192] D. Billington, D. Ernsting, T. E. Millichamp, C. Lester, S. B. Dugdale, D. Kersh, J. A. Duffy, S. R. Giblin, J. W. Taylor, P. Manuel, *et al.*, "Magnetic frustration, short-range correlations and the role of the paramagnetic Fermi surface of $PdCrO_2$," Scientific reports **5**, 12428 (2015).

[193] O. Klemperer, "On the annihilation radiation of the positron," Mathematical Proceedings of the Cambridge Philosophical Society **30**, 347–354 (1934).

[194] S. B. Dugdale and J. Laverock, "Recovering the fermi surface with 2d-ACAR spectroscopy in samples with defects," Journal of Physics: Conference Series **505**, 012046 (2014).

[195] J. Laverock, T. D. Haynes, M. A. Alam, and S. B. Dugdale, "Experimental determination of the state-dependent enhancement of the electron-positron momentum density in solids," Phys. Rev. B **82**, 125127 (2010).

[196] S. B. Dugdale, J. Laverock, C. Utfeld, M. A. Alam, T. D. Haynes, D. Billington, and D. Ernsting, "The Bristol HIDAC 2D-ACAR Spectrometer," Journal of Physics: Conference Series **443**, 012083 (2013).

[197] A. Damascelli, "Probing the Electronic Structure of Complex Systems by ARPES," Physica Scripta **T109**, 61 (2004).

[198] M. P. Seah and W. A. Dench, "Quantitative electron spectroscopy of surfaces: A standard data base for electron inelastic mean free paths in solids," Surface and Interface Analysis **1**, 2–11 (1979).

[199] J. D. Koralek, J. F. Douglas, N. C. Plumb, J. D. Griffith, S. T. Cundiff, H. C. Kapteyn, M. M. Murnane, and D. S. Dessau, "Experimental setup for low-energy laser-based angle resolved photoemission spectroscopy," Review of Scientific Instruments **78**, 053905 (2007).

[200] H. Iwasawa, "High-resolution angle-resolved photoemission spectroscopy and microscopy," Electronic Structure **2**, 043001 (2020).

[201] A. Bansil, R. Markiewicz, C. Kusko, M. Lindroos, and S. Sahrakorpi, "Matrix element and strong electron correlation effects in ARPES from cuprates," Journal of Physics and Chemistry of Solids **65**, 1417 – 1421 (2004).

[202] D. Shoenberg, "Theory of the de Haas-van Alphen effect," Journal of Physics F: Metal Physics **18**, 49–61 (1988).

[203] N. Hiraoka, M. Itou, T. Ohata, M. Mizumaki, Y. Sakurai, and N. Sakai, "A new X-ray spectrometer for high-resolution Compton profile measurements at SPring-8," Journal of Synchrotron Radiation **8**, 26–32 (2001).

[204] Y. Sakurai and M. Itou, "A Cauchois-type X-ray spectrometer for momentum density studies on heavy-element materials," Journal of Physics and Chemistry of Solids **65**, 2061–2064 (2004).

[205] J. M. Jauch and F. Rohrlich, *The Theory of Photons and Electrons: The Relativistic Quantum Field Theory of Charged Particles with Spin One-Half*, 2nd ed. (Springer Publishing Company, Incorporated, 2012).

[206] R. Ribberfors and K. F. Berggren, "Incoherent-x-ray-scattering functions and cross sections $(\frac{d\sigma}{d\Omega'})_{\text{incoh}}$ by means of a pocket calculator," Phys. Rev. A **26**, 3325–3333 (1982).

[207] P. Eisenberger and P. M. Platzman, "Compton Scattering of X Rays from Bound Electrons," Phys. Rev. A **2**, 415–423 (1970).

[208] S. Huotari, K. Hämäläinen, S. Manninen, S. Kaprzyk, A. Bansil, W. Caliebe, T. Buslaps, V. Honkimäki, and P. Suortti, "Energy dependence of experimental Be Compton profiles," Phys. Rev. B **62**, 7956–7963 (2000).

[209] S. Huotari, K. Hämäläinen, S. Manninen, A. Issolah, and M. Marangolo, "Asymmetry of Compton profiles," Journal of Physics and Chemistry of Solids **62**, 2205–2213 (2001).

[210] P. Holm, "Relativistic Compton cross section for general central-field Hartree-Fock wave functions," Phys. Rev. A **37**, 3706–3719 (1988).

[211] J. A. Duffy, "What we can learn from magnetic Compton scattering: Application to the determination of spin polarization," Journal of Physics: Conference Series **443**, 012011 (2013).

[212] J. M. Luttinger and J. C. Ward, "Ground-State Energy of a Many-Fermion System. II," Phys. Rev. **118**, 1417–1427 (1960).

[213] J. M. Luttinger, "Fermi Surface and Some Simple Equilibrium Properties of a System of Interacting Fermions," Phys. Rev. **119**, 1153–1163 (1960).

[214] A. Rosch, "Breakdown of Luttinger's theorem in two-orbital Mott insulators," The European Physical Journal B **59**, 495–502 (2007).

[215] T. D. Stanescu, P. Phillips, and T.-P. Choy, "Theory of the Luttinger surface in doped Mott insulators," Phys. Rev. B **75**, 104503 (2007).

[216] L. Lam and P. M. Platzman, "Momentum density and Compton profile of the inhomogeneous interacting electronic system. I. Formalism," Phys. Rev. B **9**, 5122–5127 (1974).

[217] N. Shiotani, Y. Tanaka, Y. Sakurai, N. Sakai, M. Ito, F. Itoh, T. Iwazumi, and H. Kawata, "Compton Scattering Study of Electron Momentum Density in Vanadium," Journal of the Physical Society of Japan **62**, 239–245 (1993).

[218] Y. Sakurai, S. Kaprzyk, A. Bansil, Y. Tanaka, G. Stutz, H. Kawata, and N. Shiotani, "A high-resolution Compton scattering study of Cu: experiment and theory," Journal of Physics and Chemistry of Solids **60**, 905 – 910 (1999).

[219] S. Wakoh and M. Matsumoto, "Correlation correction on Compton profiles of V and Cr," Journal of Physics: Condensed Matter **2**, 797–807 (1990).

[220] S Wakoh and M Matsumoto and M Tokii, "Compton profiles of aluminium corrected by the electron correlation effect," Journal of Physics: Condensed Matter **12**, 9725–9734 (2000).

[221] M. Matsumoto, T. Sano, and S. Wakoh, "Electron Correlation Effect on the Directional Compton Profiles of Mg," Journal of the Physical Society of Japan **68**, 1035–1039 (1999).

[222] Y. Kubo, "Effects of Electron Correlations on Compton Profiles of Li and Na in the *GW* Approximation," Journal of the Physical Society of Japan **66**, 2236–2239 (1997).

[223] Y. Kubo, "Electron correlation effects on Compton profiles of Cr in the *GW* approximation," Journal of Physics and Chemistry of Solids **62**, 2199–2203 (2001).

[224] V. Olevano, A. Titov, M. Ladisa, K. Hämäläinen, S. Huotari, and M. Holzmann, "Momentum distribution and Compton profile by the ab initio GW approximation," Phys. Rev. B **86**, 195123 (2012).

[225] S. M. Khidzir, F. Maulida, and W. A. T. W. Abdullah, "*GW* approximation study of the Compton profile of ZnSe," Radiation Effects and Defects in Solids **172**, 664–677 (2017).

[226] D. Benea, J. Minár, L. Chioncel, S. Mankovsky, and H. Ebert, "Magnetic Compton profiles of Fe and Ni corrected by dynamical electron correlations," Phys. Rev. B **85**, 085109 (2012).

[227] L. Chioncel, D. Benea, H. Ebert, I. Di Marco, and J. Minár, "Momentum space anisotropy of electronic correlations in Fe and Ni: An analysis of magnetic Compton profiles," Phys. Rev. B **89**, 094425 (2014).

[228] L. Chioncel, D. Benea, S. Mankovsky, H. Ebert, and J. Minár, "Static corrections versus dynamic correlation effects in the valence band Compton profile spectra of Ni," Phys. Rev. B **90**, 184426 (2014).

[229] D. Benea, J. Minár, H. Ebert, and L. Chioncel, "Magnetic Compton profiles of disordered $Fe_{0.5}Ni_{0.5}$ and ordered FeNi alloys," Phys. Rev. B **97**, 144408 (2018).

[230] M. Brancewicz, M. Pylak, A. Andrejczuk, E. Żukowski, L. Dobrzyński, Y. Sakurai, M. Itou, and H. Sormann, "Compton Profile Study and Electron Momentum Density Reconstruction in Hexagonal Mg," Journal of the Physical Society of Japan **82**, 074702 (2013).

[231] Y. Sakurai, N. Hiraoka, M. Itou, M. Mizumaki, T. Ohata, A. Deb, H. Toyokawa, M. Suzuki, and N. Sakai, "Background noise in a Cauchois-type high-resolution Compton scattering spectrometer at SPring-8," Journal of Physics and Chemistry of Solids **62**, 2099–2102 (2001).

[232] N. Sakai, "Simulation of Compton Double Scatterings of Circularly Polarized -Rays by Magnetic Electrons," Journal of the Physical Society of Japan **56**, 2477–2485 (1987).

[233] F. Biggs, L. B. Mendelsohn, and J. B. Mann, "Hartree-Fock Compton profiles for the elements," Atomic Data and Nuclear Data Tables **16**, 201–309 (1975).

[234] D. Billington, *Electron-phonon superconductivity in Y and La based intermetallics and metallic magnetic frustration in* $PdCrO_2$, PhD Thesis, University of Bristol (2014).

[235] D. Ernsting, *Electron momentum density studies of the electronic structure of complex systems: measurements and ab initio calculations*, PhD Thesis, University of Bristol (2015).

[236] T. E. Millichamp, *A bulk half-metal and an unexpected Fermi surface*, PhD Thesis, University of Bristol (2017).

[237] S. P. Collins, D. Laundy, T. Connolley, G. van der Laan, F. Fabrizi, O. Janssen, M. J. Cooper, H. Ebert, and S. Mankovsky, "On the possibility of using x-ray compton scattering to study magnetoelectrical properties of crystals," Acta Crystallographica Section A: Foundations and Advances **72**, 197–205 (2016).

[238] D. Ernsting, D. Billington, T. Haynes, T. Millichamp, J. Taylor, J. Duffy, S. Giblin, J. Dewhurst, and S. Dugdale, "Calculating electron momentum densities and Compton profiles using the linear tetrahedron method," Journal of Physics: Condensed Matter **26**, 495501 (2014).

[239] C. Guillot, Y. Ballu, J. Paigné, J. Lecante, K. P. Jain, P. Thiry, R. Pinchaux, Y. Pétroff, and L. M. Falicov, "Resonant Photoemission in Nickel Metal," Phys. Rev. Lett. **39**, 1632–1635 (1977).

[240] T. C. Leung, C. T. Chan, and B. N. Harmon, "Ground-state properties of Fe, Co, Ni, and their monoxides: Results of the generalized gradient approximation," Phys. Rev. B **44**, 2923–2927 (1991).

[241] D. E. Eastman, F. J. Himpsel, and J. A. Knapp, "Experimental Band Structure and Temperature-Dependent Magnetic Exchange Splitting of Nickel Using Angle-Resolved Photoemission," Phys. Rev. Lett. **40**, 1514–1517 (1978).

[242] E. Dietz, U. Gerhardt, and C. J. Maetz, "Exchange Splitting in Nickel," Phys. Rev. Lett. **40**, 892–896 (1978).

[243] F. J. Himpsel, J. A. Knapp, and D. E. Eastman, "Experimental energy-band dispersions and exchange splitting for Ni," Phys. Rev. B **19**, 2919–2927 (1979).

[244] D. E. Eastman, F. J. Himpsel, and J. A. Knapp, "Experimental Exchange-Split Energy-Band Dispersions for Fe, Co, and Ni," Phys. Rev. Lett. **44**, 95–98 (1980).

[245] A. I. Lichtenstein, M. I. Katsnelson, and G. Kotliar, "Finite-Temperature Magnetism of Transition Metals: An ab initio Dynamical Mean-Field Theory," Phys. Rev. Lett. **87**, 067205 (2001).

[246] J. Braun, J. Minár, H. Ebert, M. I. Katsnelson, and A. I. Lichtenstein, "Spectral Function of Ferromagnetic 3*d* Metals: A Self-Consistent LSDA + DMFT Approach Combined with the One-Step Model of Photoemission," Phys. Rev. Lett. **97**, 227601 (2006).

[247] J. Sánchez-Barriga, J. Braun, J. Minár, I. Di Marco, A. Varykhalov, O. Rader, V. Boni, V. Bellini, F. Manghi, H. Ebert, M. I. Katsnelson, A. I. Lichtenstein, O. Eriksson, W. Eberhardt, H. A. Dürr, and J. Fink, "Effects of spin-dependent quasiparticle renormalization in Fe, Co, and Ni photoemission spectra: An experimental and theoretical study," Phys. Rev. B **85**, 205109 (2012).

[248] A. Hausoel, M. Karolak, E. Şaşıoğlu, A. Lichtenstein, K. Held, A. Katanin, A. Toschi, and G. Sangiovanni, "Local magnetic moments in iron and nickel at ambient and Earth's core conditions," Nature communications **8**, 1–9 (2017).

[249] M. A. G. Dixon, J. A. Duffy, S. Gardelis, J. E. McCarthy, M. J. Cooper, S. B. Dugdale, T. Jarlborg, and D. N. Timms, "Spin density in ferromagnetic nickel: A magnetic Compton scattering study," Journal of Physics: Condensed Matter **10**, 2759–2771 (1998).

[250] Y. Kubo and S. Asano, "Magnetic Compton profiles of iron and nickel," Phys. Rev. B **42**, 4431–4446 (1990).

[251] D. N. Timms, A. Brahmia, M. J. Cooper, S. P. Collins, S. Hamouda, D. Laundy, C. Kilbourne, and M. C. S. Lager, "Spin dependent anisotropy in the momentum density of ferromagnetic nickel metal," Journal of Physics: Condensed Matter **2**, 3427–3429 (1990).

[252] H. Ebert, "Fully relativistic band structure calculations for magnetic solids - Formalism and Application," in *Electronic Structure and Physical Properties of Solids*, Vol. 535, edited by H. Dreyssé (Springer, Berlin, 2000) p. 191.

[253] H. Ebert and *et al.*, "The Munich SPR-KKR package," https://software.pan-data.eu/software/111/spr-kkr.

[254] J. Minár, L. Chioncel, A. Perlov, H. Ebert, M. I. Katsnelson, and A. I. Lichtenstein, "Multiple-scattering formalism for correlated systems: A KKR-DMFT approach," Phys. Rev. B **72**, 045125 (2005).

[255] F. Aryasetiawan, M. Imada, A. Georges, G. Kotliar, S. Biermann, and A. I. Lichtenstein, "Frequency-dependent local interactions and low-energy effective models from electronic structure calculations," Phys. Rev. B **70**, 195104 (2004).

[256] T. Miyake and F. Aryasetiawan, "Screened Coulomb interaction in the maximally localized Wannier basis," Phys. Rev. B **77**, 085122 (2008).

[257] H. A. Ceeh, J. A. Weber, P. Böni, M. Leitner, D. Benea, L. Chioncel, H. Ebert, J. Minár, D. Vollhardt, and C. Hugenschmidt, "Local electron-electron interaction strength in ferromagnetic nickel determined by spin-polarized positron annihilation," Scientific Reports **6**, 20898 (2016).

[258] I. Di Marco, J. Minár, S. Chadov, M. I. Katsnelson, H. Ebert, and A. I. Lichtenstein, "Correlation effects in the total energy, the bulk modulus, and the lattice constant of a transition metal: Combined local-density approximation and dynamical mean-field theory applied to Ni and Mn," Phys. Rev. B **79**, 115111 (2009).

[259] J. Kolorenč, A. I. Poteryaev, and A. I. Lichtenstein, "Valence-band satellite in ferromagnetic nickel: LDA+DMFT study with exact diagonalization," Phys. Rev. B **85**, 235136 (2012).

[260] F. Aryasetiawan, J. M. Tomczak, T. Miyake, and R. Sakuma, "Downfolded Self-Energy of Many-Electron Systems," Phys. Rev. Lett. **102**, 176402 (2009).

[261] E. Şaşıoğlu, C. Friedrich, and S. Blügel, "Effective Coulomb interaction in transition metals from constrained random-phase approximation," Phys. Rev. B **83**, 121101 (2011).

[262] J. Minár, H. Ebert, and L. Chioncel, "A self-consistent, relativistic implementation of the LSDA+DMFT method," The European Physical Journal Special Topics **226**, 2477–2498 (2017).

[263] L. V. Pourovskii, M. I. Katsnelson, and A. I. Lichtenstein, "Correlation effects in electronic structure of actinide monochalcogenides," Phys. Rev. B **72**, 115106 (2005).

[264] M. T. Czyżyk and G. A. Sawatzky, "Local-density functional and on-site correlations: The electronic structure of La_2CuO_4 and $LaCuO_3$," Phys. Rev. B **49**, 14211–14228 (1994).

[265] J. Minár, S. Mankovsky, O. Šipr, D. Benea, and H. Ebert, "Correlation effects in fcc-Fe_xNi_{1-x} alloys investigated by means of the KKR-CPA," Journal of Physics: Condensed Matter **26**, 274206 (2014).

[266] H. A. Mook, "Magnetic Moment Distribution of Nickel Metal," Phys. Rev. **148**, 495–501 (1966).

[267] H. Danan, A. Herr, and A. J. P. Meyer, "New Determinations of the Saturation Magnetization of Nickel and Iron," Journal of Applied Physics **39**, 669–670 (1968).

[268] J. A. Duffy, J. W. Taylor, S. B. Dugdale, C. Shenton-Taylor, M. W. Butchers, S. R. Giblin, M. J. Cooper, Y. Sakurai, and M. Itou, "Spin and orbital moments in Fe_3O_4," Phys. Rev. B **81**, 134424 (2010).

[269] D. Benea, S. Mankovsky, and H. Ebert, "Fully relativistic description of magnetic Compton profiles with an application to UFe_2," Phys. Rev. B **73**, 094411 (2006).

[270] Y. Kakutani, Y. Kubo, A. Koizumi, N. Sakai, B. L. Ahuja, and B. K. Sharma, "Magnetic Compton Profiles of Fcc-Ni, Fcc-$Fe_{50}Ni_{50}$ and Hcp-Co," Journal of the Physical Society of Japan **72**, 599–606 (2003).

[271] Z. Major, S. Dugdale, R. Watts, J. Laverock, J. Kelly, D. Hedley, and M. Alam, "Refining Fermi surface topologies from ab initio calculations through momentum density spectroscopies," Journal of Physics and Chemistry of Solids **65**, 2011–2016 (2004).

[272] A. Liebsch, "Effect of Self-Energy Corrections on the Valence-Band Photoemission Spectra of Ni," Phys. Rev. Lett. **43**, 1431–1434 (1979).

[273] C. S. Wang and J. Callaway, "Band structure of nickel: Spin-orbit coupling, the Fermi surface, and the optical conductivity," Phys. Rev. B **9**, 4897–4907 (1974).

[274] F. Weling and J. Callaway, "Semiempirical description of energy bands in nickel," Phys. Rev. B **26**, 710–719 (1982).

[275] L. Sponza, P. Pisanti, A. Vishina, D. Pashov, C. Weber, M. van Schilfgaarde, S. Acharya, J. Vidal, and G. Kotliar, "Self-energies in itinerant magnets: A focus on Fe and Ni," Phys. Rev. B **95**, 041112 (2017).

[276] J. Arblaster, *Selected Values of the Crystallographic Properties of Elements* (ASM International, 2018).

[277] R. D. Parker and M. H. Halloran, "Experimental study of the Fermi surface of vanadium," Phys. Rev. B **9**, 4130–4137 (1974).

[278] B. Perić, T. Valla, M. Milun, and P. Pervan, "On the electronic structure of vanadium: the angular resolved photoelectron spectroscopy of V(100) surface," Vacuum **46**, 1181–1183 (1995).

[279] P. Pervan, T. Valla, M. Milun, A. B. Hayden, and D. P. Woodruff, "Photoemission and inverse photoemission spectroscopy of V(100)," Journal of Physics: Condensed Matter **8**, 4195–4204 (1996).

[280] N. Shiotani, T. Okada, T. Mizoguchi, and H. Sekizawa, "Angular Distribution of Positron Annihilation Radiation in Vanadium and Niobium-Experiment," Journal of the Physical Society of Japan **38**, 423–430 (1975).

[281] S. Wakoh, Y. Kubo, and J. Yamashita, "Angular Distribution of Positron Annihilation Radiation in Vanadium and Niobium-Theory," Journal of the Physical Society of Japan **38**, 416–422 (1975).

[282] A. A. Manuel, R. Sachot, P. Descouts, M. Peter, R. M. Singru, and A. K. Singh, "Study of the electron momentum distribution in vanadium by positron annihilation," Solid State Communications **45**, 799–801 (1983).

[283] A. K. Singh and R. M. Singru, "Application of the Lock-Crisp-West theorem to vanadium and paramagnetic chromium," Journal of Physics F: Metal Physics **14**, 1751–1760 (1984).

[284] A. K. Singh, A. A. Manuel, R. M. Singru, R. Sachot, E. Walker, P. Descouts, and M. Peter, "Electron momentum distribution and Fermi surface of vanadium studied by positron annihilation," Journal of Physics F: Metal Physics **15**, 2375–2396 (1985).

[285] M. Matsumoto and S. Wakoh, "Two-Dimensional Angular Correlation Distributions of Positron Annihilation Radiation in Vanadium and Chromium," Journal of the Physical Society of Japan **55**, 3948–3959 (1986).

[286] L. M. Pecora, A. C. Ehrlich, A. A. Manuel, A. K. Singh, M. Peter, and R. M. Singru, "Momentum density of vanadium: A reconstruction from two-dimensional positron-annihilation data," Phys. Rev. B **37**, 6772–6782 (1988).

[287] S. B. Dugdale, M. A. Alam, H. M. Fretwell, M. Biasini, and D. Wilson, "Application of maximum entropy to extract Fermi surface topology from positron annihilation measurement," Journal of Physics: Condensed Matter **6**, L435–L443 (1994).

[288] R. J. Hughes, S. B. Dugdale, Z. Major, M. A. Alam, T. Jarlborg, E. Bruno, and B. Ginatempo, "Evolution of the Fermi surface and the oscillatory exchange coupling across Cr and Cr-based alloys," Phys. Rev. B **69**, 174406 (2004).

[289] J. A. Weber, D. Benea, W. H. Appelt, H. Ceeh, W. Kreuzpaintner, M. Leitner, D. Vollhardt, C. Hugenschmidt, and L. Chioncel, "Electronic correlations in vanadium revealed by electron-positron annihilation measurements," Phys. Rev. B **95**, 075119 (2017).

[290] D. A. Cardwell and M. J. Cooper, "The effect of exchange and correlation on the agreement between APW and LCAO Compton profiles and experiment," Journal of Physics: Condensed Matter **1**, 9357–9367 (1989).

[291] A. J. Rollason, R. S. Holt, and M. J. Cooper, "Directional Compton profiles and the electron density distribution in vanadium," Philosophical Magazine B **47**, 51–62 (1983).

[292] A. Sihi and S. K. Pandey, "A detailed electronic structure study of Vanadium metal by using different beyond-DFT methods," The European Physical Journal B **93**, 1–8 (2020).

[293] P. Bromiley, "Products and Convolutions of Gaussian Probability Density Functions," (2014).

[294] G. Stollhoff, "Compton Scattering and Electron Correlations in the Transition Metals," Europhysics Letters **29**, 463–468 (1995).

[295] D. G. Lock, V. H. C. Crisp, and R. N. West, "Positron annihilation and Fermi surface studies: a new approach," Journal of Physics F: Metal Physics **3**, 561–570 (1973).

[296] W. L. McMillan, "Transition Temperature of Strong-Coupled Superconductors," Phys. Rev. **167**, 331–344 (1968).

[297] G. S. Knapp and R. W. Jones, "Determination of the electron-phonon enhancement factor from specific-heat data," Phys. Rev. B **6**, 1761–1767 (1972).

[298] E. I. Harris-Lee, A. D. N. James, and S. B. Dugdale, "An investigation of the sensitivity of the Fermi surface to the treatment of exchange and correlation," (2021), arXiv:2103.02532 [cond-mat.str-el] .

[299] E. G. Barbagiovanni, D. J. Lockwood, P. J. Simpson, and L. V. Goncharova, "Quantum confinement in Si and Ge nanostructures: Theory and experiment," Applied Physics Reviews **1**, 011302 (2014).

[300] A. Ashrafi, "Quantum Confinement: An Ultimate Physics of Nanostructures," (American Scientific Publishers, 2011) Chap. 10, pp. 1–67.

[301] L. Colakerol, T. D. Veal, H.-K. Jeong, L. Plucinski, A. DeMasi, T. Learmonth, P.-A. Glans, S. Wang, Y. Zhang, L. F. J. Piper, P. H. Jefferson, A. Fedorov, T.-C. Chen, T. D. Moustakas, C. F. McConville, and K. E. Smith, "Quantized Electron Accumulation States in Indium Nitride Studied by Angle-Resolved Photoemission Spectroscopy," Phys. Rev. Lett. **97**, 237601 (2006).

[302] T.-C. Chiang, "Photoemission studies of quantum well states in thin films," Surf. Sci. Rep. **39**, 181 (2000).

[303] J. Liu, M. Kareev, D. Meyers, B. Gray, P. Ryan, J. W. Freeland, and J. Chakhalian, "Metal-Insulator Transition and Orbital Reconstruction in Mott-Type Quantum Wells Made of $NdNiO_3$," Phys. Rev. Lett. **109**, 107402 (2012).

[304] S. G. Jeong, T. Min, S. Woo, J. Kim, Y.-Q. Zhang, S. W. Cho, J. Son, Y.-M. Kim, J. H. Han, S. Park, H. Y. Jeong, H. Ohta, S. Lee, T. W. Noh, J. Lee, and W. S. Choi, "Phase Instability amid Dimensional Crossover in Artificial Oxide Crystal," Phys. Rev. Lett. **124**, 026401 (2020).

[305] J. K. Kawasaki, C. H. Kim, J. N. Nelson, S. Crisp, C. J. Zollner, E. Biegenwald, J. T. Heron, C. J. Fennie, D. G. Schlom, and K. M. Shen, "Engineering Carrier Effective Masses in Ultrathin Quantum Wells of IrO_2," Phys. Rev. Lett. **121**, 176802 (2018).

[306] K. Yoshimatsu, K. Horiba, H. Kumigashira, T. Yoshida, A. Fujimori, and M. Oshima, "Metallic quantum well states in artificial structures of strongly correlated oxide," Science **333**, 319 (2011).

[307] M. Izumi, Y. Ogimoto, Y. Konishi, T. Manako, M. Kawasaki, and Y. Tokura, "Perovskite superlattices as tailored materials of correlated electrons," Mater. Sci. Eng. B **84**, 53 (2001).

[308] A. Ohtomo and H. Y. Hwang, "A high-mobility electron gas at the $LaAlO_3/SrTiO_3$ heterointerface," Nature **427**, 423 (2004).

[309] H. Y. Hwang, Y. Iwasa, M. Kawasaki, B. Keimer, N. Nagaosa, and Y. Tokura, "Emergent phenomena at oxide interfaces," Nature Mater. **11**, 103 (2012).

[310] J. Chakhalian, J. W. Freeland, A. J. Millis, C. Panagopoulos, and J. M. Rondinelli, "Colloquium: Emergent properties in plane view: Strong correlations at oxide interfaces," Rev. Mod. Phys. **86**, 1189–1202 (2014).

[311] M. Kobayashi, K. Yoshimatsu, E. Sakai, M. Kitamura, K. Horiba, A. Fujimori, and H. Kumigashira, "Origin of the anomalous mass renormalization in metallic quantum well states of strongly correlated oxide $SrVO_3$," Phys. Rev. Lett. **115**, 076801 (2015).

[312] F. Lechermann, "Oxide Heterostructures from a Realistic Many-Body Perspective," in *Handbook of Materials Modeling: Applications: Current and Emerging Materials*, edited by W. Andreoni and S. Yip (Springer International Publishing, Cham, 2018) pp. 1–20.

[313] K. Maiti, D. D. Sarma, M. J. Rozenberg, I. H. Inoue, H. Makino, O. Goto, M. Pedio, and R. Cimino, "Electronic structure of $Ca_{1-x}Sr_xVO_3$: A tale of two energy scales," Europhysics Letters **10**, 246 (2001).

[314] A. Liebsch, "Surface versus Bulk Coulomb Correlations in Photoemission Spectra of $SrVO_3$ and $CaVO_3$," Phys. Rev. Lett. **90**, 096401 (2003).

[315] J. Laverock, J. Kuyyalil, B. Chen, R. P. Singh, B. Karlin, J. C. Woicik, G. Balakrishnan, and K. E. Smith, "Enhanced electron correlations at the $Sr_xCa_{1-x}VO_3$ surface," Phys. Rev. B **91**, 165123 (2015).

[316] H. Ishida, D. Wortmann, and A. Liebsch, "Electronic structure of $SrVO_3$(001) surfaces: A local-density approximation plus dynamical mean-field theory calculation," Phys. Rev. B **73**, 245421 (2006).

[317] A. Ramadan, R. Gould, and A. Ashour, "On the Van der Pauw method of resistivity measurements," Thin Solid Films **239**, 272–275 (1994).

[318] J. Yano and V. K. Yachandra, "X-ray absorption spectroscopy," Photosynthesis research **102**, 241 (2009).

[319] L. J. P. Ament, M. van Veenendaal, T. P. Devereaux, J. P. Hill, and J. van den Brink, "Resonant inelastic x-ray scattering studies of elementary excitations," Rev. Mod. Phys. **83**, 705–767 (2011).

[320] F. M. F. de Groot, M. Grioni, J. C. Fuggle, J. Ghijsen, G. A. Sawatzky, and H. Petersen, "Oxygen 1s x-ray-absorption edges of transition-metal oxides," Phys. Rev. B **40**, 5715–5723 (1989).

[321] M. Kasrai, W. Lennard, R. Brunner, G. Bancroft, J. Bardwell, and K. Tan, "Sampling depth of total electron and fluorescence measurements in Si L- and K-edge absorption spectroscopy," Applied Surface Science **99**, 303–312 (1996).

[322] M. Gu, S. A. Wolf, and J. Lu, "Transport phenomena in $SrVO_3/SrTiO_3$ superlattices," J. Phys. D: Appl. Phys. **51**, 10LT01 (2018).

[323] M. M. Qazilbash, M. Brehm, B.-G. Chae, P.-C. Ho, G. O. Andreev, B.-J. Kim, S. J. Yun, A. V. Balatsky, M. B. Maple, F. Keilmann, H.-T. Kim, and D. N. Basov, "Mott transition in vo2 revealed by infrared spectroscopy and nano-imaging," Science **318**, 1750–1753 (2007).

[324] S. Bhandary and K. Held, "Self-energy self-consistent density functional theory plus dynamical mean field theory," (2019), arXiv:1904.02967v1 [cond-mat.str-el] .

[325] J. Laverock, M. Gu, V. Jovic, J. W. Lu, S. A. Wolf, G. Watson, R. M. Qiao, W. Yang, and K. E. Smith, "Electronic reconstructions at the interface of $SrVO_3$/$SrTiO_3$ superlattices," unpublished (2021).

[326] S. Okamoto, "Anomalous mass enhancement in strongly correlated quantum wells," Phys. Rev. B **84**, 201305 (2011).

[327] H. Oka, Y. Okada, T. Hitosugi, and T. Fukumura, "Two distinct surface terminations of $SrVO_3$ (001) ultrathin films as an influential factor on metallicity," Appl. Phys. Lett. **113**, 171601 (2018).

[328] G. Wang, Z. Wang, M. Meng, M. Saghayezhian, L. Chen, C. Chen, H. Guo, Y. Zhu, E. W. Plummer, and J. Zhang, "Role of disorder and correlations in the metal-insulator transition in ultrathin $SrVO_3$ films," Phys. Rev. B **100**, 155114 (2019).

[329] I. Matsuda, T. Ohta, and H. W. Yeom, "In-plane dispersion of the quantum-well states of the epitaxial silver films on silicon," Phys. Rev. B **65**, 085327 (2002).

[330] K. Yoshimatsu, E. Sakai, M. Kobayashi, K. Horiba, T. Yoshida, A. Fujimori, M. Oshima, and H. Kumigashira, "Determination of the surface and interface phase shifts in metallic quantum well structures of perovskite oxides," Phys. Rev. B **88**, 115308 (2013).

[331] C. H. Ahn, S. Gariglio, P. Paruch, T. Tybell, L. Antognazza, and J.-M. Triscone, "Electrostatic Modulation of Superconductivity in Ultrathin $GdBa_2Cu_3O_{7-x}$ Films," Science **284**, 1152 (1999).

[332] H. Chen, A. J. Millis, and C. A. Marianetti, "Engineering Correlation Effects via Artificially Designed Oxide Superlattices," Phys. Rev. Lett. **111**, 116403 (2013).

[333] S. Samanta, S. B. Mishra, and B. R. K. Nanda, "Quantum well structure of a double perovskite superlattice and formation of a spin-polarized two-dimensional electron gas," Phys. Rev. B **98**, 115155 (2018).

[334] P. Giannozzi, O. Andreussi, T. Brumme, O. Bunau, M. Buongiorno Nardelli, M. Calandra, R. Car, C. Cavazzoni, D. Ceresoli, M. Cococcioni, N. Colonna, I. Carnimeo, A. Dal Corso, S. de Gironcoli, P. Delugas, R. A. DiStasio Jr, A. Ferretti, A. Floris, G. Fratesi, G. Fugallo, R. Gebauer, U. Gerstmann, F. Giustino, T. Gorni, J. Jia, M. Kawamura, H.-Y. Ko, A. Kokalj, E. Küçükbenli, M. Lazzeri, M. Marsili, N. Marzari, F. Mauri, N. L. Nguyen, H.-V. Nguyen, A. Otero-de-la Roza, L. Paulatto, S. Poncé, D. Rocca, R. Sabatini, B. Santra, M. Schlipf, A. P. Seitsonen, A. Smogunov, I. Timrov, T. Thonhauser, P. Umari, N. Vast,

X. Wu, and S. Baroni, "Advanced capabilities for materials modelling with QUANTUM ESPRESSO," J. Phys.: Condens. Matter **29**, 465901 (2017).

[335] N. Parragh, G. Sangiovanni, P. Hansmann, S. Hummel, K. Held, and A. Toschi, "Effective crystal field and Fermi surface topology: A comparison of d- and dp-orbital models," Phys. Rev. B **88**, 195116 (2013).

[336] J. M. Tomczak, M. Casula, T. Miyake, and S. Biermann, "Asymmetry in band widening and quasiparticle lifetimes in $SrVO_3$: Competition between screened exchange and local correlations from combined GW and dynamical mean-field theory GW + DMFT," Phys. Rev. B **90**, 165138 (2014).

[337] G. Rohringer, H. Hafermann, A. Toschi, A. A. Katanin, A. E. Antipov, M. I. Katsnelson, A. I. Lichtenstein, A. N. Rubtsov, and K. Held, "Diagrammatic routes to nonlocal correlations beyond dynamical mean field theory," Rev. Mod. Phys. **90**, 025003 (2018).

[338] M. van Schilfgaarde, T. Kotani, and S. Faleev, "Quasiparticle Self-Consistent GW Theory," Phys. Rev. Lett. **96**, 226402 (2006).

[339] J. M. Tomczak, "QSGW+DMFT: an electronic structure scheme for the iron pnictides and beyond," Journal of Physics: Conference Series **592**, 012055 (2015).

[340] J. M. Tomczak, P. Liu, A. Toschi, G. Kresse, and K. Held, "Merging GW with DMFT and non-local correlations beyond," The European Physical Journal Special Topics **226**, 2565–2590 (2017).